From a better use of instrumentation to new detection methods in NMR and EPR spectroscopy

Jean-Baptiste Verstraete



A thesis presented for the degree of

Doctor of Philosophy

St Peter's College, University of Oxford

Michaelmas term 2022

Abstract

NMR and EPR spectroscopy are two of the most important techniques to get quantitative, structural or dynamical information on molecular systems. After covering the fundamentals of these magnetic resonance techniques, this thesis explores ways to improve the usage of current spectrometers and to create new instruments altogether using different detection methods with quantum sensing.

First, to deal with bandwidth and oscillating magnetic field limitations typically present for ^{19}F nuclei in NMR or unpaired electrons in EPR, improved methods based on frequency-swept pulses are presented. The implementation of the CHORUS sequence in EPR spectroscopy is detailed. New pulse sequences, namely CHORUS-CPMG, PROCHORUS and superposed frequency-swept pulses, are presented in the context of solution-state NMR spectroscopy.

Then, on-the-fly optimisation is proposed as a tool to automate EPR experiments and even develop new ones. A software package, ESR-POISE, was released to allow EPR users with commercial spectrometers to access such methods.

Finally, the construction of a spectrometer which can conduct magnetic resonance at unconventionally small scales thanks to quantum sensors (NV centres) is detailed. After describing design choices for the different elements of the instrument, a focus is made on the static magnetic field with Finite Element Analysis.

Acknowledgements

"[...] s'étant élevés jusqu'à un certain degré où ils nous ont portés, le moindre effort nous fait monter plus haut, et avec moins de peine et moins de gloire nous nous trouvons au-dessus d'eux."

Blaise Pascal à propos des anciens (Traité du vide, 1647), lui-même reposant vraisemblalement sur Bernard de Chartres ici.

First, I want to thank my supervisor Dr. Mohammadali Foroozandeh not only for the excellence of his guidance, but also for the great deal of effort he deployed whenever I requested help.

I am also deeply grateful for the co-supervision of Prof. Tim Claridge who always welcomed my questions and provided insightful feedback.

For his teaching of EPR and apparently limitless patience at the spectrometer, I am greatly indebted to Dr. William Myers from CAESR.

I am grateful to all the members of our research group for great discussions and sitting through my (many) presentations. Dr. Jonathan Yong and Dr. David Goodwin made my job on feedback loop optimisation incredibly easier than it could have been. I am also excited to see what the work conducted with Simon Hulse and Ali Sherzad is going to produce in the future.

I am deeply thankful for Kevin Valentine's assistance, which was critical to the understanding and ordering of the electronics for the NV spectrometer. I am thankful

to Dr. Claudia Tait for feedback on ESR-POISE and to my friend from past material engineering days, Dr. Romain Caniou, for reintroducing me to finite element analysis.

I want to thank the EPSRC Doctoral Training Partnership for their funding support during the course of my DPhil.

I also thank all my former teachers, for allowing to stand on the shoulders of giants. In particular, I appreciate my former engineering school, INSA Rennes, whose quality of education I am realising more and more. For introducing me to academia through the door of tribology, I want to thank Prof. Amílcar Ramalho from the University of Coimbra in Portugal. For trusting me despite my lack of knowledge in NMR, indirectly sparking the work of this thesis, I want to thank my master's project supervisors, Dr. François Kayser and Dr. Beatriz Basterra-Beroiz from Luxembourg. I can confidently say that I would not have felt prepared to enroll in a doctoral program without the effort and time spent by Beatriz to improve my professional and academic skills.

I also want to thank my great friend Gaël who has always incited me to aim higher. I am so grateful for all the friends I met in Oxford, they made my life wonderful over the course of my thesis: my fellow engineer Guglielmo, my paradise lockdown crew Eden, Piyush, Prerna, and Stefanos, other Peter's friends Cat, Leo, Manu, Niamh, Pauline, and Pia to name just a few.

Sarah, thank you so much for all the support and happiness you have brought into my life, I have had so much fun with you and I look forward to many more happy years, miluji tě!

Last but not least, I thank my family whom I love very dearly: the three best sisters, Anne-Marie, Jeanne and Guillemette for their unconditional love, my parents and my grandparents for teaching me far more important lessons than available in any syllabus. Je vous aime très fort, gros bisous à tous!

Contents

List of publications and presentations **ix**

List of Figures **xi**

List of Tables **xiv**

Acronyms **xv**

Introduction **1**

1 Magnetic resonance fundamentals **4**

1.1 Magnetic resonance theory 4

1.1.1 Spin 4

1.1.2 Spin system quantum description 5

1.1.3 Zeeman interactions 6

1.1.4 Spin-spin interactions 9

1.1.5 Density operator 10

1.2 Experiment basics 13

1.2.1 Oscillating magnetic field $\boldsymbol{B_1}$ 13

1.2.2 Excitation and inversion pulses 15

1.2.3 Offset evolution during delays 16

1.2.4 Offset refocusing 17

1.2.5 Coupling evolution 19

1.3 Data acquisition, processing and analysis 21

1.3.1 Signal detection . . . 21
1.3.2 Frequency domain and post-processing . . . 23
1.3.3 Analysis . . . 25
1.4 Relaxation . . . 28
1.4.1 Longitudinal relaxation . . . 29
1.4.2 Transverse relaxation . . . 29
1.5 Experiment examples . . . 31
1.5.1 Relaxation time measurements . . . 31
1.5.2 Perfect-echo . . . 33
1.5.3 DEER . . . 35
1.5.4 EDNMR . . . 37

2 Frequency-swept pulse sequences design and implementation 39
2.1 Introduction . . . 39
2.2 Theory . . . 42
2.2.1 Definition and parametrisation . . . 42
2.2.2 Spin dynamics simulation . . . 45
2.2.3 Adiabaticity factor, peak amplitude, and flip angle . . . 47
2.2.4 Pulse compression . . . 49
2.2.5 Offset refocusing with instantaneous flip approximation . . . 51
2.2.6 Off-resonance effects and phase roll . . . 55
2.3 ESR spectroscopy: CHORUS implementation . . . 59
2.3.1 Background . . . 59
2.3.2 Materials and methods . . . 59
2.3.3 Sequence parametrisation and calibration . . . 65
2.3.4 x-LiPc at X-band . . . 70
2.3.5 Bisnitroxide at Q-band . . . 71
2.4 NMR spectroscopy: design of new schemes . . . 74
2.4.1 Background . . . 74

2.4.2 Materials and methods . . . 76
2.4.3 CHORUS-CPMG . . . 79
2.4.4 PROCHORUS . . . 81
2.4.5 Sequences overlap . . . 88
2.5 Outlook . . . 93

3 On-the-fly optimisation of ESR experiments 94
3.1 Introduction . . . 94
3.2 Materials and methods . . . 96
3.2.1 ESR-POISE software . . . 96
3.2.2 Pulse simulation and generation . . . 96
3.2.3 Sample and hardware . . . 97
3.2.4 Experiments . . . 98
3.2.5 Data processing . . . 99
3.3 Basic application examples . . . 100
3.3.1 Optimisation of a single parameter . . . 100
3.3.2 Optimisation of multiple parameters . . . 102
3.4 Advanced application examples . . . 104
3.4.1 DEER pump pulse . . . 104
3.4.2 Hardware compensation . . . 107
3.5 Outlook . . . 111

4 Design of a spectrometer with NV centres as quantum sensors 112
4.1 Introduction . . . 112
4.2 General design . . . 116
4.2.1 Diamond . . . 116
4.2.2 Static magnetic field . . . 117
4.2.3 Optical excitation . . . 119
4.2.4 MW pumping & fluorescence detection . . . 122
4.3 Field homogeneity study with FEA . . . 123

4.3.1 Introduction . . . 123
4.3.2 Theory . . . 123
4.3.3 Methods . . . 125
4.3.4 Results and discussion . . . 128
4.3.5 Study conclusion . . . 131
4.4 Outlook . . . 132

Summary **133**

Appendices **135**

A Software packages for FS pulse sequence design . . . 136
A.1 Pulse generation in MATLAB with `MRChirpLab` . . . 136
A.2 Pulse generation in PYTHON with `mrpypulse` . . . 141
B B_1-sensitivity maps . . . 144
C Optimal control pulse in ESR spectroscopy . . . 146
C.1 Background . . . 146
C.2 Materials and methods . . . 146
C.3 Results . . . 147
C.4 Outlook . . . 148
D ESR-POISE user Guide . . . 149
D.1 Presentation . . . 149
D.2 Installation . . . 150
D.3 Set up an optimisation . . . 153
D.4 Run an optimisation . . . 158
D.5 Built-in parameters . . . 159
D.6 Modules . . . 160
D.7 Troubleshoot . . . 169
E Optimisation tables . . . 171
E.1 Signal phase setup . . . 171
E.2 MPFU channels phase setup . . . 172

E.3 Magnetic field tweak 173
E.4 Flip angle calibration 173
E.5 CHORUS amplitudes setup 174
E.6 DEER pump pulse optimisation 174
E.7 CHORUS hardware compensation 175
F NV spectrometer inventory 176
G NV spectrometer additional views 181

List of publications and presentations

Some of the content of this dissertation, in particular the chapters 2 and 3, has been presented elsewhere in the forms indicated below.

Publications

- Verstraete J.-B., Myers W. K., Foroozandeh M. Chirped ordered pulses for ultra-broadband ESR spectroscopy. *The Journal of Chemical Physics*, **154**, 094201 (2021)
- Verstraete J.-B., Foroozandeh M. Improved design of frequency-swept pulse sequences. *Journal of Magnetic Resonance*, 107146 (2022)
- Verstraete J.-B., Yong J. R. J., Goodwin D. L., Myers W. K., Foroozandeh M. Towards fully optimised and automated ESR spectroscopy. *Chemical Communications* (2022)

Talks

- Verstraete J.-B., Myers W. K., Foroozandeh M. A chorus of chirps for broadband ESR spectroscopy. *RSC ESR annual meeting*, Cardiff, United Kingdom, April 2021.
- Verstraete J.-B., Yong J. R. J., Goodwin D. L., Myers W. K., Foroozandeh M. On-the-fly optimisation of ESR with POISE. *RSC ESR annual meeting*, St Andrews,

United Kingdom, June 2022.

- Verstraete J.-B. Magnetic resonance methods developments *AstraZeneca Third Year DPhil and Fourth Year CDT DPhil Talks*, Oxford, United Kingdom, June 2022.
- Verstraete J.-B., Yong J. R. J., Goodwin D. L., Myers W. K., Foroozandeh M. On-the-fly optimisation of ESR experiments. *EUROMAR*, Utrecht, Netherlands, July 2022.

Posters

- Verstraete J.-B., Yong J. R. J., Goodwin D. L., Myers W. K., Foroozandeh M. Automated Optimisation of ESR experiments with POISE. *RSC ESR annual meeting*, St Andrews, United Kingdom, June 2022.
- Verstraete J.-B., Foroozandeh M. Improved frequency-swept pulse sequences for broadband B_1-tolerant magnetic resonance applications. *NMR DG Postgraduate meeting*, Manchester, United Kingdom, June 2022.
- Verstraete J.-B., Foroozandeh M. Improved frequency-swept pulse sequences. *EUROMAR*, Utrecht, Netherlands, July 2022.

List of Figures

1.1 Scheme of pulse acquire, Hahn-echo and Hahn-echo field-sweep 19
1.2 Example of experimental NMR FID 22
1.3 Synthetic signal for a single offset in time- and frequency-domain . . . 24
1.4 Simulated pulse-acquire spectrum for coupled spins 25
1.5 Example of simulated spectrum for an anisotropic spin system 26
1.6 Example of multiplet J-modulation with Hahn-echo 27
1.7 Example of simulated spectrum for a nitroxide 28
1.8 Scheme of sequences for relaxation times measurements 31
1.9 Scheme of the perfect-echo sequence and its CPMG version 33
1.10 Example of multiplet J-modulation suppression with perfect-echo . . . 35
1.11 Scheme of the 4-pulse DEER sequence and example of DEER trace . . 37
1.12 Scheme of EDNMR sequence and spectrum 38

2.1 Illustration of basic frequency-swept pulse properties 40
2.2 Chirped and HS^1 pulses representations 44
2.3 Effect of TBP on simulated inversion profiles 50
2.4 Sketch of offset evolution for frequency-swept pulse sequences 53
2.5 Representation and y-magnetisation maps of KB and CHORUS 56
2.6 KB and CHORUS phase correction with polynomial fitting 57
2.7 ESR samples structures 62
2.8 Resonators and receiver profiles, AWG non-linearity 66
2.9 CHORUS profile simulation for ESR implementation 67
2.10 Calibration maps for KB and CHORUS implementation in ESR 69

2.11 X-band x-LiPc profiles 70
2.12 Q-band bisnitroxide spectra 72
2.13 Further comparison of Q-band bisnitroxide spectra from KB and CHORUS 72
2.14 Scheme of the CHEESY CHORUS sequence 73
2.15 CHEESY CHORUS spectrum of bisnitroxide 74
2.16 Cartesian representation of KB-CPMG and CHORUS-CPMG 79
2.17 B_1 spatial distribution used for simulation 80
2.18 Simulated and experimental profiles for KB-CPMG and CHORUS-CPMG 80
2.19 T_2 decays obtained with KB-CPMG and CHORUS-CPMG 81
2.20 Simulated excitation profiles of two compressed CHORUS versions . . . 82
2.21 Sketch of PROCHORUS with chemical shifts and J-couplings evolution 83
2.22 Representation of PROCHORUS sequences 85
2.23 Simulated excitation profiles of PROCHORUS on coupled spins 86
2.24 Experimental excitation profiles of PROCHORUS on coupled spins . . 87
2.25 Representation of sequences with superposed and non-superposed FS pulses 89
2.26 Simulated excitation profile of overlapped chirped pulse sequences . . . 90
2.27 Simulated excitation profile of overlapped HS^1 pulse sequences 91
2.28 Experimental excitation profile of overlapped HS^1 pulse sequences . . . 91

3.1 Flowchart for feedback loop optimisation with ESR-POISE 95
3.2 Scheme of single parameter optimisation basic examples 100
3.3 Scheme of multiple parameters optimisation basic examples 102
3.4 Flip angle optimisation and grid search results 103
3.5 Scheme of DEER pump pulse optimisation 104
3.6 Simulated profiles for 4-pulse DEER observer and pump pulses 105
3.7 Experimental DEER traces before and after optimisation 106
3.8 Scheme of CHORUS compensation with ESR-POISE 108
3.9 Simulation of excitation profiles for CHORUS pulses compensation . . . 109
3.10 CHORUS representation before and after ESR-POISE compensation. . 109

3.11 CHORUS optimisations experimental results 110
3.12 CHORUS optimisations second set of experimental results 110

4.1 Schemes of NV centre and its energy level diagram 113
4.2 Scheme of NV magnetometry basic sequence principle 115
4.3 Close up views of diamond prism and sample 117
4.4 Right and front view of the static magnetic field system 118
4.5 Scheme of the NV spectrometer optic path 119
4.6 NV spectrometer optical table views 121
4.7 FEA study geometry setup and generated mesh 126
4.8 Results of geometric parameters study: 2D slices 129
4.9 Results of geometric parameters study: B_0 variation 130
4.10 Results of geometric parameters study: inhomogeneity variation 131

A.1 UML diagram of `mrpypulse` module 143

B.1 B_1-sensitivity maps for 1.53 ms and 3 ms CHORUS 144
B.2 B_1-sensitivity maps for chirped pulse sequence with and without overlap 144
B.3 B_1-sensitivity maps for HS^1 pulse sequences with and without overlap . 145

C.1 ESCALADE excitation pulse results 147

D.1 Flowchart of ESR-POISE optimisation with modules 160

G.1 NV spectrometer overall views 181
G.2 NV spectrometer optic table top views 182

List of Tables

1.1 Set of 16 operators describing a two-spin system 20

2.1 Summary of some existing frequency-swept pulse schemes 58
2.2 Parameters for CHORUS and KB sequence generation 60
2.3 Parameters for CHORUS and KB pulse generation at X-band 60
2.4 Parameters for CHORUS and KB pulse generation at Q-band 61
2.5 Summary of results for overlap potential of common FS schemes 92

3.1 Parameters for CHORUS pulse generation for ESR-POISE 97

E.1 Results of coarse signal phase optimisation 171
E.2 Results of fine signal phase optimisation 172
E.3 Results of single MPFU channel phase optimisation 172
E.4 Results of four consecutive MPFU channel phase optimisations 173
E.5 Results of static magnetic field optimisation 173
E.6 Results of flip angle calibration optimisation 174
E.7 Results of CHORUS amplitudes setup optimisation 174
E.8 Results of DEER pump pulse selectivity optimisation 175
E.9 Results of CHORUS hardware compensation optimisation 175
F.1 NV spectrometer parts list 176

Acronyms

1D	one Dimensional.
2D	two Dimensional.
3D	three Dimensional.
ABSTRUSE	Adjustable, Broadband, Sech/Tanh Rotation Uniform Selective Excitation.
AC	Alternating Current.
AM	Amplitude-Modulated.
AOM	Acousto-Optic Modulator.
APD	Avalanche PhotoDiode.
AWG	Arbitrary Waveform Generator.
BFGS	Broyden–Fletcher–Goldfarb–Shanno.
BIR	B_1-Insensitive Rotation.
BOBYQA	Bound Optimization BY Quadratic Approximation.
CAD	Computer Aided Design.
CHEESY	Chirped Echo EPR SpectroscopY.
CHORUS	CHirped ORderded pulse for Ultra-broadband Spectroscopy.
COSY	COrrelation SpectroscopY.
CPMG	Carr-Purcell-Meiboom-Gill.
CVD	Chemical Vapour Deposition.
CW	Continuous-Wave.
CYCLOPS	CYCLically Ordered Phase Sequence.

DAQ	Data Acquisition.
DC	Direct Current.
DEER	Double Electron-Electron Resonance.
DNP	Dynamic Nuclear Polarisation.
DOI	Digital Object Identifier.
DSV	Diameter of a Spherical Volume.
ED-EPR	Echo-Detected EPR.
EDNMR	ELDOR-Detected NMR.
ELDOR	Electron-Electron DOuble Resonance.
ENDOR	Electron Nuclear Double Resonance.
EPR	Electron Paramagnetic Resonance.
ESCALADE	Efficient Spin Control using Analytical Lie Algebraic Derivatives.
ESEEM	Electron Spin Echo Envelope Modulation.
ESR	Electron Spin Resonance.
FEA	Finite Element Analysis.
FEM	Finite Element Methods.
FFT	Fast Fourier Transform.
FID	Free Induction Decay.
FM	Frequency-Modulated.
FS	Frequency-Swept.
FT	Fourier Transform.
FWHM	Full Width at Half Maximum.
HMBC	Heteronuclear Multiple Bond Correlation.
HS	Hyperbolic-Secant.
HSQC	Heteronuclear Single-Quantum Coherence.
HTA	High Turning Angle.
I/Q	In-Phase/Quadrature.

INADEQUATE	Incredible Natural Abundance Double QUantum Transfer Experiment.
KB	Kunz-Böhlen or Kunz-Bodenhausen.
MDS	MultiDimensional Search.
MNR	Modulation-to-Noise Ratio.
MPFU	Microwave Pulse Forming Unit.
MRI	Magnetic Resonance Imaging.
MRS	Magnetic Resonance Spectroscopy.
MW	Micro-Wave.
NMR	Nuclear Magnetic Resonance.
NOE	Nuclear Overhauser Effect.
NQR	Nuclear Quadrupole Resonance.
NV	Nitrogen Vacancy.
ODMR	Optically Detected Magnetic Resonance.
OOP	Object-Oriented Programming.
OPSL	Optically Pumped Semiconductor Laser.
PCI	Peripheral Component Interconnect.
PDFO	Powell's Derivative-Free Optimization solvers.
PELDOR	Pulse Electron-Electron DOuble Resonance.
POISE	Parameter Optimisation by Iterative Spectral Evaluation.
PROCHORUS	PeRfect echO CHORUS.
RIDME	Relaxation Induced Dipolar Modulation Enhancement.
RMS	Root Mean Square.
RTC	Reversible Temperature Coefficient.
SIFTER	SIngle Frequency TEchnique for Refocusing dipolar couplings.
SNR	Signal-to-Noise Ratio.
SS-NMR	Solid-State NMR.
TBP	Time Bandwidth Product.

TIR	Total Internal Reflection.
TM	Transmitter Monitor.
TTL	Transistor-Transistor Logic.
TWT	Traveling-Wave Tube.
UML	Unified Modelling Language.
ZFS	Zero-Field Splitting.

Introduction

Magnetic resonance concerns spin, a property of elementary particles, and its "resonance" with an applied static magnetic field. This physical phenomenon can be leveraged by applying electromagnetic waves, called pulses, which allows for the detection of a signal emitted back by the spins.

This signal is rich in information about the studied system and since the discovery of magnetic resonance about 70 years ago, magnetic resonance techniques have found a wide range of applications, in particular for nuclei with Nuclear Magnetic Resonance (NMR) and electrons with Electron Paramagnetic Resonance (EPR), also called Electron Spin Resonance (ESR).

Familiar to the general public through their most common application in medicine in the form of Magnetic Resonance Imaging (MRI), magnetic resonance techniques also play an essential role in helping humans to *see* the extraordinarily small world of atoms and molecules. In particular, whether used for routine checks or cutting-edge research, NMR and EPR spectroscopy are amongst the most important analytical tools for chemists, biologists, physicist, and materials scientists.

The improvement paths for magnetic resonance techniques can be classified in the following ways [1–3]:

- Conventional developments built upon
    - Better usage of current hardware, e.g., with sample preparation, new pulse sequences for data acquisition, or novel data post-processing tools.
    - Increase of the static magnetic field strength for better sensitivity and reso-

lution.
    - Improving the signal measurement devices, for instance with superior oscillating magnetic field properties, or more efficient induction/detection schemes.
    - Hyperpolarization techniques for sensitivity enhancement.
- Unconventional developments relying on fundamentally different detection approaches with
    - Specific methods, e.g. Optically Detected Magnetic Resonance (ODMR) techniques of certain systems.
    - General methods such as the use of quantum sensors to measure the signal emitted by the spins.

This thesis explores the two extremes from the spectrum of magnetic resonance method developments, with two chapters dedicated to advances which rely on commercially available hardware, and one chapter on the construction of a new type of spectrometer. The focus is often made on EPR spectroscopy and solution-state NMR spectroscopy but the concepts developed throughout the dissertation are not restricted to these domains.

With the aim of presenting EPR and NMR spectroscopy together, the first chapter covers the magnetic resonance concepts relevant for the understanding of the rest of the thesis.

In the second chapter, the challenge of building robust experiments for large spectral width and inhomogeneous oscillating magnetic fields is investigated with frequency-swept pulses. After presenting some state-of-the-art sequences thanks to simple descriptions, the application of the CHORUS sequence to EPR spectroscopy is presented. Then, liquid-state NMR spectroscopy is used as a function upon which new sequences such as CHORUS-CPMG, PROCHORUS and superposed frequency-swept sequences are developed.

The third chapter proposes on-the-fly optimisation as a solution to automate standard and non-standard EPR experimental procedures, and even create new ones. To make this technique available to the greatest number of spectroscopists, the user-

friendly package ESR-POISE was developed, and its capacity to conduct on-the-fly optimisation of ESR demonstrated on a variety of experiments.

The fourth chapter explores the idea of using spin itself to detect the magnetic resonance signal from other spins. Such an unconventional approach requires home-built equipment and the chapter details the construction of a spectrometer relying on a quantum sensor, the Nitrogen Vacancy (NV) found in the diamond lattice. Based on the available literature, the design of each of the five systems essential to sensing protocols with NV centres is first addressed. The static magnetic field choice is then supported by Finite Element Analysis (FEA).

Chapter 1

Magnetic resonance fundamentals

This chapter does not describe magnetic resonance exhaustively but rather introduces key concepts for understanding the work of this thesis. Detailed explanations of magnetic resonance techniques and applications can be found in textbooks on NMR [4–7] and EPR [8–10] spectroscopy.

1.1 Magnetic resonance theory

1.1.1 Spin

Spin is a quantum property of particles designating their intrinsic angular momentum. A particle spin is characterised by its spin angular momentum quantum number S which can take integer and half-integer values. This particle spin exhibits $2S + 1$ quantised energy levels and consequently presents $2S$ allowed transitions, potentially exploitable by magnetic resonance techniques to retrieve information on the system.

For example, for $S = 1/2$, there are two states $m_S = -1/2$ and $m_S = +1/2$, which give rise to one energy transition. If $S = 0$, the particle is invisible to magnetic resonance spectroscopy techniques.

Electrons and some nuclei have non-zero intrinsic angular momentum characterised by their spin angular momentum quantum numbers, traditionally denoted S and I

respectively. Particles of interest to magnetic resonance include unpaired e^- ($S = 1/2$), ^{1}H ($I = 1/2$), ^{2}H ($I = 1$), ^{13}C ($I = 1/2$), ^{14}N ($I = 1$), ^{15}N ($I = 1/2$) or ^{19}F ($I = 1/2$). The rest of this chapter proceeds with spin-$\frac{1}{2}$s as most of the thesis deals with such systems. An example of a spin system with total angular momentum higher than 1/2 is described in section 4.1.

1.1.2 Spin system quantum description

Since spin is a quantum property, quantum theory is essential to describe a spin system. The time-dependent version of the Schrödinger equation [11] states that for a wavefunction $|\Psi(t)\rangle$ describing a system at a time t

$$\frac{\partial |\Psi(t)\rangle}{\partial t} = -\frac{\mathrm{i}}{\hbar}\hat{\mathcal{H}} |\Psi(t)\rangle , \tag{1.1}$$

where $\hbar$ is the reduced Planck constant and $\hat{\mathcal{H}}$ is the Hamiltonian, an operator describing the system dynamics. The solution to the Schrödinger equation can be expressed with the energy eigenvalues of $\hat{\mathcal{H}}$, meaning that $\hat{\mathcal{H}}$ describes the spin system. Magnetic resonance experiments can be loosely described as measuring $\hat{\mathcal{H}}$ energy eigenvalues to experimentally characterise spin systems. Such energies are generally presented as their corresponding angular frequencies $\omega = E/\hbar$ and $\hbar$ is therefore dropped from equations.

Quantum theory associates an observable operator $\hat{\boldsymbol{S}}$ to spin (e.g. contained in $\hat{\mathcal{H}}$), which can be expressed by a set of three dimensionless operators $\hat{S}_x$, $\hat{S}_y$, and $\hat{S}_z$.

For a spin-$\frac{1}{2}$, these operators can be expressed in a Cartesian representation with the Pauli spin matrices which are specified here with the identity operator $\hat{E}$ [12]:

$$\hat{S}_x = \frac{1}{2}\begin{bmatrix} 0 & 1 \\ 1 & 0 \end{bmatrix}, \quad \hat{S}_y = \frac{1}{2}\begin{bmatrix} 0 & -\mathrm{i} \\ \mathrm{i} & 0 \end{bmatrix}, \quad \hat{S}_z = \frac{1}{2}\begin{bmatrix} 1 & 0 \\ 0 & -1 \end{bmatrix}, \quad \hat{E} = \begin{bmatrix} 1 & 0 \\ 0 & 1 \end{bmatrix}. \tag{1.2}$$

These will later be useful for computing the dynamics of a spin system during magnetic resonance experiments. In addition, the convenient raising and lowering operators $\hat{S}^+$

and $\hat{S}^-$ can be expressed with

$$\hat{S}^+ = \hat{S}_x + \mathrm{i}\hat{S}_y, \text{ and } \hat{S}^- = \hat{S}_x - \mathrm{i}\hat{S}_y \tag{1.3}$$

1.1.3 Zeeman interactions

The spin energy levels introduced in subsection 1.1.1 are degenerate, meaning that they do not present any exploitable transitions as they are. This degeneracy can however be lifted by the application of a static magnetic field. This splitting of spectral lines, called the Zeeman effect, constitutes the basis of magnetic resonance, where the static magnetic field is conventionally unidirectional and along the axis z, as in $\boldsymbol{B} = (B_x, B_y, B_z) = (0, 0, B_0)$.

Note that "magnetic field flux density" formally designates B (in T) and "magnetic field strength" designates the closely related H (in $\mathrm{A\,m^{-1}}$), where $H = B/\mu_0$ in a vacuum with μ_0 the vacuum magnetic permeability [13]. This difference between B and H is only relevant in subsection 4.3.2 of this thesis. As is common practice in magnetic resonance, the rest of the text therefore uses the z-component of the static magnetic field as the "magnetic field" B_0 (expressed in T).

The Zeeman effect is caused by the interaction of the magnetic field with the magnetic moment of the spins $\hat{\boldsymbol{\mu}} = (\mu_x, \mu_y, \mu_z)$. For a nuclear spin $\hat{\boldsymbol{I}}$

$$\hat{\boldsymbol{\mu}} = \gamma \hat{\boldsymbol{I}}, \tag{1.4}$$

where γ is the gyromagnetic ratio of the spins [12]. For electron spins, the convention of the g-factor (or g value) is normally preferred with $\gamma_e = g_e \mu_B/\hbar$ where μ_B is the Bohr magneton. The Hamiltonian of a single nuclear spin placed in a static magnetic field B_0 is

$$\hat{\mathcal{H}} = -\hat{\boldsymbol{\mu}} \cdot \boldsymbol{B} = -(\mu_x B_x + \mu_y B_y + \mu_z B_z) = -\mu_z B_0 = -\gamma \hat{I}_z B_0. \tag{1.5}$$

The Zeeman interaction is at the centre of Nuclear Magnetic Resonance (NMR) spectroscopy and Electron Paramagnetic Resonance (EPR) spectroscopy, also referred to as Electron Spin Resonance (ESR) spectroscopy.

At equilibrium, the nuclear spin is said to be polarised along z and presents $(2I+1)$ eigenfunctions Ψ_{m_I} such that

$$\hat{I}_z \Psi_{m_I} = m_I \hbar \Psi_{m_I}, \tag{1.6}$$

These also serve as eigenfunctions of the Hamiltonian with

$$\begin{aligned} \hat{\mathcal{H}} \Psi_{m_I} &= -\gamma B_0 \hat{I}_z \Psi_{m_I} \\ &= -m_I \hbar \gamma B_0 \Psi_{m_I}. \end{aligned} \tag{1.7}$$

For $I = 1/2$, the $m_I = +1/2$ and $m_I = -1/2$ eigenstates of $\hat{\mathcal{H}}$, are respectively called α (spin-up) and β (spin-down). Their energies can be expressed as

$$E_\alpha = -\frac{1}{2}\hbar\gamma B_0 \quad \text{and} \quad E_\beta = +\frac{1}{2}\hbar\gamma B_0, \tag{1.8}$$

and create an allowed transition of energy

$$\Delta E_{\alpha\beta} = E_\beta - E_\alpha = \hbar\gamma B_0. \tag{1.9}$$

As mentioned earlier, energies are reported through their frequencies in magnetic resonance. Here, this defines the Larmor frequency

$$\omega_0 = -\gamma B_0, \tag{1.10}$$

expressed in $\mathrm{rad\,s^{-1}}$. At equilibrium, the spin can thus be thought of as precessing along z at the Larmor frequency ω_0. This precession can be viewed as resonance of the spins with the magnetic field, which is linked to the coining of the term magnetic resonance.

Additionally, the magnetic field from the orbitals of nuclei is perturbed by B_0 and can be thought of as a shield acting against it. This consequently modifies the Zeeman interaction depending on the chemical environment of the nucleus. The chemical shielding constant σ describes this effect, as in

$$\hat{\mathcal{H}} = -\gamma(1-\sigma)\hat{I}_z B_0. \tag{1.11}$$

For electrons, the convention of the g-factor $g_e = \hbar\gamma_e/\mu_B$ is preferred for the Zeeman effect. Deviations from this value contain information about the system in a similar way to the chemical shift, but their origin stems from orbital angular momentum and spin-orbit interactions (not further detailed here). The deviations are contained in the g value of the system which gives the Hamiltonian

$$\hat{\mathcal{H}} = \frac{\mu_B g}{\hbar}\hat{S}_z B_0, \tag{1.12}$$

where the negative sign is dropped to report g as a positive quantity ($\gamma_e < 0$ and $g_e < 0$).

In practice, and most notably in solid systems, anisotropy can further split the energy levels and Zeeman interactions need to be described as tensors. For instance, the anisotropic electron spin interaction can be described with the g-tensor $\boldsymbol{g}$. For a single electron, equation (1.12) becomes

$$\hat{\mathcal{H}} = \frac{\mu_B}{\hbar}\boldsymbol{g}\cdot\hat{\boldsymbol{S}}\cdot\boldsymbol{B}, \tag{1.13}$$

where the frame of reference can be chosen such that $\boldsymbol{g}$ is diagonalised as

$$\boldsymbol{g} = \begin{bmatrix} g_x & 0 & 0 \\ 0 & g_y & 0 \\ 0 & 0 & g_z \end{bmatrix}. \tag{1.14}$$

An example of g anisotropy is shown later in figure 1.5, but isotropic interactions are reported in the rest of the text for simplicity.

1.1.4 Spin-spin interactions

Studied systems typically have several spins which can interact which each other in different ways and further split the energy levels. One of the most basic is the dipolar coupling which represents the interaction of the spins as dipoles through space. Assuming that their wavefunctions are well separated, the spins can be approximated as point dipoles. For two nuclear spins $\hat{\boldsymbol{I}}_{\mathbf{1}}$ and $\hat{\boldsymbol{I}}_{\mathbf{2}}$ of the sort which present a dipolar coupling ω_{dd}, the Hamiltonian is

$$\hat{\mathcal{H}} = -\gamma_1(1-\sigma_1)\hat{I}_{1z}B_0 - \gamma_2(1-\sigma_2)\hat{I}_{2z}B_0 - \omega_{dd}(1-3\cos^2\theta)\hat{I}_{1z}\hat{I}_{2z}, \tag{1.15}$$

where θ is the angle between B_0 and the inter-spin vector. This Hamiltonian is simplified with the secular approximation, by neglecting the dipolar non-secular terms (assumes high static magnetic field compared to interaction magnitude) and the dipolar pseudo-secular terms (assumes weak coupling, ω_{dd} much smaller than the difference between the chemical shift terms). The dipolar coupling ω_{dd} is defined as

$$\omega_{dd} = \frac{\mu_0\gamma_1\gamma_2\hbar}{4\pi r^3}, \tag{1.16}$$

in which r is the distance between the spins. This spatial dependence can be used as a ruler, an essential concept for all Nuclear Overhauser Effect (NOE) techniques in NMR [7]. Dipolar couplings between electrons also exists and are the cornerstone of dipolar spectroscopy in EPR [8].

The interaction between a nucleus and an electron spin is grouped in the hyperfine interaction. The Hamiltonian for a nuclear spin $\hat{\boldsymbol{I}}$ and an electron spin $\hat{\boldsymbol{S}}$ with an

isotropic hyperfine coupling a is

$$\hat{\mathcal{H}} = -\gamma(1-\sigma)\hat{I}_z B_0 + \mu_B g \hat{S}_z B_0 + a\hat{\boldsymbol{I}} \cdot \hat{\boldsymbol{S}}. \tag{1.17}$$

As hyperfine couplings are typically not straightforward to measure, EPR spectroscopy uses a range of so-called hyperfine spectroscopy techniques to obtain them.

In a molecule, nuclei can interact through their bonds in what is described as the scalar coupling or J-coupling. For two nuclei $\hat{\boldsymbol{I}}_{\mathbf{1}}$ and $\hat{\boldsymbol{I}}_{\mathbf{2}}$ coupled with J_{12} (in Hz),

$$\hat{\mathcal{H}} = -\gamma_1(1-\sigma_1)\hat{I}_{1z} B_0 - \gamma_2(1-\sigma_2)\hat{I}_{2z} B_0 + 2\pi J_{12}\hat{\boldsymbol{I}}_{\mathbf{1}} \cdot \hat{\boldsymbol{I}}_{\mathbf{2}}. \tag{1.18}$$

Scalar coupling between nuclei of the same nature are called homonuclear couplings, while scalar couplings between nuclei of different nature are called heteronuclear couplings. This interaction is of great importance to NMR spectroscopy. Chemical structure determination methods for liquid-state routinely leverage homonuclear coupling in experiments such as COrrelation SpectroscopY (COSY) or Incredible Natural Abundance Double QUantum Transfer Experiment (INADEQUATE), and heteronuclear couplings in experiments such as Heteronuclear Multiple Bond Correlation (HMBC) or Heteronuclear Single-Quantum Coherence (HSQC) [7].

Examples of other interactions not described here include the exchange interaction or the quadrupolar coupling, present for $I > 1/2$. An example of the Zero-Field Splitting (ZFS) interaction, which occurs when several unpaired electron wavefunctions overlap ($S > 1/2$), is also detailed in section 4.1.

1.1.5 Density operator

In practice, magnetic resonance techniques deal with spin ensembles which are polarised along the B_0 direction z. This polarisation is small and only a statistical average over the sample, giving rise to bulk magnetisation $\boldsymbol{M} = (M_x, M_y, M_z)$.

To get results from quantum theory, which directly relate to the bulk magnetisation

and therefore the magnetic resonance signal, it is practical to introduce the density operator $\hat{\rho}$ defined as

$$\hat{\rho} = \sum_i p_i \left|\Psi_i\right\rangle \left\langle\Psi_i\right|, \tag{1.19}$$

where p_i represent the probability of observing the corresponding state $\langle\Psi_i|$. The density operator can be expressed as a linear combination of the angular momentum operators and unity operator

$$\hat{\rho} = q_E\hat{E} + q_x\hat{S}_x + q_y\hat{S}_y + q_z\hat{S}_z. \tag{1.20}$$

These coefficients directly relate to the spin state which can be measured with magnetic resonance techniques.

For an isolated electron spin at equilibrium in a magnetic field along z, $q_x = 0, q_y = 0$, and the exact value of the constant of proportionality is unimportant such that $q_z = 1$, yielding the density operator

$$\hat{\rho}_{eq} = \hat{S}_z, \tag{1.21}$$

The density operator $\hat{\rho}$ allows for the computation of spin dynamics with the time dependent Liouville-von Neumann equation, which states

$$\frac{\partial\hat{\rho}(t)}{\partial t} = -\mathrm{i}[\hat{\mathcal{H}}(t), \hat{\rho}(t)]. \tag{1.22}$$

For an initial state at $t = 0$ and a final state at $t = t_{\text{fin}}$, the solution to this equation is given by

$$\hat{\rho}(t_{\text{fin}}) = \exp\Big(-\mathrm{i}\hat{\mathcal{H}}t_{\text{fin}}\Big)\hat{\rho}(0)\exp\Big(\mathrm{i}\hat{\mathcal{H}}t_{\text{fin}}\Big) \tag{1.23}$$

for a time invariant Hamiltonian. For example, the Hamiltonian for free evolution of an electron spin at equilibrium is given by $\hat{\mathcal{H}} = \omega_0\hat{S}_z$. For the single spin from equation (1.21), the system evolution for a duration τ is

$$\hat{\rho}(\tau) = \exp\Big(-\mathrm{i}\omega_0\hat{S}_z\tau\Big)\hat{\rho}_{eq}\exp\Big(\mathrm{i}\omega_0\hat{S}_z\tau\Big), \text{ for } n \in \mathbb{N}. \tag{1.24}$$

Using a Taylor's expansion, the exponential term can be expressed as

$$\exp\Big(\mathrm{i}\omega_0\hat{S}_z\tau\Big) = 1 + \mathrm{i}\omega_0\tau\hat{S}_z + \frac{(\mathrm{i}\omega_0\tau)^2\hat{S}_z^2}{2!} + ... + \frac{(\mathrm{i}\omega_0\tau)^n\hat{S}_z^n}{n!}. \tag{1.25}$$

From equation (1.2), it can be inferred that

$$\hat{S}_z^{2k} = \frac{1}{2^{2k}}\hat{E} \quad \text{and} \quad \hat{S}_z^{2k+1} = \frac{1}{2^{2k}}\hat{S}_z, \text{ for } k \in \mathbb{N}. \tag{1.26}$$

These expressions can substitute the even and odd n terms in the exponential expansion, revealing a cosine and a sine Taylor expansion of $\omega_0\tau/2$. These are reduced and the result with the matrix $\hat{E}$ and $\hat{S}_z$ is combined to yield

$$\exp\Big(\mathrm{i}\omega_0\hat{S}_z\tau\Big) = \begin{bmatrix} \cos(\omega_o\tau) + \mathrm{i}\sin(\omega_0\tau) & 0 \\ 0 & \cos(\omega_o\tau) - \mathrm{i}\sin(\omega_0\tau) \end{bmatrix}. \tag{1.27}$$

After an equivalent reasoning for $\exp\Big(-\mathrm{i}\omega_0\hat{S}_z\tau\Big)$, the matrix multiplication result from equation (1.24) can be simplified with the Pythagorean trigonometric identity and gives the density operator

$$\hat{\rho}(\tau) = \frac{1}{2}\begin{bmatrix} 1 & 0 \\ 0 & -1 \end{bmatrix} = \hat{S}_z, \tag{1.28}$$

,

meaning that $\hat{\rho}_{eq}$ does not evolve under $\hat{S}_z$.

Magnetic resonance experiments can be described in the same way, by appending several operations and computing the final density operator. For example, the equation to solve for two time periods t_1 and t_2, which are associated with their respective time-independent, Hamiltonian H_1 and H_2, would be

$$\hat{\rho}(t_1 + t_2) = \exp\Big(-\mathrm{i}\hat{\mathcal{H}}_2 t_2\Big)\exp\Big(-\mathrm{i}\hat{\mathcal{H}}_1 t_1\Big)\hat{\rho}(0)\exp\Big(\mathrm{i}\hat{\mathcal{H}}_1 t_1\Big)\exp\Big(\mathrm{i}\hat{\mathcal{H}}_2 t_2\Big). \tag{1.29}$$

1.2 Experiment basics

Magnetic resonance experiments essentially consist of various spin state manipulations, followed by the recording of the signal from the spin's observable states.

1.2.1 Oscillating magnetic field $\boldsymbol{B_1}$

Magnetic resonance is conventionally detected by induction when the spins precess in the xy-plane and generate a current by induction. To bring the spins in the xy-plane, an oscillating magnetic field $\boldsymbol{B_1}$ is applied orthogonally to $\boldsymbol{B} = (0, 0, B_0)$. For instance, the Hamiltonian for a single nuclear spin $\hat{\boldsymbol{I}}$ is

$$\hat{\mathcal{H}} = -\omega_0 \hat{I}_z - \gamma \hat{\boldsymbol{I}} \cdot \boldsymbol{B_1}. \tag{1.30}$$

Here, we work with a $\boldsymbol{B_1}$ field which is circular polarised and applied in the xy-plane, as in

$$\boldsymbol{B_1} = \begin{pmatrix} B_1 \cos(\omega_c \tau + \phi) \\ B_1 \sin(\omega_c \tau + \phi) \\ 0 \end{pmatrix}, \tag{1.31}$$

where B_1 is the field strength, ω_c the frequency at which $\boldsymbol{B_1}$ is applied (carrier frequency), τ the duration of application, and ϕ is a phase factor. It is assumed here that $\omega_c \ll \omega_1$ to neglect the counter-rotating component of the field.

The $\boldsymbol{B_1}$ field is generally expressed in frequency units with $\boldsymbol{\omega_1} = -\gamma \boldsymbol{B_1}$. The Hamiltonian therefore becomes

$$\hat{\mathcal{H}} = -\omega_0 \hat{I}_z + \omega_1 \left(\cos(\omega_c \tau + \phi) \hat{I}_x + \sin(\omega_c \tau + \phi) \hat{I}_y \right), \tag{1.32}$$

where the field amplitude $\omega_1 = -\gamma B_1$.

To describe experiments, it is practical to transform to a so-called rotating frame, here rotating at the carrier frequency ω_c and used in the rest of the text. This gives a

time-independent Hamiltonian

$$\hat{\mathcal{H}} = -\Omega \hat{I}_z + \omega_1 \left(\cos(\phi) \hat{I}_x + \sin(\phi) \hat{I}_y \right), \tag{1.33}$$

where $\Omega = \omega_0 - \omega_c$ is the offset. In the presence of chemical shift, $\Omega = \omega_0(1-\sigma) - \omega_c$ (in $\mathrm{rad\,s^{-1}}$).

On the spectrometer, $\boldsymbol{\omega_1}$ is applied as a pulse whose parameters can be chosen. For example, a pulse applied on resonance ($\omega_c = \omega_0$) and along x ($\phi = 0$) has a Hamiltonian

$$\hat{\mathcal{H}}_{\mathrm{P},x} = \omega_1 \hat{I}_x. \tag{1.34}$$

For a pulse of duration τ_p, the density operator becomes

$$\begin{aligned} \rho(\tau_p) &= \exp\left(-\mathrm{i}\hat{\mathcal{H}}_{\mathrm{P},x}\tau_p\right)\sigma(0)\exp\left(\mathrm{i}\hat{\mathcal{H}}_{\mathrm{P},x}\tau_p\right) \\ &= \exp\left(-\mathrm{i}\omega_1\tau_p\hat{I}_x\right)\sigma(0)\exp\left(\mathrm{i}\omega_1\tau_p\hat{I}_x\right). \end{aligned} \tag{1.35}$$

With a method similar to the ones applied to solve the evolution of a single spin under free evolution (see equation (1.23) onward), the exponential terms can be expressed as a matrices and the whole expression becomes

$$\begin{aligned} \rho(\tau_p) &= \frac{1}{2}\begin{bmatrix} \cos(\omega_1\tau_p) & \mathrm{i}\sin(\omega_1\tau_p) \\ -\mathrm{i}\sin(\omega_1\tau_p) & -\cos(\omega_1\tau_p) \end{bmatrix} \\ &= \frac{1}{2}\cos(\omega_1\tau_p)\begin{bmatrix} 1 & 0 \\ 0 & -1 \end{bmatrix} + \frac{1}{2}\sin(\omega_1\tau_p)\begin{bmatrix} 0 & \mathrm{i} \\ -\mathrm{i} & 0 \end{bmatrix} \\ &= \cos(\omega_1\tau_p)\hat{I}_z - \sin(\omega_1\tau_p)\hat{I}_y, \end{aligned} \tag{1.36}$$

showing that the pulse can bring the spin in the xy-plane, more precisely on $\hat{I}_y$ here.

Because such pulses are considered to rotate any offset of interest as if it were on resonance, these pulses are referred to as non-selective or hard pulses; in contrast to soft pulses which are selective and do not affect any offset as if it was on resonance.

Additionally, the pulse waveform can be changing in time, forming a so-called shaped pulse. Pulses with a changing amplitude can be referred to as Amplitude-Modulated (AM) pulses while pulses with a changing phase are often called Frequency-Modulated (FM) pulses, as will be further detailed in chapter 2.

1.2.2 Excitation and inversion pulses

Pulses are described more easily with their flip angle

$$\alpha = \omega_1 \tau_p. \tag{1.37}$$

For example, the effect of the pulse on x from equation (1.36) can be written as

$$\rho(\tau_p) = \cos(\alpha)\hat{I}_z - \sin(\alpha)\hat{I}_y. \tag{1.38}$$

The flip angle α effectively indicates where the spins are taken. By choosing an appropriate pulse amplitude ω_1 and duration τ_p, α can be adjusted to $\pi/2$ and equation (1.36) becomes

$$\hat{\rho}(\tau_p) = -\hat{I}_y. \tag{1.39}$$

This operator can generate the induction signal to record a Free Induction Decay (FID), a basic magnetic resonance signal (see section 1.3 for more details).

A single $\pi/2$-pulse (90°) followed by the recording of an FID is called a pulse-acquire and is represented in figure 1.1a. More generally, pulses which are designed to yield transverse magnetisation are named excitation pulses. Despite generating less measurable magnetisation, a better sensitivity can sometimes be achieved by adjusting their flip angle to values different from $\pi/2$, e.g. because of relaxation.

If the flip angle is π, equation (1.36) turns into

$$\hat{\rho}(\tau_p) = -\hat{I}_z, \tag{1.40}$$

an operation that changes the sign of $\hat{I}_z$, referred to as an inversion. The pulse can be designated as a π-pulse or 180° pulse.

Pulses can be appended to form sequences which can be adapted to create magnetic resonance experiments. The duration between each pulse of a sequence is named a delay, and their effect is the subject of the next subsection.

1.2.3 Offset evolution during delays

Once the spins are in the xy-plane, they start evolving according to their offset Ω. The Hamiltonian for offset evolution is

$$\hat{\mathcal{H}} = \Omega \hat{I}_z. \tag{1.41}$$

For an offset evolution of duration τ (a delay), this Hamiltonian gives the following density operator:

$$\hat{\rho}(\tau) = \exp\Big(\mathrm{i}\Omega\tau\hat{I}_z\Big)\rho(0)\exp\Big(-\mathrm{i}\Omega\tau\hat{I}_z\Big). \tag{1.42}$$

Taking a starting state $\rho(0) = -\hat{I}_y$, the density operator can be computed as follows

$$\begin{aligned}
\hat{\rho}(\tau) &= \begin{bmatrix} \exp(-\mathrm{i}\Omega\tau) & 0 \\ 0 & \exp(\mathrm{i}\Omega\tau) \end{bmatrix} \begin{bmatrix} 1 & 0 \\ 0 & -1 \end{bmatrix} \begin{bmatrix} \exp(\mathrm{i}\Omega\tau) & 0 \\ 0 & \exp(-\mathrm{i}\Omega\tau) \end{bmatrix} \\
&= \frac{1}{2} \begin{bmatrix} 0 & \mathrm{i}\exp(-\mathrm{i}\Omega\tau) \\ -\mathrm{i}\exp(-\mathrm{i}\Omega\tau) & 0 \end{bmatrix} \\
&= \frac{1}{2} \begin{bmatrix} 0 & \mathrm{i}\cos(\Omega\tau) + \sin(\Omega\tau) \\ -\mathrm{i}\cos(\Omega\tau) + \sin(\Omega\tau) & 0 \end{bmatrix} \\
&= \frac{1}{2}\sin(\Omega\tau) \begin{bmatrix} 0 & 1 \\ 1 & 0 \end{bmatrix} + \frac{\mathrm{i}}{2}\sin(\Omega\tau) \begin{bmatrix} 0 & 1 \\ -1 & 0 \end{bmatrix} \\
&= \sin(\Omega\tau)\hat{I}_x - \cos(\Omega\tau)\hat{I}_y.
\end{aligned} \tag{1.43}$$

This result means that the spins are rotating in the xy-plane, in a direction which

depends on the sign of their offset and the Larmor frequency. In NMR, the offset evolution is sometimes referred to as the chemical shift evolution.

The outcome of such calculations are well-known and can be used directly to speed up reasoning with a shorthand notation. The operation of applying a Hamiltonian $\hat{\mathcal{H}}$ for a duration τ, starting from the initial density operator $\hat{\rho}(0)$ and ending with the final density operator ρ_τ, is summed up with

$$\hat{\rho}_0 \xrightarrow{\hat{H}\tau} \hat{\rho}_\tau. \tag{1.44}$$

As an example, the result of the offset evolution from equation (1.43) can thus be summarised with

$$-\hat{I}_y \xrightarrow{\Omega\tau\hat{I}_z} \sin(\Omega\tau)\hat{I}_x - \cos(\Omega\tau)\hat{I}_y. \tag{1.45}$$

For pulses, the exponential rotation operator $\hat{R}_l(\alpha) = \exp\left(\mathrm{i}\alpha\hat{I}_l\right)$ is further introduced where $l \in [x, y, z]$ stands for the axis about which the rotation is done. For instance, the effect of a pulse computed from equation (1.35) to equation (1.38) becomes

$$\hat{I}_z \xrightarrow{\hat{R}_x(\alpha)} \cos(\alpha)\hat{I}_z - \sin(\alpha)\hat{I}_y. \tag{1.46}$$

1.2.4 Offset refocusing

In many magnetic resonance experiments, offset evolution needs to be refocused to get to an exploitable spin state such as the one yielded by a pulse-acquire. For example, EPR instrumentation is usually severely limited by a long dead time, the duration after a pulse during which no signal can be recorded. EPR experiments therefore commonly generate the detected magnetic resonance signal far from the last pulse, requiring the offset evolution to be refocused.

In order to refocus offset evolution after an excitation pulse, we first describe the

spin evolution of a following delay of duration τ with

$$\hat{S}_z \xrightarrow{\hat{R}_x(\pi/2)} -\hat{S}_y \xrightarrow{\Omega\tau\hat{S}_z} -\cos(\Omega\tau)\hat{S}_y + \sin(\Omega\tau)\hat{S}_x. \tag{1.47}$$

Then, the spins are inverted thanks to a π-pulse and evolve for τ in the opposite direction, cancelling the effect of the first evolution. This sequence, named Spin-echo, is represented in figure 1.1 and can be analysed with

$$\begin{aligned}
-\cos(\Omega\tau)\hat{S}_y + \sin(\Omega\tau)\hat{S}_x &\xrightarrow{\hat{R}_x(\pi)} \cos(\Omega\tau)\hat{S}_y + \sin(\Omega\tau)\hat{S}_x \\
&\xrightarrow{\Omega\tau\hat{S}_z} \cos(\Omega\tau)\cos(\Omega\tau)\hat{S}_y - \sin(\Omega\tau)\cos(\Omega\tau)\hat{S}_x \\
&\qquad + \cos(\Omega\tau)\sin(\Omega\tau)\hat{S}_x + \sin(\Omega\tau)\sin(\Omega\tau)\hat{S}_x \\
&= \left[\cos^2(\Omega\tau) + \sin^2(\Omega\tau)\right]\hat{S}_y \\
&= \hat{S}_y.
\end{aligned} \tag{1.48}$$

At the end of the sequence, the spins are therefore in the same state $\hat{S}_y$ (with a phase factor changing the sign) which can be used to record a signal. This experiment is also often referred to as a Hahn-echo, after its discoverer's name and the name of the signal created by the refocusing process [14].

Pulse EPR spectroscopy regularly makes use of the Hahn-echo in conjunction with a sweep of B_0 to record the EPR spectrum, an experiment referred to as Echo-Detected EPR (ED-EPR) or Hahn-echo field-sweep [10], represented in figure 1.1c. This principle of encoding information in the echo for an experimental parameter variation is also employed in plenty of EPR experiments, for instance with the DEER observer sequence (see subsection 1.5.3). Like many other magnetic resonance sequences, the DEER observer sequence relies on the principle of forming more echoes by adding several blocks of type $\tau - \pi - \tau$.

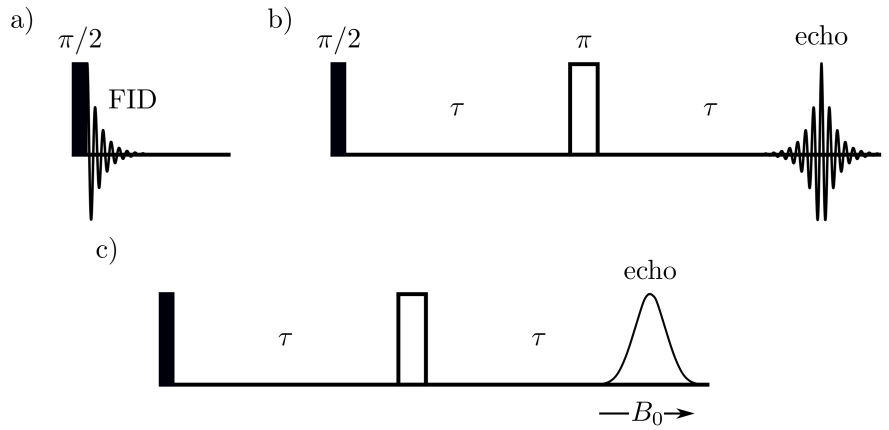


Figure 1.1: Scheme of a) the pulse acquire, b) the Hahn-echo, c) and the Hahn-echo field-sweep. The abscissa stands for the duration of the experiment and the ordinate for the pulse/signal amplitude (not to scale). As is conventional in Nuclear Magnetic Resonance (NMR), the excitation pulses are represented by filled rectangle boxes and the inversion/refocusing pulses are represented by unfilled rectangle boxes. The arrow indicates the sweep of the variable. For the field sweep, this means that B_0 is varied while the echo is recorded. To represent the echo's lack of spectral information, the signal is represented as simpler. All these conventions are kept in the rest of the dissertation.

1.2.5 Coupling evolution

Hahn-echoes can be affected by spin-spin interactions. For example, despite an expected stronger magnetisation decay, longer delays can produce more intense echoes in a DEER observer sequence under specific circumstances. This can happen in systems where nuclear-electron and nuclear-nuclear couplings lead to strong nuclear-spin-driven decoherence [15]. Here, the effect of homonuclear J-couplings on a simple Hahn-echo is described in detail.

For this, the operators describing a spin system with two nuclear spins $\hat{\boldsymbol{I}}_1$ and $\hat{\boldsymbol{I}}_2$ are introduced in table 1.1.

Two nuclear spins $\hat{\boldsymbol{I}}_{\mathbf{1}}$ and $\hat{\boldsymbol{I}}_{\mathbf{2}}$ are coupled with a scalar coupling J_{12}. By assuming a weak coupling regime ($J_{12} \ll |\Omega_2 - \Omega_1|$), the secular approximation of equation (1.18)

[6] yields the Hamiltonian

$$\hat{\mathcal{H}} = -\Omega_1 \hat{I}_{1z} - \Omega_2 \hat{I}_{2z} + 2\pi J_{12} \hat{I}_{1z} \hat{I}_{2z}. \tag{1.49}$$

Description	Operator
Identity operator	$\hat{E}$
$\hat{\boldsymbol{I}}_1$ z-magnetisation	$\hat{I}_{1z}$
$\hat{\boldsymbol{I}}_1$ in-phase x- and y-magnetisation	$\hat{I}_{1x}, \hat{I}_{1y}$
$\hat{\boldsymbol{I}}_2$ z-magnetisation	$\hat{I}_{2z}$
$\hat{\boldsymbol{I}}_2$ in-phase x- and y-magnetisation	$\hat{I}_{2x}, \hat{I}_{2y}$
$\hat{\boldsymbol{I}}_1$ anti-phase x- and y-magnetisation	$\hat{I}_{1x}\hat{I}_{2z}, \hat{I}_{1y}\hat{I}_{2z}$
$\hat{\boldsymbol{I}}_2$ anti-phase x- and y-magnetisation	$\hat{I}_{2x}\hat{I}_{1z}, \hat{I}_{2y}\hat{I}_{1z}$
Multiple-quantum coherence	$\hat{I}_{1x}\hat{I}_{2x}, \hat{I}_{1y}\hat{I}_{2y}$
Longitudinal two-spin order (non-equilibrium population)	$\hat{I}_{1z}\hat{I}_{2z}$

Table 1.1: Set of 16 operators describing a two-spin system.

We focus on the spin $\hat{\boldsymbol{I}}_1$ to understand the system evolution. The evolution of the offset is refocused by the Hahn-echo, and therefore only the coupling evolution $2\pi J_{12}\tau \hat{I}_{1z}\hat{I}_{2z}$ is taken into account, the effect of which is directly given here. The π pulse is considered on each spin sequentially with $\hat{R}_{1x}(\pi), \hat{R}_{2x}(\pi)$. This gives the following sequence where the final expression is simplified with trigonometric identities:

$$\begin{aligned}
-\hat{I}_{1y} &\xrightarrow{2\pi J_{12}\tau \hat{I}_{1z}\hat{I}_{2z}} -\cos(\pi J_{12}\tau)\hat{I}_{1y} + \sin(\pi J_{12}\tau) 2\hat{I}_{1x}\hat{I}_{1z} \\
&\xrightarrow{\hat{R}_{1x}(\pi),\, \hat{R}_{2x}(\pi)} \cos(\pi J_{12}\tau)\hat{I}_{1y} - \sin(\pi J_{12}\tau) 2\hat{I}_{1x}\hat{I}_{2z} \\
&\xrightarrow{2\pi J_{12}\tau \hat{I}_{1z}\hat{I}_{2z}} \cos(\pi J_{12}\tau)\cos(\pi J_{12}\tau)\hat{I}_{1y} - \sin(\pi J_{12}\tau)\cos(\pi J_{12}\tau) 2\hat{I}_{1x}\hat{I}_{2z} \\
&\qquad\qquad - \cos(\pi J_{12}\tau)\sin(\pi J_{12}\tau) 2\hat{I}_{1x}\hat{I}_{2z} - \sin(\pi J_{12}\tau)\sin(\pi J_{12}\tau)\hat{I}_{1y} \\
&= \left[\cos^2(\pi J_{12}\tau) - \sin^2(\pi J_{12}\tau)\right] \hat{I}_{1y} - 2\sin(\pi J_{12}\tau)\cos(\pi J_{12}\tau) 2\hat{I}_{1x}\hat{I}_{2z} \\
&= \cos(2\pi J_{12}\tau)\hat{I}_{1y} - \sin(2\pi J_{12}\tau) 2\hat{I}_{1x}\hat{I}_{2z}.
\end{aligned} \tag{1.50}$$

For a heteronuclear spin system, $\hat{\boldsymbol{I}}_2$ would not be affected by the pulses and this result cannot be used. For a homonuclear spin system, a similar result can be obtained

with $\hat{\boldsymbol{I}}_2$.

In most cases, $\hat{I}_{1y}$ is therefore modulated by a cosine affecting the signal in an effect referred to as J-modulation and further detailed in the next section. However, the y-magnetisation $\hat{I}_{1y}$ from equation (1.47) can be retrieved by fixing the delay duration with $\tau = 1/(2J_{12})$, therefore refocusing the J-coupling evolution. More generally, the idea of refocusing a spin interaction to eliminate its effects on the signal is referred to as dynamical decoupling [16].

1.3 Data acquisition, processing and analysis

1.3.1 Signal detection

The precession of the magnetisation in the xy-plane, as described in subsection 1.2.3, creates a current picked up by induction, in a nearby coil for NMR spectroscopy, or in a resonator for EPR spectroscopy. This signal is ordinarily measured with its phase (quadrature detection), giving a real and a complex part respectively associated with $\hat{I}_x$ and $\hat{I}_y$.

For one spin at offset Ω, the signal produced (FID) S_1 can be expressed as

$$S_1(t) = S_0 \left[\cos(\Omega t + \phi) + \mathrm{i}\sin(\Omega t + \phi)\right] \exp(-Rt). \tag{1.51}$$

where S_0 is the initial signal amplitude, ϕ is the initial signal phase, and R is a damping factor characterising the decay of the signal. More details on signal decay are given in section 1.4.

For a system with n spins, the sum of their individual signals simply form the overall signal

$$S(t) = \sum_{i=1}^{n} S_0^{(n)} \left[\cos(\Omega_n t + \phi_n) + \mathrm{i}\sin(\Omega_n t + \phi_n)\right] \exp(-R_n t). \tag{1.52}$$

An example of experimental data of that type is depicted in figure 1.2.

The echo signal is formed by the spin coming into phase ($t < 0$) and dephasing

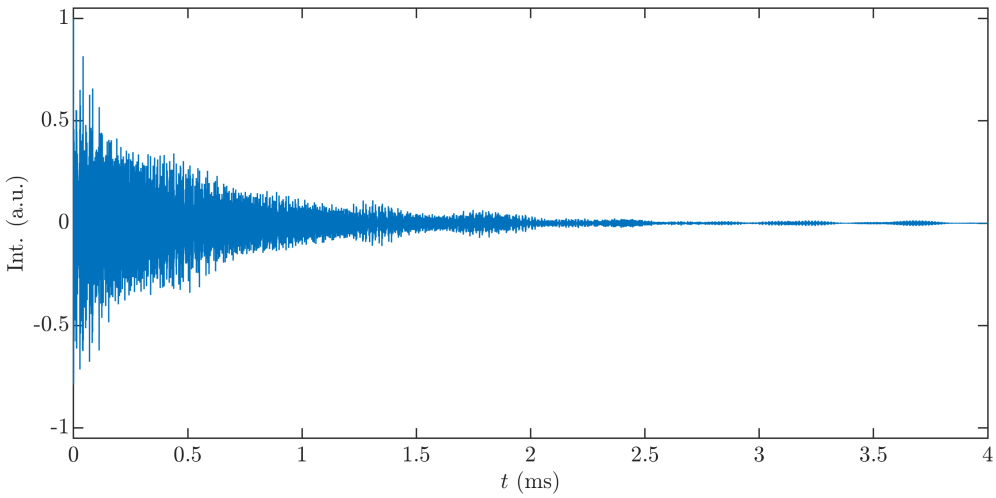


Figure 1.2: Experimental ^{1}H FID of 4-fluorophenyl-boromic acid in DMSO (160 mg for 600 µL). The signal was recorded over a time t after a pulse-acquire experiment at a Larmor frequency of 400 MHz, and is presented with its normalised intensity in ordinate.

again ($t > 0$) for an echo centred at $t = 0$. The echo can be thought of as two FIDs decaying in opposite time directions from their commonly shared point at $t = 0$.

The signal sensitivity can be increased by recording several scans and averaging them. The Signal-to-Noise Ratio (SNR) increases proportionally to the square root of the number of scans in the presence of white noise.

In addition, phase cycling can be performed to select the desired quantum coherences during sequences or to correct for instrumental errors. Phase cycling relies on pulse and receiver phase variations which are arranged in combinations to be executed on different scans. For instance, the Exorcycle scheme suppresses additional quantum coherences generated by imperfect refocusing pulses. Another example is the CYCLically Ordered Phase Sequence (CYCLOPS) scheme which mitigates quadrature imbalance and DC-offsets. Quadrature imbalance arises when the x and y channels are not orthogonal or unequal in intensity. DC-offsets are non-zero values that are present on the channels even in the absence of signal [5].

1.3.2 Frequency domain and post-processing

Time domain signals are difficult to interpret, as is apparent on the FID from figure 1.2. Instead, the frequency domain directly presents the energy transitions (linked to the Hamiltonian eigenvalues seen in subsection 1.1.2) at their frequency.

The most straightforward way to access this domain is to measure the signal intensity for a range of B_0 values and relate it to the frequency domain using equation (1.10). For instance, ED-EPR uses the echo intensity to encode the EPR spectrum during a field-sweep. More generally in magnetic resonance, such sweeps of the field are applied in experiments referred to as Continuous-Wave (CW).

However, these kinds of techniques are slow and only used when the hardware does not have enough bandwidth to record all the spin system frequencies in the signal itself. Otherwise, the Fourier Transform (FT) is largely employed to process the time-domain magnetic resonance signal $S(t)$ into the magnetic resonance spectrum $S(\omega)$.

By expressing the signal from equation (1.51) as a complex exponential, its FT can be written as

$$S(\omega) = S_0 \exp(\mathrm{i}\phi) \int_0^\infty \exp\left[(\mathrm{i}\Omega - R)t\right]\, dt. \tag{1.53}$$

After calculation, this expression can be rearranged as the complex number

$$S(\omega) = S_0 \exp(\mathrm{i}\phi) \left[A(\omega) + \mathrm{i}D(\omega)\right], \tag{1.54}$$

with its amplitude S_0, phase factor ϕ, absorption part $A(\omega)$, and dispersion part $D(\omega)$. $A(\omega)$ and $D(\omega)$ are expressed as

$$A(\omega) = \frac{R}{R^2 + (\Omega - \omega)^2} \quad \text{and} \quad D(\omega) = \frac{\Omega - \omega}{R^2 + (\Omega - \omega)^2}. \tag{1.55}$$

Typically, $\phi = 0$ so that the real part of the spectrum is represented by $A(\omega)$ and the imaginary part by $D(\omega)$.

For a single spin-$\frac{1}{2}$, such absorption spectrum $A(\omega)$ presents itself as a Lorentzian

peak centred on the spin offset Ω, as plotted in figure 1.3b.

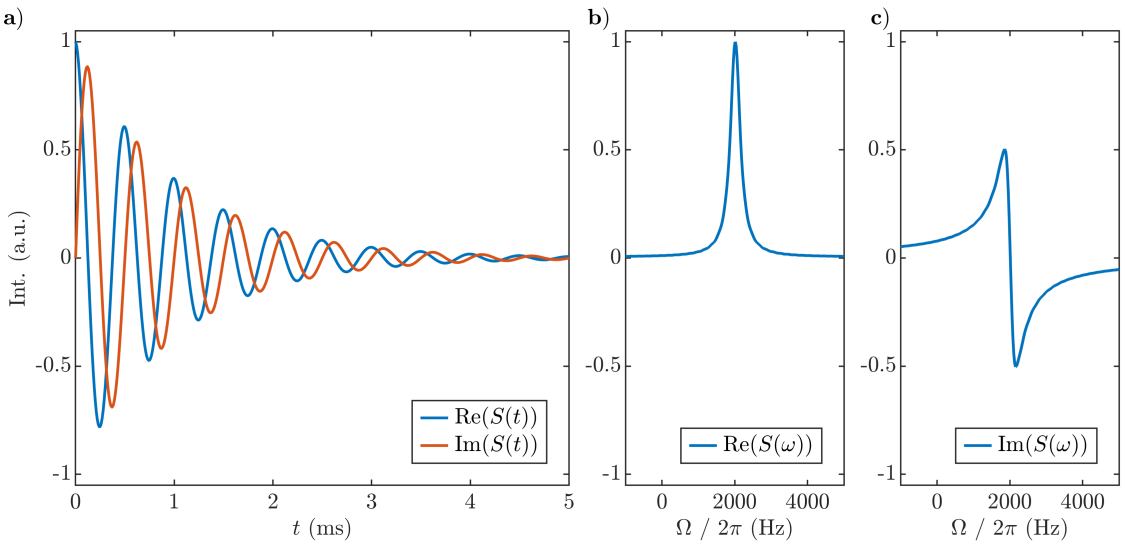


Figure 1.3: Synthetic signal for a single offset Ω (a) in the time-domain, and in the frequency domain with the (b) absorption and (c) dispersion signals centred at $\Omega/2\pi$ on the frequency (offset) axis. The following parameters were used to generate the FID: $\Omega/2\pi = 2\,\text{kHz}$, $R = 1\,\text{ms}$, $\phi = 0$, and $t \in [0, 5]$ ms with $\Delta t = 10\,\mu\text{s}$. The data were zero-filled to 8016 points and the intensity (ordinate) normalised.

In practice, the FT operation is realised with discrete points and is implemented in matrix form as the Fast Fourier Transform (FFT).

The interval which separates the time domain points Δt, or sampling rate, limits the maximum frequency which can be picked up, per the Nyquist condition. The width of the spectrum, referred to as spectral window sw, is therefore given by $sw = 1/(2\Delta t)$.

The spectrum number of points per frequency unit, called the spectrum resolution, can be increased by recording the signal for a longer time. This is limited by the noise, which gets proportionally stronger as the signal decays.

A variety of processing techniques can improve the quality of a spectrum. Zero-filling artificially increases the spectrum resolution by adding data points in the time domain which do not carry information (i.e. $S = 0$ after the end of the signal). Zeroth order phase correction ϕ_0 adjusts the absorption and dispersion proportions. For example, a signal with non-zero initial phase ϕ will present a mixture of absorption and dispersion

in its real and imaginary parts. First order correction ϕ_1 is convenient to correct for the offset evolution occurring if the signal is not recorded from time $t = 0$ (e.g. because of dead time). Baseline correction can ensure that the spectrum is levelled at the intensity $S_0 = 0$. Window functions attribute different weights to different parts of the time-domain signal. For instance, the intensity of the end of the time-domain signal can be reduced to avoid truncation artifacts or even improve sensitivity in the frequency domain at the cost of lower resolution.

1.3.3 Analysis

The absorption mode spectrum is typically preferred for data analysis as it shows the centre frequency and intensity of peaks more directly, and is less prone to peak overlap.

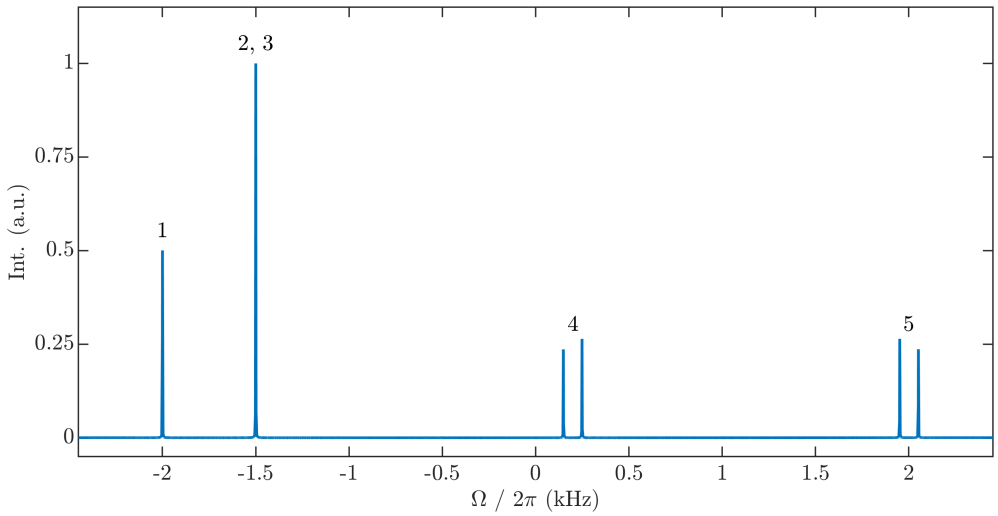


Figure 1.4: Simulated pulse-acquire spectrum for 5 spins at the offsets $\Omega/2\pi = -2$, -1.5, -1.5, 0.2, and 2 kHz, with a coupling $J_{45} = 100$ Hz between the spins 4 and 5. The intensity is presented as normalised but the relative peak intensity are significant. The simulation was conducted with SPINACH v2.5.5459 [17].

To easily compare spectra recorded at different B_0 values, NMR spectroscopists work with the chemical shift scale, which relates the resonance frequencies to a reference

compound in ppm with [4]

$$\delta = (\sigma_{ref} - \sigma) \times 10^6 = \frac{\Omega - \Omega_{ref}}{\omega_0} \times 10^6. \tag{1.56}$$

A scale presenting the offset values in kHz is preferred in this dissertation which often focuses on pulses and their offset-dependent effects.

While the spectrum's absolute intensity is usually not meaningful, relative intensities between different signals are quantitative under appropriate conditions. The intensity can be easily characterised by taking the integral of the signal in the frequency domain. For example, in figure 1.4, the peak integral at $-2\,\mathrm{kHz}$ is only half of the peak integral at $-1.5\,\mathrm{kHz}$. This is because two spins with the same offset contribute to the intensity of the latter. This information can be used to quantify equivalent spins from the same spin system (e.g. two ^{1}H in rotating CH_2) or even different spin systems (e.g. the proportion of two compounds in a solution).

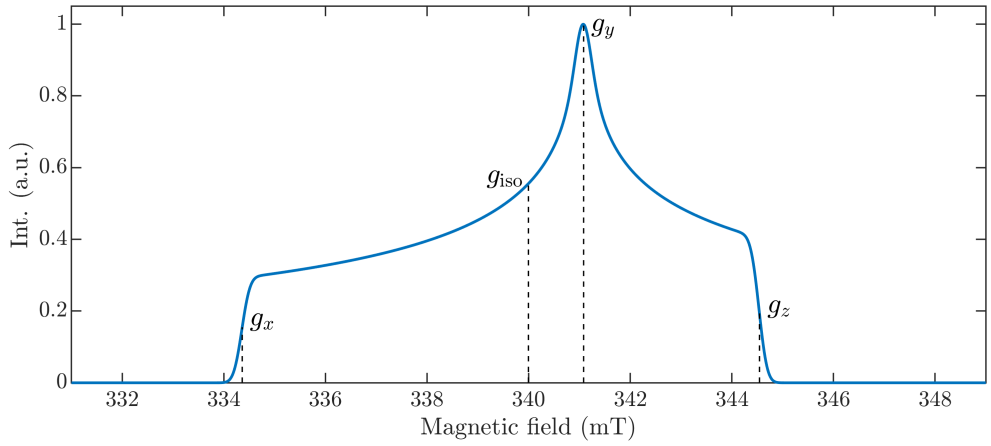


Figure 1.5: Simulated field-sweep spectrum for an anisotropic spin system with one electron spin-$\frac{1}{2}$ (see equation (1.13)) with $g_x = 2.03$, $g_y = 1.99$, and $g_z = 1.97$; $g_{\mathrm{iso}} = (g_x + g_y + g_z)/3$. The simulation was conducted at 9.5 GHz with EasySpin v5.2.28 [18] and the spectrum normalised.

Anisotropic interactions give rise to non-Lorentzian lineshapes. Figure 1.5 shows an example of a spectrum for a system with an anisotropic g-value. Such spectra formed by anisotropic interactions are named powder patterns. Note that this field-sweep spectrum is plotted as a function of the field strength as is common practice for CW data. Although the absorption mode is used here, it is also frequent to plot CW spectra in dispersion mode and when relevant, the peak-to-peak linewidth in magnetic field units (width between positive and negative peaks of the dispersion lineshape).

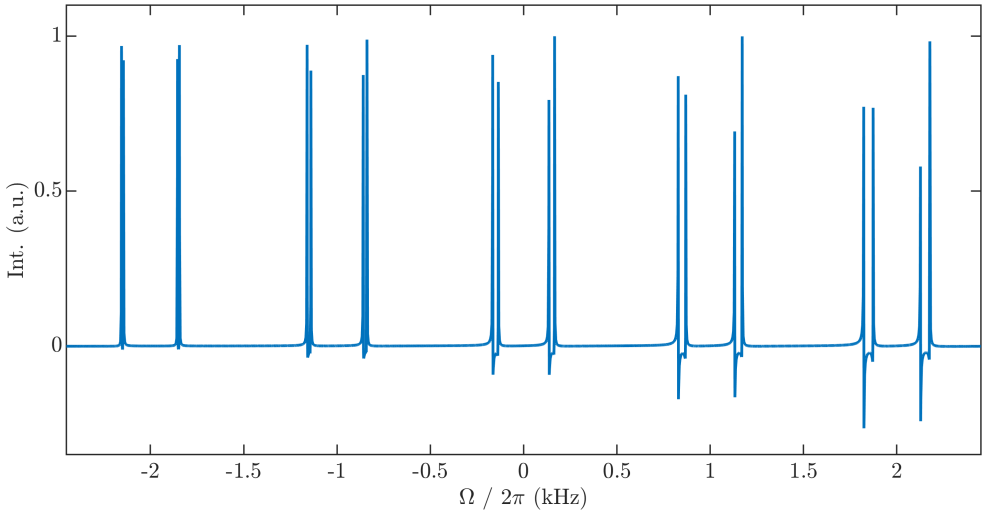


Figure 1.6: Simulated Hahn-echo spectrum for 10 spins, grouped in pairs of coupled spins with increasing J-couplings from 10 to 50 Hz. The simulation was conducted with a Hahn-echo delay of $\tau = 2$ ms using SPINACH v2.5.5459 [17] and the spectrum normalised.

Spin-spin interactions can also be observed in the spectrum as they split the Zeeman energy levels and create new observable transitions. For example, the spin 4 and 5 peaks from figure 1.4 are split in two by the J-coupling. They form so-called doublets centred at the spins offsets. The coupling constant is simply given by the peaks separation; here $J_{45} = 100$ Hz. The difference in intensity between peaks of the same doublet is called the roofing effect, and increases as the coupling becomes increasingly comparable to the frequency difference between the coupled spins ($\Delta\Omega$). This simple description of the coupling effect on the spectrum only holds in the weak coupling limit (i.e. $J \ll \Delta\Omega$).

More generally, the product operator formalism developed here does not hold in the strong coupling regime.

Figure 1.6 illustrates the effect of J-coupling evolution discussed in subsection 1.2.5 in the case where $\tau \ll 1/2J$ (far from Hahn-echo coupling refocusing condition). The spectrum of coupled spins was simulated for a Hahn-echo with a delay $\tau = 2\,\text{ms}$, allowing the couplings to evolve for a total duration of 4 ms. As can be seen in the figure, higher J-coupling values evolve faster and therefore modulate the spectrum more substantially.

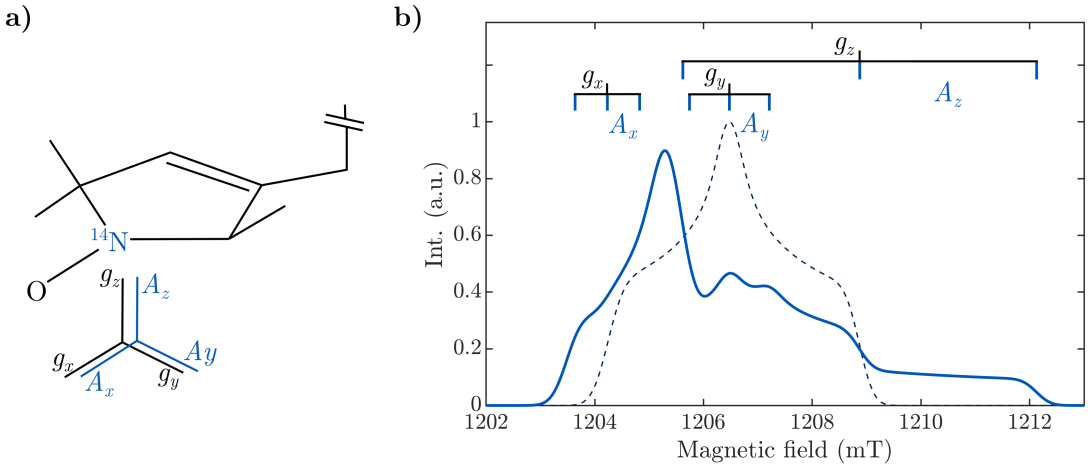


Figure 1.7: Nitroxide a) structure and b) simulated field-sweep spectrum (typical EPR spectrum). The spin system was set up with one electron spin-$\frac{1}{2}$ with an anisotropic g-tensor ($g_x = 2.0101$, $g_y = 2.0064$, and $g_z = 2.0024$), which corresponds to the spectrum in dotted black. The blue spectrum stands for the system with an added anisotropic hyperfine interaction with ^{14}N ($S = 1$, $a_x = 16.7\,\text{MHz}$, $a_y = 20.6\,\text{MHz}$, and $a_z = 91.2\,\text{MHz}$), which further splits it into triplet patterns. The simulation was conducted at 33.88 GHz with EasySpin v5.2.28 [18] and the spectra normalised.

Finally, spin-spin interactions analysis is further complicated in case of anisotropy or total angular momentum higher than 1/2, as illustrated in figure 1.7 which presents a typical nitroxide spectrum (type of sample commonly used in EPR).

1.4 Relaxation

Up until now, the signal has been assumed to decay exponentially with a damping factor R. In practice, a multitude of spin interactions govern the decay dynamics and

require long theoretical explanations to be properly characterised [4, 6, 8, 19, 20]. Such a rigorous description is not necessary for this dissertation and the signal decay is here only described through the notions of spin longitudinal relaxation and spin transverse relaxation.

1.4.1 Longitudinal relaxation

Spin longitudinal relaxation represents the relaxation back to equilibrium along the z-axis. A mono-exponential decay with a relaxation rate R_1 commonly models the signal with

$$|M_z(t)| = M_z^0 \exp(-tR_1), \tag{1.57}$$

where M_z^0 is the original amplitude of z-magnetisation.

The more intuitive longitudinal relaxation time constant $T_1 = 1/R_1$ is used in practice. For example, T_1 dictates the time interval necessary for the system to come back close to equilibrium between scans. A value equal or larger than $5T_1$ translates to recovery of 99.3% or more magnetisation to equilibrium and is typically advised [7, 21].

1.4.2 Transverse relaxation

The time-domain signal decay described in subsection 1.3.1 mainly occurs in the transverse plane because the spins experience different magnetic fields.

First, the spins are subject to local magnetic field differences arising from spin-spin interactions in the sample. As part of the spin system itself, this relaxation is considered intrinsic and is described by the relaxation time constant T_2.

Second, B_0 inhomogeneities from the hardware quickly lead to spins dephasing described by the relaxation time constant $T_2^{\Delta B_0}$. For NMR spectroscopy, this is usually the main driving factor for the signal decay mentioned in the previous section and consequently, for the high homogeneity requirements for B_0 on NMR spectrometers.

Third, diffusion causes the spins to experience different magnetic fields over time (e.g. through motion of nearby molecules). Diffusion can also give rich information on

the systems and a whole field of experiments is dedicated to it in NMR spectroscopy [7]. This term is rarely explicitly addressed but is noted here as T_2^{diff} for completeness.

In NMR spectroscopy, a single exponential decay can be used to model transverse relaxation with

$$|M_{xy}(t)| = |M_{xy}^0| \exp(-tR_2^*), \tag{1.58}$$

where $|M_{xy}^0|$ is the absolute value of the initial transverse magnetisation and R_2^* the transverse relaxation rate (ordinarily $R_2^* \gg R_1$). The spin-spin interaction relaxation time constant T_2, the static magnetic field inhomogeneity relaxation time constant $T_2^{\Delta B_0}$, and the diffusion relaxation time constant T_2^{diff} relate to $T_2^* = 1/R_2^*$ such that

$$\frac{1}{T_2^*} = \frac{1}{T_2^{\Delta B_0}} + \frac{1}{T_2} + \frac{1}{T_2^{\text{diff}}}. \tag{1.59}$$

As mentioned in the previous section, longer signals enable a higher spectral resolution. In fact, the peak width is proportional to T_2^* for the Lorentzian peaks typically found in solution-state NMR spectroscopy. The measurement of T_2 gives information about the spin system but also more pragmatically places an upper bound on the duration of a pulse sequence.

In EPR spectroscopy, particularly in solids, the signal decay is often linked to additional processes which make the characterisation of the transverse relaxation less straightforward. In the absence of motion, dipolar couplings between neighbouring spins contribute to transverse relaxation through spin diffusion. However, relaxation is also often dependent on the used pulses because of instantaneous diffusion, i.e. when a pulse flips spins which are dipole coupled to the spins from the observed signal. Spin flips happening on different parts of the broad spectra can also be a major factor to relaxation, a phenomena called spectral diffusion. In addition, T_1 can be comparable to T_2 (typically at high temperatures) and can thus substantially contribute to the signal decay, further making T_2 measurements more complicated.

All these mechanisms' (and others not detailed here) importance may vary greatly between samples and it is preferred to characterise the signal decay with the phase

memory time T_M [22, 23], which is linked to the experiment used to measure it, as further explained in subsection 1.5.1 on relaxation measurement experiments.

1.5 Experiment examples

A great variety of magnetic resonance experiments exist to retrieve information from spin systems. This subsection only illustrates a subset of this diversity by going over a few examples relevant to the rest of the thesis: relaxation time measurement sequences, perfect-echo, 4-pulse Double Electron-Electron Resonance (DEER) and ELDOR-Detected NMR (EDNMR).

1.5.1 Relaxation time measurements

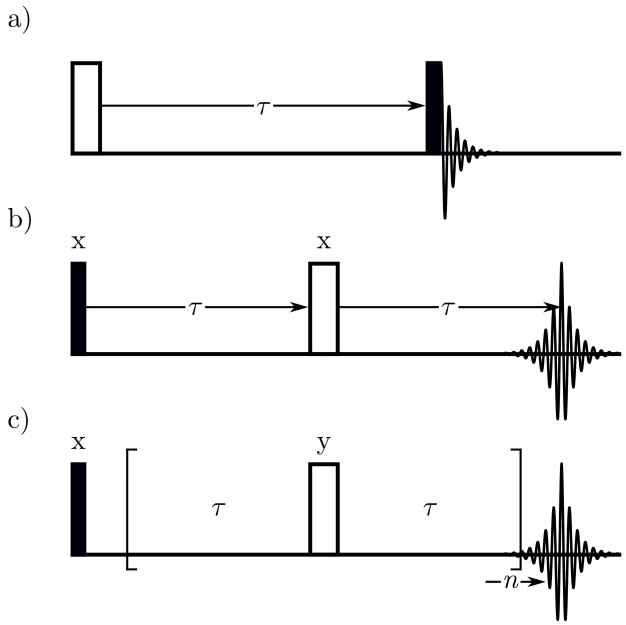


Figure 1.8: Scheme of sequences for relaxation times measurements: a) inversion recovery for T_1, b) Hahn-echo with increasing delay, and c) CPMG with increasing n for T_2. The letters above the pulses indicate the phases of the pulses. Here, the excitation pulse phase is chosen as x. The CPMG uses a different phase on the inversion pulse (on y, phase shift of $\pi/2$) for a compensation effect of pulse length errors on even echoes.

A simple way to measure T_1 is to apply the inversion recovery sequence $\pi - \tau - \pi/2$

[24]. For example, it can be described with

$$\hat{S}_z \xrightarrow{\hat{R}_x(\pi)} \hat{S}_{-z} \xrightarrow{\Omega\tau\hat{S}_z} \hat{S}_{-z} \xrightarrow{\hat{R}_x(\pi/2)} \hat{S}_y, \tag{1.60}$$

in which the final magnetisation amplitude carries the damping factor $\exp(-\tau/T_1)$. The return of the magnetisation to equilibrium (recovery) is recorded by measuring the signal amplitude for an increasing τ, and T_1 can be extracted by fitting the obtained curve. In EPR, the final $\pi/2$-pulse is replaced with a Hahn-echo [23].

In a similar fashion to the inversion recovery, the simplest way to measure T_2 is to track the decay of echo intensity with an increasing delay duration, this time with a Hahn-echo [7]. Because spin systems often present complicated relaxation effects as seen previously, EPR spectroscopy uses this Hahn-echo sequence to directly characterise signal decay with the stretched exponential model

$$|M_{xy}(\tau)| = |M^0_{xy}| \exp(-(2\tau/T_M)^x), \tag{1.61}$$

where T_M is called the phase memory time, τ is the Hahn-echo delay duration (doubled as 2τ to represent the duration of the total magnetisation evolution), and x is the stretched exponent which indicates the shape of the decay. For example, $x = 1$ stands for a monoexponential decay and $x = 2$ a Gaussian decay. x contains information about the system dynamics and typically $x \in [0.5, 3]$. In addition to the complicated relaxation effects, T_2 measurements in EPR are subject to instrumentation limitations which impede extensive use of the long sequence commonly employed in NMR spectroscopy [21, 25].

This special sequence, the Carr-Purcell-Meiboom-Gill (CPMG) sequence [26, 27], prevents decoherence contributions from the environment which arise during the Hahn-echo duration extension (e.g. diffusion) and which perturb the measurement of T_2.

Using the principle briefly mentioned in subsection 1.2.4 of chaining refocusing elements, the CPMG is formed by repetitions of Hahn-echoes with equal delay duration.

For T_2 measurement purposes, the CPMG yields the echo intensity as a function of time as more refocusing blocks are added to the sequence. The blocks are customarily counted with n, which also indicates the number of echoes formed by the sequence. While most famous for T_2 measurements, the CPMG sequence has found a wide range of other applications in magnetic resonance [28–30].

1.5.2 Perfect-echo

The refocusing of homonuclear coupling by a Hahn-echo presented in subsection 1.2.5 presents a limitation if long delays are required. For instance, diffusion measurements, which use the Hahn-echo with an increasing delay from the previous subsection as a basis, can suffer from poor coupling refocusing. In the case of the CPMG, homonuclear coupling refocusing with short delays can also call for a number of pulses too high to be implemented for reasons associated with hardware constraints or sample heating.

The perfect echo sequence offers an elegant way to eliminate the effect of homonuclear J-modulation [31–33]. A perfect echo can be obtained by placing a 90° pulse with a $\pi/2$ phase shift (relative to the excitation pulse) in the middle of two Hahn-echoes as depicted in figure 1.9a.

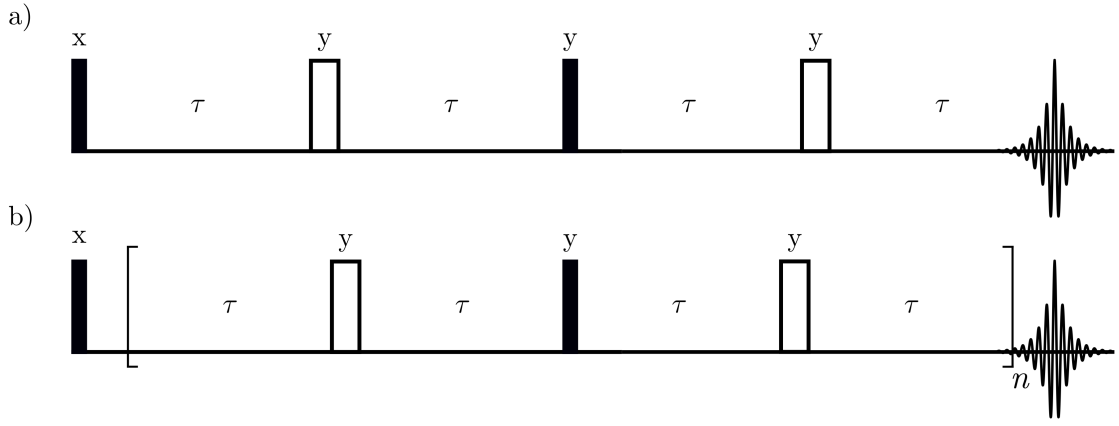


Figure 1.9: Scheme of a) the perfect-echo sequence and b) its CPMG version.

To illustrate how this works, we can refer to the system from subsection 1.2.5 with two weakly coupled spins $\hat{\boldsymbol{I}}_1$ and $\hat{\boldsymbol{I}}_2$. With the offsets considered as refocused by the

sequence, the result from equation (1.47) is adapted to a π pulse on y and extended to the two spins to serve as the starting point of the analysis before the phase shifted 90° pulse. From there, analysis of the J-coupling evolution with $\eta = \pi J_{12}\tau$ gives

$$
\begin{aligned}
&-(\hat{I}_{1y}+\hat{I}_{2y})\cos 2\eta + 2(\hat{I}_{1x}\hat{I}_{2z}+\hat{I}_{2x}\hat{I}_{1z})\sin 2\eta \\
&\quad\xrightarrow{\hat{R}_{1y}(\pi/2),\,\hat{R}_{2y}(\pi/2)} -(\hat{I}_{1y}+\hat{I}_{2y})\cos(2\eta) - 2(\hat{I}_{1x}\hat{I}_{2z}+\hat{I}_{2x}\hat{I}_{1z})\sin 2\eta \\
&\quad\xrightarrow{2\pi J_{12}\tau \hat{I}_{1z}\hat{I}_{2z}} -(\hat{I}_{1y}+\hat{I}_{2y})(\cos 2\eta\cos\eta + \sin 2\eta\sin\eta) \\
&\qquad\qquad + 2(\hat{I}_{1x}\hat{I}_{2z}+\hat{I}_{2x}\hat{I}_{1z})(\sin 2\eta\cos\eta - \cos 2\eta\sin\eta) \\
&\quad\xrightarrow{\hat{R}_{1y}(\pi),\,\hat{R}_{2y}(\pi)} -(\hat{I}_{1y}+\hat{I}_{2y})(\cos 2\eta\cos\eta + \sin 2\eta\sin\eta) \\
&\qquad\qquad - 2(\hat{I}_{1x}\hat{I}_{2z}+\hat{I}_{2x}\hat{I}_{1z})(\sin 2\eta\cos\eta - \cos 2\eta\sin\eta) \\
&\quad\xrightarrow{2\pi J_{12}\tau \hat{I}_{1z}\hat{I}_{2z}} -(\hat{I}_{1y}+\hat{I}_{2y}) \\
&\qquad\qquad (\cos 2\eta\cos^2\eta + \sin 2\eta\sin\eta\cos\eta + \sin 2\eta\cos\eta\sin\eta - \cos 2\eta\sin^2\eta) \\
&\qquad\qquad - 2(\hat{I}_{1x}\hat{I}_{2z}+\hat{I}_{2x}\hat{I}_{1z}) \\
&\qquad\qquad (\sin 2\eta\cos^2\eta - \cos 2\eta\sin\eta\cos\eta - \cos 2\eta\cos\eta\sin\eta - \sin 2\eta\sin^2\eta) \\
&= -(\hat{I}_{1y}+\hat{I}_{2y})\left[\cos 2\eta(\cos^2\eta - \sin^2\eta) + 2\sin 2\eta\sin\eta\cos\eta\right] \\
&\qquad - 2(\hat{I}_{1x}\hat{I}_{2z}+\hat{I}_{2x}\hat{I}_{1z})\left[\sin 2\eta(\cos^2\eta - \sin^2\eta) - 2\cos 2\eta\sin\eta\cos\eta\right] \\
&= -(\hat{I}_{1y}+\hat{I}_{2y})(\cos^2\eta + \sin^2\eta) - 2(\hat{I}_{1x}\hat{I}_{2z}+\hat{I}_{2x}\hat{I}_{1z})(\sin 2\eta\cos 2\eta - \cos 2\eta\sin 2\eta) \\
&= -(\hat{I}_{1y}+\hat{I}_{2y}).
\end{aligned}
\tag{1.62}
$$

The final result has been simplified with trigonometric identities and shows that homonuclear J-coupling evolution has been refocused at the end of the sequence (see figure 1.10 for example spectra). The perfect echo can even be repeated in a CPMG fashion as seen in figure 1.9b [33].

The refocusing condition does not work when more than one coupling is present, as multiple-quantum coherence (e.g. $\hat{I}_{1x}\hat{I}_{2z}\hat{I}_{3z}$ for three spins) will not evolve into single-quantum coherence. Nevertheless, the resulting absorption spectrum can be substantially improved [32]. The efficiency of the sequence also starts to break down as

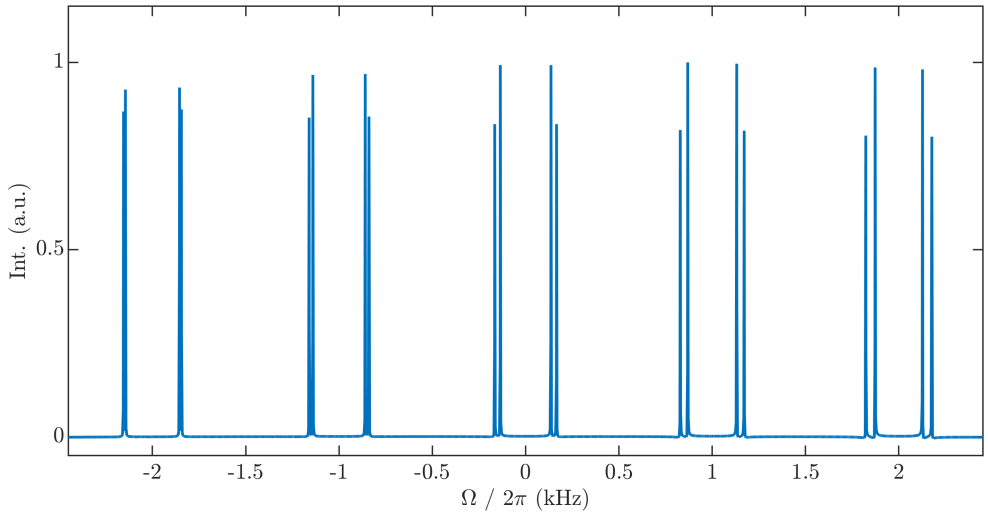


Figure 1.10: Simulated perfect-echo spectrum for 10 spins, grouped in pairs of coupled spins with increasing J-couplings from 10 to 50 Hz (same spin system and coupling evolution duration as figure 1.6). The simulation was conducted with a a perfect-echo delay $\tau = 1$ ms (total coupling evolution of 4 ms) using SPINACH v2.5.5459 [17] and the obtained spectrum normalised.

the strong coupling regime is approached [31].

The perfect echo technique has been applied to various NMR domains such as diffusion measurements [33–35], T_2 filtration [33], and solvent suppression [36]. In EPR spectroscopy, the solid echo produced by SIngle Frequency TEchnique for Refocusing dipolar couplings (SIFTER) arise from the same sequence, but used there to suppress dipolar coupling evolution [22].

1.5.3 DEER

While spin-spin interaction evolution can degrade data quality, it also contains information which can instead be harnessed. In EPR, dipolar spectroscopy aims to determine the dipolar coupling between two unpaired electrons using the influence of the coupling evolution. As mentioned in subsection 1.1.4, this information can then be used as a ruler to measure distances, e.g. in biology.

The Pulse Electron-Electron DOuble Resonance (PELDOR), or Double Electron-

Electron Resonance (DEER) sequence, is often used for dipolar spectroscopy [25, 37]. The idea of the sequence is to generate dipolar coupling modulation in a controlled manner on a pump channel at frequency ω_{pump}. This modulation manifests itself in an echo created on an observer channel at frequency ω_{obs}. To illustrate this, we take the Hamiltonian of two weakly coupled electron spins ($|\Omega_1 - \Omega_2| \gg \omega_{dd}$)

$$\hat{\mathcal{H}} = -\Omega_1 \hat{\boldsymbol{S}}_{\mathbf{1}} B_0 - \Omega_2 \hat{\boldsymbol{S}}_{\mathbf{2}} B_0 - \omega_{dd}(1 - 3\cos^2\theta)\hat{S}_{1z}\hat{S}_{2z} \tag{1.63}$$

where θ is the angle between B_0 and the inter-spin vector.

Such a system exhibits two doublets centred at Ω_1 and Ω_2 and split by $\omega_{dd}(1-\cos^2\theta)$. The DEER sequence can be set up with an observer channel exciting exclusively $\hat{\boldsymbol{S}}_{\mathbf{1}}$ ($\omega_{\text{obs}} = \Omega_1$). In the absence of pump, the dipolar coupling evolution is refocused by the echo sequence. The pump placed on $\hat{\boldsymbol{S}}_{\mathbf{2}}$ ($\omega_{\text{pump}} = \Omega_2$) inverts the coupling evolution direction and generates echo modulation.

For the 4-pulse DEER sequence [38], two Hahn-echoes with delays τ_1 and τ_2 yield the observer channel echo. The pump pulse comprises a single inversion pulse whose position in time is monitored relative to the first refocused echo t_d (see figure 1.11). The echo is modulated according to

$$V(\mathrm{t}) = \cos\left(\omega_{dd}(1 - 3\cos^2\theta)t_d\right). \tag{1.64}$$

The dipolar coupling can be extracted from the so-called DEER trace, the echo intensity variation. In practice, DEER data analysis commonly needs advanced models (e.g. for glassy frozen solutions), which require advanced data processing techniques not described here but easily available through software packages [39–41]. An example of experimental data is shown in figure 1.11b.

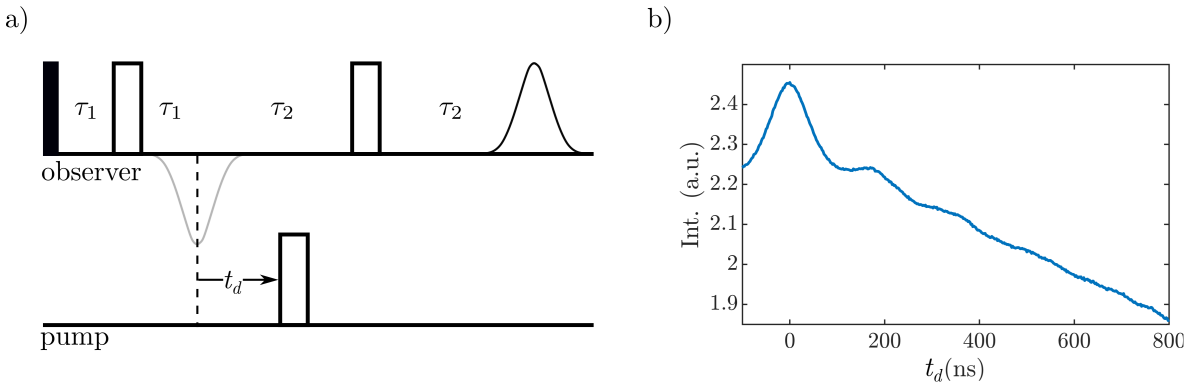


Figure 1.11: Scheme of a) the 4-pulse DEER sequence and b) example of DEER trace recorded with that sequence (raw trace from unoptimised data in subsection 3.4.1). The echo intensity is plotted against the delay t_d between the first echo and the pump pulse.

1.5.4 EDNMR

As briefly mentioned in subsection 1.1.4, the hyperfine interaction is not straightforward to measure. For typical paramagnetic systems, the EPR spectrum gets too crowded, and the NMR spectrum has both low resolution and sensitivity due to paramagnetic effects.

Detecting NMR through EPR is a good way to circumvent this problem, and is the goal of hyperfine spectroscopy, which encompasses three main techniques: Electron Spin Echo Envelope Modulation (ESEEM), Electron Nuclear Double Resonance (ENDOR) and ELDOR-Detected NMR (EDNMR). Here we focus on EDNMR in which the E stands for Electron-Electron DOuble Resonance (ELDOR) [42].

Like DEER, the EDNMR experiment relies on an observer and pulse channel. The simplest sequence is based on the use of a Hahn-echo as an observer and a High Turning Angle (HTA) pulse as a pump as illustrated in figure 1.12a. The HTA pulse is a long selective pulse aiming at activating so-called forbidden transitions. Forbidden transitions are transitions in which both a nucleus and an electron's states change. These are multiple-quantum transitions; examples of multiple-quantum coherence operators for nuclei were presented in table 1.1. If the HTA pulse is applied at the forbidden

transition frequency, some observable magnetisation is lost. When the EPR spectrum is recorded by the observer pulses, holes are therefore observed. A hole pattern can be recorded across the full spectrum by changing the frequency of the HTA pulse ω_{pump}.

The EDNMR spectrum can thus be obtained by subtracting the hole pattern from the EPR spectrum. The EDNMR spectrum is plotted against $\Delta\omega = \omega_{\text{obs}} - \omega_{\text{pump}}$ to directly give the nuclear frequencies. In its centre, the HTA pulse fully saturates an allowed EPR transition ($\omega_{\text{obs}} = \omega_{\text{pump}}$), therefore creating a central peak on the EDNMR spectrum (central blind spot).

The spin system of equation (1.17) can be used to illustrate the principle of the experiment. $\hat{\boldsymbol{S}}$ is characterised by a doublet, separated by the hyperfine coupling a on the EPR spectrum. The EDNMR spectrum consists of two doublets, separated by the hyperfine coupling and centred at the Larmor frequency of $\hat{\boldsymbol{I}}$, as shown in figure 1.12b.

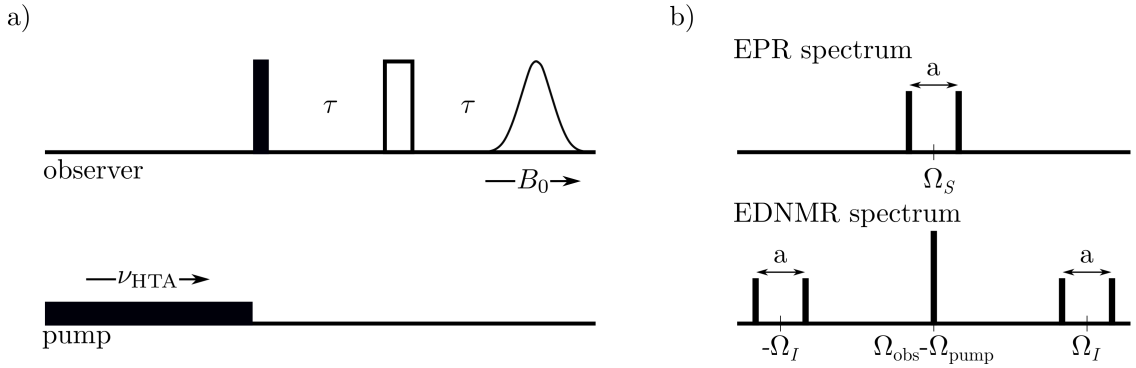


Figure 1.12: Scheme of a) EDNMR sequence with echo detection, and b) EPR and EDNMR spectra for a spin system with an electron spin coupled to a nuclear spin with a hyperfine coupling a.

Chapter 2

Frequency-swept pulse sequences design and implementation

2.1 Introduction

A great number of magnetic resonance experiments can benefit from pulses able to reach wide bandwidths while being tolerant to instrumental imperfections. For example, EPR or ^{19}F NMR spectroscopy are often limited by the microwave and radio-frequency power respectively available on the spectrometer. These limitations can accumulate in multi-pulse experiments, further degrading experiment performance.

Frequency-Swept (FS) pulses, also called Frequency-Modulated or adiabatic pulses, can offer tolerance to B_1 inhomogeneity and operate over broad spectral widths as pictured in figure 2.1. Introduced in the 1980s [43–48], the development of frequency-swept pulses was mainly driven until the 2000s by *in vivo* Magnetic Resonance Imaging (MRI) and spectroscopy (MRS) for their tolerance to B_1 inhomogeneities and selectivity [49–56], and by high-resolution liquid-state NMR for their capacity to span wide chemical shift ranges [57–64]. Important applications from that period include heteronuclear decoupling [65–75], robust CPMGs [76–78] or the idea of using a frequency-swept pulses in conjunction with a gradient, which sparked work on zero-quantum suppression [79]

and spatiotemporal encoding [80, 81].

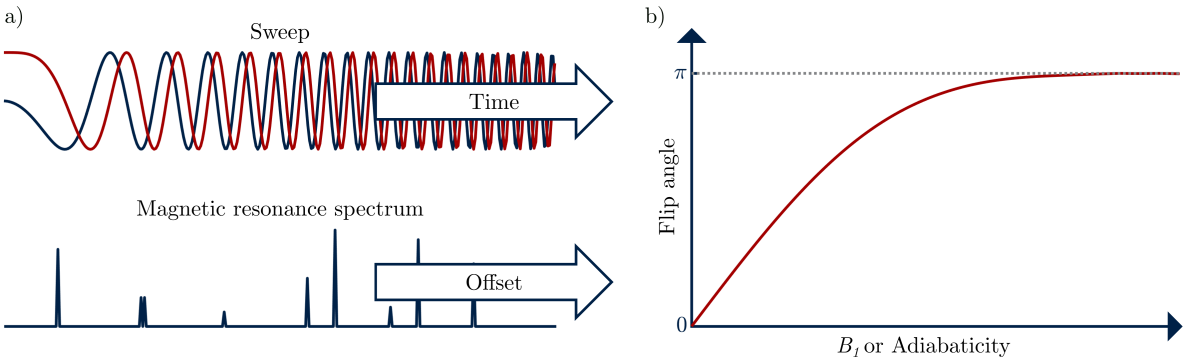


Figure 2.1: Illustration of basic frequency-swept pulse properties with a) the basis for their broadband properties, a waveform going through the spectrum as it is swept, and b) the basis for their B_1-insensitivity, the adiabaticity, which makes the flip angle constant after the pulse amplitude passes a certain threshold. The sweep is represented by it Cartesian components C_x and C_y, defined more precisely later on.

In the last two decades, those applications were further refined [82–90] and new ones were developed [91–97] (such as single-scan NMR [98–101]), but other domains of magnetic resonance have emerged as even stronger drivers for the interest in frequency-swept pulses. Prior to the 2000s, only a few literature references can be found in those domains such as in SS-NMR [102] or ESR [103]. However, from the 2000s onwards, static [104–111] and dynamic [112–121] SS-NMR with frequency-swept pulses became particularly active. Furthermore, the introduction of new fast microwave Arbitrary Waveform Generator (AWG) technology during the early 2010s [122–125] made it possible to generate frequency-swept microwave pulses for unpaired electrons. This has lead to active research on FS pulses in ESR [126–129], as most ESR experiments are subject to strong hardware constraints and bandwidth requirements far exceeding the ones from conventional hard pulses [8]. Applications include established methods in dipolar spectroscopy with DEER [130–136], RIDME [135, 137, 138] and SIFTER [139, 140], and in hyperfine spectroscopy with ESEEM [141, 142], and HYSCORE [141]. Thanks to the additional capacities offered by the pulses, new experiments have also emerged [143–147].

Other magnetic resonance domains also started to report the use of frequency-

swept pulses during the last decade with work in single-sided NMR [148, 149], Dynamic Nuclear Polarisation (DNP) [150–153] and Nitrogen Vacancy (NV) sensing [154–157].

While frequency-swept pulses often offer a wider excitation bandwidth [95], broadband and/or B_1-tolerant methods can also be developed with composite pulses [158–164] and optimal control theory techniques [122, 165–171] although it should be noted that there is no clear distinction between all these pulse design techniques. For instance, the B_1-Insensitive Rotation (BIR) pulse family comprises frequency-swept pulses designed using a composite pulse approach [51, 52, 65, 172]. Another example is the investigation of combinations of frequency-swept pulses with optimal control techniques [110, 173].

For further reading on FS pulses, the reader is also referred to various reviews [173–176], in particular from a recent issue of the Journal of Magnetic Resonance on frequency-swept pulses [177–181].

The implementation of frequency-swept pulses in a pulse sequence is typically less straightforward than that of hard pulses or Amplitude-Modulated (AM) pulses. As they affect different parts of the spectrum at different times, they commonly require specific sets of matched pulses and delay durations [53, 57, 63, 91, 94, 97, 182] and at times, individual pulse elements must be tweaked [62, 97] to accomplish their desired effects.

In the first section of this chapter, we address this challenge by introducing the theory of established frequency-swept pulses and pulse sequences with simple concepts [97, 126, 129, 178, 183], allowing us to use and further develop new frequency-swept pulse sequences. In the subsequent section, we focus on the application of an established frequency-swept sequence, CHORUS, to the challenging domain of ESR spectroscopy. In the third section, solution-state NMR spectroscopy is the context for the design of new broadband B_1-tolerant frequency-swept pulse sequences with CPMG, perfect echo, and shorter superposed basic frequency-swept sequences.

2.2 Theory

2.2.1 Definition and parametrisation

The general parametric waveform $\mathcal{S}$ of a frequency-swept pulse is commonly expressed as

$$\mathcal{S}(t) = \omega_1(t) \exp\left[\mathrm{i}\phi(t)\right], \tag{2.1}$$

in which the amplitude envelope, $\omega_1(t)$, and phase, $\phi(t)$, are two real continuous functions, which are time-dependent in contrast to the hard pulses described in section 1.2. The phase $\phi(t)$ can be written as a function of the frequency sweep $\omega(t)$ with

$$\phi(t) = \int \omega(t)\, \mathrm{d}t, \tag{2.2}$$

for a pulse of duration τ_p.

A wide variety of frequency sweep functions have been proposed [52, 73, 184, 185] to form frequency-swept pulses, but the two most commonly encountered are the hyperbolic tangent [47] and the linear chirp [43].

Hyperbolic tangent frequency modulation is often associated with a hyperbolic secant smoothing function to form so-called tanh/sech pulses, also referred to as hyperbolic secant (HS) pulses [47].

Linear chirp frequency modulation is usually paired with a function to smooth the extremities of the pulse, such as WURST [186] or quarter-sine [183], forming pulses which are often designated as WURST or chirped pulses.

In this thesis, frequency-swept pulses expressions rely on the six following parameters [178]:

- $\omega_{1,\mathrm{max}} = \gamma B_{1,\mathrm{max}}$, peak amplitude ($\mathrm{rad\,s^{-1}}$)
- ΔF, bandwidth (Hz)
- τ_p, duration (s)
- ϕ_0, overall phase (rad)

- δ_t, time offset (s)
- δ_f, frequency offset (Hz)

The peak amplitude is customarily expressed in Hz for convenience, with $\nu_{1,\max} = \omega_{1,\max}/(2\pi)$. The targeted bandwidth ΔF is usually wider than the effective bandwidth, ΔF_eff, as a result of the smoothing on the amplitude envelope. The overall phase ϕ_0 grants control of the total phase of the pulse, typically for use in phase cycling. δ_t modifies the temporal position of the pulse (i.e. where it is situated in the sequence), and δ_f allows for the adjustment of its spectral position through its central frequency (i.e. where it acts on the spectrum with respect to the carrier frequency). For instance, in a DEER experiment, the position of a FS pump pulse on the EPR spectrum can be controlled with δ_f.

For chirped pulses, a super-Gaussian distribution is chosen here to define the amplitude envelope as [178]

$$\omega_1(t) = \omega_{1,\max} \exp\left[-2^{n+2}\left(\frac{t-\delta_\mathrm{t}}{\tau_\mathrm{p}}\right)^n\right], \tag{2.3}$$

where n is a smoothing factor. The frequency sweep function can be expressed as

$$\omega(t) = \frac{2\pi\Delta F(t-\delta_\mathrm{t})}{\tau_\mathrm{p}} + 2\pi\delta_\mathrm{f}, \tag{2.4}$$

corresponding to the phase

$$\phi(t) = \phi_0 + \frac{\pi\Delta F(t-\delta_\mathrm{t})^2}{\tau_\mathrm{p}} + 2\pi\delta_\mathrm{f}(t-\delta_\mathrm{t}). \tag{2.5}$$

For HS pulses, an HS^1 pulse, a representative of the HS^n pulse family [174, 184], is employed. An HS^1 pulse amplitude envelope is specified with a secant function as

$$\omega_1(t) = \omega_{1,\max}\,\mathrm{sech}\left[\beta(t-\delta_\mathrm{t})\right], \tag{2.6}$$

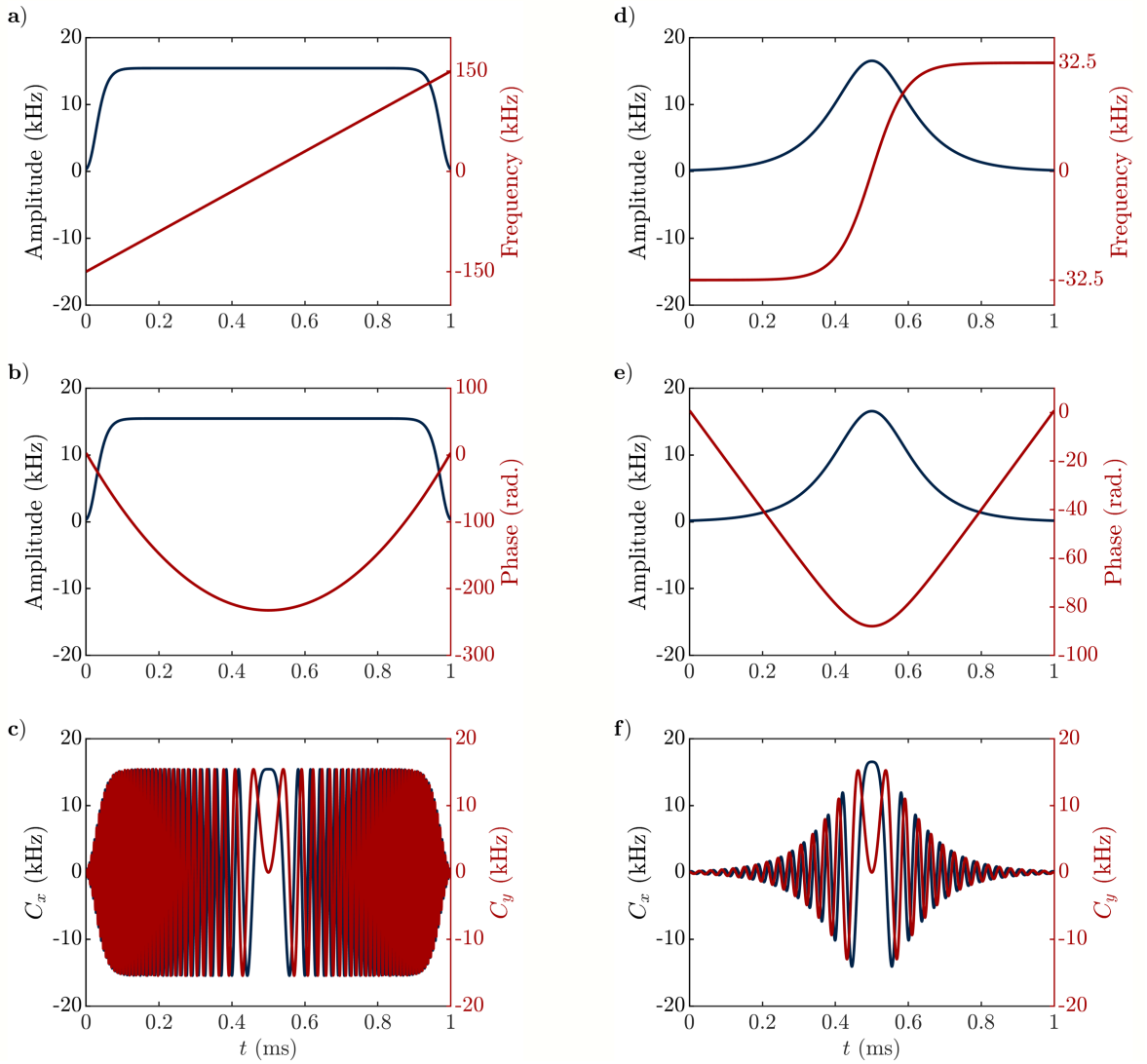


Figure 2.2: Amplitude (black) and frequency sweep (red) representation, polar representation (amplitude in black and phase in red) and Cartesian representation (components C_x in black and C_y in red) of a), b), c) a chirped and d), e), f) an HS^1 pulse, respectively. The chirped pulse presents a bandwidth $\Delta F = 300\,\mathrm{kHz}$ and a smoothing parameter $n = 26$ ($\sim$10% smoothing). The HS^1 presents a bandwidth $\Delta F = 65\,\mathrm{kHz}$ and a smoothing parameter $\beta = 10.6/\tau_\mathrm{p}$. Both pulses share the following parameters: duration $\tau_\mathrm{p} = 1\,\mathrm{ms}$, adiabaticity factor $\mathcal{Q}_0 = 5$ ($\nu_{1,\mathrm{max}} = 15.45\,\mathrm{kHz}$), and $t_\mathrm{res} = 0.5\,\mu\mathrm{s}$.

and its frequency sweep as

$$\omega(t) = \pi\Delta F \tanh\left[\beta(t-\delta_\mathrm{t})\right] + 2\pi\delta_\mathrm{f}, \tag{2.7}$$

corresponding to the phase

$$\phi(t) = \phi_0 + \frac{\pi \Delta F}{\beta} \ln\big[\cosh\left[\beta(t - \delta_\mathrm{t})\right]\big] + 2\pi\delta_\mathrm{f}(t - \delta_\mathrm{t}). \tag{2.8}$$

β is a smoothing parameter, commonly fixed to $10.6/\tau_\mathrm{p}$ to smooth $\omega_1(t)$ to about 1% of $\omega_{1,\mathrm{max}}$ at the pulse end [91].

The Cartesian components of the pulse can be easily expressed with

$$C_x(t) = \omega_1(t)\cos\left[\phi(t)\right],\ C_y(t) = \omega_1(t)\sin\left[\phi(t)\right]. \tag{2.9}$$

In practice, the waveform of the pulse is discretised with a time resolution t_res, which must satisfy the Nyquist condition for the highest frequency of the sweep. Experimentally, the hardware imposes a minimum t_res but the Nyquist condition can be made easier to satisfy by centring the sweep width ΔF at offset zero ($\delta_\mathrm{f} = 0$), thus going from $-\Delta F/2$ to $+\Delta F/2$, with $t \in [\delta_\mathrm{t} - \tau_\mathrm{p}/2, \delta_\mathrm{t} + \tau_\mathrm{p}/2]$).

2.2.2 Spin dynamics simulation

While it does not provide an intuitive understanding, simulation can be used to accurately predict the behaviour of frequency-swept pulses. When designing broadband pulses, this is generally done on a range of spin-$\frac{1}{2}$s placed at different offsets along the bandwidth of interest. Their signal forms a spectrum called an inversion (e.g. in figure 2.3) or excitation profile (e.g. in figure 2.6). When the study of coupling is of interest, groups of coupled spins can be used to create similar profiles (e.g. in figure 2.23). B_1-insensitivity can be studied by plotting the pulses' effect on magnetisation for a range of pulses' amplitudes (different field strength B_1). This is often paired with excitation/inversion profiles in a 2D fashion (e.g. in appendix B). The total signal is formed by all the spins from the sample's active volume and spatial inhomogeneities of the oscillating magnetic field over that volume can lead to sensitivity loss and phase errors. To investigate them, simulated magnetisation results for different values of field

strength B_1 can be averaged (see figures 2.17 and 2.18). Phase cycling can be included in a similar manner by averaging the results from the different steps of the cycle.

Here, the core of the simulation is a single spin-$\frac{1}{2}$ $\hat{\boldsymbol{I}}$, which can be described using the Cartesian basis set $\mathcal{L} = \left[\hat{I}_x, \hat{I}_y, \hat{I}_z\right]$ where $\hat{I}_\alpha,\ \alpha \in [x, y, z]$ represent the Pauli matrices from equation (1.2).

For a single spin-$\frac{1}{2}$ at resonance offset Ω, the Hamiltonian under a hard pulse, was specified in equation (1.32) with a field $\boldsymbol{\omega_(1)}$ characterised by an amplitude ω_1 and a phase ϕ. For a frequency-swept pulse, the Hamiltonian can be similarly built by simply using a time dependent field $\boldsymbol{\omega_(1)}(t)$ with an amplitude $\omega_1(t)$ and phase $\phi(t)$. Here, the related pulse Cartesian coordinates, as seen in equation (2.9), are employed to express the Hamiltonian as

$$\hat{\mathcal{H}}(t) = C_x(t)\hat{I}_x + C_y(t)\hat{I}_y + \Omega\hat{I}_z. \tag{2.10}$$

Also needed as time-dependent to describe frequency-swept pulses, the density operator $\hat{\rho}(t)$ can be written with the time-dependent version of equation (1.20) as

$$\hat{\rho}(t) = q_x(t)\sigma_x + q_y(t)\sigma_y + q_z(t)\sigma_z, \tag{2.11}$$

where $\mathbf{q}(t) = [q_x(t), q_y(t), q_z(t)]^\intercal \in \mathbb{R}^3$ is a time-dependent unit vector which stands for the position of the spin on a Bloch sphere. As previously seen with equation (1.22), the evolution of the density operator is specified by the Liouville–von Neumann equation. Here, with (2.10) and (2.11), this equation can be transformed from SU(2) to SO(3) and expressed as [178]

$$\begin{bmatrix} \dot{q}_x(t) \\ \dot{q}_y(t) \\ \dot{q}_z(t) \end{bmatrix} = \begin{bmatrix} 0 & -\Omega & C_y(t) \\ \Omega & 0 & -C_x(t) \\ -C_y(t) & C_x(t) & 0 \end{bmatrix} \begin{bmatrix} q_x(t) \\ q_y(t) \\ q_z(t) \end{bmatrix}. \tag{2.12}$$

To solve (2.12), piece-wise constant propagation of the pulse is considered. The Cartesian components of the pulse $C_x(t)$ and $C_y(t)$ are discretised in $C_{x,n}$ and $C_{y,n}$,

which refer to the n^{th} segment of the pulse. The solution to (2.12) is therefore written as $\mathbf{a}(t + t_{\text{res}}) = \mathcal{R}_n \mathbf{a}(t)$ with

$$\mathcal{R}_n = \exp\left[\begin{pmatrix} 0 & -\Omega & C_{y,n} \\ \Omega & 0 & -C_{x,n} \\ -C_{y,n} & C_{x,n} & 0 \end{pmatrix} t_{\text{res}}\right]. \tag{2.13}$$

The Rodrigues rotation formula can be used to efficiently compute a vector rotation in space [187]. It is based on the approximation of the exponential of a skew-symmetric matrix Λ as

$$e^{\Lambda} = \mathbb{I} + \frac{\sin\lambda}{\lambda}\Lambda + \frac{1-\cos\lambda}{\lambda^2}\Lambda^2, \tag{2.14}$$

where $\mathbb{I}$ is the identity matrix and λ can be defined here as $\lambda = t_{\text{res}}\sqrt{C_{x,n}^2 + C_{y,n}^2 + \Omega^2}$.

The final state of the spin after a pulse of N segments can be expressed as $\mathbf{a}(\tau_{\text{p}}) = \mathcal{R}_N \mathcal{R}_{N-1} ... \mathcal{R}_2 \mathcal{R}_1 \mathbf{a}(0)$ where each segment can be computed with equation (2.14). For an excitation profile, a range of q_x, q_y, and q_z from equation (2.11) is respectively correlated to the x-, y-, and z-magnetisation yielded by the pulse or sequence.

An implementation of this method can be found in the MATLAB toolbox `MRChirpLab` [188], and further details on this package are given in appendix A. Compared to a previous implementation relying on orthogonal rotation matrices [97], computation is about three times faster thanks to this approach.

2.2.3 Adiabaticity factor, peak amplitude, and flip angle

To understand frequency-swept pulses, it is practical to define their adiabaticity factor [189]

$$\mathcal{Q}(t) = \frac{\omega_{\text{eff}}(t)}{\left|\frac{\mathrm{d}\zeta(t)}{\mathrm{d}t}\right|}, \tag{2.15}$$

where $\omega_{\text{eff}}(t) = \sqrt{\omega_1^2(t) + \Omega^2}$ is the amplitude of the effective field $\boldsymbol{\omega}_{\text{eff}}(\boldsymbol{t})$, Ω is the resonance offset, and ζ is the angle between the effective field $\boldsymbol{\omega}_{\text{eff}}(\boldsymbol{t})$ and applied field

$\boldsymbol{\omega_1(t)}$, defined from

$$\zeta(t) = \tan^{-1}\left(\frac{\Omega + \frac{\mathrm{d}\phi(t)}{\mathrm{d}t}}{\omega_1(t)}\right). \tag{2.16}$$

With this definition, adiabaticity can be understood as how well the magnetisation follows the changing effective field during a frequency-swept pulse, in contrast to hard pulses where the magnetisation rotates about a static effective field.

The peak amplitude of the pulse can be calculated thanks to the adiabaticity factor at the pulse centre $\mathcal{Q}_0 = \mathcal{Q}(t = \tau_\mathrm{p}/2)$, defined for an on-resonance spin ($\Omega = 0$) at the centre of the pulse ($\delta_\mathrm{t} = \tau_\mathrm{p}/2$), where $\delta_\mathrm{f} = 0$ and $t \in [0, \tau_\mathrm{p}]$.

Thanks to equations (2.3), (2.5), (2.15), and (2.16), the adiabaticity factor for a chirped pulse [126, 190] $\mathcal{Q}_0^\mathrm{CH}$ can be defined as

$$\omega_{1,\mathrm{max}}^\mathrm{CH} = \sqrt{\frac{2\pi\Delta F\mathcal{Q}_0^\mathrm{CH}}{\tau_\mathrm{p}}}. \tag{2.17}$$

Equivalently, an HS[1] pulse adiabaticity factor $\mathcal{Q}_0^\mathrm{HS}$ can be expressed with equations (2.6), (2.8), (2.15), (2.16) as

$$\omega_{1,\mathrm{max}}^\mathrm{HS} = \sqrt{\pi\beta\Delta F\mathcal{Q}_0^\mathrm{HS}}. \tag{2.18}$$

The adiabaticity factor can be used to obtain the flip angle α [126] thanks to a well-approximated solution of the Landau-Zener formula [191–194]:

$$\mathcal{Q}_0 = \frac{2}{\pi}\ln\left(\frac{2}{\cos(a)+1}\right). \tag{2.19}$$

For example, $\mathcal{Q}_0 = 0.441$ gives a $\pi/2$ excitation. Higher values of $\mathcal{Q}_0$ make the flip angle approach π asymptotically. This is the mechanism behind the B_1-insensitivity of frequency-swept pulses: the flip angle does not vary much when the adiabaticity factor is high enough (depicted earlier in figure 2.1b). $\mathcal{Q}_0 = 5$ is often picked for a π adiabatic inversion [190]. However, such high $\mathcal{Q}_0$ values are also associated with longer pulses (see next subsection) which can hinder the experiment sensitivity in case

of relatively fast relaxation. In addition, higher adiabaticity factors can be associated with generating unwanted multiple quantum coherence in coupled systems (particularly in EPR). Therefore, despite poor B_1-tolerance, optimal $\mathcal{Q}_0$ values may be much lower (e.g. 1 or 2) for some systems [126].

While both HS^1 and chirped pulses can be broadband and B_1-tolerant, HS^1 pulses minimise power deposition and are more selective than chirps. However, equations (2.17) and (2.18) show that the peak amplitude ($\omega_{1,\max}$) of an HS^1 pulse is $\sqrt{\tau_p\beta/2}$ times higher than the one of a chirped pulse for a given τ_p and ΔF. Chirps therefore present a much lower peak amplitude and are consequently usually preferred for ultra-broadband applications [97, 186]. When a compromise is required, the HS^n family offers solutions with HS pulses that approach a chirp behaviour as their indices n increase [174, 184].

2.2.4 Pulse compression

A simple strategy to pick appropriate parameters can start by first choosing a target bandwidth ΔF, taking into account smoothing effects when appropriate as $\Delta F_{\text{eff}} < \Delta F$. From there, the pulse can be compressed as much as possible by reducing its duration τ_p and raising its peak amplitude, $\nu_{1,\max}$ to the maximum power accessible on the instrument.

This can however be limited by the Time Bandwidth Product (TBP $= \tau_p \Delta F$) of the pulse, a quantity indicative of a pulse's "chirpiness" and found in various domains such as radars [195], acousto-optics [196], optics [197], MRI [86, 88, 198–200], and NMR [60, 104]. In the context of magnetic resonance, the TBP is also referred to as the modulation depth [189], or R-factor [63] of the pulse. A low TBP is a reflection of a lack of phase-modulation from the pulse and therefore leads to hindered uniformity of the pulse inversion/excitation profile through ripples and distortions. This can consequently reduce the pulse effective bandwidth and selectivity [60, 201]. For example, figure 2.3b illustrates a case where the targeted bandwidth is only reached by a chirped pulse with high enough TBP.

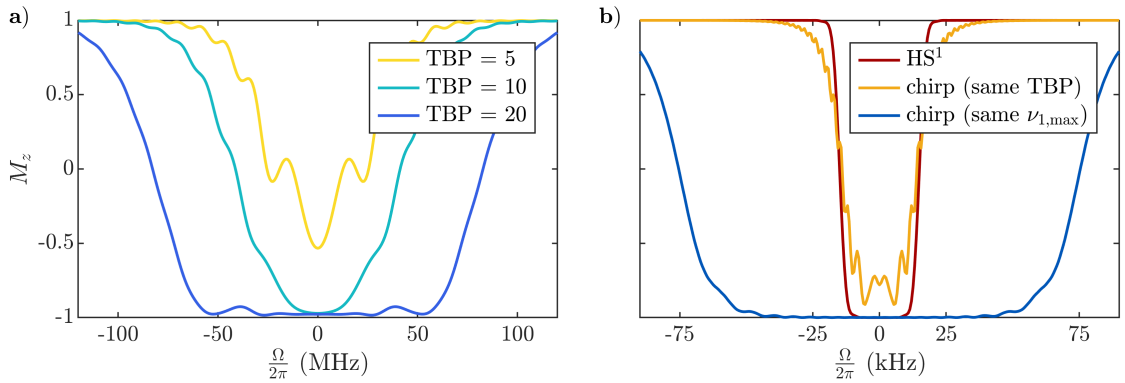


Figure 2.3: Simulated inversion profiles (z-magnetisation M_z) illustrating the effect of the Time Bandwidth Product (TBP = $\Delta F \tau_\mathrm{p}$). In a), profiles for ESR chirped pulses generated with $\tau_\mathrm{p} = 100\,\mathrm{ns}$, $\nu_{1,\mathrm{max}}$=30 MHz, $t_\mathrm{res} = 0.625\,\mathrm{ns}$, and 20% quarter-sine smoothing, but varying in adiabaticity factors: $Q = [11.3, 5.6, 2.8]$ and targeted bandwidths: ΔF=[50, 100, 200] MHz, corresponding to TBP of 5, 10, and 20 respectively. In b), profiles for NMR HS^1 and chirped pulses with the same duration $\tau_\mathrm{p} = 500\,\mu\mathrm{s}$ and adiabaticity factor $\mathcal{Q}_0 = 5$ ($t_\mathrm{res} = 0.5\,\mu\mathrm{s}$). Parameters of the HS^1 pulse were $\nu_{1,\mathrm{max}} = 15.9\,\mathrm{kHz}$, $\Delta F = 30\,\mathrm{kHz}$ and $\beta = 10.6/\tau_\mathrm{p}$. The chirped pulse with the same TBP as the HS^1 pulse does not reach the target bandwidth ($\Delta F = 30\,\mathrm{kHz}$), but the disparity between the two pulse amplitudes ($\nu_{1,\mathrm{max}} = 6.9\,\mathrm{kHz}$ against $15.9\,\mathrm{kHz}$) can be used to target a much wider bandwidth $\Delta F = 159\,\mathrm{kHz}$ thanks to a new chirp with the same $\nu_{1,\mathrm{max}}$.

Chirped pulses are more sensitive to the TBP than HS^1 pulses, presenting more degraded inversion/excitation profiles in the regime of very low TBP (e.g. <10) for a sought effective bandwidth ΔF_eff. However, thanks to their lower $\nu_{1,\mathrm{max}}$ requirements, they can target a bandwidth ΔF larger than necessary, consequently increasing their TBP, and allowing them to reach the original effective bandwidth objective [129], as can be seen on figure 2.3b.

Another limiting factor can be sample heating, linked to the total energy dissipated E_tot, which is itself proportional to $\tau_\mathrm{p} \times \nu_{1,\mathrm{max}}^2$. In the case of a chirped pulse, equation (2.17) states that $\nu_{1,\mathrm{max}}^2 \propto 1/\tau_\mathrm{p}$. Therefore, the dissipated energy stays constant for a given bandwidth ΔF and adiabaticity factor $\mathcal{Q}_0$ when the pulse is compressed by lowering its duration and increasing its power.

2.2.5 Offset refocusing with instantaneous flip approximation

The instantaneous flip approximation is a simple way to understand the evolution of the resonance offsets occurring during frequency-swept pulses without resorting to simulation. The approximation relies on considering a particular resonance offset as affected by a frequency-swept pulse at a unique segment of the pulse waveform whose duration tends to zero. By inferring the segment flip angle from the pulse $\mathcal{Q}_0$ (see subsection 2.2.3), the mechanisms of frequency-swept pulses and pulse sequences for inversion [43–48], refocusing [63, 182, 202], and excitation [53, 57, 62, 91, 94, 97, 183] can be apprehended with ease.

The instantaneous flip approximation relies on a given arbitrary resonance offset Ω, reached by the frequency sweep at a fraction α of the pulse duration, as in

$$\alpha = \frac{\Omega - 2\pi\delta_{\mathrm{f}}}{2\pi\Delta F} + \frac{1}{2}, \text{ with } \alpha \in [0, 1]. \tag{2.20}$$

For a single frequency-swept π-pulse of duration τ_π, there is no offset evolution in the inversion case, i.e. when the pulse is applied on a longitudinal magnetisation ($\hat{I}_z$). However, if the initial magnetisation is transverse (e.g. $\hat{I}_x$), Ω evolves for $\alpha\tau_\pi$ before the instantaneous flip point and for $(1-\alpha)\tau_\pi$ after that point, as is illustrated on figure 2.4a. This point effect can be expressed with an instantaneous π rotation along the x axis, $\hat{R}_x(\pi)$, and the overall pulse effect can be represented as

$$\alpha\tau_\pi \quad — \quad \hat{R}_x(\pi) \quad — \quad (1-\alpha)\tau_\pi,$$

where the offset Ω evolves in opposite directions before and after the instantaneous flip point. This opposition of the rotation directions is indicated with a change of sign opposition in the refocusing condition equation

$$[\alpha - (1-\alpha)]\tau_\pi = 0, \tag{2.21}$$

which is only satisfied for $\alpha = 1/2$ (also see figure 2.4a). After the pulse, the signal S thus carries an offset-dependent phase factor

$$S = \frac{\hat{I}^+}{2} \exp\left(\frac{\mathrm{i}\tau_\pi \Omega^2}{\pi \Delta F}\right). \tag{2.22}$$

However, a refocusing condition satisfied for all α can be created by inserting a second identical π-pulse [182], as in

$$(2\alpha - 1)\tau_\pi - (2\alpha + 1)\tau_\pi = 0, \tag{2.23}$$

yielding a fully-compensated signal (see figure 2.4b). In addition, two delays of equal duration τ_d can be inserted between and after the two pulses without disturbing the refocusing condition from equation (2.23). More broadly, frequency-swept pulse sequences can be easily extended by inserting delays of the same duration at points with opposite directions of offset evolution.

A different way to refocus the transverse magnetisation is to use three frequency-swept π-pulses [63] of durations τ_1, τ_2, and τ_3. The corresponding refocusing condition equation,

$$(2\alpha - 1)\tau_1 + (1 - 2\alpha)\tau_2 + (2\alpha - 1)\tau_3 = 0, \tag{2.24}$$

now has several solutions [202]. For instance, $\tau_1 = \tau_2/2 = \tau_3$ solves the equation with a central pulse twice as long as the other two (see figure 2.4c). Another solution is $\tau_1 = -\tau_2 = \tau_3/2$, where the last pulse is the one twice as long as the others while the second pulse has a reversed frequency sweep direction, indicated by the duration's opposite sign. Although this sequence is twice as long as the two-pulse refocusing, it can be employed as a single element delivering a net π rotation, and arbitrary delays of the same duration can be placed on either side of it, like for a hard π-pulse.

For a single excitation frequency-swept pulse applied on z-magnetisation ($\hat{I}_z$) for a duration τ_β, a resonance offset Ω evolves for $(1 - \alpha)\tau_\beta$ after the instantaneous flip. For simplicity, we illustrate this with a $\pi/2$-pulse of duration $\tau_{\pi/2}$ but this holds for lower

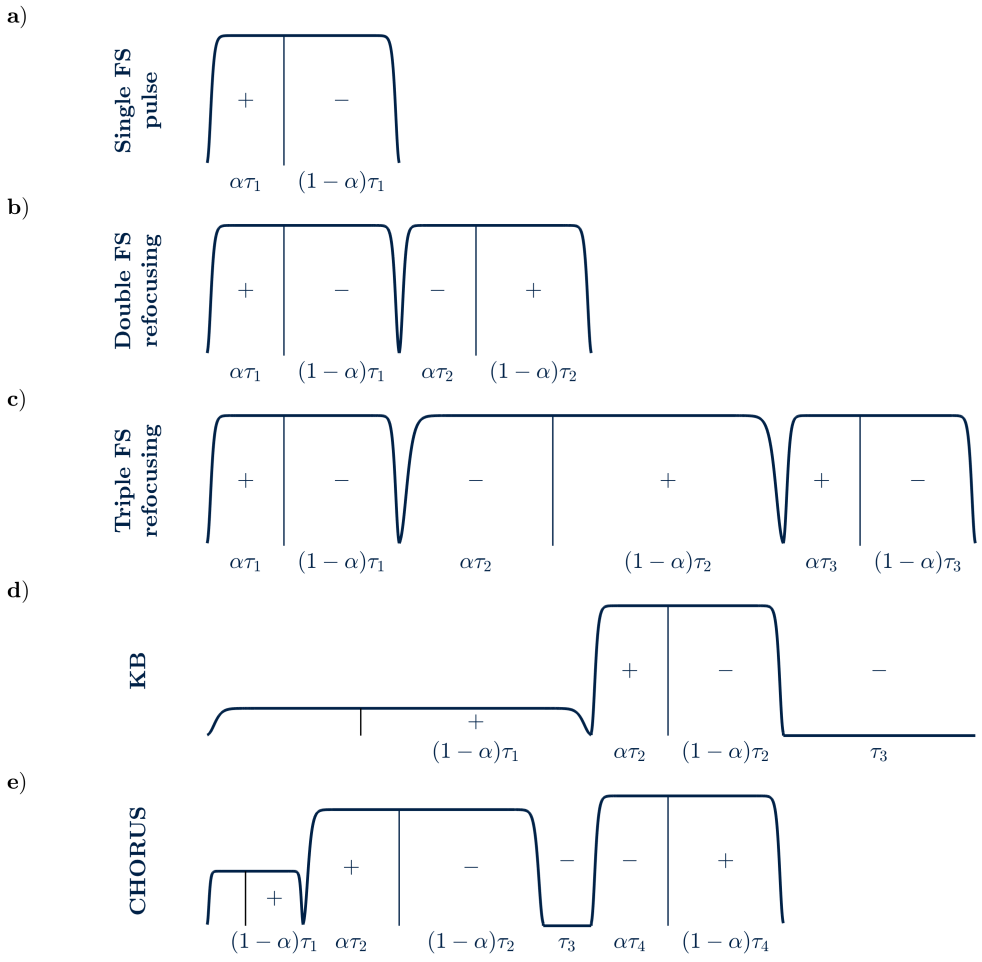


Figure 2.4: Sketch of frequency-swept building blocks with resonance offset (chemical shift) evolution: a) single pulse, b) double-refocusing, c) triple-refocusing, d) Kunz-Bodenhausen excitation, and e) CHORUS excitation. The vertical lines indicate the positions of the instantaneous flip for one particular offset reached by the frequency sweep at a fraction α. On each side of the lines, the opposite directions of offset evolution are represented by the "+" and "−" signs. At the bottom, the components for the refocusing condition are indicated. All sequences are represented with the envelope of chirped pulses.

flip angles:

$$\hat{R}_x(\pi/2) \quad \text{—} \quad (1-\alpha)\tau_{\pi/2}.$$

This leads the signal after the pulse to carry a phase which is quadratic in Ω:

$$S = \frac{\hat{I}^{+}}{2} \exp\left(-\frac{\mathrm{i}\tau_{\pi}\Omega\left(\pi\Delta F - \Omega\right)}{2\pi\Delta F}\right). \tag{2.25}$$

In order to refocus the signal, Kunz in MRI (with HS pulses) [53, 54] and Böhlen and Bodenhausen in NMR (with chirped pulses) [57, 59] proposed the idea of using an additional π-pulse and a delay (see figure 2.4d). The sequence refocusing condition is

$$(1-\alpha)\tau_{\pi/2} - (2\alpha+1)\tau_{\pi} + \tau_{\mathrm{delay}} = 0, \tag{2.26}$$

and can be solved with

$$\tau_{\pi/2} = 2\tau_{\pi} = 2\tau_{\mathrm{delay}}. \tag{2.27}$$

This gives the following sequence effect, refocusing offsets for all values of α:

$$\hat{R}_x(\pi/2) \quad -\!\!- \quad \left(1-\frac{\alpha}{2}\right)\tau_{\pi/2} \quad -\!\!- \quad \hat{R}_x(\pi) \quad -\!\!- \quad \left(1-\frac{\alpha}{2}\right)\tau_{\pi/2}.$$

The total duration of the two-pulse sequence is determined by the minimum available duration for a π-pulse τ_{ref} and therefore fixed at $4\tau_{\mathrm{ref}}$. This sequence is designated as KB (Kunz-Böhlen or Kunz-Bodenhausen) for brevity in the rest of the text.

Another way to refocus the offset evolution from a frequency-swept excitation pulse is to use three pulses, a concept which forms the basis of the Adjustable, Broadband, Sech/Tanh Rotation Uniform Selective Excitation (ABSTRUSE) [91] (with HS pulses) and CHirped ORderded pulse for Ultra-broadband Spectroscopy (CHORUS) [94, 97] (with chirped pulses) excitation sequences. After the excitation pulse of duration τ_1, two refocusing pulses of duration τ_2 and τ_4 with an interpulse delay of duration τ_3 are used to refocus the magnetisation (see figure 2.4e):

$$(1-\alpha)\tau_1 - (2\alpha+1)\tau_2 + \tau_3 + (2\alpha+1)\tau_4 = 0. \tag{2.28}$$

A solution for optimal compression can be expressed as

$$[\tau_1, \tau_2, \tau_3, \tau_4] = [\tau_{\text{exc}}, \tau_{\text{ref}} + \tau_{\text{exc}}/2, \tau_{\text{exc}}/2, \tau_{\text{ref}}], \tag{2.29}$$

where τ_{exc} and τ_{ref} represent the minimum duration of a $\pi/2$- and π-pulse, respectively. The three-pulse sequence has a duration of $2\,(\tau_{\text{exc}} + \tau_{\text{ref}})$ and is counter intuitively shorter than the two-pulse sequence by $2\,(\tau_{\text{ref}} - \tau_{\text{exc}})$, as illustrated in figure 2.5. However, instrument dead time, normally incorporated in the final delay of the two-pulse sequence, has to be added to the three-pulse sequence which limits the duration gain from the three-pulse sequence on instrumentation presenting an important dead time (typically in EPR, see subsection 2.3.3). A more important benefit of the three-pulse sequence is its higher B_1-tolerance as discussed in the next subsection.

2.2.6 Off-resonance effects and phase roll

Previously, the instantaneous flip angle approximation was considered only for spins on resonance, but each segment of the pulse also affects off-resonance spins. Consequently, spins acquire an offset-dependent phase during an excitation frequency-swept pulse, which appears as a second-order phase roll across the spectrum when refocused by a single pulse. More importantly, this phase roll makes the KB sequence very sensitive to B_1 inhomogeneity, which can be present over the sample's active volume (important for liquid-state NMR spectrometers) or over different offset frequencies (important for ESR resonators).

Pulses or composite events can mitigate the overall B_1-induced phase variations

$$\varphi_{t=T} \propto \int_0^T \mathbf{B}_{1,\text{eff}} dt, \tag{2.30}$$

where $\mathbf{B}_{1,\text{eff}} = \mathbf{B}_1^0 + \delta\mathbf{B}_1(\mathbf{r}, t, \nu)$ and $\delta\mathbf{B}_1(\mathbf{r}, t, \nu)$ stands for the nominal field variations in spatial, temporal, and frequential dimensions.

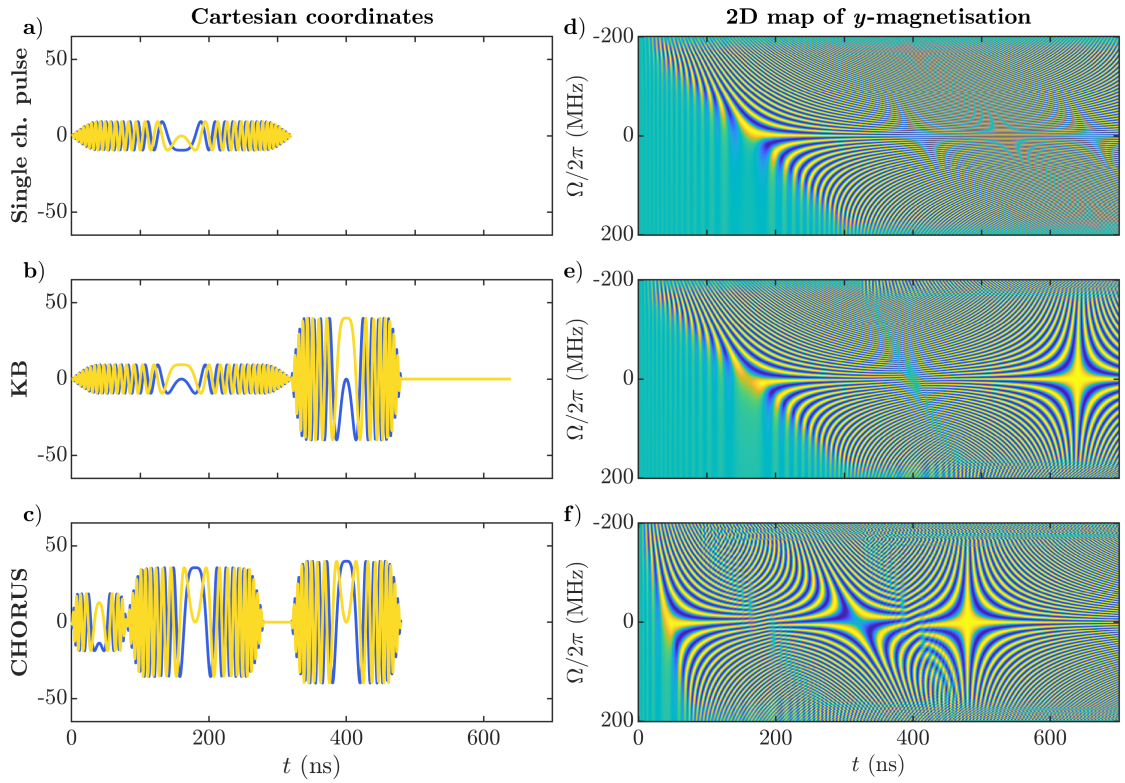


Figure 2.5: Cartesian representation (C_x in blue and C_y in yellow) of a) single chirped pulse excitation, b) Kunz-Bodenhausen and c) CHORUS excitation sequences with simulated 2D maps of y-magnetisation as a function of time and offsets in d), e) and f), respectively. The end of the sequences is indicated by the interruption of their components and a refocused echo can be found at that position on the 2D maps of the KB and CHORUS sequences. All the sequences were built with the same constraints (ESR X-band values in tables 2.2 and 2.3).

In order to make a B_1-tolerant excitation sequence, the sign of $\mathbf{B}_{1,\text{eff}}$ should be changed to compensate for the first induced variations. This is achieved by the three-pulse excitation sequences via the addition of a π-pulse [96]. In addition, these sequences' extra degree of freedom also allows for stronger compression of the excitation pulse which minimises residual phase roll across the spectrum.

For both two- and three-pulse excitation, the phase roll across the spectrum can be corrected thanks to the one-to-one relationship between time and frequency of frequency-swept pulses [95, 97, 203]. However, tweaking of the excitation pulse for the two-pulse excitation only improves the spectrum appearance [62] and cannot correct for B_1-sensitivity (see figure B.2a and figure B.2c in Appendix B for an example of this).

In practice, the phase correction can be applied by fitting the phase response of the pulse sequence to a polynomial and applying it as a phase correction to the excitation pulse [95, 97], as depicted in figure 2.6.

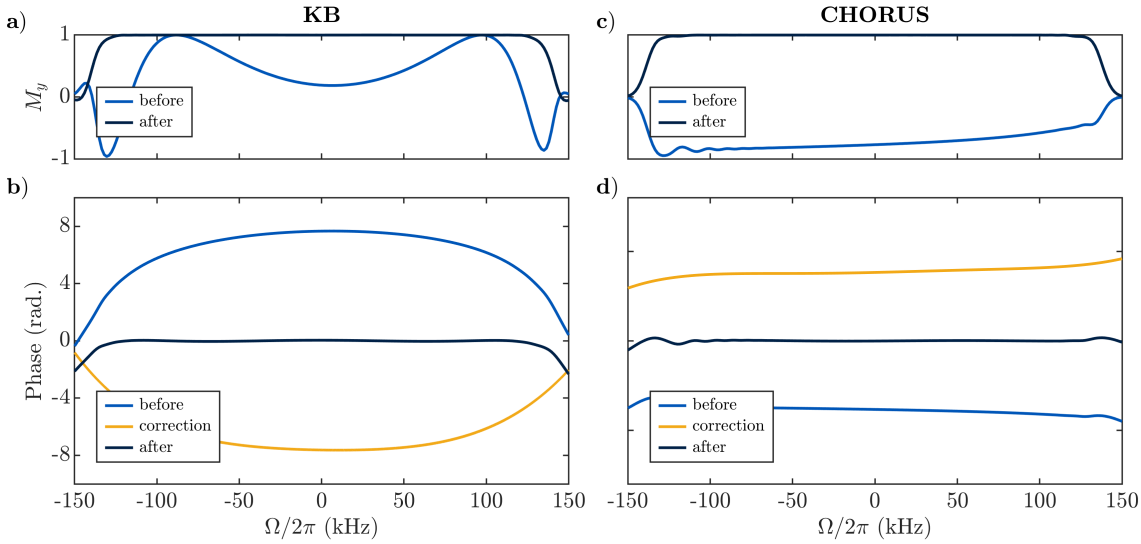


Figure 2.6: Simulated excitation profiles (y-magnetisation M_y) and their phase ($\arctan(M_y/M_x)$) before (blue) and after (black) applying a polynomial phase correction (yellow): in a) and b) for the KB sequence, and in c) and d) for the CHORUS sequence. Both sequences were built with the same constraints described in subsection 2.4.2.

Another more general solution is to induce an arbitrary quadratic phase by optimising the overall phases (ϕ_0) and frequency offsets (δ_f) of the pulses to minimise the residual phase dispersion [178]:

$$\underset{\phi_0,\delta_f}{\arg\min}\, \boldsymbol{M}_\mathrm{tar}^\mathrm{T}\boldsymbol{M}_\mathrm{fin} + \alpha\,\mathrm{Var}[\phi(\boldsymbol{M}_\mathrm{fin})], \tag{2.31}$$

where $\boldsymbol{M}_\mathrm{tar}$ is the magnetisation target state for the optimisation, and $\boldsymbol{M}_\mathrm{fin}$ is the magnetisation final state after the pulse sequence (computed at each optimiser evaluation for a set of ϕ_o and δ_f). In case of unsatisfactory results, the variance of the magnetisation phase $\mathrm{Var}(\phi)$ can be added with a constant weighting its importance, α. An algorithm such as L-BFGS, the Limited-Memory approximation of the Broyden–Fletcher–Goldfarb–Shanno (BFGS) algorithm [204], can be applied to conduct the optimisation in practice.

Although the optimisation technique cannot be applied for the second-order phase correction of the KB sequence, it offers greater flexibility. For example, only one pulse (with 2 parameters) is enough to adjust an excitation sequence with 3 frequency-swept pulses. Adding more pulses can also result in small improvements to the phase correction.

Table 2.1 compiles a summary of the frequency-swept pulse sequences seen in this section. These can be implemented as-is, or used to design other frequency-swept pulse sequences by considering them as simple building blocks, and/or remodelling them with the notions discussed above.

Table 2.1: Summary of some existing frequency-swept pulse schemes.

Sequence name	**Function**	$\boldsymbol{B_1}$**-tolerance**	**Phase roll**	**Reference(s)**
Single FS pulse	Inversion	Very high	No	[43, 44, 46]
Double FS pulse	Compensated refoc.	Very high	No	[182]
Triple FS pulse	Refocusing	Very high	No	[63]
Kunz/Böhlen-Bodenhausen	Excitation	Low	$1^{\mathrm{st}}/2^{\mathrm{nd}}$ order	[53, 57, 62, 183]
ABSTRUSE/CHORUS	Excitation	High	1^{st} order	[91, 94, 97]

2.3 ESR spectroscopy: CHORUS implementation

2.3.1 Background

Most ESR experiments are limited by the available excitation bandwidth from the spectrometer and can therefore take great advantage of broadband pulses which extend over this bandwidth. Optimal control theory pulses have been difficult to implement for reasons detailed in appendix C, but frequency-swept pulses have been researched and applied extensively for inversion/refocusing [123, 124, 130–137] and excitation [128, 135, 138–147]. However, there is only a single publication prior to 2020 which investigates excitation with three frequency-swept pulses, using ABSTRUSE [126].

This section covers the implementation of the ultra-broadband excitation sequence CHORUS in ESR spectroscopy. Straightforward parametrisation and calibration of the sequence is presented along with its experimental excitation profile and a standard sample application to compare the performance of the sequence to two-chirp excitation.

2.3.2 Materials and methods

Pulse generation and simulation

The chirped pulse sequences were generated, simulated and optimised with the version 1.0 of the `MRChirpLab` package [205] on MATLAB R2019b (see appendix A for more details). Resonator-compensated pulses were generated with EASYSPIN v5.2.28 [18].

The parameter used for generation of the sequences were selected according to the process described in subsection 2.3.3, and are grouped in table 2.2. To respect instrumental constraints, all pulse and delay durations were adjusted to be even integers in ns, with a time resolution $t_{\mathrm{res}} = 0.625\,\mathrm{ns}$. Individual pulse parameters are detailed in tables 2.3 and 2.4.

Table 2.2: Parameters used for sequence generation at X-band and Q-band for the CHORUS and KB sequences. The maximum available pulse amplitude $\nu_{1,\max}$ is dictated by the instrument. The bandwidth ΔF is chosen according to the sample spectral width and the resonator profile. $\mathcal{Q}_0^{\text{ref}}$ represents the refocusing pulses adiabaticity factor. The effective bandwidth ΔF_{eff} is the bandwidth actually reached by the sequence (shorter than ΔF due to pulse smoothing). Both sequences present the same minimum TBP acceptable for compression of the pulses $\text{TBP}_{\min} = 32$. The minimum pulse durations for excitation τ_{exc} and refocusing τ_{ref} are obtained from the other parameters (see subsection 2.3.3 for more details). The complete lists of pulse parameters is available in tables 2.3 and 2.4).

	$\nu_{1,\max}$ (MHz)	ΔF (MHz)	$\mathcal{Q}_0^{\text{ref}}$	Smooth.	ΔF_{eff} (MHz)	τ_{exc} (ns)	τ_{ref} (ns)
X-band	39.89	400	4	12.5%	300	80	200
Q-band	37.32	350	3	15%	245	92	166

Table 2.3: Parameters used for pulse generation of the CHORUS and KB sequences at X-band. The sequences' general parameters seen in table 2.2 establish the main constraints and the pulses are then determined according to their duration and flip angle fixed by the sequences refocusing requirements. The two bottom lines indicate the total duration of the sequences, without and with the acquisition dead-time.

	CHORUS			**Kunz-Bodenhausen**	
	pulse 1	**pulse 2**	**pulse 3**	**pulse 1**	**pulse 2**
ν_1 **(MHz)**	18.74	35.68	39.89	9.37	39.89
$\mathcal{Q}_0$	0.441	4	4	0.441	4
τ_{p} **(ns)**	80	200	160	320	160
TBP	32	80	64	128	64
τ_{seq} **(ns)**		480		640	
$\tau_{\text{seq+dead-time}}$ **(ns)**		660		640	

Samples

Experimental excitation profiles are generally obtained with a sample which present a single narrow line (see 2.3.4 for more details). Here, they were characterised at X-band with such a sample, a single point x-LiPc (figure 2.7a), a microcrystalline powder from the P4mm space group, in which electrons are delocalised over columnar lithium phthalocyanine stacks. The sample total volume was about $0.25\,\text{cm}^3$ and was prepared under a vacuum. It presented the following EPR properties: g-value of 2.00226 $\pm$0.00002 [206], Fourier transform linewidth of 200 kHz at 294K (CW-ESR peak-to-peak

Table 2.4: Parameters used for pulse generation of the CHORUS and KB sequences at Q-band. The sequences' general parameters seen in table 2.2 establish the main constraint and the pulses are then determined according to their duration and flip angle fixed by the sequences' refocusing requirements. The two bottom lines indicate the total duration of the sequences, without and with the acquisition dead-time.

	CHORUS			**Kunz-Bodenhausen**	
	pulse 1	**pulse 2**	**pulse 3**	**pulse 1**	**pulse 2**
$\boldsymbol{\nu_1}$ **(MHz)**	16.34	31.73	37.32	10.12	37.32
$\boldsymbol{\mathcal{Q}_0}$	0.441	3	3	0.441	3
$\boldsymbol{\tau_p}$ **(ns)**	92	166	120	240	120
TBP	32.2	58.1	42	84	42
$\boldsymbol{\tau_{seq}}$ **(ns)**		424		480	
$\boldsymbol{\tau_{seq+dead-time}}$ **(ns)**		604		480	

linewidth of 4.5 µT), $T_1 = 4.5\,\mu s$, and phase memory time $T_M = 2.3\,\mu s$ with a stretched exponential value x=0.88.

The application examples were conducted at Q-band with a bisnitroxide, 2,6-bis[(((2, 2,5,5-tetramethyl-1-oxypyrrolin3-yl)-carboxyl)oxy)]-anthracene [207] (figure 2.7b). The sample was prepared by dilution in a polymer matrix and filled the resonator height with an inner diameter of 1 mm. It presented the following EPR properties at 80 K: $T_1 = 188\,\mu s$ and phase memory time $T_M = 1.46\,\mu s$, with a stretch value $x = 0.78$. At room temperature, $T_1 = 10.5\,\mu s$ and $T_M = 0.56\,\mu s$, with a stretch value $x = 0.79$.

Hardware

A Bruker BioSpin Elexsys II E580 spectrometer served for all experiments. For X-band measurements, a resonator Bruker BioSpin ER4118-MS2-W1 was employed with a Traveling-Wave Tube (TWT) amplifier Applied Systems Engineering model 117. For Q-band measurements, a dielectric TE01δ resonator Bruker EN 5107D2 was used with a TWT amplifier Applied Systems Engineering model 187Ka (L3 Electron Devices, model 8922HP-1 TWT). Low temperature was maintained at 50 K thanks to cryogenic liquid helium flow with an Oxford Instruments CF935O cryostat and Mercury instrument temperature controller.

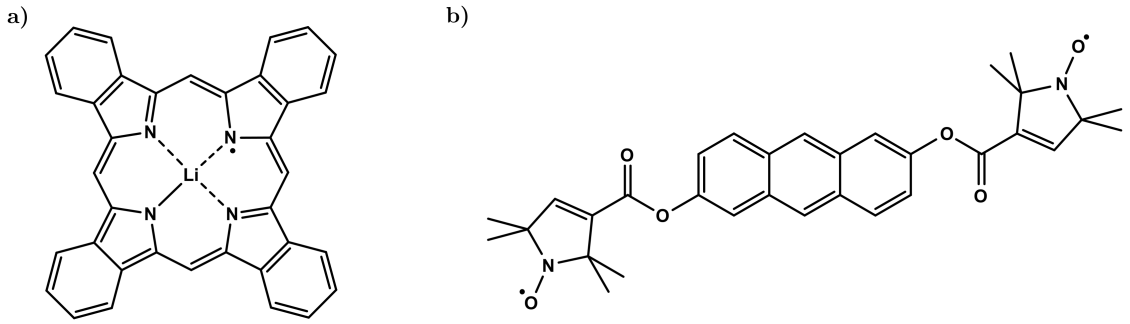


Figure 2.7: Structures of ESR samples used: a) x-LiPc and b) bisnitroxide. The x-LiPc electron spin does not present any anisotropy or coupling and its spectrum therefore exhibits a single resonance line ($g = 2.00226$). The bisnitroxide solid-state spectrum is a powder pattern due to anisotropy of $\mathbf{g}$ ($g_x = g_y = 2.0085, g_z = 2.0024$) and its hyperfine interaction with the neighbouring ^{14}N ($I = 1, a_x = a_y = 16\,\text{MHz}, a_z = 90\,\text{MHz}$). Other hyperfine couplings also exist (^{1}H, ^{13}C) but have little impact on the powder spectrum. In addition, a dipolar coupling is present between the two electrons, of about 6.7 MHz for a distance separation of around 2.0 nm (values reported for sample in [207]).

A SpinJet AWG, based on a Teledyne SP Devices SDR14 Peripheral Component Interconnect (PCI) board, generated the pulses with a time resolution of 0.625 ns for a corresponding sampling rate of 1.6 gigasamples per second ($\text{GS}\,\text{s}^{-1}$). For a centred frequency-swept pulse, the Nyquist frequency should allow a maximum sweep of 1.6 GHz. However, strong practical restrictions from analog electronics limit the -1 dB bandwidth to 180 MHz (10% amplitude variation) and the -3 dB bandwidth to 330 MHz (30% amplitude variation).

The receiver includes the Bruker BioSpin SpecJet III and video amplifier VAMP III with a theoretical bandwidth of 1 GHz (2 $\text{GS}\,\text{s}^{-1}$), although once again limited by practical considerations. A combined profile of the AWG and receiver is reported in figure 2.8.

Experiments

At X-band and Q-band, a nutation experiment yielded the resonator profiles [124] shown figure 2.8, which were further used for the generation of the resonator-compensated pulses at Q-band.

For the AWG/receiver profile, the signal was recorded without the TWT amplifier and resonator, directly from the AWG through the Transmitter Monitor (TM) path. A total of 401 points were acquired from $-400\,\mathrm{MHz}$ to $400\,\mathrm{MHz}$ with a $10\,\mu\mathrm{s}$ pulse, and the subsequent signal intensity was measured at the receiver.

The KB sequence was run with a 16-step phase cycle and a receiver phase set to select the coherence order -1. CYCLOPS was applied on the excitation pulse for quadrature imbalance and DC leakage (4-step) and Exorcycle was applied on the refocusing pulse to select the coherence transfer pathway (4-step). The whole phase cycle, with subscripts for the repetition number, can be expressed as

$$\begin{aligned}
\phi_1 &= [0_4,\ 90_4,\ 180_4,\ 270_4], \\
\phi_2 &= [0,\ 90,\ 180,\ 270]_4, \\
\phi_{\mathrm{rec}} &= +\phi_1 - 2\phi_2.
\end{aligned}$$

The CHORUS sequence was run with the same individual pulse cycles, giving the following 64-step phase cycle:

$$\begin{aligned}
\phi_1 &= [0_{16},\ 90_{16},\ 180_{16},\ 270_{16}], \\
\phi_2 &= [0,\ 90,\ 180,\ 270]_{16}, \\
\phi_3 &= [0_4,\ 90_4,\ 180_4,\ 270_4]_4, \\
\phi_{\mathrm{rec}} &= -\phi_1 + 2\phi_2 - 2\phi_2.
\end{aligned}$$

Subsection 2.3.3 presents the calibration process for the sequence pulse amplitudes. Additionally, DC leakage at the carrier frequency was first corrected by balancing the I/Q channels output. In practice, this was conducted at high power attenuation in transmitter mode by reducing a highly averaged signal to zero with adjustments of the bias of the I/Q channels in the SpinJet AWG control panel.

Measurements with the x-LiPc sample were conducted at X-band with a carrier frequency set at $9.45\,\mathrm{GHz}$ and a temperature of $293\,\mathrm{K}$. Pseudo-FIDs were recorded

by adjusting the sequence timings to only record half of the echo. To obtain the frequency-swept pulse sequence excitation profiles, 41 pseudo-FIDs (half of the echo) were recorded with 8k complex points and 20 averages per scan, at regular steps during a 20 mT field-sweep. This is equivalent to 41 spectra recorded with a carrier frequency stepped by 14 MHz from -280 MHz to 280 MHz. For comparison, the same process was performed for a pulse-acquire sequence with a 6 ns excitation pulse and a 4-step phase cycle (CYCLOPS). A total of 81 FIDs were recorded over a 40 mT field with 16k complex points and 10 averages per scan.

Refocused echo measurements with the bisnitroxide sample were conducted at Q-band with a carrier frequency set at 33.80 GHz and at a temperature of 293 K. The KB experiment was carried out with 256 averages per scan and the CHORUS experiment with 1024. Both were acquired with 512 complex points. For comparison, a Hahn-echo experiment was run with 2 ns and 4 ns pulses and a 16-step phase cycle (CYCLOPS and Exorcycle). The echo was recorded with 1k complex points and 200 averages per scan. For reference, a field-swept Hahn-echo was carried out with 300 points over 20 mT using 1024 complex points and 256 averages per scan for the echo.

EDNMR measurements were conducted on the bisnitroxide sample at Q-band with a carrier frequency set at 33.95 GHz and at a temperature of 50 K. The Chirped Echo EPR SpectroscopY (CHEESY) experiment was conducted with the CHORUS sequence in the observer channel. The CHORUS sequence was generated with resonator-compensated pulse from a newly-acquired resonator profile. The observed echo was recorded with 512 complex points and 64 averages per scan. For the pump channel, the HTA pulse employed a Gaussian shape for a duration of 4 µs. The pump frequency was swept from −250 MHz to 250 MHz in 501 steps of 1 MHz.

Data processing

The Xepr software (Bruker BioSpin) and Matlab R2019b were used for all post-processing and plotting of the data. Data from Xepr were imported in Matlab environment with EasySpin v5.2.28 [18].

For excitation profiles at X-band, post-processing of individual FIDs comprised zero-filling to 2k complex points, followed by Fourier transformation. Individual spectra were then summed and their phase corrected thanks to the MATLAB-NMR library [208].

For spectra at Q-band, post-processing comprised zero-filling to 2k complex points, followed by Fourier transformation and phase correction in XEPR. The number of averages per scan, the number of scans in the phase cycle and the video gain were accounted for when comparing two spectra on the same scale. The field-sweep data was transformed to the frequency-domain, centred at 33.8 GHz, flipped around that point, and normalised to serve as a reference.

For the CHEESY experiment, post-processing comprised zero-filling the echoes to 1k complex points, followed by Fourier transformation, and phase correction in XEPR. The dimension with the HTA frequency variation was interpolated to 1k complex points. The obtained squared 2D dataset was then sheared and projected on its x- and y-axis by summing the data.

All simulation code and experimental data, with the pulse shapes used to record it, (in BRUKER XEPR format) are accessible in the version 1.0 of `MRChirpLab` [205].

2.3.3 Sequence parametrisation and calibration

Sequence parametrisation in light of hardware constraints

A major constraint to frequency-swept pulses use in ESR is the modification of the pulse shapes caused by non-linear effects from the hardware, mainly the microwave components. This effect can be characterised by measuring a resonator profile [122]. Thus, making such a measurement is the first step to design an appropriate CHORUS sequence. Resonator profiles, such as the one presented in figures 2.8a and b, therefore helped to identify the appropriate carrier frequency, the maximum peak amplitude $\nu_{1,\max}$, and the targeted bandwidth ΔF for the sequence. After further picking an adiabaticity factor of the refocusing pulses $\mathcal{Q}_0^{\text{ref}}$ and the minimum Time Bandwidth Product $\text{TBP}_{\min}$, the pulse compression method described in subsection 2.2.4 was ap-

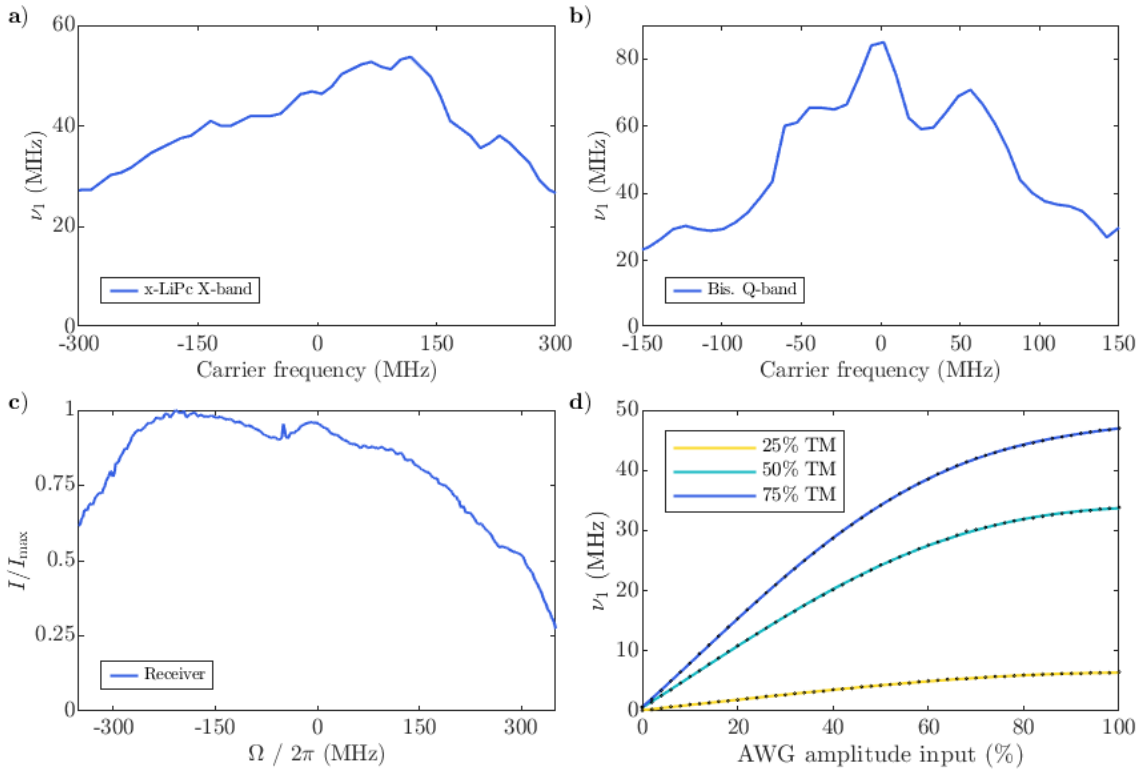


Figure 2.8: Characterisation of EPR spectrometer limitations. Resonator profile of a) x-LiPc sample at X-band and room temperature (centred at 9.45 GHz), and b) of bisnitroxide sample at Q-band and 50 K (centred at 33.945 GHz). c) Combined AWG and receiver profile recentred at 9.45 GHz and normalised. A spike artefact coming from the DC offset (leakage from I/Q mixing at transmitter frequency) is present in the middle of the profile. d) Pulse amplitude ν_1 as a function of the input percentage amplitude for the AWG at 9.45 GHz (saturation of power amplifier). Data from different Transmitter Monitor (TM) level percentage (carrier level) measurements are plotted. For all plots, more experimental details can be found in subsection 2.3.2.

plied to get the minimum excitation pulse duration τ_{exc} and refocusing pulse duration τ_{ref}. The sequence timings were then obtained from equation (2.27) $\tau_{\pi/2} = 2\tau_\pi = 2\tau_{\text{delay}}$ for KB, and equation (2.29) $[\tau_1, \tau_2, \tau_3, \tau_4] = [\tau_{\text{exc}}, \tau_{\text{ref}} + \tau_{\text{exc}}/2, \tau_{\text{exc}}/2, \tau_{\text{ref}}]$ for CHORUS. This ensured maximum compression while respecting the user requirements and the instrument constraints (X-band sequences also previously plotted in figures 2.5b and c). In addition, pulses compensating for hardware effects can be generated [124, 125], i.e. from the resonator profiles.

Spin dynamics simulation (seen in subsection 2.2.2) ensured that $\mathcal{Q}_0^{\text{ref}}$ and $\text{TBP}_{\min}$

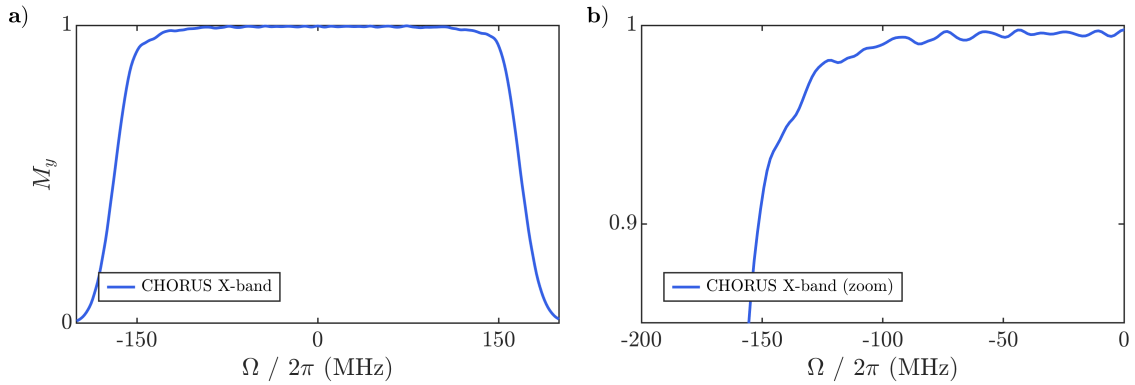


Figure 2.9: Simulated excitation profile for the CHORUS sequence a) over 400 MHz and b) close up on its left-side transition region. The sequence was built with the X-band values from tables 2.2 and 2.3. This type of simulation ensures that the chosen sequence parameters result in a uniform excitation profile.

would produce a uniform excitation profile. For example, X-band pulse parameters values from tables 2.2 and 2.3 give the excitation profile from figure 2.9 for CHORUS. The reduced TBP chosen for strong compression slightly distorts the excitation profile. Some ripples, up to 0.85% variation of the y-magnetisation, can indeed be observed between -100 MHz and 100 MHz (excitation passband). Only 91% and 94% of the fully excited magnetisation were also obtained at respectively -150 MHz and $+150$ MHz, indicating that the sequence did not achieve its full desired effect at the extremities of the effective bandwidth (excitation stopband). These distortions were considered tolerable when considering the range of variations introduced by the hardware.

Another important experimental restriction is the dead time required by the spectrometer hardware. After the last pulse end, it took about 90 ns to the acquisition trigger on our system. This duration can be integrated in the final delay of the KB sequence, but should be added at the end of the CHORUS sequence. To respect the three chirped pulse sequence refocusing condition, an additional delay with the same duration should also be placed between the two refocusing pulses. Here, this made the CHORUS sequence actually longer than the KB sequence, by 3% for the X-band values and 26% for the Q-band values.

Finally, frequency-swept pulses can excite forbidden transitions which can be present

in ESR spin systems. This effect, sometimes desirable depending on the application, gets stronger for an increasing number of frequency-swept pulses [126]. The CHORUS sequence is therefore expected to activate more forbidden transitions than the KB sequence. In addition, for particularly broad spectra, using more frequency-swept pulses could lead to weak echoes due to enhanced spectral diffusion. Nonetheless, no signal intensity difference was observed between the KB and CHORUS sequences in the present work on the x-LiPc and bisnitroxide samples.

Calibration

The adjustment of the relative amplitudes of the pulses can be viewed as a straightforward optimisation problem by considering equation (2.30), and looking for the minimum $^{d\varphi}/_{dB_1}$ for a range of ν_1 values around the desired ν_1 with

$$\left\{\nu_{1,\pi}^{(1)}, \nu_{1,\pi}^{(2)}\right\} = \underset{\nu_{1,\pi}^{(1)},\nu_{1,\pi}^{(2)}}{\arg\min} \left(\frac{d\varphi}{d\nu_1}\right) \tag{2.32}$$

Using the amplitudes given by equation (2.17) simply equates to solving this optimisation offline, as is the case in NMR. In contrast, due to limitations of the ESR hardware, the chirped pulse amplitudes obtained from equation (2.17) cannot be simply input as they are on the ESR spectrometer.

As shown on figure 2.8d, the effective amplitude percentages which act as experimental inputs to the spectrometer (referred to as "input amplitude" here) are indeed not linearly correlated to the actual output amplitude, because of the saturation of the power amplifier placed after the AWG. In addition, this relationship between the input and output amplitudes varies with the Transmitter Monitor (TM) level. Therefore, the optimisation must be solved experimentally through calibration.

For the KB sequence, the calibrated values were found by varying both of the sequence input amplitudes in a 2D fashion, linearly and independently. On the obtained 2D map, the optimal values were found at the maximum absolute value of the signal intensity. Figure 2.10a presents the result of such experiment for the x-LiPc at X-band.

Here, the $\pi/2$- and π-pulses presented optimal experimental input amplitudes of 14% and 58%, respectively.

For the CHORUS sequence, several calibration steps were necessary:

(i) A linear variation of the $\pi/2$-pulse input amplitude yielded an optimum at the maximum absolute value of the signal intensity. To account for off-resonance effects, the carrier was also moved for the measurement thanks to a field shift of 1 mT. For the x-LiPc sample at X-band, an optimum input amplitude of 35% was found.

(ii) For the π-pulses, a calibration similar to the KB sequence was performed, with the input amplitude of the $\pi/2$-pulse kept at the value from step (i). The two input amplitudes of the π-pulses were varied linearly and independently to get a 2D map of the absolute value of the signal intensities, on which the maximum indicates the calibrated input amplitude. In the case of x-LiPc sample at X-band, the data from figure 2.10b give optima at 80% and 95% for the π-pulses input amplitudes. As shown on the 2D map, the signal intensity increases sharply to reach a plateau once the input amplitudes of the refocusing pulses exceed a certain threshold, implying a successful adiabatic refocusing of the signal.

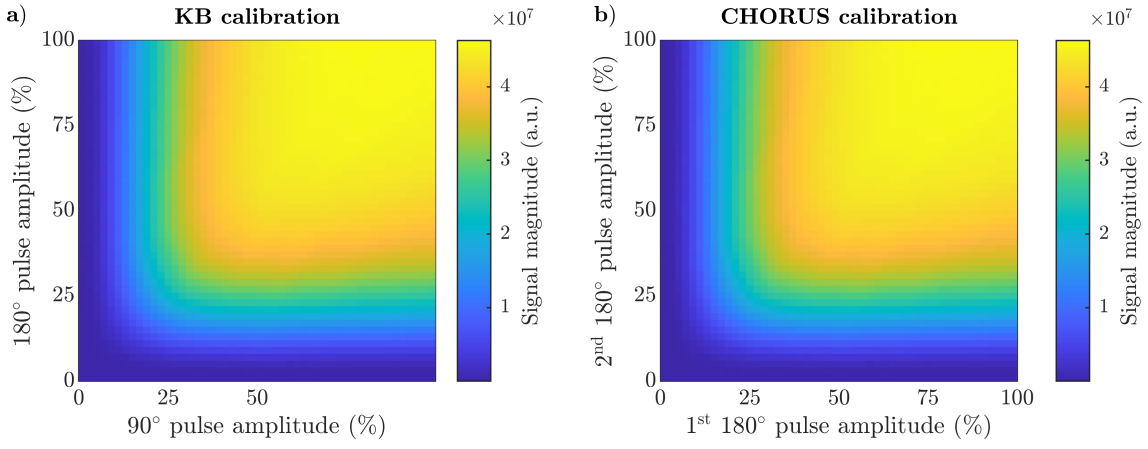


Figure 2.10: Experimental calibration maps of the input amplitude for a) both pulses from the KB scheme, and b) for the refocusing pulses from the CHORUS schemes (x-LiPc sample at X-band).

2.3.4 x-LiPc at X-band

In NMR spectroscopy, the effect of a pulse or a pulse sequence over a certain bandwidth can be measured by sweeping the carrier frequency over the corresponding range of offset frequencies. The resulting experimental inversion or excitation profile is the collective response of all spectra, generally obtained from a sample with a single narrow line [61–63, 91, 95, 97, 183].

For ESR spectroscopy, similar methods have been reported with examples of samples present in the literature that include Fluoranthenyl-hexafluorophosphate [122], or a γ-irradiated Herasil glass rod [126]. The time-domain signal has also been employed to get the excitation profile by employing an echo integral [143]. Here, Lithium Phthalocyanine (x-LiPc in figure 2.7a) was used for the thin single narrow line presented by its spectrum. This sample's ESR half width at half maximum has indeed been reported at a value of 150-450 kHz, for measurements conducted on its powder format at X-band and room temperature [209].

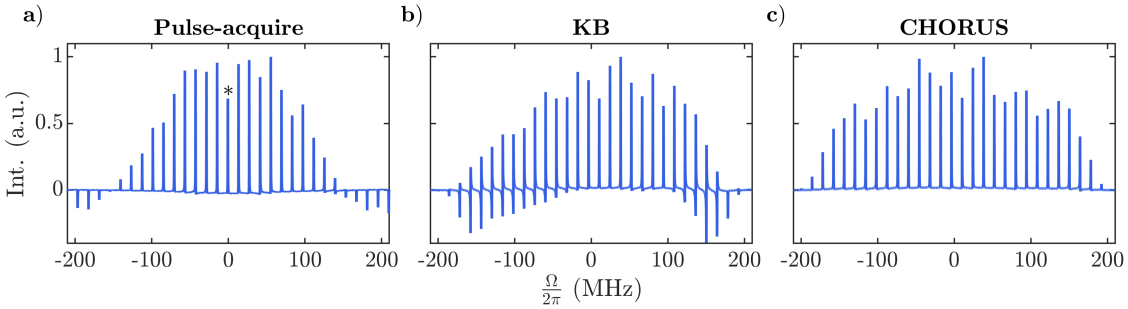


Figure 2.11: Experimental excitation profiles for the a) pulse-acquire, b) KB and c) CHORUS schemes. All the spectra were recorded with the x-LiPc sample at 9.45 GHz and normalised to one. The asterisk at 0 MHz marks a distortion from the DC offset.

Because the frequency-dependent effects from the ESR instrumentation should be accounted for, the static magnetic field was swept in place of the carrier frequency. Figure 2.11 presents a comparison of the resulting excitation profiles from the uncorrected and uncompensated KB and CHORUS sequences, and from a pulse-acquire for reference. While both frequency-swept pulse sequences offer an improved bandwidth,

CHORUS yielded significantly better uniformity. Nevertheless, its profile still presents an important intensity variation, up to about 50% at the ends of the 300 MHz effective bandwidth.

Evidently stronger than predicted by simulation from figure 2.9, this distortion is caused by the different restrictions imposed by the hardware. The loaded shape is first deformed by the power amplifier after the output from the Arbitrary Waveform Generator (AWG) [125]. The microwave component of the spectrometer (mainly the TWT and resonator [124]) distorts it further before it is effectively applied to the spins [122]. These components again disturb the induced signal and the receiver frequency response imposes a final modification of the recorded signal. Figure 2.8d presents a combined profile of the AWG and receiver demonstrating the frequency-dependent variation of the signal intensity due to their limitation. Here, a signal variation of 17% is observed over the bandwidth of interest.

The CHORUS sequence also gave an overall signal intensity 6% higher than the KB sequence, indicative of a robustness to spatial B_1 inhomogeneities as described in subsection 2.2.6. This robustness has also been previously associated to a gain of sensitivity in NMR spectroscopy [95, 97], which will be further exploited in subsection 2.4.3.

2.3.5 Bisnitroxide at Q-band

For a more realistic illustration of CHORUS applications in ESR, a bisnitroxide sample, presented in figure 2.7b, was used at Q-band with a temperature of 50 K. A spectrum recorded with a Hahn-echo field-sweep served as reference to compare Fourier transform spectra from a Hahn-echo, the KB and the CHORUS sequences, as seen on figure 2.12. As the resonator characteristics are much more constraining at Q-band compared to X-band, the resonator profile from figure 2.8 was employed to apply resonator compensation to the frequency-swept pulse sequences. This significantly improved the result from CHORUS as demonstrated on figure 2.13b.

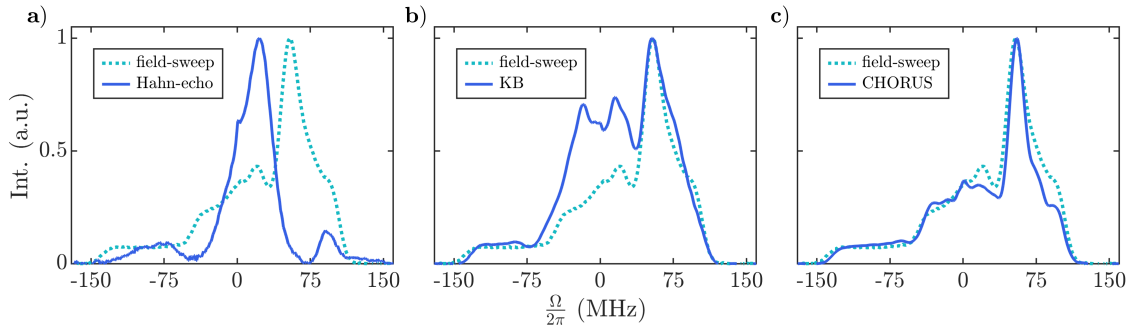


Figure 2.12: Q-band experimental powder spectra from a) Hahn-echo, b) Kunz-Bodenhausen and c) CHORUS sequences in dark blue. In dotted light blue, a field-sweep measurement serves as reference (target). The spectra were recorded with the bisnitroxide sample at 33.80 GHz and normalised to one. For interpretation, see similar spectra on figure 1.7. The asterisk at 0 MHz marks a distortion from the DC offset.

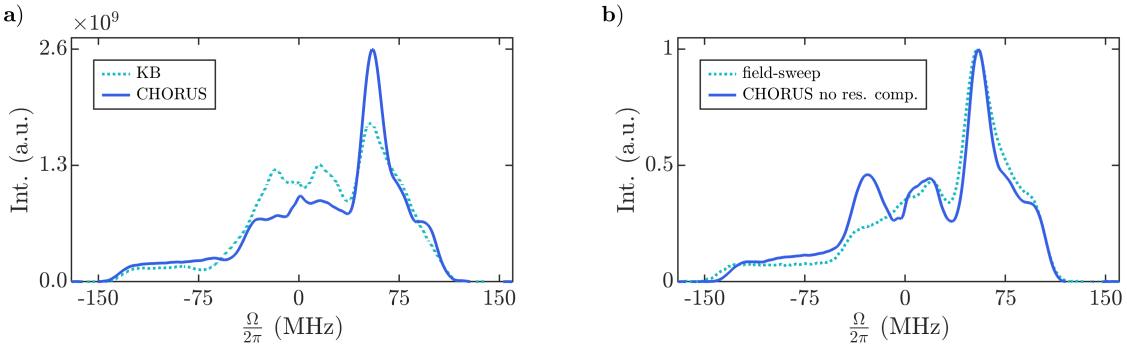


Figure 2.13: Experimental spectra of bisnitroxide at Q-band. a) Same plot comparison of KB in dotted light blue and CHORUS in dark blue (data also on figures 2.12b and c). b) Data from the CHORUS sequence run without resonator-compensated pulses in dark blue and in dotted light blue, field-sweep measurement serving as reference (target).

Figure 2.13a shows that the intensity of the signal collected by CHORUS is 47% higher than the one from the KB sequence (at global maximum). This difference is more important at Q-band as spatial B_1 inhomogeneities are more severe at higher fields. Thanks to the CHORUS sequence robustness to both spatial and frequential B_1 inhomogeneities, the three chirped pulse scheme produced the excitation spectrum the closest to the reference spectrum, as displayed in figure 2.12c.

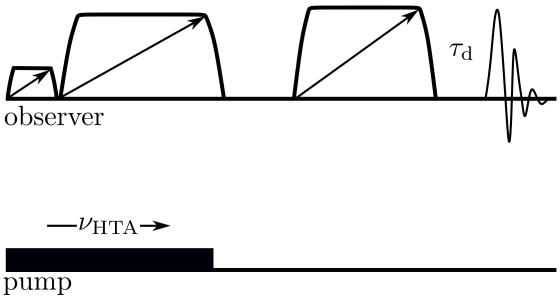


Figure 2.14: Scheme of the CHEESY-EDNMR sequence set up with the CHORUS sequence as the detection of the hole pattern. τ_d stands for the dead time during which no signal can be recorded. The arrow indicates a sweep of the HTA pulse frequency.

As a practical demonstration, EDNMR was conducted with chirped pulses in the observer channel, an experiment referred to as CHEESY-detected NMR [146]. In place of the originally proposed KB sequence, the CHORUS sequence was placed as the observer channel of the EDNMR experiment (see figure 2.14). EDNMR with chirped pulses relies on changing spin populations via forbidden transitions driven by the HTA pulse just like EDNMR with hard pulses as seen in subsection 1.5.4.

In contrast to the hard pulses, the chirped pulses can get the full ESR spectrum in a single shot, gaining an additional dimension at no cost. However, the data has to be sheared and the HTA pulses frequency dimension requires about twice as many points. In addition, the Lorentzian fit which is sometimes used in conventional EDNMR to get rid of the central blind spot cannot be applied.

The EDNMR spectra obtained by conventional methods and CHEESY-detected NMR can differ because of orientation selection. Orientation selection refers to the fact that only certain crystallite orientations are excited by hard pulses (due to their limited bandwidth) when anisotropic interactions are present. Consequentially, CHEESY-detected NMR orientation is linked to the HTA pulse instead of the observer pulses which means that the detection resolution is not linked to the observer sequence anymore (assuming that the detection window is appropriate). Figure 2.15 displays the CHEESY CHORUS spectrum.

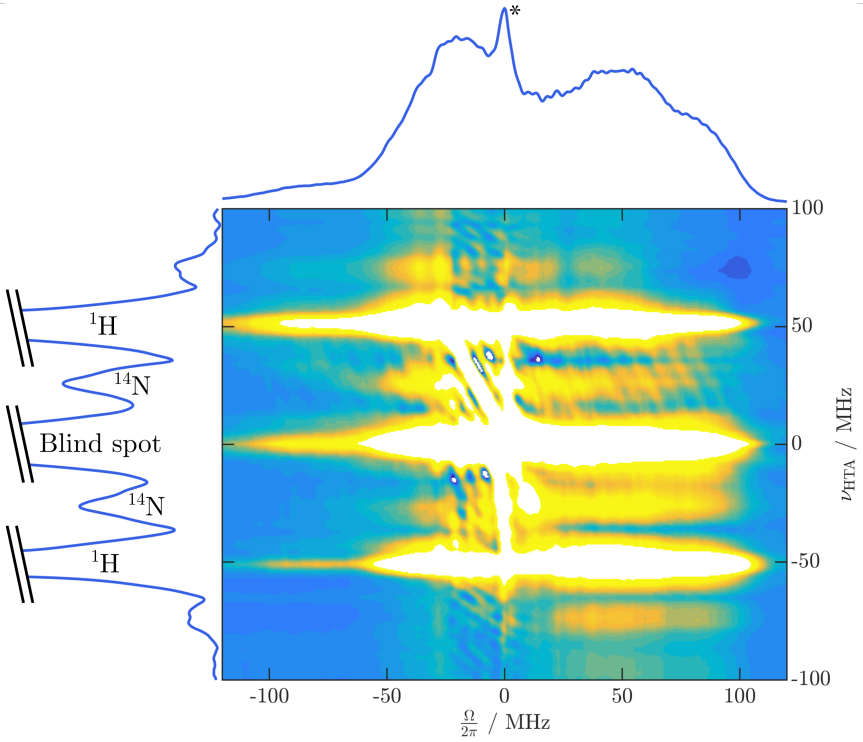


Figure 2.15: CHEESY EDNMR experimental magnitude 2D spectrum recorded with the CHORUS sequence as observer (bisnitroxide sample at Q-band). The y-axis projection reveals the EDNMR spectrum with the blind spot as the central peak. The ^{1}H transitions form an unresolved doublet (coupling to one unpaired electron) far more intense than the triplet created by the ^{14}N ($I = 1$) since there are more equivalent ^{1}H than ^{14}N, which also has a lower gyromagnetic ratio. The central peak of the triplet is masked by the blind spot. The peaks on the further side of the spectrum are double quantum transition or ^{1}H+^{14}N combination frequencies (the rest of similar transitions are buried under the ^{1}H and ^{14}N peaks). The asterisk at 0 MHz marks a distortion from the DC offset (leakage from I/Q mixing).

2.4 NMR spectroscopy: design of new schemes

2.4.1 Background

Although liquid-state NMR is much less demanding than EPR in terms of bandwidth, some nuclei still exhibit dispersions of chemical shift too wide to be practically covered by hard pulses. In the push for higher sensitivity and resolution with ever-increasing B_0, this dispersion is expected to become more common and with it, the need for broadband

pulses. Additionally, while not subject to B_1 variations over a range of frequencies such as the one imposed by the resonator in EPR, solution NMR instruments can exhibit strong B_1 inhomogeneity over the sample's active volume. For these reasons, it is relevant to present several broadband B_1-tolerant sequences in this section in the context of liquid-state NMR. However, the developed schemes and principles are applicable to other magnetic resonance domains.

First, we examine the concept of broadband CPMG, an idea unsurprisingly explored extensively in the literature given the many applications of this sequence. Using composite and optimal control pulses, diverse versions of broadband CPMG have been reported, mostly at reduced bandwidth but with shorter pulses compared to regular frequency-swept pulses [210–216]. Several designs employing hard pulses for excitation and chirped or HS[1] pulses as refocusing elements have also been explored [78, 83, 217–219]. Using frequency-swept pulses for both excitation and refocusing has been proposed in stray-field NMR [148, 149] and ultra-wideline solid-state NMR [105–107]. Finally, a combination of frequency-swept pulses and optimal control theory has been researched in the context of ultra-wideline solid-state NMR [110]. However, all reports of CPMG using frequency-swept pulses for both excitation and refocusing base themselves on the KB sequence [53, 57, 62, 183] or similar variants. Joining CHORUS [94, 97] and a train of refocusing blocks, we demonstrate here how to build a new broadband and B_1-tolerant CPMG, CHORUS-CPMG.

Some sequences cannot be formed by simply appending blocks but can be built by directly addressing their more complicated refocusing conditions. To illustrate this, we investigate the idea of a broadband B_1-tolerant perfect echo. Frequency-swept pulse sequences are indeed inherently much longer than their hard-pulse counterparts and therefore more prone to homonuclear J-modulation. This can be somewhat circumvented by using shorter pulse sequences, e.g. by sacrificing some uniformity or sensitivity. Recent work has also leveraged the flexibility of optimal control theory to create very short single broadband excitation pulses at the cost of some correctable first-order phase modulation [220]. In contrast, for long sequences, the perfect-echo appears as

an elegant solution to fully or partially suppress homonuclear J-modulation. Shortly after the original publication of the sequence presented in this thesis [203], a broadband perfect-echo designed with optimal control pulses has even been proposed [221]. In EPR, a version of SIFTER (sequence similar to the perfect echo) was proposed with frequency-swept pulses, although based on the KB sequence [139]. Here, we introduce a broadband B_1-tolerant perfect-echo excitation sequence with frequency-swept pulses, PeRfect echO CHORUS (PROCHORUS).

As mentioned in the previous paragraph, frequency-swept pulse sequences are usually considered long. However, they offer some design flexibility and, similarly to composite pulses, they can be combined or concatenated, as briefly alluded to in section 2.2. In addition, overlapped or superposed pulses can be created by adding their waveform. When first introduced by Ermakov et al. [61], waveform superposition was employed for reduction of a KB sequence duration by almost 50% [61]. In later MRI studies, adiabatic spin echoes with self-refocusing pulses were also shortened thanks to the same idea [222, 223]. Here, we extend this notion to other frequency-swept pulse schemes.

2.4.2 Materials and methods

Pulse generation and simulation

The chirped and HS^1 pulse sequences were generated, simulated, and optimised with the version 1.1 of the `MRChirpLab` package [188] on MATLAB R2020a (see appendix A for more details). SPINACH v2.5.5459 [17] was used for further simulation on B_1 spatial inhomogeneities for CHORUS-CPMG and on coupled spin systems for PROCHORUS.

For all the sequences introduced here, the adiabaticity factors of the excitation $\mathcal{Q}_0^{\text{exc}}$ and refocusing $\mathcal{Q}_0^{\text{ref}}$ were fixed at 0.441 and 5, respectively. Minimum durations of excitation $\tau_{\text{exc}} = 0.5\,\text{ms}$ and refocusing $\tau_{\text{ref}} = 1\,\text{ms}$ were picked with a time resolution of $t_{\text{res}} = 0.5\,\mu\text{s}$. For all the chirped pulses, the bandwidth was $\Delta F = 300\,\text{kHz}$ with a smoothing of about 12% ($n = 20$ in equation (2.3)), yielding an effective bandwidth ΔF_{eff} of about 225 kHz. Chirped sequences therefore had a minimum TBP of 150

and maximum peak amplitude of 15.45 kHz. In the case of HS^1 pulses, $\Delta F = 60$ kHz with $\beta = 10.6/\tau_\mathrm{p}$ were chosen to give the same sequence maximum peak amplitude of 15.45 kHz, and a sequence minimum TBP of 30.

For the broadband CPMG sequences, the frequency-swept pulses of the double FS refocusing block were separated by 10 ms delays. For comparison of the KB-CPMG and CHORUS-CPMG sequences, their first echo positions were matched by adding a delay of 0.5 ms on each side of the last pulse from the CHORUS scheme.

For the PROCHORUS simulation, all sequences were fixed at a total duration of 8 ms, except for the single excitation with a hard pulse. The duration of the hard $\pi/2$- and π-pulses were set to 12 µs and 24 µs, respectively. The perfect echo sequence with hard pulses made use of an interpulse delay of 1.982 ms. The compressed PROCHORUS sequence was extended to 8 ms by inserting delays between pulses.

Details on superposed sequences are given in subsection 2.4.5.

Samples

The excitation profiles of uncoupled spins were recorded using a sample of doped water as it produces a single strong peak and a short T_1 to reduce the waiting time spent between scans. More precisely, a solution of 1% D_2O/H_2O with 0.1 mg/mL $GdCl_3$ was employed.

The excitation profiles of coupled spins were recorded for PROCHORUS using a sample of pentafluorobenzene at a concentration of 50 mmol/L in DMSO-d_6.

Hardware

A Bruker Avance Neo 400 MHz spectrometer (Bruker BioSpin) with a broadband Smart probe served to record all the spectra at 298 K.

Experiments

For CPMG experimental profiles, the KB-CPMG and CHORUS-CPMG sequences were run with 16- and 64-step phase cycle, respectively. A 312.5 kHz spectral window, 64 scans, and 64k complex point were used with ^{1}H detection.

For PROCHORUS experimental profiles, the CHORUS and PROCHORUS sequences were run with 16- and 64-step phase cycle, respectively. A 300 kHz spectral window, 64 scans, and 60000 complex point were used with ^{19}F detection.

For experimental profiles of non-superposed and superposed HS^{1} pulses, the KB and ABSTRUSE sequences were run with 4- and 16-step phase cycles, respectively. The same phase cycles were used for the sequences with the superposed HS^{1} pulses. Each step of the phase cycle was generated and loaded into TopSpin as an overlapped pulse with individual pulses presenting the appropriate total phase ϕ_0. A 78 kHz spectral window, 16 scans, and 64k complex point were used with ^{1}H detection.

Data processing

The TopSpin software (Bruker BioSpin) and Matlab R2020a were used for all post-processing and plotting of the data. Data from TopSpin were imported in Matlab environment with the `RBNMR` function [224] and the Matlab-NMR library [208] was used for further phase correction in Matlab when necessary.

For CPMG experimental profiles, post-processing comprised zero-filling to 256k complex points, followed by Fourier transformation. The `t1t2` module from TopSpin was used to fit with the integral values obtained from the T_2 decays.

For PROCHORUS experimental profiles, post-processing comprised zero-filling to 256k complex points, followed by Fourier transformation.

For experimental profiles of the non-superposed and superposed versions of HS^{1} pulses, post-processing comprised zero-filling to 128k complex points, followed by Fourier transformation.

All simulation code and experimental data, with the pulse shapes and programs

used to record it (in BRUKER TOPSPIN format), are accessible through the DOI: 10.17632/3js9dzmv9p.2.

2.4.3 CHORUS-CPMG

A CPMG of frequency-swept pulses can be created by simply appending a train of refocusing elements to an excitation element. Both blocks should be broadband and tolerant to B_1 variations for the sequence to also present those characteristics. Using the KB sequence as the excitation element can result in a considerable signal loss as this scheme is very sensitive to B_1 inhomogeneity. Application of the CHORUS sequence in place of the KB scheme can simply address this limitation.

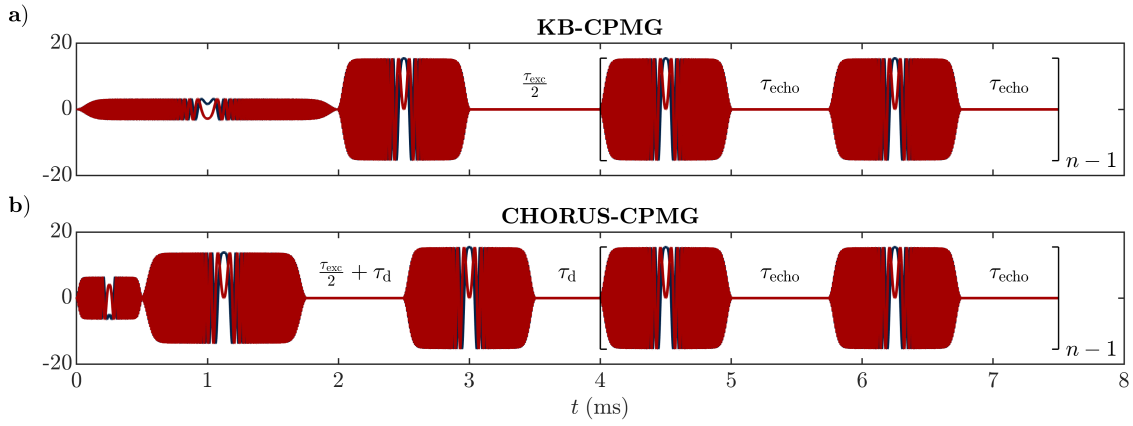


Figure 2.16: Cartesian representation of a) KB-CPMG and b) CHORUS-CPMG sequences. Both CPMGs are plotted with $n = 2$, $\tau_d = 0.5\,\text{ms}$, and are set up with the same chirped pulse parameters' constraints, described in subsection 2.4.2. CHORUS-CPMG includes an additional delay $\tau_{\text{echo}} = 0.75\,\text{ms}$ to match the duration of the KB-CPMG.

Appending a train of double frequency-swept pulse blocks as refocusing elements gives two CPMGs to be compared: the KB-CPMG and CHORUS-CPMG, respectively shown in figures 2.16a and b. To adapt the length of the sequences and minimise their energy dissipation, delays τ_{echo} and τ_{d} were added to the sequence. Simulations of excitation profile were conducted with the B_1 profile from figure 2.17 and are displayed in figure 2.18a. These results, as well as similar experimental results shown in figure 2.18b,

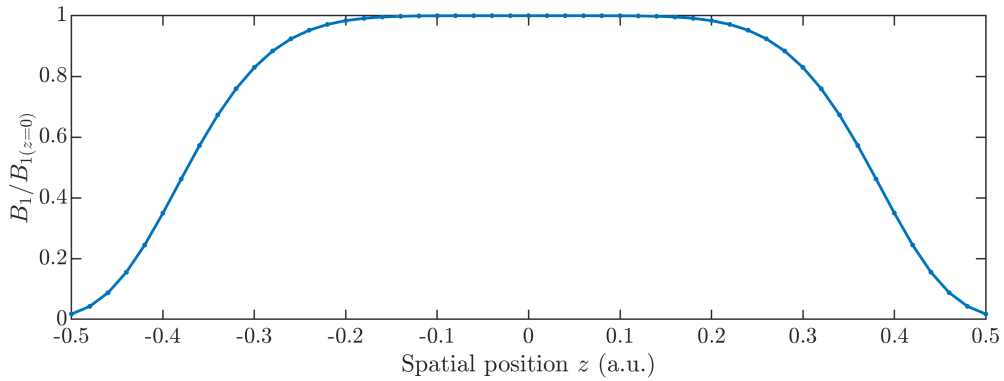


Figure 2.17: $\boldsymbol{B_1}$ field strength distribution over the sample's active volume used for simulation of B_1 spatial inhomogeneities in amplitude. The profile was modelled in 1D along z with $\frac{B_1(z)}{B_1(z=0)} = \exp(-2^8 z^6)$, for $z \in [-0.5, 0.5]$.

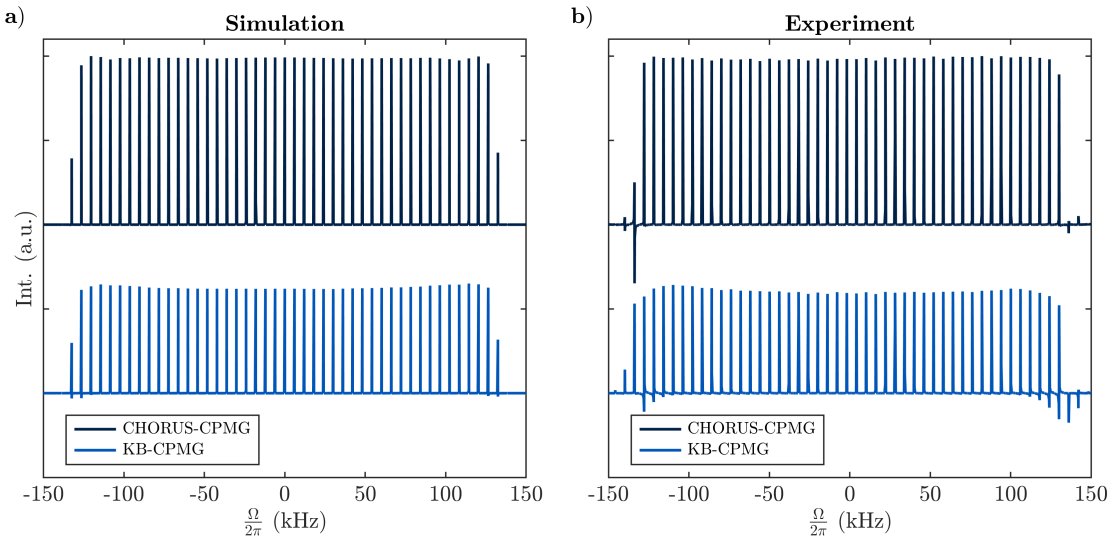


Figure 2.18: a) Simulated and b) experimental excitation profiles for CHORUS-CPMG (in black) and KB-CPMG (in blue) sequences with refocusing elements set up for $n = 7$ and $\tau_d = 10\,\text{ms}$ (see subsection 2.4.2 for more pulse sequence details). SPINACH v2.5.5459 [17] was used to simulate the profiles with spatial B_1 inhomegeneities from the super-Gaussian B_1 profile presented in figure 2.17.

demonstrate that CHORUS-CPMG offers better sensitivity and uniformity. Presently, a nearly twofold improvement in sensitivity is achieved with the CHORUS-CPMG sequence.

These gains are preserved over the train of refocusing block as depicted in figure 2.19 with results of relaxation measurements for 8 offsets spread across the profiles. In total,

the KB-CPMG gave an average T_2 of 153.2 ms with a standard deviation of 2.1 ms and CHORUS-CPMG an average T_2 of 149.4 ms with a standard deviation of 0.9 ms.

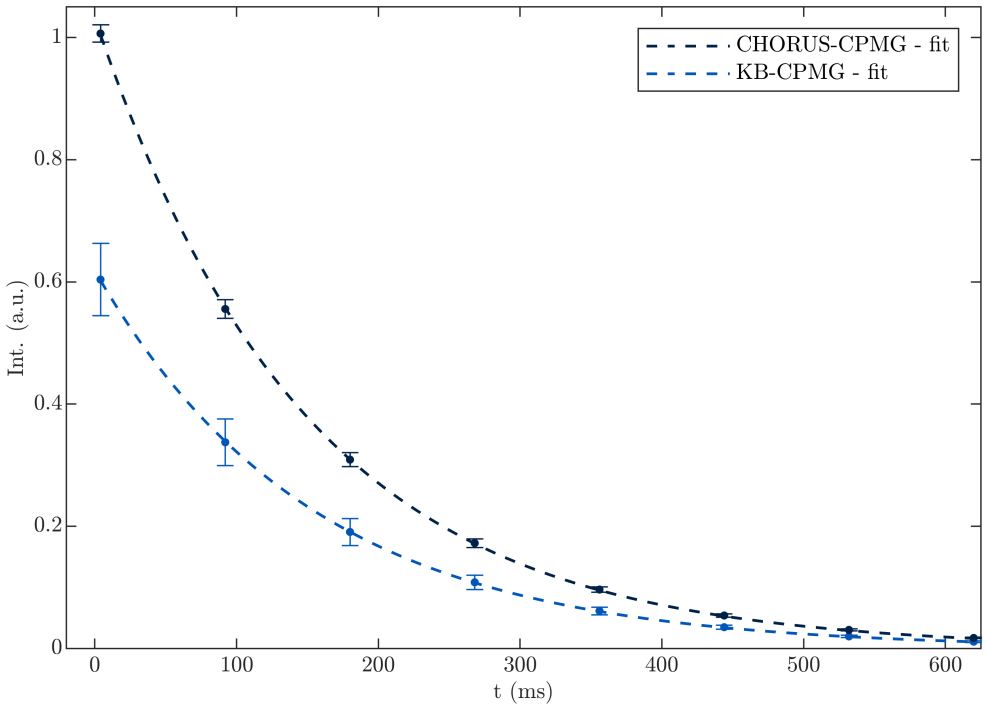


Figure 2.19: T_2 decays obtained with the CHORUS-CPMG (black) and KB-CPMG (blue) from 8 spectra taken across the excitation profile from figure 2.18. The data were acquired with 1, 5, 9, 13, 17, 21, 25, and 29 loops for 5 repetitions. The data is plotted as the average integral values with error bars indicating 3 standard deviations, and their corresponding T_2 fits.

Although superior sensitivity and uniformity of excitation are expected, the exact magnitude of the expected gains from CHORUS-CPMG can only be predicted with some knowledge of B_1 spatial variations.

2.4.4 PROCHORUS

One downside of the CHORUS excitation sequence is that it does not refocus homonuclear J-couplings during its long pulses. This evolution leads to a J-modulation of multiplets which is also offset-dependent. To illustrate this, we take two spins $\hat{\boldsymbol{I}}_1$ and

$\hat{\boldsymbol{I}}_2$ with a scalar coupling J_{12} and where $\Omega_1 > \Omega_2$ without loss of generality. The instantaneous flip approximation allows for the representation of a chirped $\pi/2$-pulse as

$$\hat{R}_{1x}(\pi/2) \quad — \quad (\alpha_2 - \alpha_1)\tau_\mathrm{p} \quad — \quad \hat{R}_{2x}(\pi/2) \quad — \quad (1 - \alpha_2)\tau_\mathrm{p},$$

where τ_p is the pulse duration. Taking α_1 for Ω_1 and α_2 for Ω_2 from equation (2.20), the observable terms after the pulse are

$$\begin{aligned} &- \exp\left[-\mathrm{i}(\alpha_2 - 1)\tau_\mathrm{p}\Omega_2\right] \left[\frac{\mathrm{i}}{2}\cos\left[\pi J_{12}\left(\alpha_2 - 1\right)\tau_\mathrm{p}\right]\hat{I}_2^- + \mathrm{i}\sin\left[\pi J_{12}(\alpha_2 - 1)\tau_\mathrm{p}\right]\hat{I}_2^-\hat{I}_{1z}\right] \\ &+ \exp\left[-\mathrm{i}(\alpha_1 - 1)\tau_\mathrm{p}\Omega_1\right]\cos\left[\pi J_{12}(\alpha_2 - \alpha_1)\tau_\mathrm{p}\right] \\ &\quad \left[\frac{\mathrm{i}}{2}\cos\left[\pi J_{12}(\alpha_2 - 1)\tau_\mathrm{p}\right]\hat{I}_1^- + \sin\left[\pi J_{12}(\alpha_2 - 1)\tau_\mathrm{p}\right]\hat{I}_1^-\hat{I}_{2z}\right], \end{aligned} \tag{2.33}$$

which shows offset-dependent modulations for both chemical shifts and scalar couplings (result obtained with software package SpinDynamica v3.3.2 [225] in Mathematica 11.0).

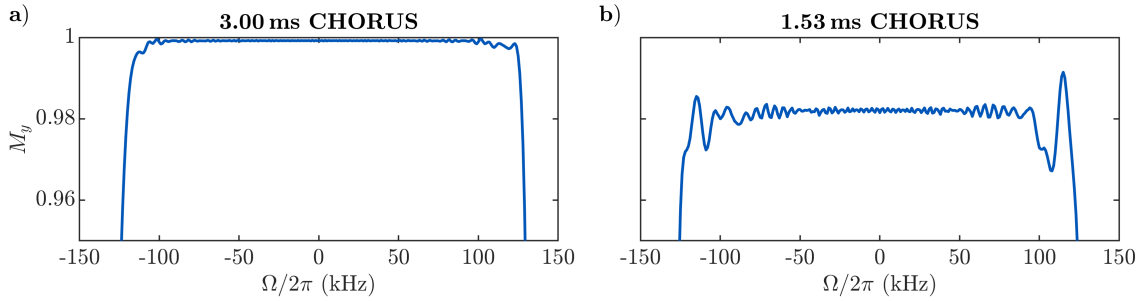


Figure 2.20: Top 5% of simulated excitation profiles for CHORUS sequences of total duration a) 3 ms ($\mathrm{TBP}_\mathrm{min} = 150$ and $\mathcal{Q}_0^\mathrm{ref} = 5$) and, b) 1.53 ms ($\mathrm{TBP}_\mathrm{min} = 50$ and $\mathcal{Q}_0^\mathrm{ref} = 3$). Both sequences were otherwise built with the same chirped pulse constraints presented in subsection 2.4.2.

This J-modulation can be prevented to some extent by compressing the pulses. For example, reducing $\mathrm{TBP}_\mathrm{min}$ and $\mathcal{Q}_0^\mathrm{ref}$ of the CHORUS sequence can halve the sequence duration without increasing its peak amplitude. However, this comes at the cost of sensitivity and uniformity losses as illustrated in figure 2.20 (see also figure B.1 in

appendix B for B_1-sensitivity map), and this technique is ultimately physically limited by the available maximum peak amplitude. Work from optimal control theory with a short single excitation pulse lowered the excitation pulse flip angle to try to address this issue [220] but this option is ineffective for the KB and CHORUS schemes which are mainly limited in duration by their long inversion pulses.

Here, we propose to integrate the CHORUS sequence into a perfect echo pulse sequence [31–33]. As described in more detail in subsection 1.5.2, this sequence suppresses J-modulation thanks to a phase shifted 90° pulse placed in between two conventional spin echoes ($90°-\tau-180°-\tau-90°_y-\tau-180°-\tau$). The PeRfect echO CHORUS (PROCHORUS) sequence is therefore built with a triple frequency-swept excitation, which refocuses the magnetisation along a 90° frequency-swept pulse presenting a shifted overall phase $\phi_0^{90°(2)} = \phi_0^{90°(1)} + \pi/2$, and two mismatched frequency-swept pulses for final refocusing of the signal.

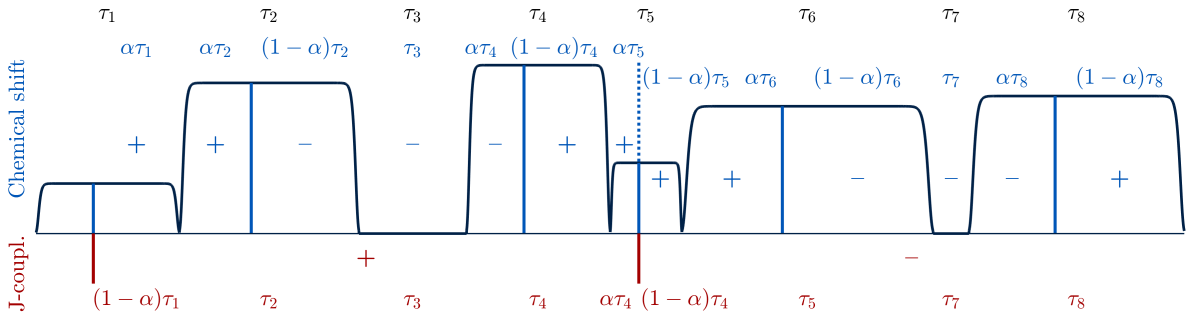


Figure 2.21: Sketch of PROCHORUS sequence with chemical shifts and J-couplings evolution, respectively represented in blue (top) and red (bottom). In black, at the very top, τ_1 to τ_8 designate the durations of the pulses and delays of the sequence.

In order to determine these elements' durations, the refocusing conditions of PROCHORUS can be expressed with equations, in a similar manner to equation (2.29) for the CHORUS sequence. Two equations are needed for the offset refocusing: one for refocusing into the quadrature 90° pulse and one for the signal at the end of the sequence. The refocusing of the J-couplings during the sequence requires an additional equation to ensure that the quadrature 90° pulse acts in the middle of the sequence for each offset.

These three refocusing conditions, to be satisfied simultaneously, are pictured in figure 2.21 and expressed as

$$\begin{bmatrix} 1-\alpha & 2\alpha-1 & -1 & 1-2\alpha & \alpha & 0 & 0 & 0 \\ 0 & 0 & 0 & 0 & 1-\alpha & 2\alpha-1 & -1 & 1-2\alpha \\ 1-\alpha & 1 & 1 & 1 & 2\alpha-1 & -1 & -1 & -1 \end{bmatrix} \begin{bmatrix} \tau_1 \\ \tau_2 \\ \tau_3 \\ \tau_4 \\ \tau_5 \\ \tau_6 \\ \tau_7 \\ \tau_8 \end{bmatrix} = \begin{bmatrix} 0 \\ 0 \\ 0 \\ 0 \end{bmatrix}. \quad (2.34)$$

To allow for the greatest compression of the sequence, the solution to equation (2.34) can be expressed in terms of the minimum durations of the excitation and refocusing pulses, respectively τ_{exc} and τ_{ref} (as seen in subsection 2.2.5). Equation (2.35) details an exact solution to equation (2.34) in that way.

$$\begin{bmatrix} \tau_1 \\ \tau_2 \\ \tau_3 \\ \tau_4 \\ \tau_5 \\ \tau_6 \\ \tau_7 \\ \tau_8 \end{bmatrix} = \tau_{\text{ref}} \begin{bmatrix} 0 \\ 1 \\ 0 \\ 1 \\ 0 \\ 1 \\ 0 \\ 1 \end{bmatrix} + \tau_{\text{exc}} \begin{bmatrix} 2 \\ 1/2 \\ 3/2 \\ 0 \\ 1 \\ 3/2 \\ 1/2 \\ 1 \end{bmatrix} \quad (2.35)$$

For example, a sequence lasting 8 ms can be obtained with the following set of durations respecting equation (2.35): 1000 µs, 1250 µs, 750 µs, 1000 µs, 500 µs, 1750 µs, 250 µs, and 1500 µs for τ_1 to τ_8, respectively.

Otherwise, a shorter solution can be found by relaxing the condition on the scalar coupling refocusing, albeit at the price of some small offset-dependent J-modulation.

$$\begin{bmatrix} \tau_1 \\ \tau_2 \\ \tau_3 \\ \tau_4 \\ \tau_5 \\ \tau_6 \\ \tau_7 \\ \tau_8 \end{bmatrix} = \tau_{\text{ref}} \begin{bmatrix} 0 \\ 1 \\ 0 \\ 1 \\ 0 \\ 1 \\ 0 \\ 1 \end{bmatrix} + \tau_{\text{exc}} \begin{bmatrix} 1 \\ 0 \\ 1 \\ 0 \\ 1 \\ 1/2 \\ 1/2 \\ 0 \end{bmatrix}. \tag{2.36}$$

For instance, a sequence with a duration 6 ms satisfies equation (2.36) timings set to 500 µs, 1000 µs, 500 µs, 1000 µs, 500 µs, 1250 µs, 250 µs, and 1000 µs for τ_1 to τ_8, respectively. The offset-dependent J-modulation which is re-introduced by this sequence goes up to a 500 µs evolution time for offsets situated at the very beginning of the sweep (lowest frequencies of the spectrum). Compressed and uncompressed versions of PROCHORUS using the timings specified in the text are shown in figure 2.22.

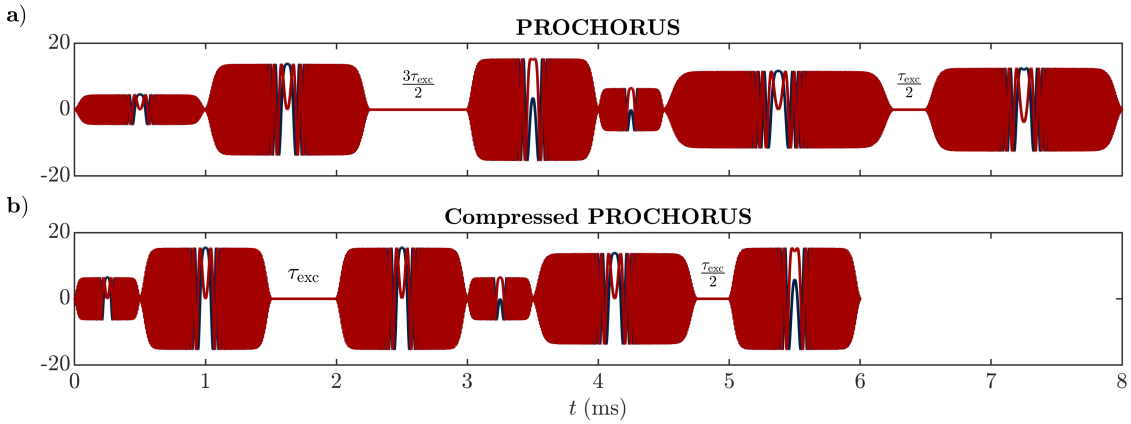


Figure 2.22: Cartesian representation of a) uncompressed PROCHORUS and b) compressed PROCHORUS. Both sequences were set up with the same chirped pulse parameters' constraints presented in subsection 2.4.2.

Any imperfect refocusing into the second 90° pulse will degrade the final signal. Therefore, phase correction, as described in subsection 2.2.6, is essential to the PROCHORUS sequence. The non-linear optimisation method was picked for its ease of implementation. At least one pulse before the central 90° pulse and one pulse after the second 180° pulse (in third position) should be tweaked, yielding a minimum of four

parameters to optimise.

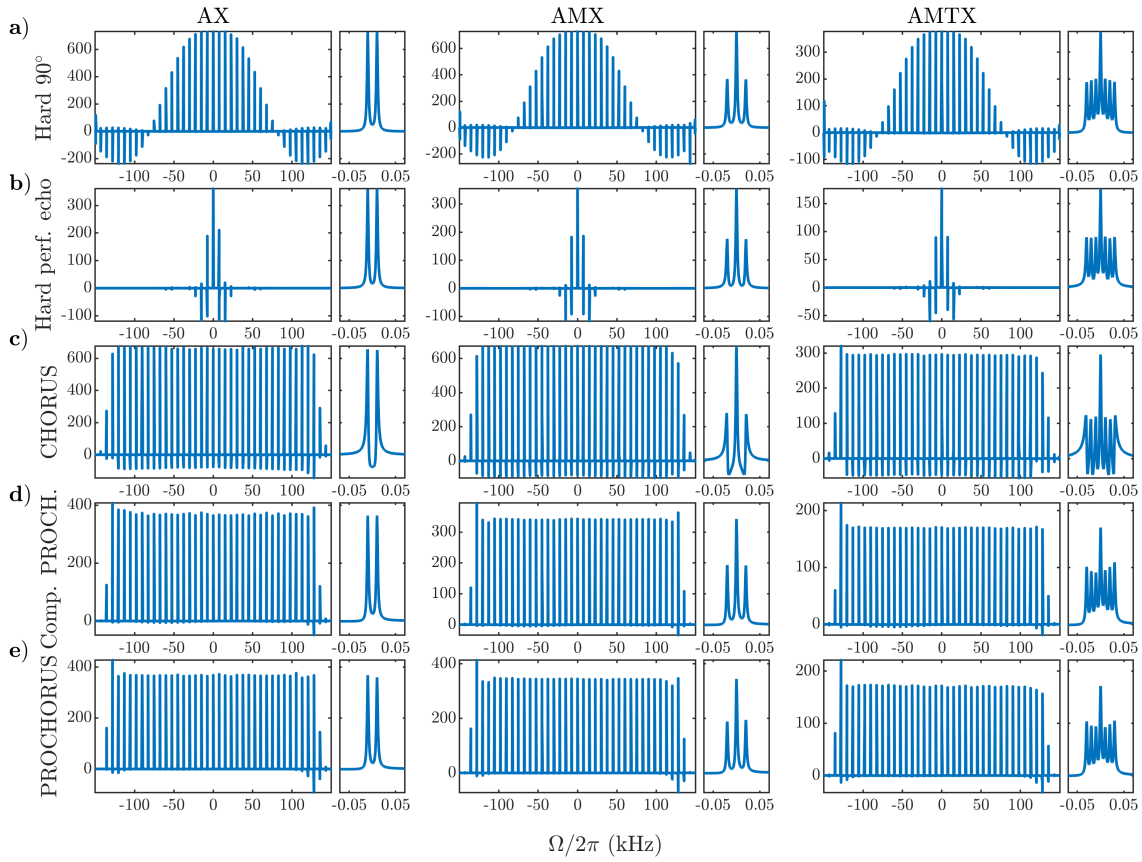


Figure 2.23: Comparison of J-modulation effects and broadband capabilities with simulated excitation profiles of coupled spin systems for a) single hard $\pi/2$-pulse excitation, b) hard-pulse perfect echo, c) CHORUS, d) PROCHORUS, and e) compressed PROCHORUS pulse sequences. The central multiplet of the profiles is represented on the right of each profile for better visualisation of the J-modulation. The following three spin systems are used: AX ($J_{\mathrm{AX}} = 20\,\mathrm{Hz}$), AMX ($J_{\mathrm{AM}} = J_{\mathrm{AX}} = 20\,\mathrm{Hz}$), and AMTX ($J_{\mathrm{AM}} = 10\,\mathrm{Hz}$, $J_{\mathrm{AT}} = 20\,\mathrm{Hz}$, $J_{\mathrm{AX}} = 30\,\mathrm{Hz}$, $J_{\mathrm{MT}} = 20\,\mathrm{Hz}$, $J_{\mathrm{MX}} = 30\,\mathrm{Hz}$, $J_{\mathrm{TX}} = 10\,\mathrm{Hz}$). Excluding the pulse-acquire which only serves as a reference for non-evolution of the coupling, all the sequences were set to a total length of 8 ms for comparison with the same duration of J-coupling evolution. Full sequence details are available in subsection 2.4.2 (frequency-swept pulses also shown in figure 2.22). The simulation was conducted with Spinach v2.5.5459 [17].

To assess the sequence effectiveness, simulation was conducted for a range of scalar coupling values from various spin-$\frac{1}{2}$ systems with two (AX), three (AMX), and four (AMTX) coupled nuclei. The excitation profiles from figure 2.23 were obtained for the

following sequences: pulse-acquire which shows the absence of J-modulation, perfect echo with hard pulses which serves as reference for expected suppressed J-modulation, PROCHORUS sequence, and compressed PROCHORUS sequence.

The PROCHORUS sequences were equally capable to the hard pulse perfect echo in terms of suppressing J-modulation. In particular, the residual J-evolution from the compressed PROCHORUS sequence was not significant because τ_{exc} is small in comparison to $1/J$.

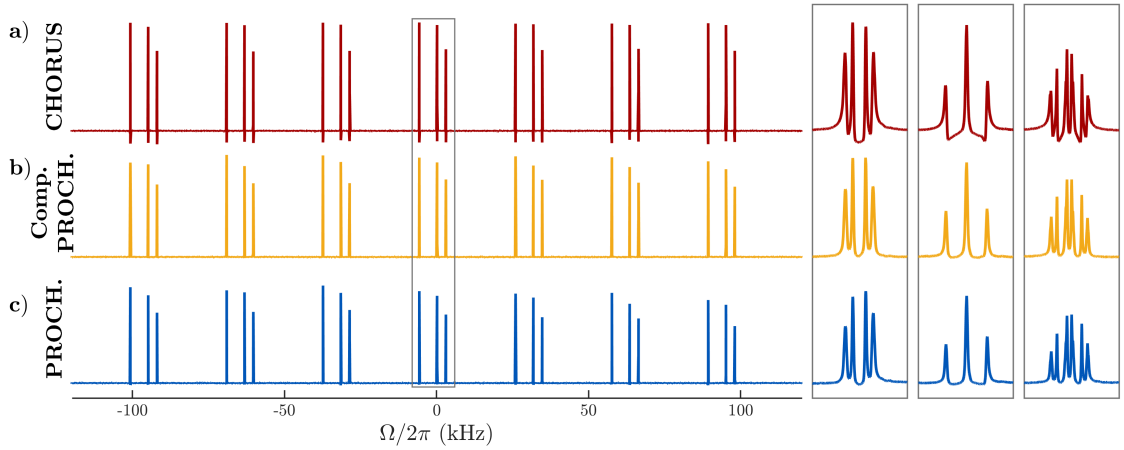


Figure 2.24: Experimental demonstration of J-modulation for a) 6 ms CHORUS, b) 6 ms (compressed) PROCHORUS and c) 8 ms PROCHORUS. Seven ^{19}F{^{1}H} spectra of pentafluorobenzene in DMSO-d_6 were recorded by stepping the carrier frequency with increments of 20 kHz. The resulting profile covers a total offset range of 200 kHz which corresponds to 532 ppm at the present ^{19}F Larmor frequency of 376 MHz. All sequences used the same parameters' constraints described in subsection 2.4.2 (perfect-echo sequences also shown in figure 2.22).

Experimental results from the CHORUS and the two versions of PROCHORUS sequences on a sample of pentafluorobenzene are also shown in figure 2.24, where both PROCHORUS sequences demonstrate again their ability to suppress J-modulation over a large bandwidth without noticeable differences between their capabilities.

2.4.5 Sequences overlap

When thinking about frequency-swept pulse sequences through the instantaneous flip approximation, it appears that offsets which are flipped at the start of the first sweep then only evolve idly before the next pulse. More generally, for a given offset during the sequence, there is a significant amount of time which is not put to use. To avoid such inefficiency during a KB sequence, a simple idea was proposed by Ermakov and co-workers: start the second pulse sweep while the first one is still taking place [61]. In order to do so, they superposed two chirped pulses waveforms and were able to shorten the sequence by almost 50%. Here, a general approach to frequency-swept pulses superposition is developed and applied to several basic schemes.

In practice, waveform superposition can be achieved by moving the pulses position parameter δ_{t}, previously shown in equations (2.3), (2.5), (2.6), and (2.8). The pulses' Cartesian components are added to get a single pulse formed of several overlapped frequency-swept pulses. To respect the refocusing condition on the sequence timings, the duration of the overlap needs to be subtracted from the sequence delays. Here, the refocusing pulses were overlapped as much as possible while avoiding significant degradation of their excitation profiles' uniformity.

Figure 2.25 illustrates the superposition of chirped pulse schemes with the KB, CHORUS and triple-refocusing sequences. One obvious disadvantage of chirped pulses overlapping, apparent on figures 2.25a, b and c, is the increase of the sequence maximum peak amplitude. A 21% increase of the KB sequence peak amplitude was necessary to shorten it by 40%. This peak amplitude increase can of course be used to make a shorter non-overlapped KB as stated in subsection 2.2.4. In that case, the overlapped sequence is only 12% shorter because of the square dependency between frequency-swept pulses duration and maximum amplitude. The CHORUS sequence can be reduced by a third but at the cost of a sequence peak amplitude increase of 84%. This increase could be limited to 31% by only overlapping the first two pulses with an overlap of $0.25\tau_{\mathrm{ref}}$ for a 25% reduction of the sequence length. While the phase correction of the KB and

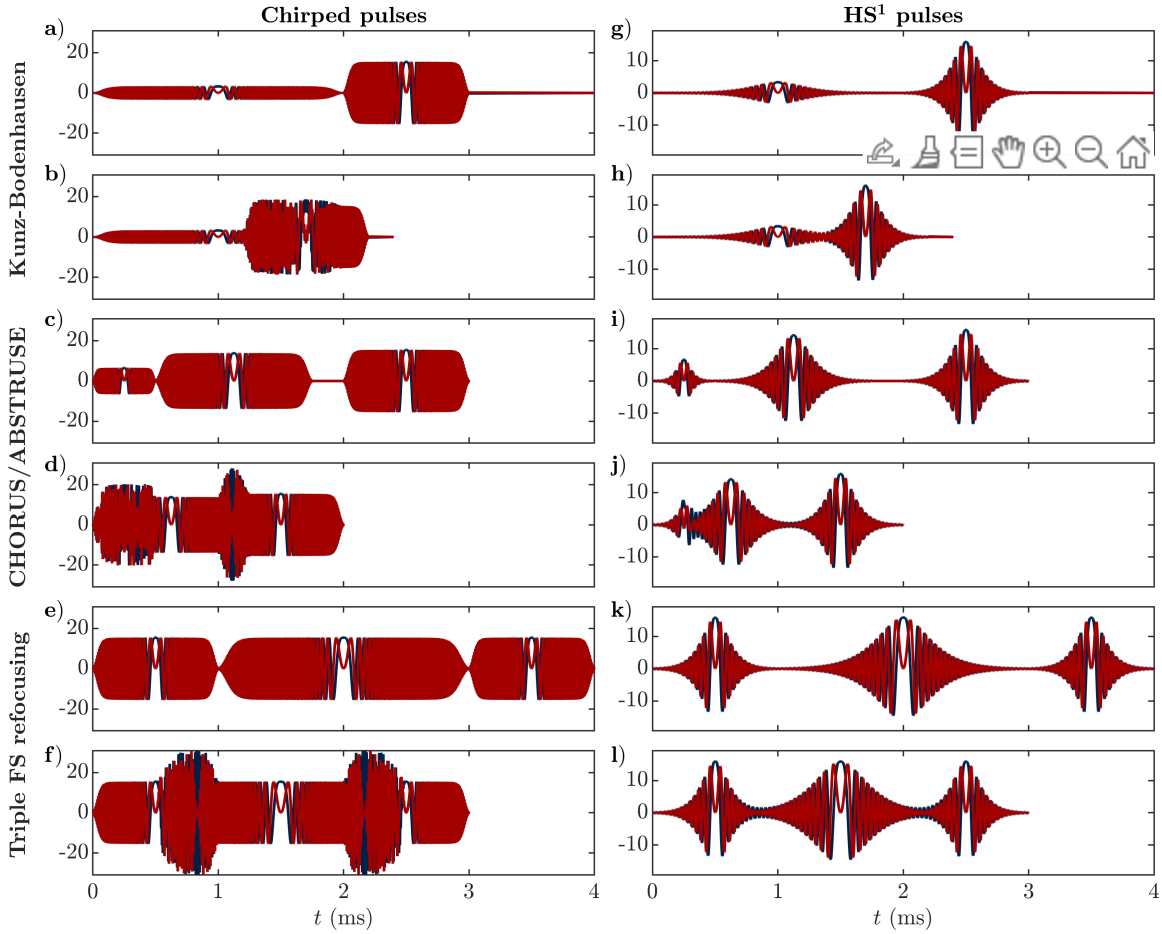


Figure 2.25: Cartesian representation of chirped (a, b, c, d, e) and HS^1 pulse sequences (f, g, h, i, j, k) with and without overlap. For chirped pulses, the following schemes are presented: the KB sequence a) without and b) with $0.8\tau_{\text{ref}}$ overlap, the ABSTRUSE sequence c) without and d) with $0.5\tau_{\text{ref}}$ overlap (complete superposition of τ_{exc}), and the triple-refocusing sequence e) without and f) with $0.5\tau_{\text{ref}}$ overlap. For HS^1 pulses, the following schemes are presented: the KB sequence, g) without and h) with $0.8\tau_{\text{ref}}$ overlap, the ABSTRUSE sequence, i) without and j) with $0.8\tau_{\text{ref}}$ overlap, and the triple-refocusing sequence k) without and l) with $0.5\tau_{\text{ref}}$ overlap. All sequences were built with the same constraints presented in subsection 2.4.2.

CHORUS sequences was easily conducted with the polynomial fitting, the B_1-tolerance of CHORUS was degraded as reported in figure B.2 of appendix B. This degradation also gets worse for longer overlap duration. In the case of the triple-pulse refocusing sequence, waveform superposition is even less attractive; for example, a peak amplitude increase of 100% only translates to a 25% reduction of the sequence length. Overall,

chirped pulses appear as poor candidates for reducing sequence duration by overlap.

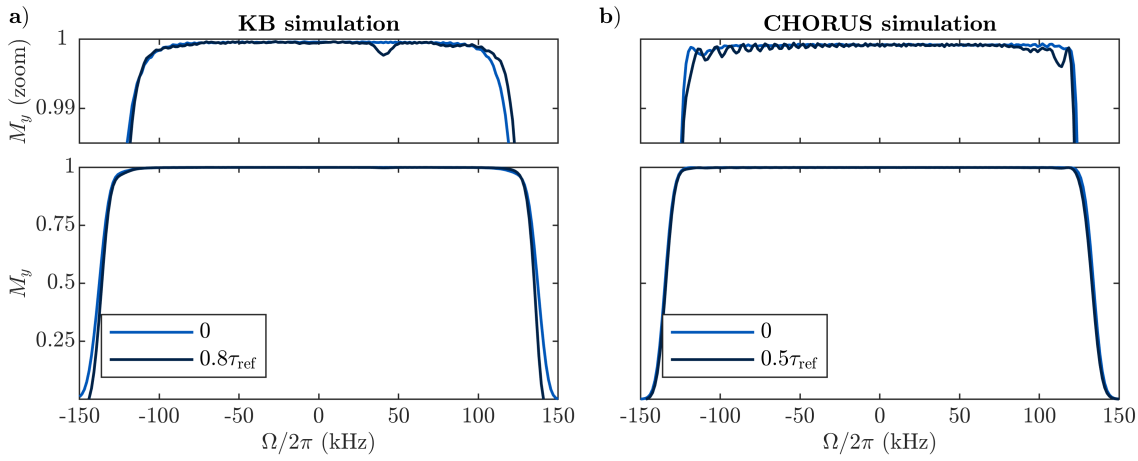


Figure 2.26: Simulated excitation profiles for chirped pulse sequences: a) KB with and without a $0.8\tau_{\mathrm{ref}}$ overlap, and b) CHORUS with and without a $0.5\tau_{\mathrm{ref}}$ overlap. The small dip at 50 kHz on the overlapped KB sequence profile corresponds to the transition from the excitation pulse into the overlapped part of the sequence. These sequences are the ones from figures 2.25a, b, c, and d and were built with the same constraints presented in subsection 2.4.2.

Alternatively, the sweep of HS^1 pulses should be less disturbed by overlap since it mainly takes place in the centre of the pulse, as previously depicted in figure 2.2. In addition, HS^1 pulses possess low amplitude extremities which allow for the superposition of KB, ABSTRUSE, and triple-refocusing sequences without significant peak amplitude increase, as displayed in figure 2.25. The overlapped KB sequence did require both a polynomial fitting and a parametric phase optimisation but the ABSTRUSE sequence was corrected with the nonlinear optimisation only. The ABSTRUSE scheme furthermore showed a better tolerance for greater overlap duration. Indeed, a degradation of only up to 1% of the magnetisation affected its excitation profile against up to 6% for the KB scheme for a 90% overlap of their refocusing pulse, as shown in figure 2.27a and b. This overlap translated into sequence length reductions of 45% and 33%, respectively.

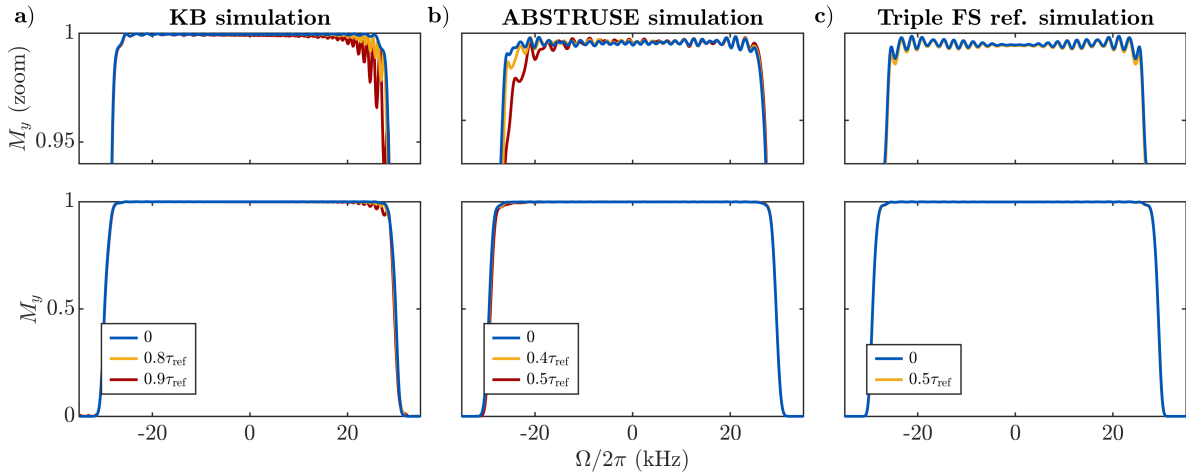


Figure 2.27: Simulated excitation profiles for HS[1] pulse sequences: a) KB, b) ABSTRUSE, and c) triple refocusing pulse sequence, without and with various overlap durations indicated on the legends. These sequences are the ones from figures 2.25g to l and were built with the same constraints presented in subsection 2.4.2.

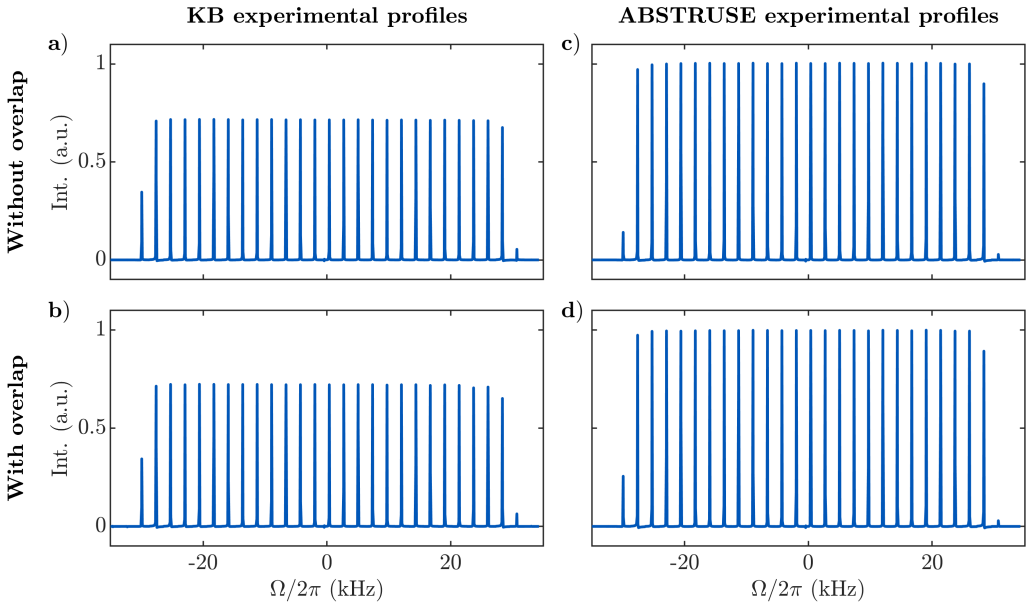


Figure 2.28: Experimental excitation profiles for HS[1] pulse sequences: KB sequence a) without and b) with $0.8\tau_{ref}$ overlap, ABSTRUSE sequence c) without and d) with $0.5\tau_{ref}$ overlap. These sequences are the ones from figures 2.25f, g, h, and i and were built with the same constraints presented in subsection 2.4.2.

The overlap duration of the triple-refocusing scheme was held at 50% of the first refocusing pulse to prevent the sequence peak amplitude from increasing. This reduced the sequence's total duration by 25% but did not affect the triple-refocusing scheme profile, which also did not require phase correction after superposition. Figure 2.27c displays the calculated excitation profiles. Importantly, the B_1-tolerance of the ABSTRUSE and triple refocusing pulse sequences appeared to be left undisturbed, as is apparent on B_1-sensitivity maps from figure B.3 in appendix B.

For experimental implementation, phase cycling was applied by generating sets of overlapped pulses with total phases ϕ_0 corresponding to each step of the cycle, as specified in previous work [61]. Experimental excitation profiles for the KB and ABSTRUSE schemes with and without overlap are shown in figure 2.28. The non-overlapped ABSTRUSE sequence served as the reference for the normalisation of the excitation profiles.

Table 2.5 presents a summary of all the superposed sequences presented in this subsection, with an assessment of the interest of the overlap.

Table 2.5: Summary of results for overlap potential of common frequency-swept pulse schemes. The table indicates the decrease of the total duration of the sequence τ_{seq}, the increase of the sequence maximum peak amplitude $\nu_{1,\text{max}}$, and the effects of the overlap on the sequence B_1-tolerance. "–" signifies that the property is unaffected.

Pulse type	**Sequence**	**Overlap**	$\frac{\boldsymbol{\Delta\tau_{\text{seq}}}}{\boldsymbol{\tau_{\text{seq}}}}$	$\frac{\boldsymbol{\Delta\nu_{1,\text{max}}}}{\boldsymbol{\nu_{1,\text{max}}}}$	$\boldsymbol{B_1}$**-tolerance**	**Overlap interest**
chirped	KB	$0.8\tau_{\text{ref}}$	-40%	+21%	Already low	Mild
chirped	CHORUS	$0.25\tau_{\text{ref}}$	-25%	+31%	Mildly lowered	Low
chirped	CHORUS	$0.5\tau_{\text{ref}}$	-33%	+84%	Strongly lowered	Low
chirped	Triple FS ref.	$0.5\tau_{\text{ref}}$	-25%	+100%	Mildly lowered	Low
HS[1]	KB	$0.8\tau_{\text{ref}}$	-40%	–	Already low	Strong
HS[1]	ABSTRUSE	$0.5\tau_{\text{ref}}$	-33%	–	–	Strong
HS[1]	Triple FS ref.	$0.5\tau_{\text{ref}}$	-25%	–	–	Strong

2.5 Outlook

Future investigations could include the applications of the sequences developed here in other practical settings, for instance diffusion NMR measurements with PROCHORUS, the use of PROCHORUS for broadband SIFTER in EPR, or applications in other magnetic resonance domains such as MRI or single-sided NMR. The concepts developed here could also be employed to create frequency-swept versions of other sequences.

An important task to conduct would be a proper statistical comparison of the pulses and pulse sequences against other broadband or B_1-tolerant solutions, such as optimal control pulses. This would need to be done under various conditions, for instance with and without Shigemi tubes which are often used to reduce the effect of B_1 spatial inhomogeneity.

In ESR spectroscopy, the CHORUS sequence could also be inserted into other sequences and it would be particularly interesting to investigate the sequence effects when dealing with other spin systems, in particular those with higher spin orders or with multiple-quantum transitions which may get activated by the pulses.

Finally, combining different pulse design methods appears to be a promising approach. For instance, some optimisation tools were used to set up frequency-swept sequences in this chapter for phase correction. In the next chapter, the implementation of CHORUS in ESR will be revisited using optimisation techniques applied at the spectrometer.

Chapter 3

On-the-fly optimisation of ESR experiments

3.1 Introduction

As illustrated in the previous chapter, hardware performance can pose strong limits on Electron Spin Resonance (ESR) spectroscopy applications [8, 173, 226]. The vast majority of ESR experiments call for the manual setup of several parameters before being run. Expert operators often further tweak the experimental parameters to get an optimal result. ESR procedures consequently require time and effort, and are sometimes too impractical to be implemented because of a lack of experience or limitation on experiment time, particularly when multiple mutually dependent parameters must be changed.

Feedback control of experiments with automated spectrometer controls is an effective way to tackle these challenges, regardless of the sample studied or the spectroscopist's skills. In order to carry such optimisation of experimental parameters, an optimiser algorithm must evaluate the goodness of the parameters using measured data, which is captured in an objective function or, as called here, a cost function [227]. The algorithm then accordingly adjusts the experimental parameters values to minimise the

cost function, repeating measurements in a feedback loop [228]. At convergence, the cost function reaches a minimum value, indicating that the parameters have been set up to deliver the most advantageous experimental result (see figure 3.1).

However, experimental conditions necessitate finding that optimum in a relatively small number of cost function evaluations (measurements), and because of the inherent data noise, without using derivatives that would usually facilitate convergence. Despite notable recent work [229, 230], these requirements prevent many applications from using common derivative-based algorithms, e.g. L-BFGS [204] previously applied in the phase correction optimisation of chapter 2.

In contrast, derivative-free algorithms [231–233] have proved to be effective for closed-loop optimisation with noisy data thanks to their resilience to noise and ability to converge in a reasonable number of cost function evaluations [234]. While employed in several domains such as laser spectroscopy [235–237], quantum information processing [238], and even organic synthesis [239–241], reports of such on-the-fly optimisation techniques have been rather rare in magnetic resonance, with only a recent handful of publications in NQR [242], NMR [243], and ESR itself [244].

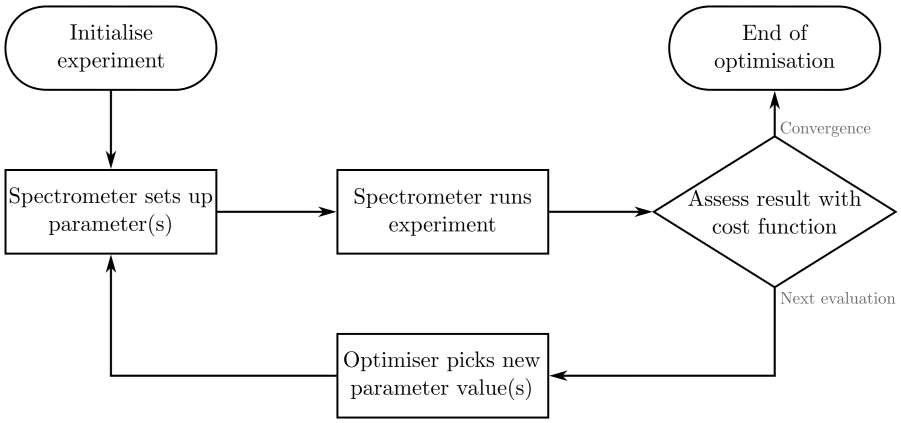


Figure 3.1: Basic flowchart describing a feedback loop optimisation conducted with ESR-POISE.

This chapter introduces a user-friendly Python package, Electron Spin Resonance Parameter Optimisation by Iterative Spectral Evaluation (ESR-POISE), for creation of on-the-fly optimisation routines in ESR spectroscopy. The code interfaces with the

Bruker BioSpin Xepr software to be fully-compatible with commercial ESR spectrometers, allowing its users to set up and optimise ESR experiments in a personalised and fully-automated manner.

3.2 Materials and methods

3.2.1 ESR-POISE software

ESR-POISE can be most easily installed via the Python package manager `pip` and the package source code is available on GitHub [245].

ESR-POISE requires Python 3 (version 3.6 at least). Particular package dependencies include the `XeprAPI` package from Bruker BioSpin, adapted by Sam Schott for Python 3.6 to 3.8 [246]. This package communicates with the Xepr software from Bruker BioSpin to control the spectrometer. In this work, Xepr version 2.8b.5 was used and Python versions 3.6, 3.7, and 3.8 were tested.

Three derivative-free optimisation algorithms are available with ESR-POISE: the MultiDimensional Search (MDS) method [247], the Nelder-Mead simplex method [231], and Bound Optimization BY Quadratic Approximation (BOBYQA), a trust-region interpolation method [232, 234]. BOBYQA yielded the best results in terms of speed and stability out of these three [243], and was thus chosen for the results reported here. However, the optimisation tables from appendix E also include outcomes obtained with the other algorithms.

More details on the package can be found in the user guide contained in appendix D.

3.2.2 Pulse simulation and generation

Almost all shaped pulses were generated, simulated and optimised with the version 1.0.0 of the `mrpypulse` package [248] in Python 3.6 to 3.8 (refer to appendix A for more details on the package).

For the simulation of hardware compensation only, the chirped pulses of CHORUS

were generated, simulated and optimised with the version 1.1 of the `MRChirpLab` package [188] on MATLAB R2020b (see appendix A for more details). Simulation of resonator effects on the pulses was conducted with EASYSPIN v5.2.28 [18]. Optimisations were run with BOBYQA using the Powell's Derivative-Free Optimization solvers (PDFO) [249].

For the 4-pulse DEER optimisation, the observer channel used Gaussian pulses with a Full Width at Half Maximum FWHM $= \tau_\mathrm{p}/2\sqrt{(2\ln(2))}$ where τ_p represents their duration, here of 84 ns. The $\pi/2$ and π pulse amplitudes were found at 65% and 100%. The delays were fixed at $\tau_1 = 200$ ns and $\tau_2 = 1000$ ns (see figure 1.11a). The pump pulse was set up as a HS^1 pulse generated from equations (2.6) and (2.8) with a bandwidth $\Delta F = 350$ MHz, a duration $\tau_\mathrm{p} = 100$ ns, and a time resolution $t_\mathrm{res} = 0.625$ ns.

For all the chirped pulses of the CHORUS sequence, the bandwidth was set at $\Delta F = 350$ MHz with a smoothing of about 12.5% (quarter-sine smoothing), yielding an effective bandwidth ΔF_eff of about 260 MHz. All pulses were generated with a time resolution $t_\mathrm{res} = 0.625$ ns and their individual parameters are available in table 3.1. In total, the CHORUS sequence was 640 ns long (with additional delays of 80 ns for dead time).

Table 3.1: Parameters of individual pulses in CHORUS experiment, namely the adiabaticity factor ($\mathcal{Q}_0$), duration (τ_p), and time-bandwidth product (TBP).

Parameter	**Chirped pulse 1**	**Chirped pulse 2**	**Chirped pulse 3**
τ_p (ns)	80	280	240
TBP (ns)	28	98	84
$\mathcal{Q}_0$	0.441	4	4

3.2.3 Sample and hardware

All experiments were conducted at X-band on a BRUKER BIOSPIN Elexsys E680 spectrometer, at a carrier frequency of 9.56 GHz (except for CHORUS compensation at 9.46 GHz and 9.56 GHz in subsection 3.4.2). All application examples of ESR-POISE were carried out with a resonator MS2 except for the MPFU phasing and DEER measurements which employed a resonator MD5.

In addition, simple tests of the optimisation scripts were conducted on the Bruker BioSpin Elexsys E580 spectrometer described in subsection 2.3.2.

The sample used for all experiments is the bisnitroxide sample already characterised in subsection 2.3.2, which can also be seen on figure 2.7b ($\omega_{dd} = 6.7\,\text{MHz}$ between the two electrons for a separation distance of around 2.0 nm [207]). Measurement for the signal phase optimisation were run at 293 K while for all other optimisations the temperature was set at 70 K.

3.2.4 Experiments

While full grid searches were conducted only once due to their long running time, optimisations were ran five times with each algorithm for comparison purposes. In order to avoid effects from instrumental drifts, these repetitions were interleaved.

A 30 dB video gain (except for DEER, at 48 dB), a 1 GHz receiver bandwidth (see subsection 2.3.2), and a recorded signal time resolution of 0.5 ns were employed for all measurements.

Studies for the optimisations of the signal phase, the pulse flip angles, and the field tweak used a Hahn-echo with a 16-step phase cycle. The obtained echoes were acquired with 256 points and 64 averages per scan. An identical setup was employed for the MPFU phase optimisation, asides from the number of averages per scan fixed at 4.

Studies for the optimisation of DEER relied on 2 points of the DEER trace with 1024 averages per scan. The full traces used an 8-step phase cycle and were acquired with 1024 points and 256 average per scans. In addition, 8 τ_1-averaging steps of 8 ns were applied. The observer pulses were set up with input amplitudes of 65% and 100%.

Studies for the optimisations of CHORUS used a 64-step phase cycle as described in subsection 2.3.2. The obtained echoes were acquired with 128 points, and 64 averages per scan for the amplitude optimisation against 32 averages per scan for the pulse compensation optimisation.

For the cost function of the pulse compensation, a field-sweep Hahn-echo was carried out with low intensity Gaussian pulses of durations 50 ns and 100 ns, 1024 points over 10 mT, using 256 averages per scan, and a 42 dB video gain.

3.2.5 Data processing

The XEPR software (BRUKER BIOSPIN), PYTHON 3.7 and MATLAB R2020b were used for all post-processing and plotting of the data.

For the DEER traces, post-processing comprised of summing and phasing of τ-averaged data in MATLAB 2020b, and background signal subtraction with the package DEERLab [41] in PYTHON 3.7.

For the data obtained with the CHORUS sequence, the echo was sliced in its centre point (i.e. the point with the maximum intensity) to circumvent 1^{st}-order phase errors. In order to increase the precision of this procedure, the echo was first interpolated with a spline to increase its time resolution. Baseline error was avoided by halving the first point of the obtained pseudo-FID. Before Fourier transforming the pseudo-FID, it was zero-filled to 8 times more points. To conduct 0^{th}-order phase correction, the spectrum with the maximum intensity was selected out of results obtained by stepping ϕ_0 was increased from $-180°$ to $180°$ in steps of $0.25°$ and the spectrum with the maximum intensity was selected. As a reference for the cost function of the CHORUS compensation, the field-sweep was transferred to the frequency-domain, flipped and normalised. The spectrum obtained with the CHORUS sequence was interpolated on the field-sweep frequency axis and normalised to enable subtraction of the two data sets.

All experimental data, with the pulse shapes and programs used to record it (in BRUKER format), and the simulation code of the resonator compensation, are accessible through the DOI: `10.17632/mg2yx7tzdn.2`.

3.3 Basic application examples

First, on-the-fly optimisation can be applied to automate basic actions which are normally conducted manually.

3.3.1 Optimisation of a single parameter

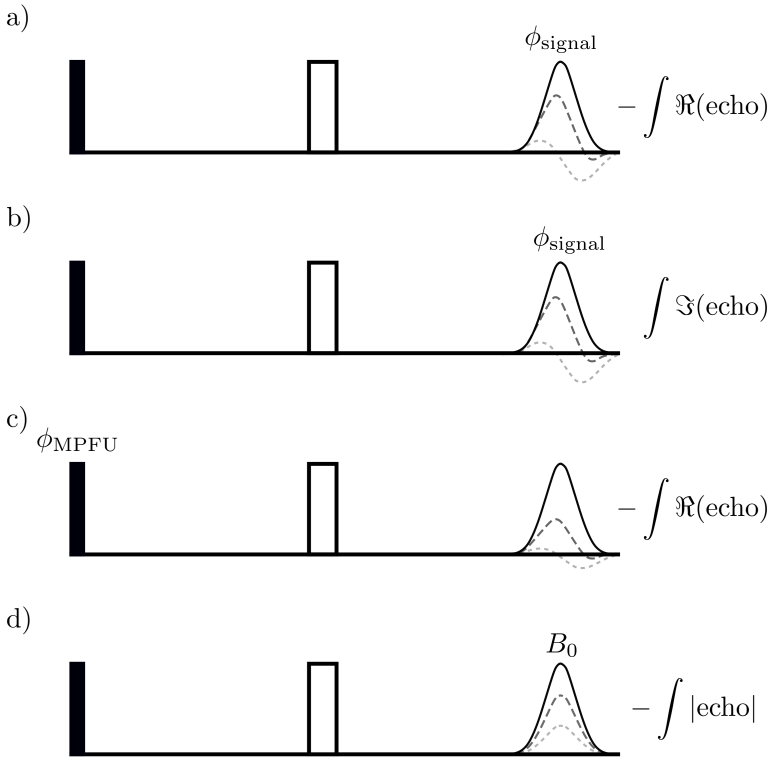


Figure 3.2: Scheme of the single parameter optimisations: a) signal phase setup, b) signal phase fine adjustment, c) MPFU channel phase and d) static magnetic field tweak. The Hahn-echo sequences under optimisation are represented with the targeted parameters on top and the cost function on the right.

An example of routine ESR procedure, used for almost every sample and experiment, is the adjustment of the signal phase to obtain an in-phase echo, for instance when using the Hahn-echo sequence (already described in subsection 1.2.4). With the signal phase input as a parameter and a cost function defined as the opposite of the real part of the echo integral (as shown in figure 3.2a), ESR-POISE maximised the in-phase echo

signal to yield an optimal signal phase; here in 10 acquisitions executed automatically in 40 seconds (see table E.1). To further emulate the actions of an advanced operator, this optimisation can be combined in the same script with a second one minimising the imaginary part of the echo (depicted in figure 3.2b). In the present case, this took an additional 30 seconds (see subsection E.1).

Sometimes, phase adjustments also need to be applied to the pulses themselves. For instance, sequences such as Relaxation Induced Dipolar Modulation Enhancement (RIDME) [250, 251] require long delays and cannot be fully loaded into the limited memory of the AWG. In that case, the pulses are emitted with the Microwave Pulse Forming Unit (MPFU) channels, which are more prone to phase errors. Such quadrature imbalances lead to poor phase cycling application, ultimately resulting in signal loss. To prevent this, the four channel phases need to be individually tuned by the user. With a similar setup to the signal phasing (see figure 3.2c), these can be adjusted automatically in four consecutive optimisations (as opposed to all four being optimised at the same time). The data in subsection E.2 shows that it takes less than two minutes to realise the entire procedure.

Obviously, ESR-POISE usage is not restricted to pulse and signal related parameters. As an example, subsection E.3 shows results of an optimisation which tweaked the static magnetic field (B_0) to place the spectrum maximum at the carrier frequency (see figure 3.2). Once again, such an optimisation can be conducted in a short amount of time, around 30 s presently.

Experienced operators should be able to conduct single parameter adjustments with ease and possibly faster. However, automation offers them worthwhile flexibility and time while lowering the barriers to entry for less proficient users.

3.3.2 Optimisation of multiple parameters

On-the-fly optimisation becomes even more useful to set up multiple interdependent parameters, and ESR-POISE can indeed easily deal with several parameters at once.

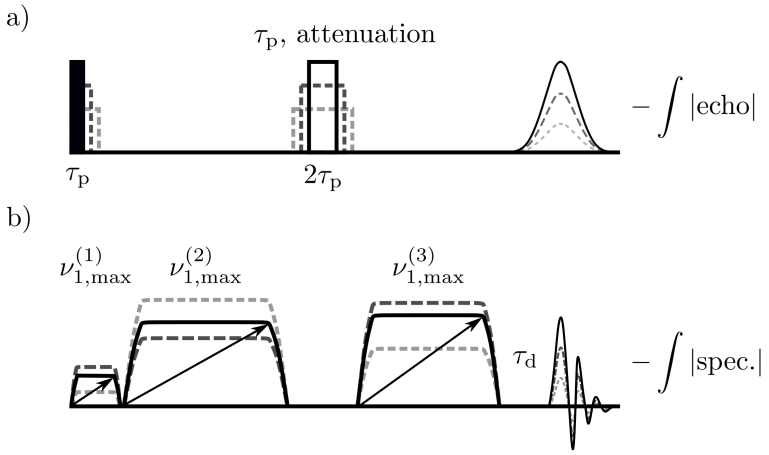


Figure 3.3: Scheme of the multiple parameters optimisations: a) calibration of a Hahn-echo flip angles parameterised with pulse lengths and amplitude, b) CHORUS sequence pulse amplitudes' calibration. The sequences under optimisation are represented with the targeted parameters on top and the cost function on the right. For the CHORUS amplitudes, the echo only begins after a dead time of duration τ_d, and is depicted with a more intricate shape indicating frequency information.

For instance, as stated in equation (1.37), the power amplitude and the length of a hard pulse define its flip angle, which is critical for the magnitude of the signal as shown by equation (1.38). Since most ESR spectrometers have limited resolution for defining the pulse duration, both of these parameters can be optimised to get the shortest pulse duration (minimising relaxation effects) while reaching the correct flip angle values. Here, the flip angles of the $\pi/2$- and π-pulses of a Hahn-echo were calibrated in order to maximise the signal magnitude, as pictured in figure 3.3a. ESR-POISE successfully optimised the parameters in 16 times fewer acquisitions than a conventional grid-based parameter search, with only 12 measurements compared to the 198 of the grid search (reported in figure 3.4 and subsection E.4). In case of relaxation largely due to instantaneous diffusion, longer pulses with lower power would be required and this method would still optimise for the duration and power yielding the strongest echoes.

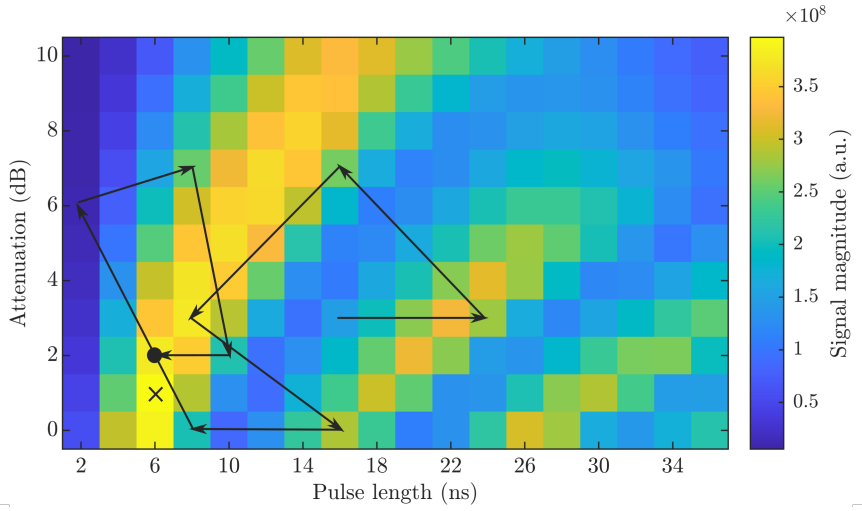


Figure 3.4: Magnitude of the echo signal mapped as a function of the parameters' combinations from the flip angle optimisation. Lower cost function values (higher signal intensity) are represented by brighter colours. The optimisation process is indicated by the series of black arrows on top of the 2D data obtained by the full grid search. The optimum found by the grid search is located by the black cross while the optimum from ESR-POISE is indicated by the black dot. For clarity, the last two cost function evaluations are not represented (more details available in subsection E.4).

As the number of parameters to optimise increases, the number of parameter combinations increases exponentially and quickly makes grid-search based methods infeasible to carry out. Methods to adjust parameters in those conditions rely on tricks in order to reduce the size of the space to explore, e.g., some knowledge of the system, subpar results, switching between different grid sizes, etc.

One example of such a method is the calibration procedure developed for previous work in this thesis on the CHORUS sequence [129]. As already described in subsection 2.3.3, the spectrometer's non-linear response forces the user to calibrate each of the amplitudes of the three chirped pulses in the sequence. However, the method proposed in subsection 2.3.3 only uses the signal at a specific point of the spectrum (on-resonance or slightly off-resonance), and sets up the pulses one after the other. For example, 50 steps can be used for each amplitude with a first adjustment of the $\pi/2$-pulse, a 2D grid search of the π-pulses, and a final readjustment of the $\pi/2$-pulse. This process reduces a parameter space containing 125000 (50^3) combinations to only 2600 measurements to

complete. ESR-POISE was simply given the three uncalibrated amplitudes, and maximised the full spectrum intensity (as illustrated figure 3.3b) to obtain calibrated pulses in only 30 acquisitions, giving a 10-fold gain on calibration speed (see subsection E.5).

3.4 Advanced application examples

On-the-fly optimisation is not limited to standard procedures such as the ones from the previous section. In particular, ESR-POISE is equipped to let the user define their own parameters and cost functions with ease, in order to adjust parameters which are difficult to modify through the spectrometer interface.

3.4.1 DEER pump pulse

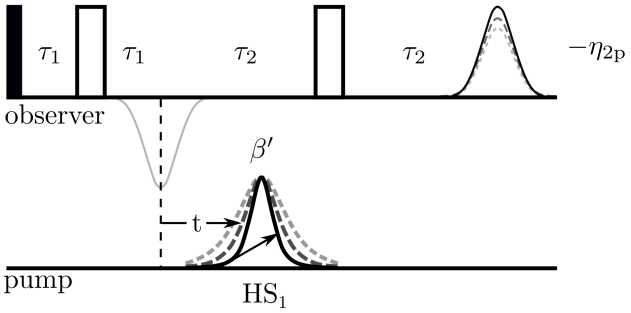


Figure 3.5: Scheme of the 4-pulse DEER pump pulse optimisation. The sequence is represented with the targeted parameters on top of the pump channel and the cost function on the right.

An illustration of an experiment which can require a particular cost function to optimise a non-standard parameter is the four-pulse DEER sequence [38], one of the most common ESR experiments (previously described in subsection 1.5.3). The best DEER traces are obtained with a pump pulse which covers as much of the EPR spectrum as possible while not overlapping with the effects from the observer pulses. For example, the more selective Gaussian pulses can be employed in the observer channel to reduce potential overlap [252]. For the pump, band-selective frequency-swept pulses can also

greatly improve the quality of the DEER traces [123, 124]. However, the specifics of the optimal shapes are generally not obvious and have been the subject of extensive research [136, 252].

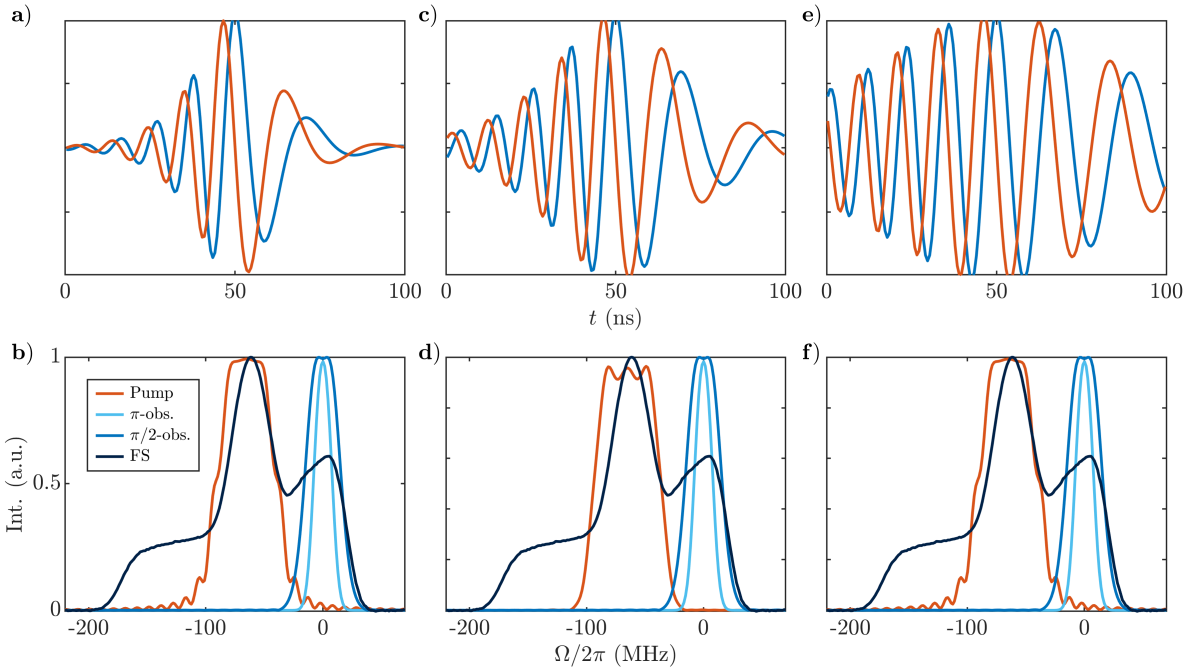


Figure 3.6: Cartesian representation of pump pulse (C_x in blue and C_y in orange) and its simulated inversion profile for: a) and b) $\beta' = 10$, c) and d) $\beta' = 6$, e) and f) $\beta' = 3$. The inversion profiles are presented in orange with the simulated profiles from Gaussian observer pulses (in blue) and an EPR spectrum from the field-sweep measurement (in dark blue). The simulation was conducted with `mrpypulse` 1.0.0 [248].

Here, we investigate the choice of the optimal selectivity factor of an HS^1 pulse set up as an inversion pump pulse. Equations (2.6) and (2.8) are used to generate the pulse shape and the exact parameter to optimise is defined as a truncation factor $\beta' = \beta\tau_\mathrm{p}$ [91]. Figure 3.6 presents some shapes and simulation results showing the theoretical effect of the pulses on the EPR spectrum. However, an optimal value for DEER measurements does not emerge clearly. Additionally, the simulation relies on assumption of B_1 strength values and does not take into account the hardware effects on the pulse shape, which are likely important [124, 143, 175] as previously seen in section 2.3, but cannot be easily incorporated into the simulation.

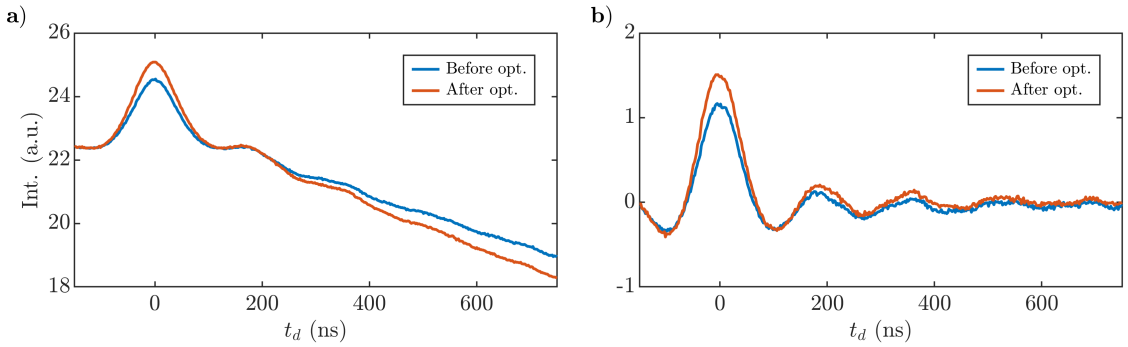


Figure 3.7: Full experimental 4-pulse DEER traces a) prior to and b) following background decay subtraction, for unoptimised ($\beta' = 10$, blue) and optimised ($\beta' = 6$, orange) HS^1 pump pulses.

ESR-POISE offered a solution by directly optimising the pulse shape before recording the DEER trace. Note that the observer pulses were also first automatically set up with a series of standard parameter optimisations and automated steps similar to the flip angle calibration and the signal phase optimisation described in the previous section. The truncation factor β' was handled as a user-defined parameter and the cost function was also adapted to maximise of the DEER trace modulation depth (see figure 3.5), which is a good indicator of the DEER trace quality. This quantity can be encompassed by η_{2p} [123, 131, 253] which only requires a two-point acquisition, being defined as the difference in intensity between the first maximum of the DEER trace and the lowest point of the following drop.

The value of η_{2p} was increased by about 20% in 3 minutes by ESR-POISE (see subsection E.6). To confirm this, 3 hours were spent to record the full trace displayed on figure 3.7, which exhibited a 23% increase in modulation depth. However, the optimised trace also had an increased background decay which can lead to a less reliable fit of the data [254]. This is one of the limits of using η_{2p} and measuring the Modulation-to-Noise Ratio (MNR) on the full traces can factor this into account [136]. Here, the optimised trace did not reveal a higher noise level and the MNR was increased by about 30%.

3.4.2 Hardware compensation

Section 2.3 presented in detail how ESR hardware limits can deform shaped pulses. Here, we look more at how such distortions can be circumvented.

Background

The effect of the hardware on a pulse is often modelled with a transfer function $h(t)$ which affects the pulse shape $f(t)$. Hardware compensation aims at building a shape $f(t)$ which would then be applied to the spins as the intended pulse $g(t)$

$$g(t) = f(t) * h(t), \tag{3.1}$$

where $*$ represents convolution. This equation can be transferred to the frequency domain with the convolution theorem, as follows:

$$\begin{aligned} \mathcal{F}\{g(t)\} &= \mathcal{F}\{f(t) * h(t)\}, \\ \implies G(s) &= F(s) \cdot H(s), \end{aligned} \tag{3.2}$$

where $\cdot$ represents point-wise product. Consequently, the knowledge of the transfer function, $h(t)$ or $H(s)$, allows for the calculation of the compensated pulse shape with

$$f(t) = \mathcal{F}^{-1}\left\{\frac{\mathcal{F}\{g(t)\}}{H(s)}\right\}. \tag{3.3}$$

Work in ESR has resulted in several ways to measure the transfer function [122, 124, 125], which are dependent not only the hardware but also on the sample, therefore preventing measurements from being reusable. However, on-the-fly optimisation can be used to find the transfer function in an efficient way, addressing both hardware and sample dependencies. A transfer function $H(s)$ of the following form is assumed:

$$H(s) = \frac{1 + bs}{1 + as}, \text{ for } a, b \in \mathbb{C}. \tag{3.4}$$

While the concept developed here is applicable to any shaped pulse or sequence of such pulses, we again focus on the CHORUS sequence, which is strongly affected by hardware effects as reported beforehand in section 2.3. The goal is to obtain uniform excitation across a wide spectrum of interest.

Results

As a proof of concept, simulation was first carried out on an excitation profile subjected to distortion from an experimental resonator profile. In order to conduct the optimisation, the cost function was defined similarly to the target on the magnetisation state specified in equation (2.31) for phase correction optimisation. Each pulse was modified with the four parameters from equation (3.4) (2 coefficients per complex number), as illustrated in figure 3.8a. Following a forced stop from the optimiser after a short number of evaluations to emulate experimental conditions, the excitation profile from figure 3.9 was strongly improved.

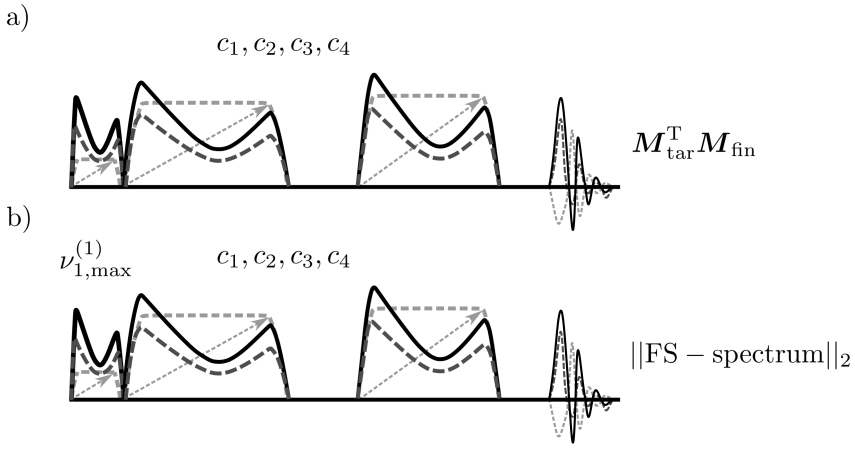


Figure 3.8: Scheme of the a) simulated and b) experimental hardware compensation optimisation conducted for the CHORUS sequence with ESR-POISE. The sequences under optimisation are represented with the targeted parameters on top and the cost function on the right.

In the experimental setting, the goal was set to a normalised reference spectrum recorded with a field-sweep. More exactly, the cost function was defined as the norm of the difference between the field-sweep spectrum and the CHORUS spectrum. The

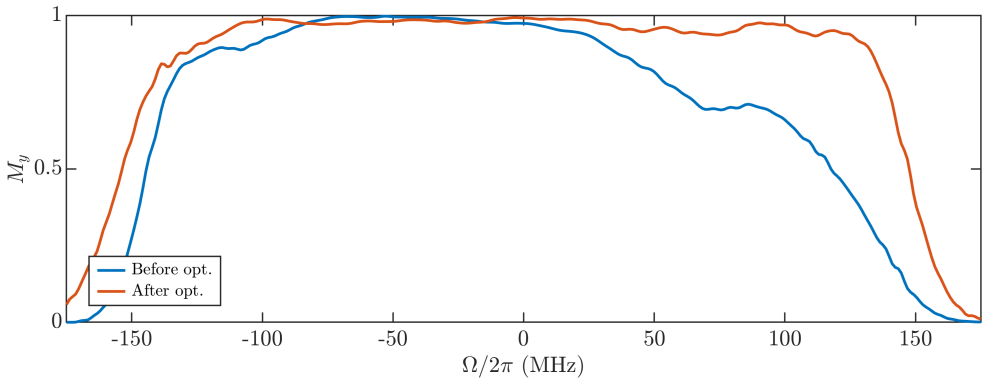


Figure 3.9: Excitation profiles simulated with CHORUS sequence a) before and b) after hardware compensation optimisation from ESR-POISE. The number of function evaluations was capped at 50. The simulation was conducted with `MRChirpLab` 1.1 [188]. EasySpin v5.2.28 [18] served to simulate the effect of an experimental resonator profile [124, 125] (profile used: figure 2.8a centred on resonator maximum).

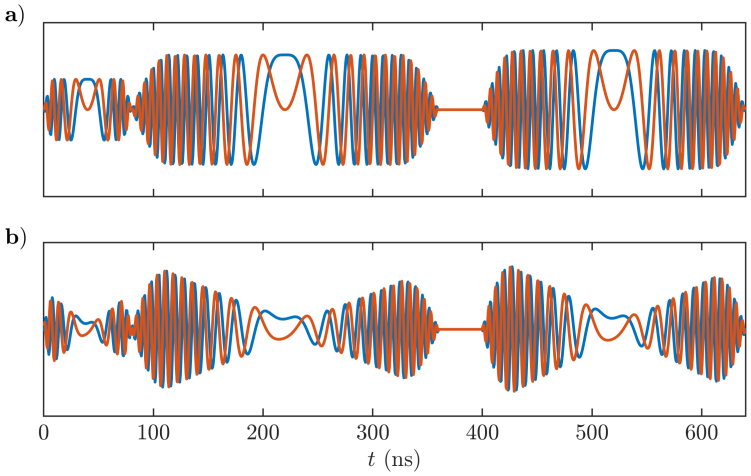


Figure 3.10: Cartesian representation of CHORUS sequence a) before b) and after experimental hardware compensation from ESR-POISE.

pulse amplitudes were first set up with the optimisation described above in subsection 3.3.2. To ensure the proper calibration of the $\pi/2$-pulse flip angle, the amplitude of the excitation pulse was added as another parameter to be optimised (see figure 3.8b). After running for 23 minutes, the five parameter optimisation yielded the compensated shapes shown in figure 3.10b. which decreased the cost function by two-fold as reported in figure 3.11 (also see subsection E.5). While 113 function evaluations were necessary to reach this result, an equivalent grid-search would have called for 530 million mea-

surements, which would have required 200 years to complete. The measurement was repeated at a different carrier frequency, with a smaller improvement of the result due to the position of the carrier frequency on the resonator profile.

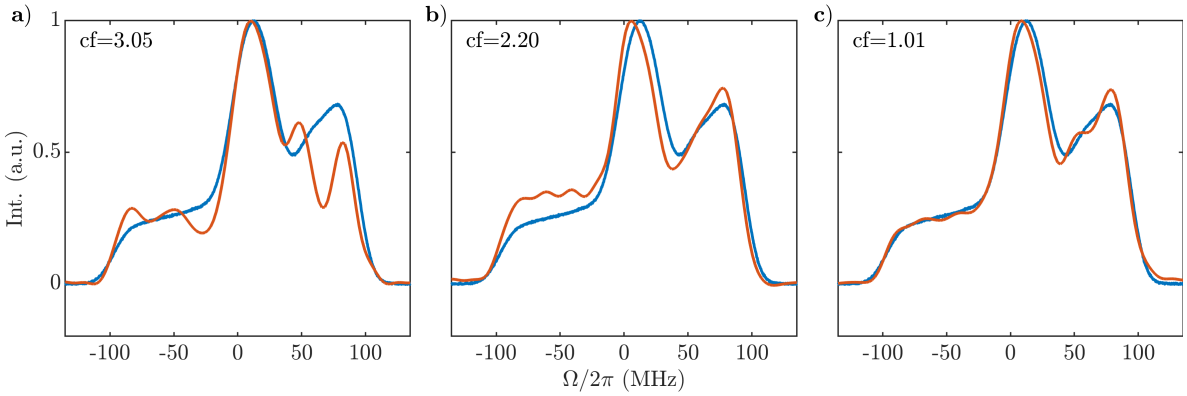


Figure 3.11: Experimental spectra (orange) from the CHORUS sequence a) before and b) after amplitude calibration optimisation (see figure 3.3b), and c) with subsequent hardware compensation by ESR-POISE starting with the setup obtained in b). The cost function final value is indicated by cf and the field-sweep measurement used for its computation (target) is plotted in blue. All data were recorded with the bisnitroxide sample at 9.46 GHz and normalised to one.

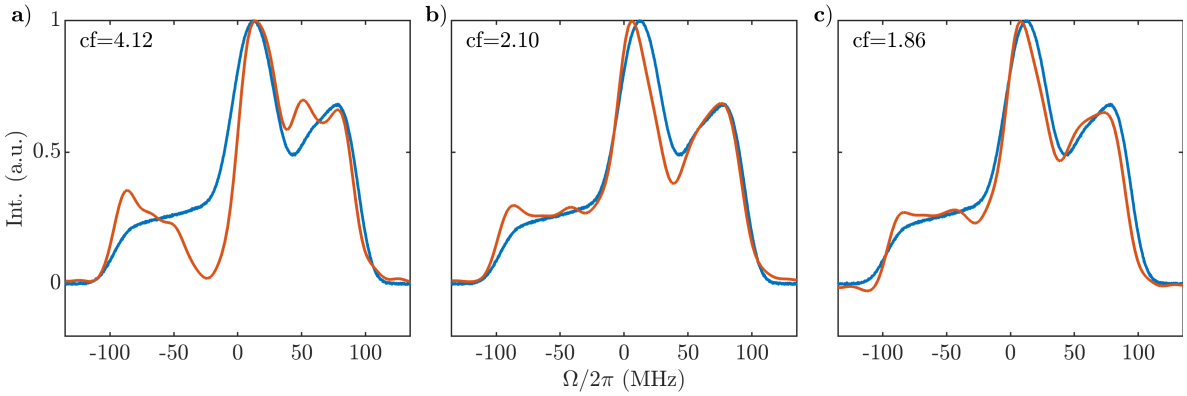


Figure 3.12: Equivalent data to figure 3.11, but for a carrier frequency 100 MHz higher.

Overall, ESR-POISE automatically set up a sequence which fully compensates for hardware effects. Other methods reported in the literature [122, 124, 125] may be used to obtain equivalent results, albeit at the cost of time-consuming setup. Such procedures could also be automated with ESR-POISE if a different method or cost function were desired.

3.5 Outlook

This chapter illustrated how a wide range of ESR experiments can be optimised with ESR-POISE. Many potential applications could be explored to fully automate standard experiments. Such procedures would require extensive tests of robustness but could allow ESR users in the future to simply drop their sample in the instrument and get valuable data without requiring experimental expertise.

With a fully open-source code written in the simple and widely used PYTHON language, ESR-POISE aims not only at being accessible, but also at being improved upon thanks to community participation. For instance, the list of available algorithms could be extended. Bayesian optimisation would be an interesting addition since it is often used as state-of-the-art algorithm for optimisations with expensive function evaluations, e.g. hyperparameter tuning of neural networks in machine learning [255].

The approaches developed here do not aim at discarding the specialist's skills but are, on the contrary, complementary. Expertise is essential to produce tailored models capturing the behaviour of the optimisation problems (e.g. distinguishing different component effects for shaped pulses compensation), which could lead to great speed and accuracy gains. Prior knowledge is also crucial to start from better initial guesses. Finally, the newly acquired speed for multi-parameter optimisations even paves the way to new experimental procedures, previously not accessible with traditional methods due to time constraints.

Chapter 4

Design of a spectrometer with NV centres as quantum sensors

4.1 Introduction

Conventional magnetic resonance techniques rely on the use of bulk samples to make up for their lack of sensitivity. Conducting magnetic resonance at small scale, in the µm-nm range, requires unconventional approaches such as measurements performed by quantum sensors [256].

A promising candidate for a magnetic resonance quantum sensor is the Nitrogen Vacancy (NV) defect in diamond. An NV consists of a nitrogen substitution and a vacancy in the diamond lattice [257], as depicted in figures 4.1a and b. For quantum sensing, the state of interest is the negatively charged NV^-, directly referred to as "NV centre" here, and which presents remarkable optoelectronic properties [258].

An NV centre forms an atom-like system with a spin $S = 1$ [259]. At room temperature, the NV centre spin state can be detected via photoluminescence, even at a single spin scale [260], and presents a long coherent time (slow relaxation) [261] allowing for lengthy quantum sensing protocols. The NV centre spin state is responsive to external magnetic fields, making it a highly sensitive Optically Detected Magnetic

Resonance (ODMR) platform to perform magnetic resonance measurement [262, 263]. In the last decade, NV centres have indeed been used to perform such measurements at unprecedentedly small scales [264–267].

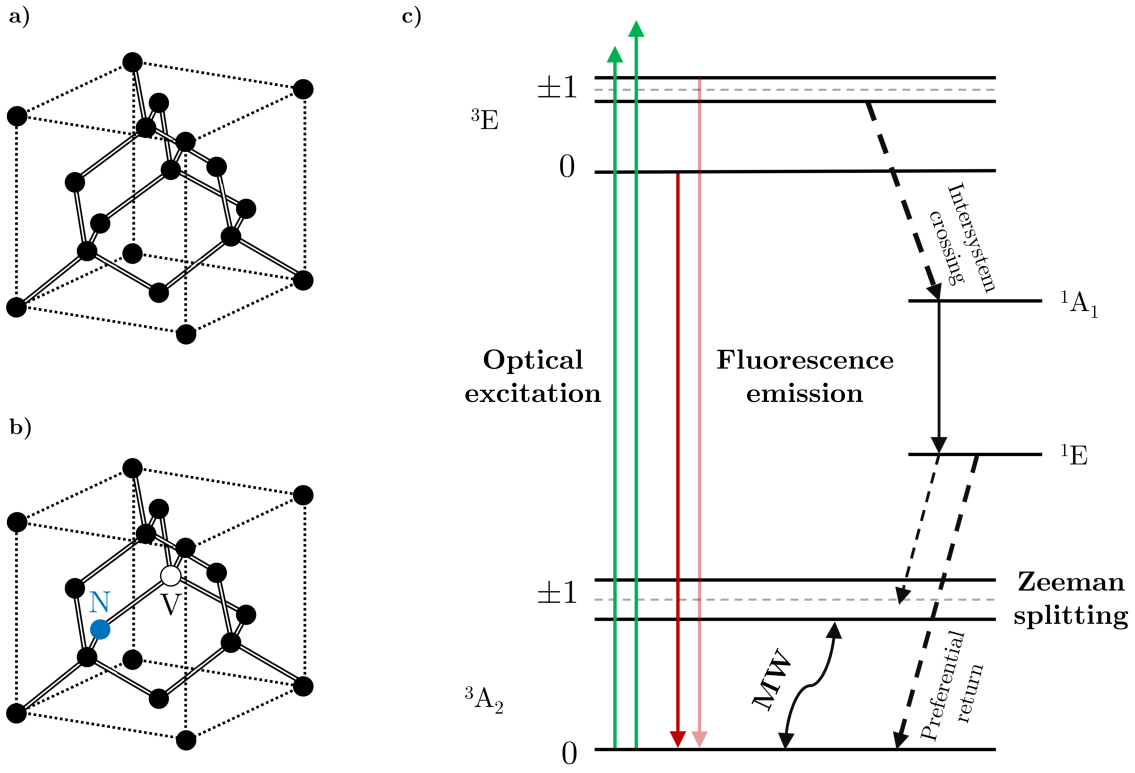


Figure 4.1: Scheme of a) lattice of diamond (carbon atoms in black) b) with example of NV defect (nitrogen in blue and vacancy in white), and c) energy level diagram of NV centre. The energy level diagram presents the system triplet ($m_s = 0$ and $m_s = \pm 1$) with its electronic ground state ^{3}A$_2$ and electronic excited state ^{3}E. ^{1}A$_1$ and E$_1$ represent the system intermediary singlet state. Highlighted in bold are the four transition which are controlled and monitored for quantum sensing protocols.

A simplified energy diagram of the NV centre is presented in figure 4.1c and is further described here to illustrate how external spins can be sensed by the NV centre.

The NV centre has a spin $S > 1/2$ and in such a case where the total spin is formed with several other spins, the unpaired electron spins can interact through spin-spin couplings. This phenomenom, sometimes paired with spin-orbit coupling, can lift the a degeneracy of the different states without an external magnetic field, the Zero-Field Splitting (ZFS) [268]. The ZFS can be represented by a tensor $\boldsymbol{D}$, which gives the

following ZFS Hamiltonian $\hat{\mathcal{H}}_D$ for two electron spins $\hat{\boldsymbol{S}}_\mathbf{1}$ and $\hat{\boldsymbol{S}}_\mathbf{2}$:

$$\hat{\mathcal{H}}_D = -\hat{\boldsymbol{S}}_\mathbf{1} \cdot \boldsymbol{D} \cdot \hat{\boldsymbol{S}}_\mathbf{2}. \tag{4.1}$$

The NV centre behaves as a triplet state with $m_s = 0$ and $m_s = \pm 1$, showing an axial ZFS. This means that the ZFS Hamiltonian can be written as:

$$\hat{\mathcal{H}}_D = D\hat{S}_z^2. \tag{4.2}$$

where D is the ZFS axial component. For the NV centre ground electronic state $^3\mathrm{A}_2$, $D = 2.87\,\mathrm{GHz}$ [259] and represents the Micro-Wave (MW) transition between the $m_s = 0$ and $m_s = \pm 1$ states (see figure 4.1c).

The triplet electronic excited state $^3\mathrm{E}$ is generally activated via optical excitation with off-resonance excitation (typically 532 nm) [269]. The system returns to its ground state directly at its 637 nm zero phonon line [270] (fluorescence emission) or via the singlet levels $^1\mathrm{A}_1$ and E_1 at a 1042 nm zero phonon line (intersystem crossing) [271].

For magnetic resonance sensing, a static magnetic field $\boldsymbol{B}$ is applied to lift the degeneracy on $m_s = \pm 1$ (Zeeman splitting), leaving the NV centre Hamiltonian as

$$\hat{\mathcal{H}} = D\hat{S}_z^2 - \gamma_e \boldsymbol{B} \cdot \hat{\boldsymbol{S}}, \tag{4.3}$$

The magnetic field direction z is chosen to coincide with the axis connecting the nitrogen atom and the vacancy of the NV centre (C_3 axis of the defect). In the presence of an external magnetic field to be observed, the Hamiltonian therefore becomes

$$\hat{\mathcal{H}} = D\hat{S}_z^2 - \gamma_e(B_0 + B_z^{\mathrm{ext}})\hat{S}_z, \tag{4.4}$$

where the field sensed by the NV centre is B_z^{ext}, since the NV centre is considered primarily sensitive along that axis.

B_z^{ext} can be detected using ODMR. The first step is to initialise the system. This starts by an optical excitation with green light to activate the system transition from the triplet electronic ground state ($^3A_2$) to the triplet electronic excited state (^3E). The system subsequently returns to its ground state via fluorescence emission and intersystem crossing. $m_s = \pm 1$ preferentially returns to the ground state $m_s = 0$ via intersystem crossing. The system is thus initialised into the $m_s = 0$ state in only a few cycles.

The next step is to drive the transition from $m_s = 0$ to $m_s = 1$ or $m_s = -1$ with MW pulses. Depending on the kind of B_z^{ext} and what is measured, various sequences are used to prepare the spin state for readout.

Another consequence of the preferential return of the $m_s = \pm 1$ state is that it emits less fluorescence than $m_s = 0$. The final step for magnetic resonance sensing is therefore to apply optical excitation again and monitor the fluorescence intensity. B_z^{ext} is inferred from the variation of the fluorescence emission. Generally a variable has to be swept, for example the MW field for CW ESR measurement or the delay between the pulses for NV-spin echo with a external AC field.

Despite differences in their details, the various sensing protocols share the same key features: the use of optical pulses for initialisation and readout, and a MW pulse sequence to extract B^{ext} (see figure 4.2) [272].

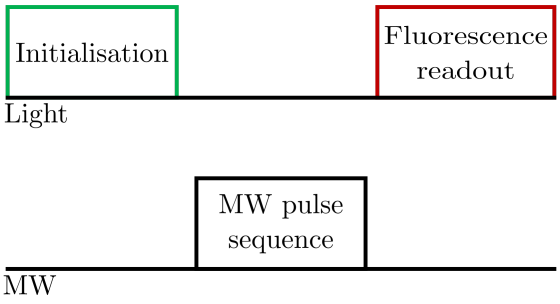


Figure 4.2: Scheme of the basics of magnetic resonance measurements with an NV centre. The three main steps are: initialisation of the spin state with green light, MW manipulations to prepare the spin state to be measured, and fluorescence measurement to read out the spin state.

In total, five elements are needed to detect magnetic resonance with NV centres:

(i) Diamond with NV centres

(ii) Static magnetic field to induce Zeeman splitting

(iii) Source for optical excitation (laser)

(iv) MW coil

(v) Detector to monitor the fluorescence

The first section of this chapter addresses the design choices for each of the five systems to build a magnetic resonance spectrometer relying on NV centres, thanks in particular to a recent protocol description from Bucher et al. [273]. In the second section, the choice of the static magnetic field design is discussed in more detail with Finite Element Analysis (FEA) simulation. All the spectrometer components are listed in appendix F and additional views of the design are provided in appendix G.

4.2 General design

4.2.1 Diamond

Diamonds used for quantum sensing are typically high purity single crystals which are grown via Chemical Vapour Deposition (CVD). Diamonds obtained in such a way contain a low concentration of NV centres and more centres can be generated for sensing applications. This is generally done via bombardment of ions or electrons to create vacancies followed by annealing at temperatures typically superior to 800 °C to create the centres [274, 275]. This is typically the procedure which is followed after purchasing a single crystal diamond from a manufacturer. The scale at which the sensor operates depends on the depth of implementation; 10 nm were chosen here.

High concentration of nitrogen can also be deliberately introduced in the diamond lattice when it is grown [276], allowing for the control of the NV centres T_2 by adjusting the ^{5}N concentration [277]. Such technologies have even recently become commercially available (e.g. DNV^{TM}-B1 from Elements Six for AC magnetometry).

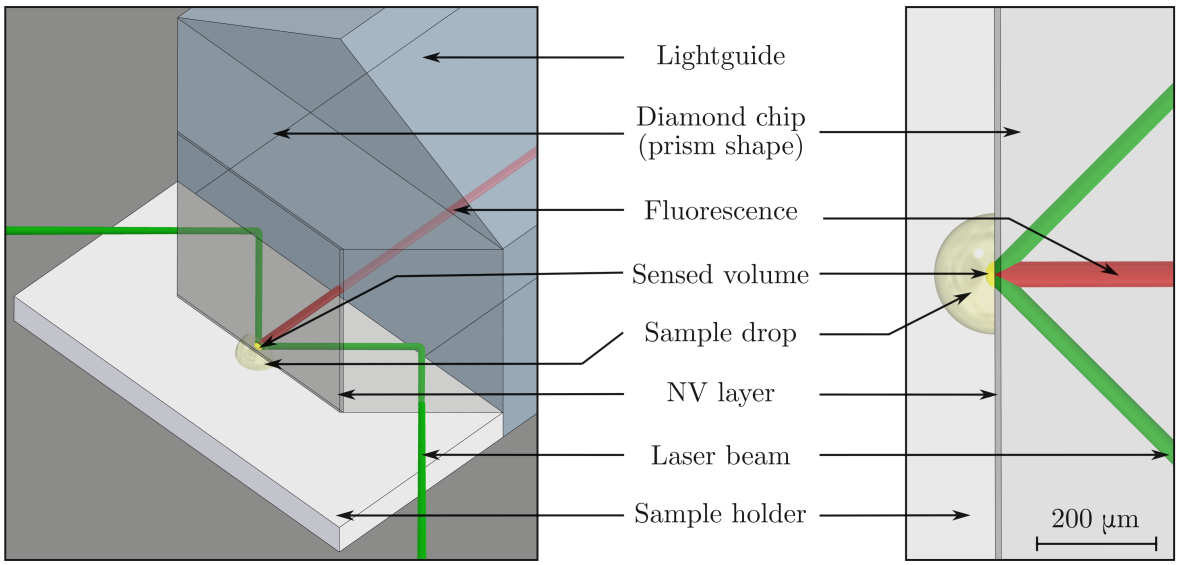


Figure 4.3: Simplified close up views of diamond prism and sample realised with Computer Aided Design (CAD) software Autodesk Inventor 2020. The NV layer and sensed volume scales have been increased by a factor of 1500 for visibility.

NV centres are usually optically excited with a laser focused on the diamond chip in a Total Internal Reflection (TIR) setup. The optical alignment and excitation effectiveness can be improved thanks to setups facilitating the TIR such as lenses designed to collect fluorescence [278] or, in endoscope-type setups, specifically shaped diamonds mounted the tip of an optical fibre [279]. Here, a prism shape inspired by previous work [280] was chosen (see figure 4.3).

4.2.2 Static magnetic field

High fields offer a higher sensitivity (at micro-scale) and resolution (at nano- and micro-scale) for NV magnetic resonance by respectively offering a stronger spin polarisation and wider separation of peaks. However, they require bulkier and more expensive equipment not only for the magnet itself, but also for the high power pulsing needed by the MW, in particular for dynamic decoupling sequences [281].

Therefore, NV magnetic resonance has mainly been investigated with relatively low static magnetic fields. Here, we picked a polarising magnetic field B_0 of several tens

of mT which needs to be stable and homogeneous over the sample volume for several hours to enable data averaging over long experiment times.

Some good candidates to create such a field are permanent magnets, often employed in low field magnetic resonance as they offer a compact and low maintenance solution to produce a stable magnetic field B_0 [282].

Permanent magnets setups can take multiple types of geometries in magnetic resonance [283]. Here, two cylindrical magnets with aligned axis and opposite poles facing each other were chosen. Being able to adjust the field direction (z) is essential to align it with the NV centre axis. The simple configuration with two facing magnets allows for controlling the field direction by moving the magnets central axis around the diamond, and the field strength by changing the distance separating the magnet faces.

The geometry of the permanent magnets and their mount are detailed in figure 4.4 and further details on the magnet choice can be found in section 4.3.

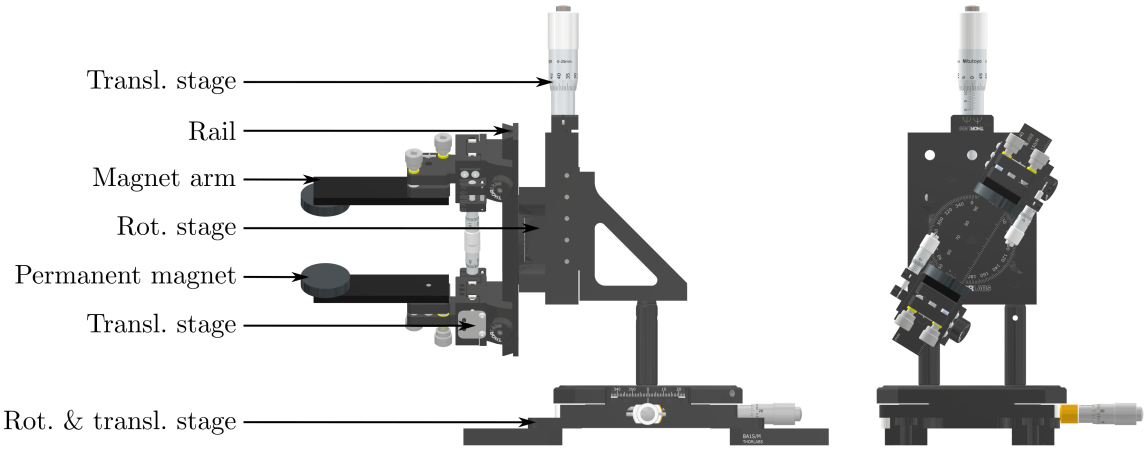


Figure 4.4: Right and front view of the static magnetic field system, realised with Computer Aided Design (CAD) software Autodesk Inventor 2020. Some individual part CAD files were obtained from Thorlabs (`https://www.thorlabs.com`, 2020 and see appendix F for more details).

4.2.3 Optical excitation

Optical excitation is done at 532 nm with a green laser of beam waist diameter 2.25 mm. The intensity noise property of the laser directly translates to intensity noise in the fluorescence data and a laser with low noise was therefore preferred. The chosen laser was the Verdi G2 from Coherent, which is based on Optically Pumped Semiconductor Laser (OPSL) technology [284] (laser with frequency conversion source). This laser presents up to 0.03% RMS intensity noise (10 Hz to 100 MHz).

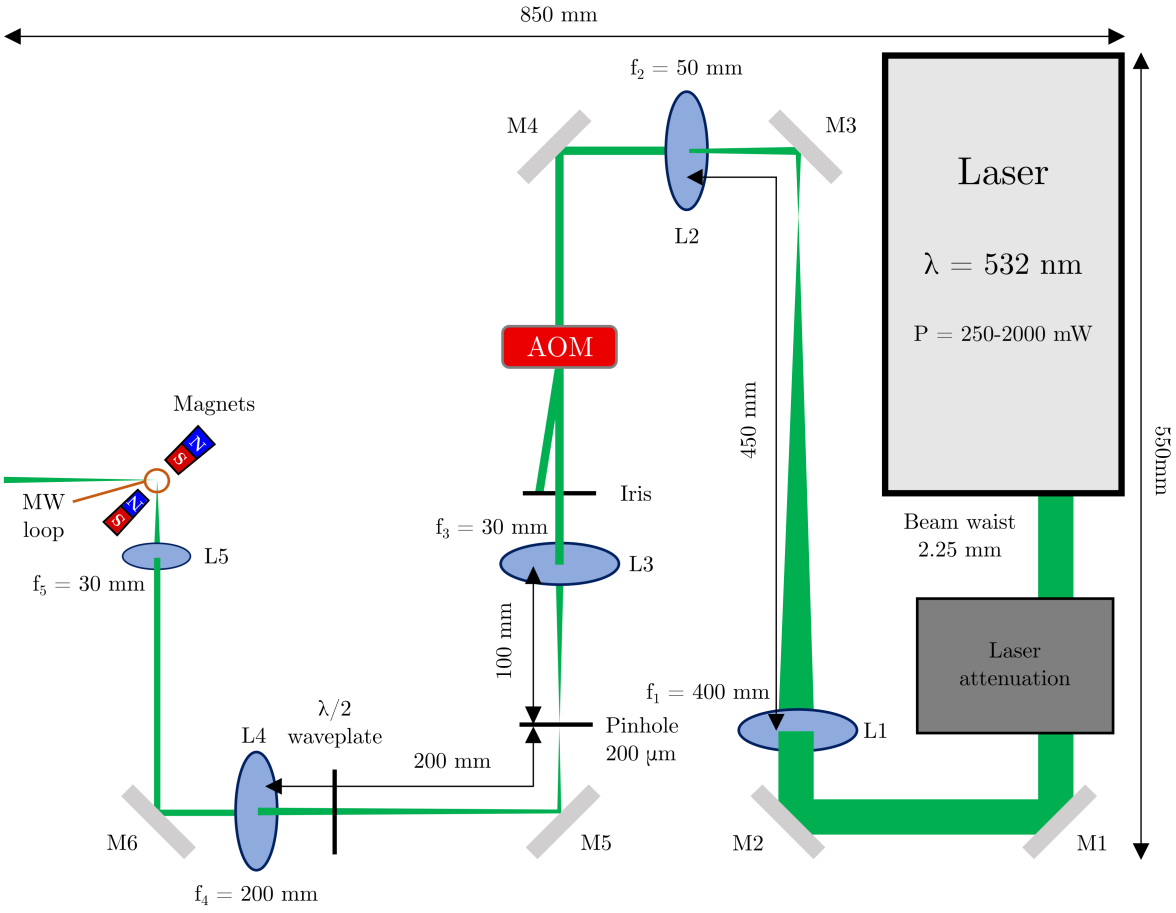


Figure 4.5: Scheme of the NV spectrometer optic path which comprises: a first telescope with the lenses L1 and L2, an AOM with an iris and a pinhole, a second telescope with the lenses L3 and L4, a half-wave plate, and the lens L5 for the final focusing of the laser on the diamond (scheme not to scale, in particular beam waist).

The laser is installed on an optic table and various optic components are set up to control and deliver the laser beam (see figure 4.5). First, a telescope constituted of two lenses is used to reduce the beam waist by a factor 8. An Acousto-Optic Modulator (AOM) is then placed in the beam path to generate the laser pulses responsible for the system initialisation and reading. After the AOM, an iris respectively blocks and lets through the 0^{th} and 1^{st} order diffraction orders from the AOM. A high extinction ratio (about 10000) should be sought to create pulses of quality. A lens then focuses the beam into a pinhole to further clean it. A subsequent lens recollimates the beam, forming a second telescope which further demagnifies the beam waist by a factor of 2. A final lens is placed at about its focal length from the diamond to focus the beam onto the diamond.

Placement of the optics is done with standard alignment techniques using mirrors to fold the beam on the optic table, irises to check for coplanarity and a white business card to visualise and avoid residual back reflections [285].

All operations of the laser should comply with laser safety regulations. The diamond prism shape eases laser safety by keeping the laser beam in one plane. Laser shields are employed to encompass the beam and beam blocks to terminate unwanted beams. A laser attenuator can be used to reduce the laser power to a safe level during alignment and a pre-alignment can also be done with a low power laser.

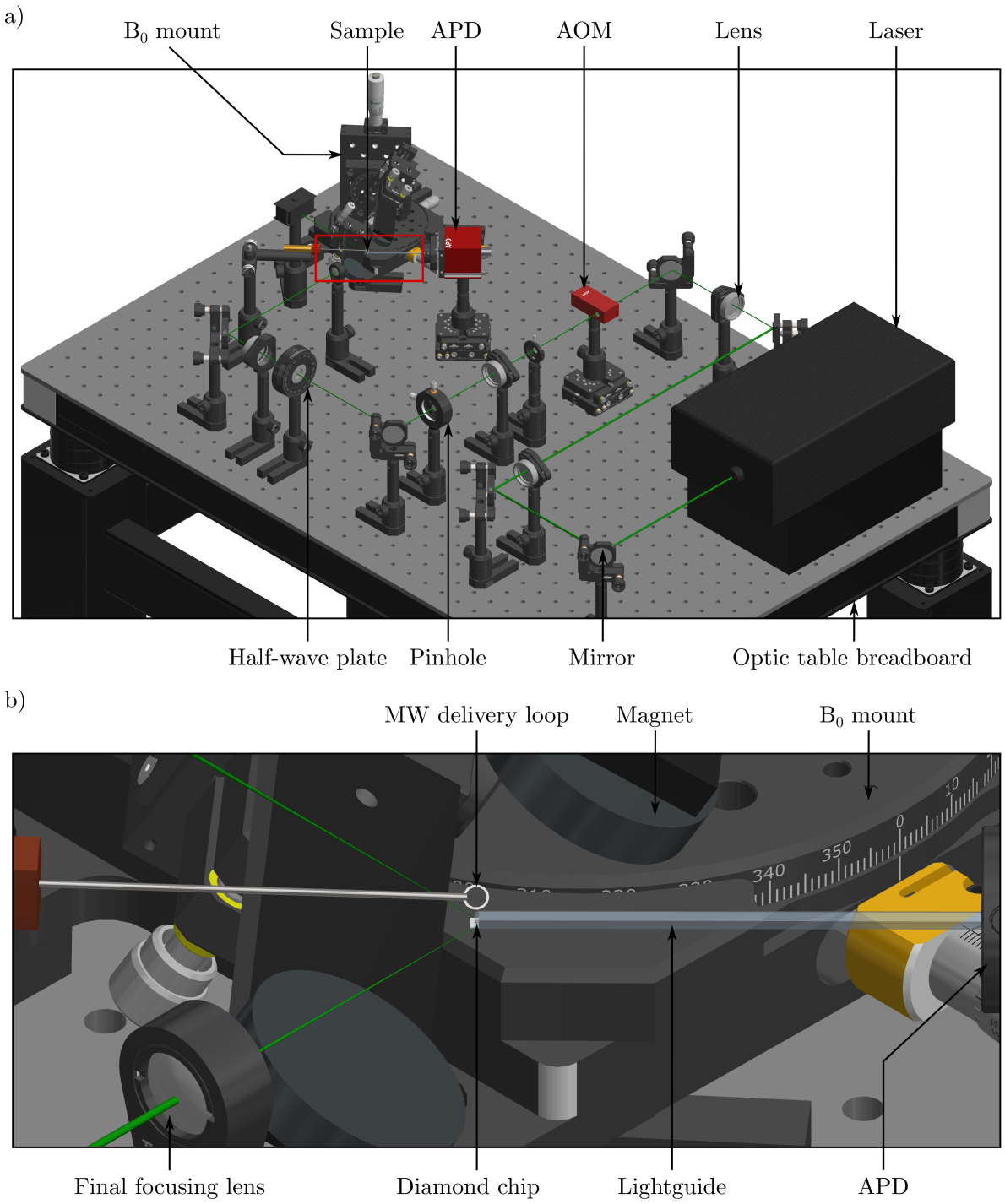


Figure 4.6: NV spectrometer optical table views: a) general and b) close up corresponding to the red rectangle in red in a). The views were realised with Computer Aided Design (CAD) software Autodesk Inventor 2020. Some individual part CAD files were obtained from Thorlabs (`https://www.thorlabs.com`, 2020 and see appendix F and for more details).

4.2.4 MW pumping & fluorescence detection

For a magnetic field of a few hundred mT, the MW source operates in the range 1-4 GHz. To be able to control the pulse phase, an In-Phase/Quadrature (I/Q) mixer should be present, whether inter internal or external. The pulse sequences could also be generated with an AWG which can generate shaped pulses. A MW amplifier can be used to increase the delivery power. For the MW delivery of this signal to the NV centres, a coaxial cable can be used, with its end stripped to expose its inner wire which is soldered into a loop.

An Avalanche PhotoDiode (APD) is employed as a photodetector for the measurement of the fluorescence. The fluorescence is directed to the APD with a lightguide of diameter smaller than the APD active area. A filter rejects non-fluorescent light, in particular the 532 nm excitation light.

The spectrometer is controlled from a computer connected to a multichannel programmable pulse generator card and a Data Acquisition (DAQ) unit to record data coming from the APD. The card sends Transistor-Transistor Logic (TTL) signals to switches for the DAQ start and stop triggers, the controls of the AOM through the AOM driver, and the MW source pulses through the I/Q channels and the MW amplifier.

The qdSpectro software package is used for control of the different elements from the computer [286].

4.3 Field homogeneity study with FEA

4.3.1 Introduction

The strength and homogeneity of a static magnetic field can be calculated using Finite Element Methods (FEM). FEM is based on the idea of breaking a continuum into multiple segments, called finite elements, to yield an approximate solution to a problem on the whole continuum [287]. First introduced in the context of structural and elasticity analysis in the 1940s, FEM is now found in a wide variety of fields to discretise real-world continuous problem [288]. Finite Element Analysis (FEA) is the application of FEM to engineering problems and generally relies on [289]

- A system definition with some objects geometry (domains) and their relevant material properties.
- A discretisation of the domains (finite elements definition) with a mesh of nodes.
- A physics model definition with the equations to solve and domains boundary conditions.
- A solver to solve the equations at the mesh nodes.

In this section, FEA is used to design a magnetic field B_0 with permanent magnets for the spectrometer with NV centres. First, the theory underlying the equations to be solved is discussed. Then, the practicality of implementation is described. Finally, the results obtained from the simulation are presented and serve to choose an appropriate setup.

4.3.2 Theory

The magnetic field created by permanent magnets can be calculated with classic electromagnetism equations.

The constitutive relation linking the magnetic flux density $\boldsymbol{B}$ to the magnetic field

strength $\boldsymbol{H}$ and the magnetisation $\boldsymbol{M}$ is defined as

$$\boldsymbol{B} = \mu_0 \mu_r (\boldsymbol{H} + \boldsymbol{M}) \tag{4.5}$$

where the magnetic vacuum permeability μ_0 is fixed and the recoil permeability μ_r depends on the material (non zero in magnetised materials).

Permanents magnets are generally characterised with the remanent magnetic flux density $\boldsymbol{B_r}$ in place of the magnetisation

$$\boldsymbol{B_r} = \mu_0 \mu_r \boldsymbol{M}. \tag{4.6}$$

After insertion of equation (4.5), this becomes

$$\boldsymbol{B} = \mu_0 \mu_r \boldsymbol{H} + \boldsymbol{B_r}. \tag{4.7}$$

The Gauss law for magnetism, $\nabla \cdot \boldsymbol{B} = 0$, can be used to get the model's equation

$$\nabla \cdot (\mu_0 \mu_r \boldsymbol{H} + \boldsymbol{B_r}) = 0. \tag{4.8}$$

As the model is a current free region, it can be stated that

$$\nabla \times \boldsymbol{H} = 0, \tag{4.9}$$

therefore implying that the magnetic field strength H can be linked to a magnetic scalar potential V_m as

$$\boldsymbol{H} = -\nabla V_m. \tag{4.10}$$

Inserting equation (4.10) into equation (4.8) yields the equation to be solved to obtain V_m and hence, the magnetic field from the permanent magnets

$$-\nabla \cdot (\mu_0 \mu_r \nabla V_m - \boldsymbol{B_r}) = 0. \tag{4.11}$$

The continuous problem from equation (4.11) can be solved spatially with FEA. The geometry is created as permanent magnet domains surrounded by an air domain. The permanent magnets domains are then assigned material properties with a recoil permeability μ_r and a remanence B_r. The remanent magnetic flux density $\boldsymbol{B_r}$ is oriented along the axis of the permanent magnets. The air domain respects

$$-\nabla^2 V_m = 0, \tag{4.12}$$

a simplified version of equation (4.11) as its remanence B_r is null.

As for boundary conditions, the normal element of the magnetic flux density is put to 0 with

$$n \cdot B = 0, \tag{4.13}$$

where n stands for the normal vector to the surface. The magnetic scalar potential is fixed with the condition

$$V_m = 0. \tag{4.14}$$

4.3.3 Methods

Parameters selection

Before proceeding with any calculation, the constraint and parameters thought to be the most important were selected to be studied.

First, the dimensions of the magnets should have an influence on the field strength and homogeneity. The following three geometric parameters were considered for the study:

- Cylinder thickness
- Cylinder diameter
- Distance between the two magnets

Second, the material determines the strength of B_r and its temperature stability. Some of the materials with the strongest remanence were considered as they favour

compact setups [283]:

- Neodymium (Nd) based magnets which present the strongest remanence.
- Samarium-cobalt (SmCo) based magnets, which are generally less powerful but more stable with respect to temperature variations.

Other possible factors which should influence the magnetic field value and homogeneity but were not taken into account include misalignment of the magnets' axis or exterior magnetic perturbations.

System and geometry definition

The two magnets and their environment were represented in a cylindrical frame of coordinates (r, ϕ, z) with r the radial distance to the centre of the magnets axis, ϕ the angular coordinate and z the height coordinate. This representation was reduced to a 2D frame ($\boldsymbol{u_r}$, $\boldsymbol{u_z}$) thanks to the axial symmetry along z. The coordinates (r, z) therefore modelled the entire geometry (see figure 4.7), which also decreased computation requirements.

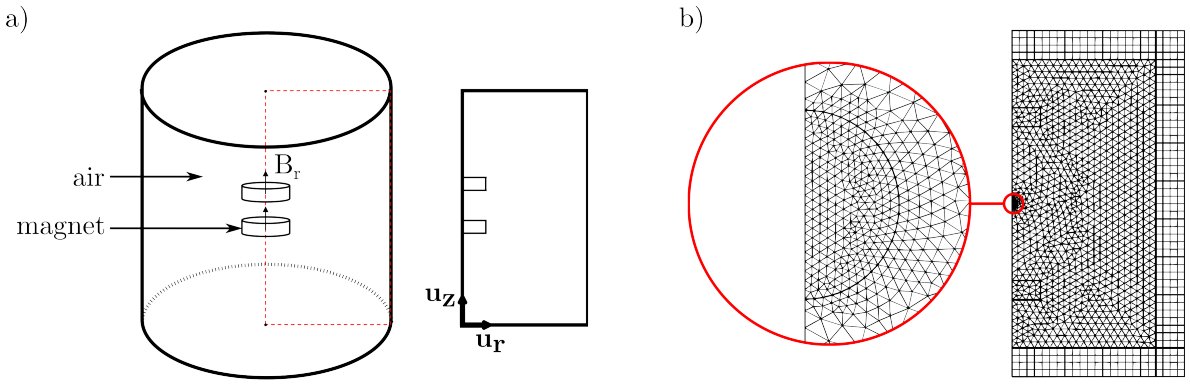


Figure 4.7: Schematic representation of the setup geometry to simulate in a) 3D and b) 2D axial symmetry. $\boldsymbol{u_r}$ and $\boldsymbol{u_z}$ represent the frame coordinates unit vectors. c) 2D mesh used for the study, generated with the following parameters, respectively for the region of interest and the rest of the model: maximum element size of 2.5 mm and 4 mm, minimum element size of 1 mm and 0.2 mm , maximum element growth rate of 1 and 1.4, curvature factor of 0.18 and 0.18.

FEA implementation

FEA of the permanent magnets was conducted with COMSOL Multiphysics 5.5. This software can perform electrostatic simulations and examples of its applications for permanent magnet design in magnetic resonance can be found in the literature [290, 291].

The geometry was generated in the software with an infinite element domain. It is represented by an infinite volume of air around the magnets, making the overall model smaller and hence, faster to solve. A small domain was created in the region of interest for magnetic resonance measurement (sphere of diameter 20 µm), at the centre of the model. A boundary condition on the outer layer of the infinite element domain was defined with equation (4.14).

The software was employed to generate a mesh with triangular elements for the model (air and magnets) and quadratic elements for the infinite element domain as illustrated in figure 4.7b. The size of the mesh elements was controlled with four parameters:

- Maximum element size
- Minimum element size
- Maximum element growth rate
- Curvature factor (boundary element size over the geometry curvature radius)

The model and the infinite element domain were defined with the same size parameters. The region of interest for magnetic resonance measurements was more finely defined as shown in the insert of figure 4.7b. The mesh progressively transitioned from the thinner mesh to the thicker, starting from the boundaries of the region of interest. This transition was controlled by the maximum element growth rate parameter (more details available in figure 4.7 caption).

The COMSOL physics module "magnetic fields, no currents" was used to implement and solve the equation described in subsection 4.3.2. For the solver start, V_m was set to an initial value of 0 over all the domains.

Field strength and inhomogeneity characterisation

The centre magnetic flux density B_0 was taken as the average value of the magnetic flux density in the region of interest. This corresponds to the area where the measurement would take place, at the location of the diamond and sample ensemble. The peak to peak inhomogeneity of the field was calculated over a Diameter of a Spherical Volume (DSV) of diameter 20 µm with [292]:

$$\text{Inhomogeneity (ppm)} = \frac{\max(B_0) - \min(B_0)}{B_0} \cdot 10^6. \tag{4.15}$$

For all field and inhomogeneity calculations, the r component was neglected as it was six orders of magnitude smaller than the z component.

4.3.4 Results and discussion

Geometry study

An arbitrary remanent magnetic field value of 0.85 T was chosen for the geometric study with a recoil permeability of 1.05 (corresponding to magnets made of SmCo). The following variations were picked for the geometric parameters: thickness t of 5, 10 and 15 mm, diameter d of 10, 20 and 30 mm), and distances of 20 to 80 mm.

The simulation allowed for computation of the range of B_0 values that each setup can span by varying the distance between the magnets as shown in figure 4.9.

The field inhomogeneity for each parameter combination is reported in figure 4.10. The inhomogeneity is lower for setups with thicker and wider magnets with the width playing the most important role of the two dimensions. Overall, all the values found are in the order of a few ppm, a relatively low number which can be explained by the small size of the region of interest compared to the usual dimensions of classic NMR and EPR spectroscopy. For reference, the field homogeneity is generally about 1 ppb over the active volume in standard NMR spectroscopy [7] and 10 ppm over 1 cm^3 in EPR spectroscopy [293]. In practice, added inhomogeneity is expected from the materials.

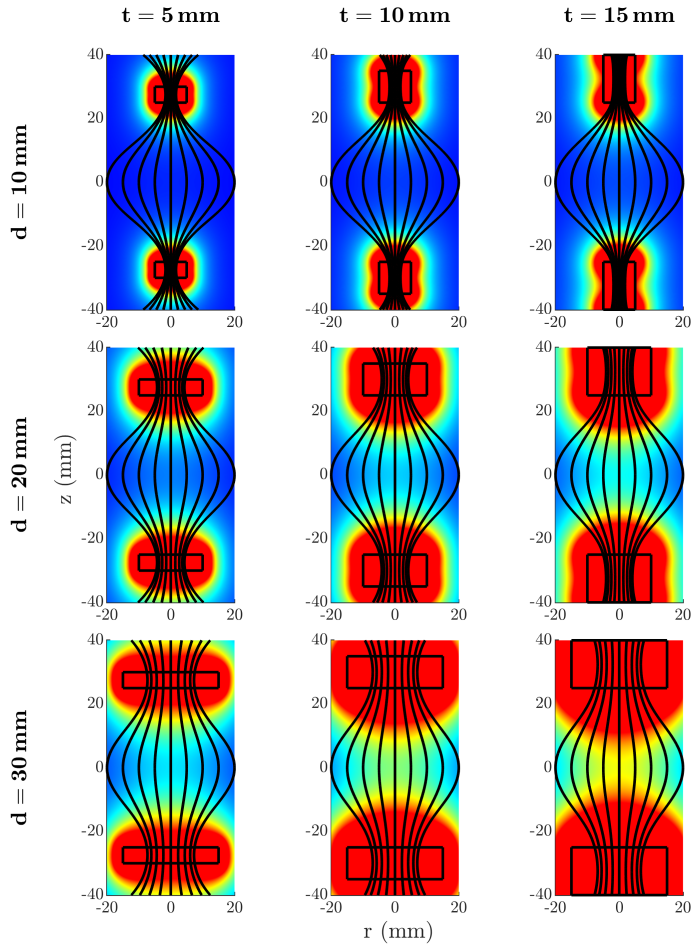


Figure 4.8: 2D centre slices of the magnetic flux density for a fixed distance of 50 mm. The different panels show the combination of thickness values (left to right, 5, 10 and 15 mm) and diameter values (top to bottom, 10, 20 and 30 mm). The black isometric lines were generated with COMSOL Multiphysics 5.5, by taking points at nine fixed distances along $z = 0$.

Material

The first difference between Nd and SmCo is the higher remanence of Nd based magnets. Nd can thus lead to a design with smaller magnets to reduce the footprint of the setup or magnets placed further from each other to increase the setup flexibility. To study this, typical values were chosen for the definitions of the recoil permeability (1.05 for both) and remanence (0.85 T for SmCo and 1.1 T for Nd) [294]. The geometry was fixed with a 20 mm diameter and a 10 mm height. The distance between the magnets was

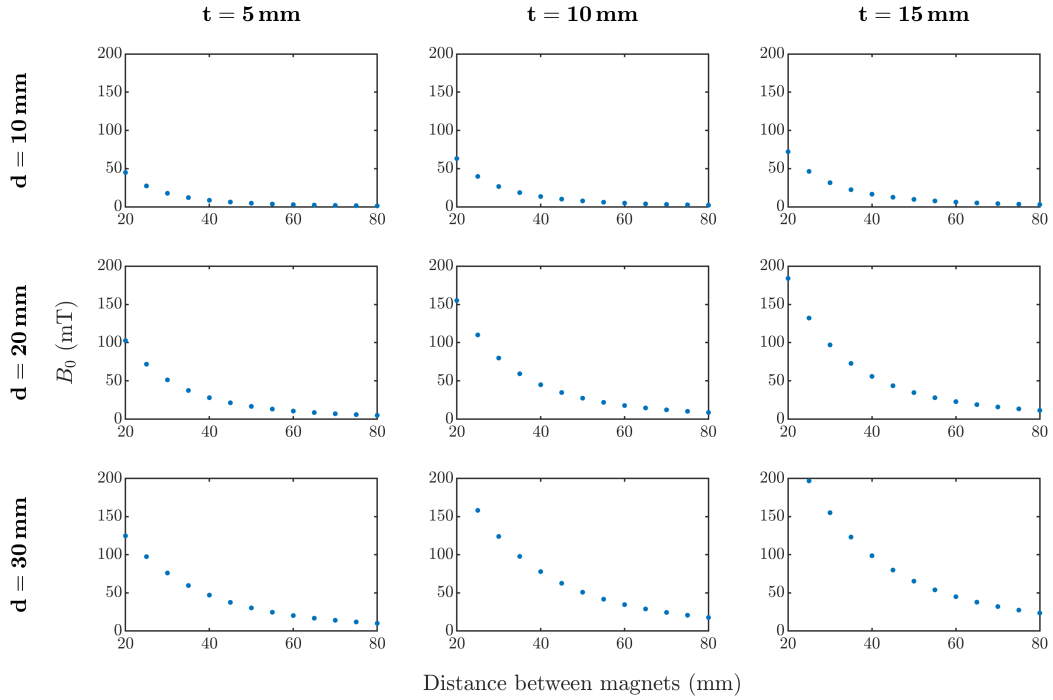


Figure 4.9: Static magnetic field B_0 values for the studied values of geometric parameters, the magnets thickness t and diameter d.

then adjusted to obtain a B_0 of 40 mT. The obtained distance values were 42.24 mm for the SmCo and 47.44 mm for Nd, demonstrating (unsurprisingly) that the Nd based magnets provided indeed a more flexible solution. In addition, the inhomogeneity was lower by about 15% for Nd (3.6 ppm vs 4.1 ppm).

The increase in field density provided by Nd based magnets therefore seemed more attractive but SmCo based magnets are more thermally stable than Nd based magnets. Typical reported Reversible Temperature Coefficient (RTC) is $-0.035\,\%/°C$ for SmCo and $-0.12\,\%/°C$ for Nd [283]. This means that a 1 °C variation is equivalent to an added inhomogeneity of 350 ppm for SmCo and 1200 ppm for Nd which is two orders of magnitude higher than the typical values obtained with FEA. The temperature stability of the material should therefore be clearly prioritised to improve the homogeneity of the field.

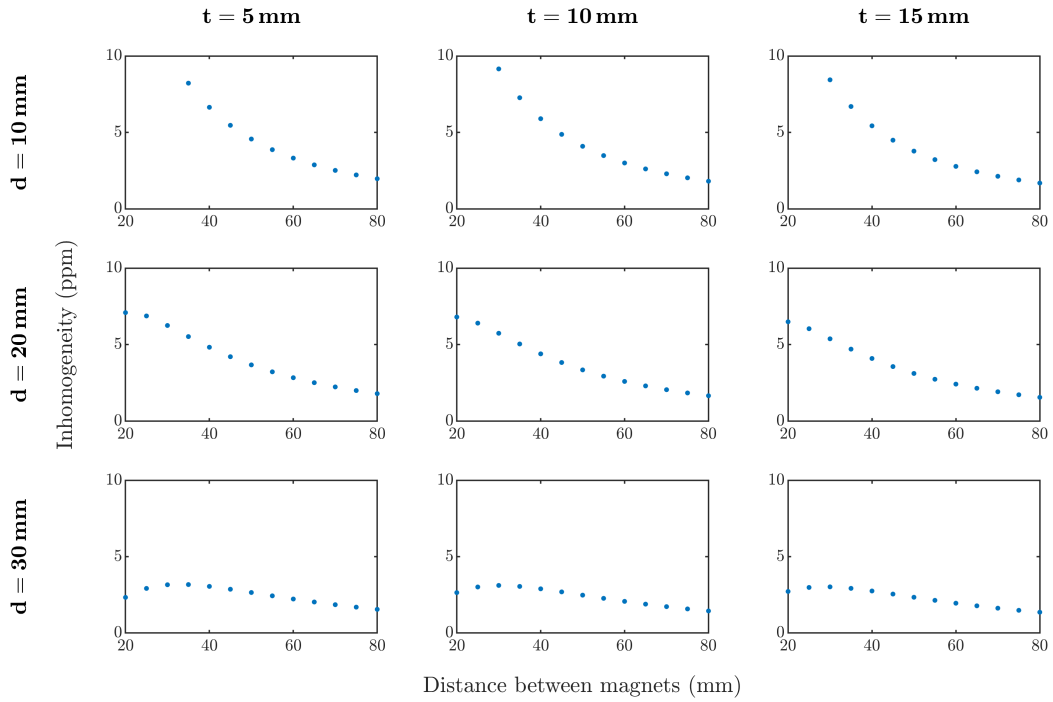


Figure 4.10: Inhomogeneity values for the studied values of geometric parameters, the magnets thickness t and diameter d.

4.3.5 Study conclusion

The gain in temperature stability was considered worth the loss in flexibility and a SmCo based magnet was chosen of diameter 29.21 mm, height 6.35 mm, remanence of 0.86 T and RTC of $-0.03\,\%/°\mathrm{C}$. For further improvement of the static magnetic field homogeneity, control of the environment's temperature appears to of great importance.

4.4 Outlook

For further work in this project, the next task would be to complete the spectrometer construction. In particular, the diamond needs to be mounted, the electronic system requires assembly, and control software should be put in place.

Once the spectrometer is built, a simple project to conduct would be the development of an on-the-fly optimisation tool for NV spectrometers. Thanks to the flexibility of the back-end developed for POISE [203, 243], the optimisation tools seen in chapter 3 can be transferred rather simply to other instruments controllable with Python 3 (which would be the case here with qdSpectro [286]). The resulting package would be easily shareable to other research groups.

Concerning the FEA, the procedure developed here is general and can be used to design a static magnetic field with different constraints or to further study the system. For instance, the full 3D model could be employed to look at the impact of magnets misalignment or the influence of external magnetic perturbations from other components of the spectrometer, albeit at the cost of increased calculation time.

Finally, investigating the application of the frequency-swept pulses seen in chapter 2 or optimal control pulses to improve sensing protocols could also lead to interesting developments, although it would require some hardware changes with the implementation of an AWG.

In the long term, NV centres could be leveraged to routinely conduct magnetic resonance at nano- and micro- scales while staying at room temperature. For example, single protein magnetic resonance [295], or nanoscale imaging measurements [296, 297] would lead to major breakthroughs in biology as many important, but not yet understood, processes happen at such scales and close to room temperature.

Summary

In this thesis, chapter 1 first introduced the necessary NMR and EPR concepts for the understanding of the proposed advances.

In chapter 2, the design of some of the most frequently encountered frequency-swept pulses and sequences were first detailed with simple strategies to further apply these sequences and create new ones. Thus, the application of a state-of-the-art scheme for broadband B_1-tolerant excitation, the CHORUS sequence, was described for EPR spectroscopy, with experimental demonstrations of its effectiveness. Subsequently, new frequency-swept pulse sequences were proposed in the context of liquid-state NMR. First, reusing the CHORUS sequence as an excitation block, a new broadband B_1-tolerant CPMG was proposed: CHORUS-CPMG. Then, the challenge of homonuclear J-coupling modulation, which builds up during the long frequency-swept pulse sequence, was addressed by proposing a new perfect-echo sequence with chirped pulses: PRO-CHORUS. Finally, some of the basic frequency-swept pulse schemes were revisited with the concept of pulse superposition to reduce the sequence durations by 25-40%. All new sequence presentations were supported by simulation and experimental data.

In chapter 3, ESR-POISE was introduced as a new tool to conduct on-fly-optimisation of experimental parameters in EPR spectroscopy with ease. Such software has the potential to offer considerable time gains of valuable instrumental time and make EPR spectroscopy more accessible. The capabilities of ESR-POISE were first demonstrated with simple automation of standard parameters adjustments: signal phase, pulse phases, static magnetic field. These were even appended in a single script ex-

ecution, allowing for full automation of setup procedures. Then, multiple parameter optimisations were shown to be particularly efficient compared to manual adjustment done with a grid-based search of all the parameters combinations. The flip angle of a Hahn-echo sequence was thus optimised and the calibration of CHORUS proposed in chapter 2 revisited with a speed gain of an order magnitude. Afterwards, examples of user-defined advanced parameters optimisation illustrated the versatility of the ESR-POISE package. The pump pulse of a 4p-DEER sequence was automatically adjusted and a new method to compensate for hardware limitations was proposed, with yet another improvement of the CHORUS sequence implementation.

In chapter 4, an entirely new research direction for magnetic resonance methods developments was investigated. Thanks to the use of quantum sensors, different forms of magnetic resonance detection have indeed emerged. Here, the NV centres, which have been used to conduct magnetic resonance at spatial scales never reached before, was at the centre of a new spectrometer construction. The design of the spectrometer was first detailed system by system. Then, FEA was used for simulations to inspect more closely the choice of permanent magnets to generate the static magnetic field.

For future work (and more generally), as highlighted in the respective outlook sections of each chapter, it is believed that transfer of ideas between projects and domains could lead to the most interesting developments of the techniques presented here.

Appendices

Appendix A
Software packages for FS pulse sequence design

A.1 Pulse generation in MATLAB with `MRChirpLab`

Presentation

The Magnetic Resonance Chirp toolbox in MATLAB, `MRChirpLab`, allows for the generation, simulation, and exportation of pulse shapes. The software was tested with MATLAB versions from going from 2019a to 2020b.

The software follows a functional programming approach where each tool is contained in a function. Three categories of functions are grouped in the following directories:

- `MRchirp`, for individual pulses
- `Sequences`, to combine individual pulses in sequences
- `Magnetization`, to simulate pulse and pulse sequence effects

The functions are located in the folder `functions`, contained in the parent folder `MRChirpLab` of the source code.

The functions can be by used by installing the module with the following steps:

- Downloading the code from GitHub [188].
- Adding the unzipped folder `functions` and its subfolders to the MATLAB path (`Home→Set Path→Add with Subfolders`).

Note that an optimiser is necessary for phase optimisation functionalities, for example `FMINLBFGS` [298].

Most functions contain a series of tests for the input variables which are grouped in functions named `grumble()`, in a similar fashion to SPINACH [17]. A lot of functions

also have a companion test function with a name of the type `function_name_test()`, also useful as examples. All functions have documentation which can be accessed with the MATLAB command `help`. In addition, the directory `Examples` contains some illustrations of the tool uses.

To shown an example of application, the output from the code generating the compressed version of CHORUS, as originally published [97], can be duplicated using the function `exc_3fs()` from `Sequences` with:

```
% sequence required parameters
par.t90min = 500e-6;                    % excitation pulse minimum duration (s)
par.t180min = 1000e-6;                  % refocusing pulse minimum duration (s)
par.bw = 300e3;                         % bandwidth (Hz)
par.tres = 0.5e-6;                      % time resolution (s)

% sequence optional parameters
par.phase_polynomial_fitting = true;  % phase correction
par.polyfit_degree = 10;
par.display_result = true;              % display simulation and correction

% sequence optional pulses parameters
par.pulse_param.amp = "sinsmoothed"; % quartersine smoothing
par.pulse_param.sm = 10;              % smoothing factor (here 10%)

chorus = exc_3fs(par);                % sequence creation

% export shapes to be input on the spectrometer
seq_TopSpin_shape_files(chorus, 'chorus_demo', path)
```

List of functions

`MRChirp`

`MRchirp()`

Returns a structure containing the different properties of a FS pulse

`hardpulse()`

Generates a hard pulse of duration tp and flip angle alpha

`plot_pulse()`

Plots the cartesian component of one pulse or several pulses contained in the structure pulse

`pulse_modif()`

Modifies the property of a FS pulse

`pulse_delta_f_correction()`

Modifies the frequency offset of a pulse

`pulse_phase_correction()`

Adds a phase correction to a pulse

`pulse_sum()`

Creates a pulse from the sum of 2 pulses' Cartesian coordinates

`pulse_TopSpin_format()`

Creates a matrix from a pulse structure in the format of a TopSpin pulse shape

`pulse_TopSpin_file()`

Creates and saves the pulse shape in a shape file for use with TopSpin

`pulse_Xepr_format()`

Creates a matrix from a pulse structure in the format of an Xepr pulse shape

`pulse_Xepr_shape_file()`

Creates and saves the pulse shape in a .shp file for Xepr use

`pulse_resonator_easyspin()`

Makes the pulse compensate for resonator effects with the resonator function from EasySpin

`tp_w1_bw_Q()`

Computes the missing parameter of the equation `2*pi*tp*w1^2 = bw*Q` for a linear chirp

`w1max_TBP_compression()`

Returns minimum acceptable duration of a linear chirp for a given maximum amplitude and minimum TBP

`w1max_TBPmin_MRChirp()`

Returns minimum acceptable duration of a frequency-swept pulse for a given maximum amplitude and minimum TBP

Sequences

`seq_add_pulse()`

Adds a pulse at the end of a sequence

`seq_add_delay()`

Adds a delay in a sequence

`polyfit_ph()`

Computes the phase correction to obtain a uniform phase with a polynomial fitting

`plot_seq()`
  Plots the components of a sequence in one figure
`seq_pulses_disp()`
  Displays basic information about the sequence pulses
`seq_param2txt()`
  Creates a file text saving different properties of the sequence
`seq_TopSpin_shape_files()`
  Saves a sequence pulses as TopSpin shape files in a directory
`seq_Xepr_shape_files()`
  Saves a sequence pulses as Xepr shape files in a directory
`phase_cycle_receiver()`
  Computes the receiver phase cycle for a given coherence transfer pathway
`seq_resonator_easyspin()`
  Makes the sequence pulses compensate for resonator effects with the function resonator from EasySpin
`seq_sum_component()`
  Returns a the component of a sequence in one vector with its corresponding time vector

`refocusing`

`ref_2fs()`
  Creates a refocusing pulse sequence with 2 FS pulses
`ref_3fs()`
  Creates a refocusing pulse sequence with 3 FS pulses

`excitation`

`exc_2fs()` Creates a double FS pulse sequence for excitation
`exc_3fs()` Creates a triple FS pulse sequence for excitation

`cpmg`

`chorus_cpmg()`
  Creates a CHORUS-CPMG pulse sequence
`KB_cpmg()`
  Creates a KB-CPMG pulse sequence

`perfect_echo`

`prochorus()`
  Creates a perfect echo chorus (PROCHORUS) pulse sequence

`overlap`

`chorus_sum()`
  Creates an overlapped version of `exc_3fs`

`doublechirp_sum()`
Creates an overlapped version of `exc_2fs`

`perfect_echo`

`ref_3chirps_sum()`
Creates an overlapped version of `ref_3fs`

`seq_sum_2TopSpin()`
Saves a sequence pulses as TopSpin shape files in the current directory

`hard`

`hard90()`
Creates a sequence with a single hard 90° pulse

`hard_spinecho()`
Creates a spin echo sequence with hard pulses $90^\circ_x - 180^\circ_y$

`hard_perfectecho()`
Creates a perfect echo sequence with hard pulses

`Magnetization`

`Rx()`
Returns the rotational matrix for a specified angle around the x-axis

`Ry()`
Returns the rotational matrix for a specified angle around the y-axis

`Rz()`
Returns the rotational matrix for a specified angle around the z-axis

`Rrod()`
Returns the rotational matrix associated with a point of a pulse (or segment of the pulse for FS and/or AM pulses)

`magn_calc_rot()`
Calculates the magnetisation at an end time after applying a list of pulses

`magn_calc_rot_full()`
Calculates the magnetisation over a time vector after applying a list of pulses

`magn_calc_rot_sum()`
Calculates the magnetisation at an end time by summing and applying a list of pulses (allows to use phase cycling with pulse sums)

`magn_phase()`
Returns the phase of the magnetisation as a vector

`plot_magn()`
Displays the magnetisation components at specified offsets

A.2 Pulse generation in PYTHON with `mrpypulse`

Mr. Py (as in PYTHON or π-pulse) Pulse is a toolbox to generate, simulate and export pulse shapes with PYTHON. The software was tested with PYTHON versions going from 3.6 up to 3.10, and essentially emulates MRChirpLab, although currently with less functionalities. In particular, `mrpypulse` still relies on orthogonal rotational matrices for simulation and only has one sequence.

The software follows an Object-Oriented Programming (OOP) approach where the tools are contained in objects and methods of said objects. The package `mrpypulse` is organised into three main modules:

- `pulse` for creation and manipulation of pulses
- `magnetization` for simulation of pulses effect on magnetisation
- `sequence` for creation and manipulation of sequence of pulses

Figure A.1 shows a Unified Modelling Language (UML) diagram which gives an overview of the package organisation.

The package can be installed easily with `pip` using `pip install mrpypulse`. The source code is hosted on GitHub [248].

Tests were written in parallel of the main code development and can be run easily using the module `pytest` with the following command to be run inside the top-level directory of `mrpypulse`: `pytest tests\`. All function contain extensive documentation which can be consulted with the function `help()` from PYTHON. In addition, examples of applications are contained in the root directory of the package under `examples`.

To demonstrate an example of application, the output from the code generating the compressed version of CHORUS, as originally published [97], can be duplicated using the class `Exc_3fs()` from `mrpypulse.sequence` with:

```
from mrpypulse import sequence as seq

# sequence required parameters
t90min = 500e-6       # excitation pulse minimum duration (s)
t180min = 1000e-6     # refocusing pulse minimum duration (s)
bw = 300e3            # bandwidth (Hz)
tres = 0.5e-6         # time resolution (s)

# sequence creation
chorus = seq.Exc_3fs(t90min, t180min, bw, tres, polyfit=True,
                     polyfit_args={"deg": 10}, plot=True,
                     pulse_args={"sm": 10})

chorus.seq2topspin() # export shapes to be input on the spectrometer
```

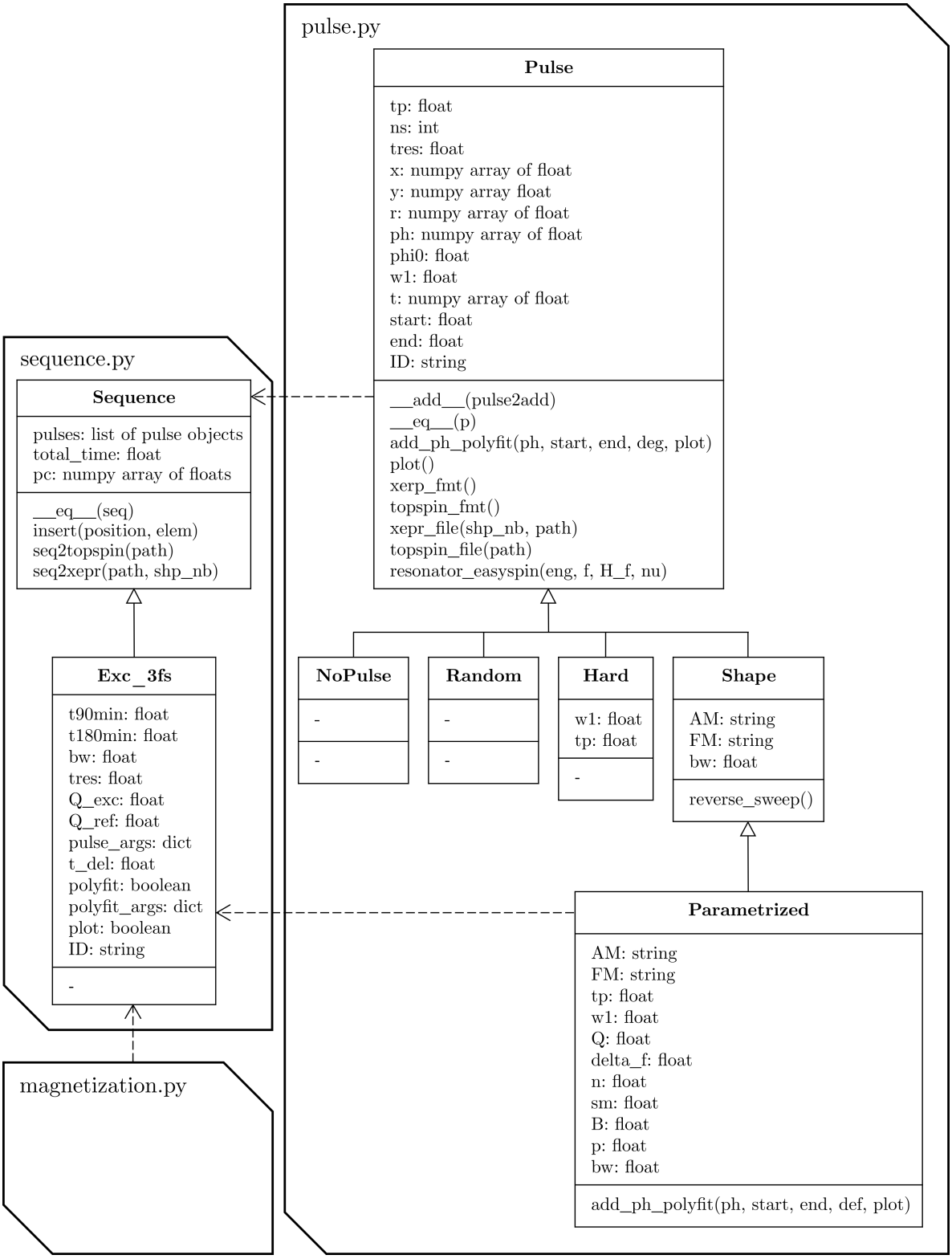


Figure A.1: Combination of module and class UML diagrams of the module `mrpypulse`

Appendix B

B_1-sensitivity maps

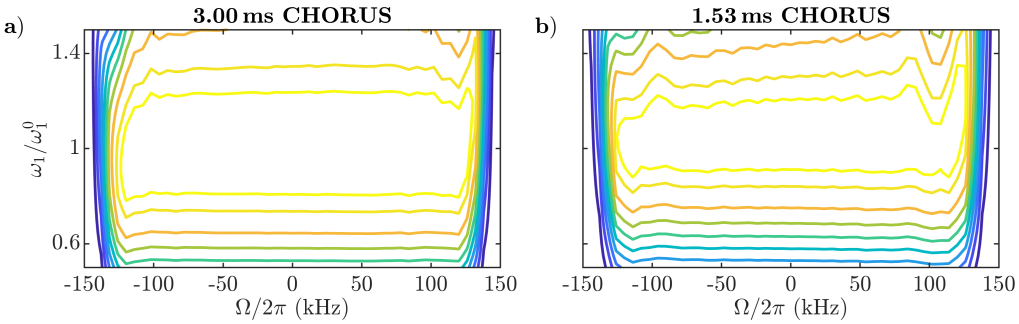


Figure B.1: Simulated B_1-sensitivity maps (highest contour line at 95%) for CHORUS sequences of total duration a) 3 ms and, b) 1.53 ms. These sequences are from the main text, see figure 2.20.

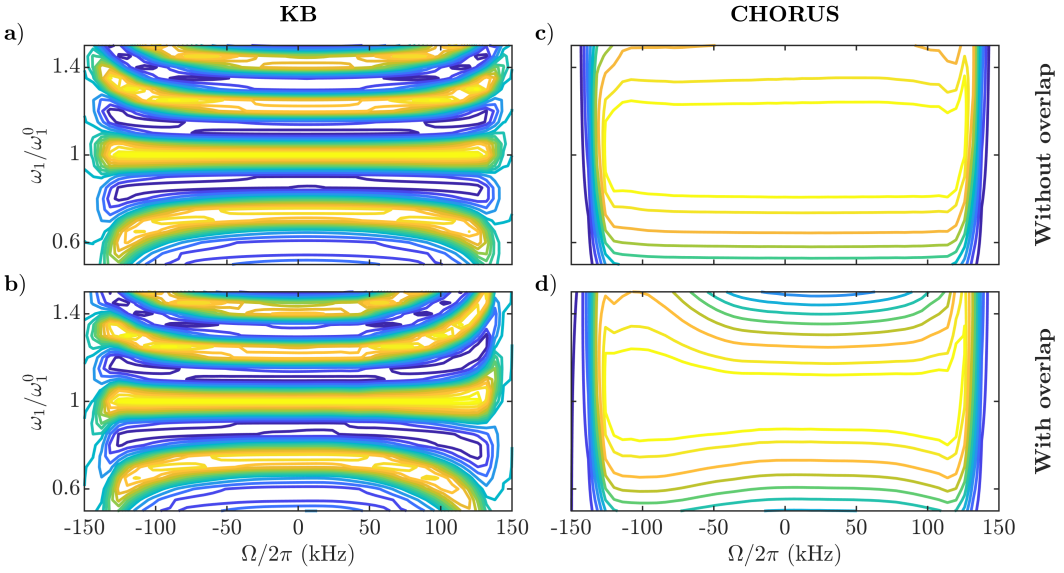


Figure B.2: Simulated B_1-sensitivity maps (highest contour line at 95%) for chirped pulse sequences: KB, a) without overlap and b) with $0.8\tau_{\text{ref}}$ overlap, and for the chirped pulse sequence CHORUS c) without overlap and c) with $0.5\tau_{\text{ref}}$ overlap. These sequences are from the main text, see figures 2.25a, b, c, and d.

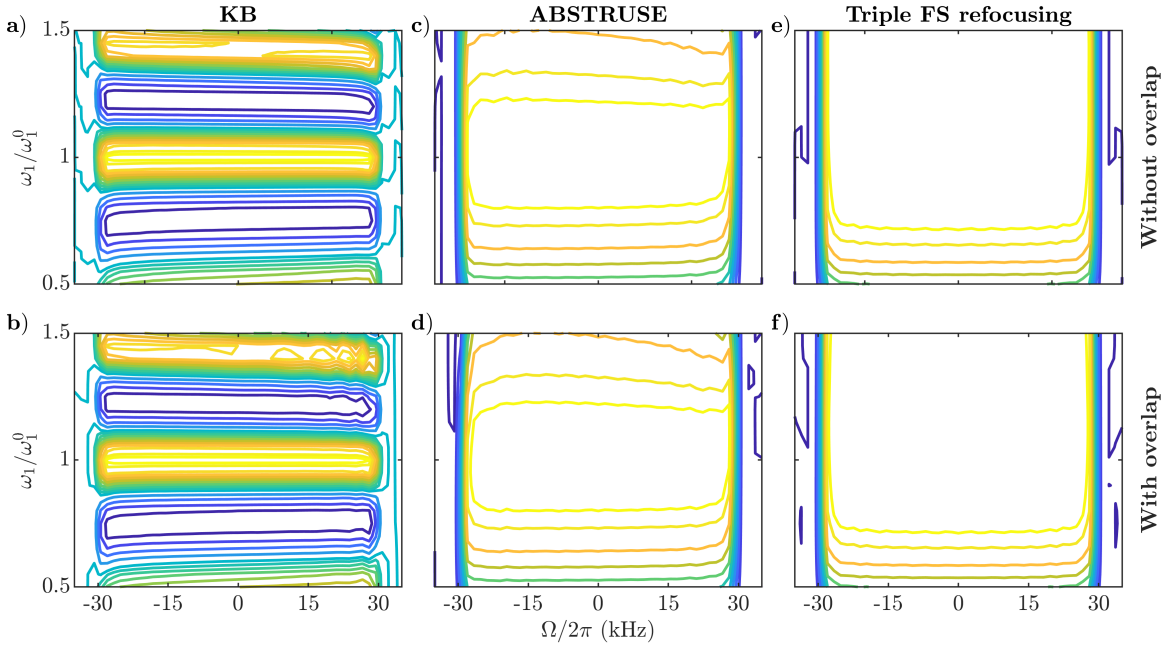


Figure B.3: Simulated B_1-sensitivity maps (highest contour line at 95%) for HS pulse sequences, KB, a) without overlap and b) with $0.8\tau_{\text{ref}}$ overlap, ABSTRUSE, c) without overlap and d) with $0.5\tau_{\text{ref}}$ overlap, and triple-refocusing, d) without overlap and e) with $0.5\tau_{\text{ref}}$ overlap. These sequences are from the main text, see figures 2.25g, h, k, l, i, and j.

Appendix C
Optimal control pulse in ESR spectroscopy

C.1 Background

Pulses can be designed by optimal control theory by letting an optimiser search for the controls of the pulse (e.g. Cartesian coordinates seen in chapter 2) which gives the closest result to a targeted state. Despite their popularity for designing broadband and B_1-tolerant pulses [165–171], there are very few investigation of their use in ESR spectroscopy [122, 244]. This is mainly due to the strong hardware constraints which affect their waveform and its effect on the spin system. In this appendix, a focus is made on the results from an excitation pulse generated with the Efficient Spin Control using Analytical Lie Algebraic Derivatives (ESCALADE) algorithm [299].

C.2 Materials and methods

The ESCALADE $\pi/2$-pulse was generated with the code available in the literature [299]. The algorithm was set up with a random guess as a starting point, a 100 spins spread across a targeted bandwidth of 300 MHz, a maximum amplitude of 50.9 MHz (36.0 MHz on each channel control), a pulse duration of 300 ns with 480 points, and 31 points equally spaced along $\pm$ 20% of B_1 inhomogeneity. The optimisation was stopped after 10000 iterations, reaching a fidelity of -0.98.

For comparison, the CHORUS sequence with the parameters from table 2.2 and table 2.3 was used.

All pulses were implemented with a 0.625 ns time resolution. A 4-step phase cycle (CYCLOPS) was applied on the ESCALADE optimal control pulse. The pulse ampli-

tude was first setup by sweeping its input amplitude and keeping the result with the maximum signal.

A Bruker BioSpin Elexsys II E580 spectrometer set up at X-band (9.45 GHz) served for acquiring experimental excitation profiles with a x-LiPc sample.

The hardware, sample, CHORUS implementation, and the procedure used to get the experimental excitation profiles were similar to the ones used in chapter 2 and are therefore described with more details in subsection 2.4.2.

C.3 Results

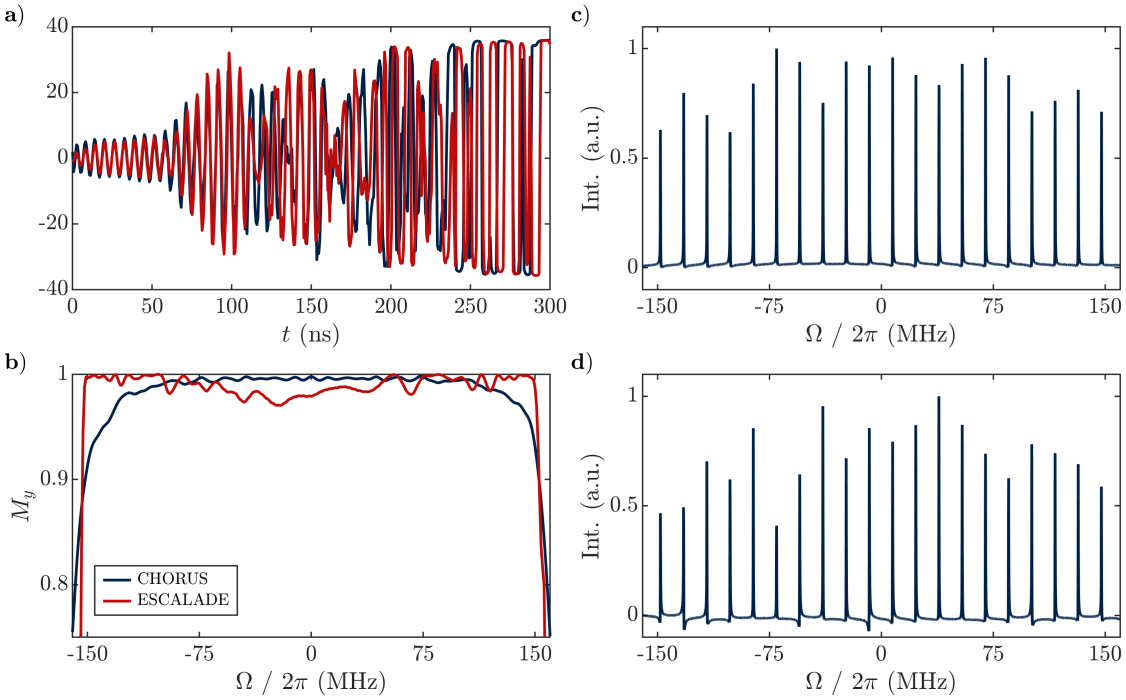


Figure C.1: ESCALADE excitation pulse results: a) Cartesian representation of the excitation pulse waveform generated by ESCALADE, b) its simulated excitation profile, compared with simulated results from the CHORUS sequence. Experimental profiles for the same c) ESCALADE pulse and d) CHORUS sequence. For better visualisation, only the top 25% of the simulated excitation profiles is shown.

Figure C.1a presents the waveform obtained by the optimisation. Despite the promising simulations results from figure C.1b, the ESCALADE excitation pulse pro-

duces much worse experimental results as can be observed on figures C.1c and d.

While the pulse presents some tolerance to B_1 inhomogeneities, the adiabatic pulses of CHORUS present a B_1 tolerance which only degrades itself progressively, without an imposed strong threshold. In addition, the waveform of the optimal control pulse is irregular and such sudden jump in amplitude or phase are more susceptible to the limitations on pulse emission.

C.4 Outlook

The optimal control pulse developed here cannot be taken from the computer to EPR hardware as it is. In general, the following would need to be addressed to successfully apply an optimal control pulse in EPR spectroscopy:

- The dead time, either by including it in the optimisation [300], or by using several pulses [221], which could even result in possible gains from cooperation of these [301]
- The pulse generation limitations from the hardware, for instance by posing a smoothing constraint on the pulse waveform [244].
- The strong B_1 inhomogeneities, for example by including the transfer function effect; either through an experimental feedback loop optimisation as already proposed in ESR [129, 244], or by including a transfer function measurement to modify the pulse shape [122, 124, 125] (could also be included in the offline optimisation). An additional idea would be to generate adiabatic shapes with optimal control theory [302].

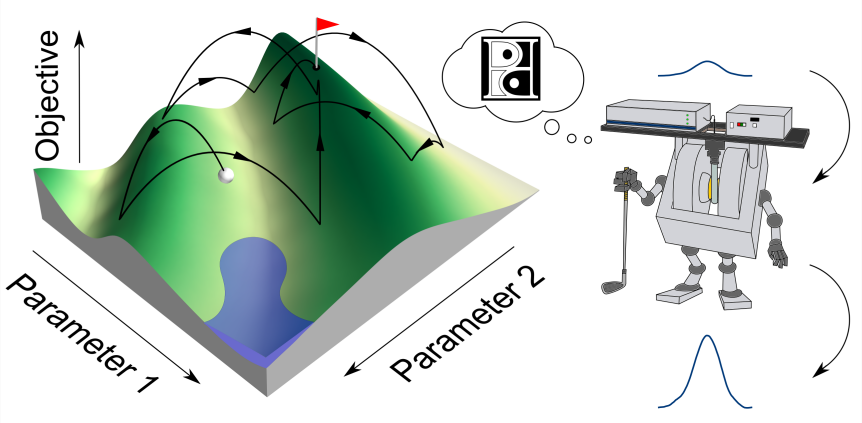
While optimal control can appear as a black box, addressing these challenges efficiently could actually open the door to new experimental solutions thanks to the potential of the algorithms to include more than Zeeman interactions during the optimisation process [167, 303], to optimise for specific experimental conditions [304], or even the possibility of optimising a whole sequences goal instead of individual pulses [305].

Appendix D

ESR-POISE user Guide

D.1 Presentation

ESR-POISE (Electron Spin Resonance Parameter Optimisation by Iterative Spectral Evaluation) is a Python package for on-the-fly optimisation of ESR parameters in Bruker BioSpin Xepr software.



In here you will find guides on setting ESR-POISE up and using it to optimise ESR applications. Depending on your level of interaction with the software, you may not need to read all of it. For example, if somebody else has already installed and set up some esrpoise scripts for you, you can probably skip to Run an optimisation. You should also skip advanced subsections for your first steps with esrpoise.

For more insight, consult the source code. In particular, have a look at the examples scripts present in the package directory (`esrpoise/examples/`).

Note:
The documentation you are currently reading is for version v1.0.1 of POISE. To check your current version of POISE, type `pip show esrpoise` in terminal.

D.2 Installation

The requirements are:

- **Xepr**. We have tested Xepr versions 2.8b.5
- **Python 3**. ESRPOISE requires a minimum version of **Python 3.6**. (We have tested up to Python 3.8.)

Installing Python 3

This is most easily done by downloading an installer from the official CPython website (`https://www.python.org/downloads/`), or via your package manager (`apt`, `yum` or similar).

On CentOS 7, you would typically need:

```
yum -y install python3
```

You might also need to tkinter with:

```
yum -y install python3-tkinter
```

Note that this creates a `python3` executable, which is independent from the previously installed Python 2 (which can still be invoked with `python`).

A particular issue we faced when setting up POISE was installing Python on CentOS 7 without administrator rights. If you are in this situation, you will have to compile the Python source code, using the following steps:

1. Download the source code for Python 3.7. We used 3.7.11, but anything should work.
2. Download the source code for Tcl/Tk (at least for now, Python needs to be compiled with tkinter for POISE to run successfully).
3. Compile Tcl/Tk, making sure to install it to a user-writable directory (e.g. your home directory).
4. Compile Python, again installing it to your home directory. This step is pretty difficult as there are certain (undocumented) compilation flags which must be passed correctly.

The following series of shell commands (give or take) worked for us, so you could simply run the following:

```
# Download source code
curl -LO https://www.python.org/ftp/python/3.7.11/Python-3.7.11.tgz
curl -LO https://prdownloads.sourceforge.net/tcl/tcl8.6.12-src.tar.gz
curl -LO https://prdownloads.sourceforge.net/tcl/tk8.6.12-src.tar.gz
tar xf Python-3.7.11.tgz
tar xf tcl8.6.12-src.tar.gz
tar xf tk8.6.12-src.tar.gz
# Install tcl/tk
cd tcl8.6.12/unix
./configure --prefix=$HOME/.local/tcltk
make
make install
cd ../../tk8.6.12/unix
./configure --prefix=$HOME/.local/tcltk
make
make install
# Install Python
cd ../../Python-3.7.11/
CPPFLAGS="-I$HOME/.local/tcltk/include" LDFLAGS="-L$HOME/.local/tcltk/lib
↪  -Wl,-rpath,$HOME/.local/tcltk/lib -ltcl8.6 -ltk8.6" ./configure
↪  --prefix=$HOME/.local/python3
↪  --with-tcltk-includes="-I$HOME/.local/tcltk/include"
↪  --with-tcltk-libs="-L$HOME/.local/tcltk/lib"
make
make install
```

One of the tested spectrometer computer also required the installation of `libffi` and `libffi-devel` before being able to `make install`.

You should then have a working installation of Python 3.7 in `~/.local/python3/bin/python`. Note that you should always use this version of Python whenever installing packages: so, it's safer to always use `/path/to/python -m pip install X` rather than just `pip install`.

Naturally, you can place this Python executable first in your `$PATH` in order to avoid having to type out the full path every time, for example by placing the following line:

```
export PATH=~/.local/python3/bin:$PATH
```

inside your `~/.bashrc` or `~/.bash_profile`.

If there are any issues, please get in touch via GitHub or email.

Installing esrpoise

Once Python 3 is installed, you can install POISE using `pip`:

```
python -m pip install esrpoise
```

(replace `python` with `python3` if necessary)

The following Python packages are required, they should get automatically installed with esrpoise if you do not already have them:

- **numpy**
- **XeprAPI**
- **pybobyqa**

Updating POISE

Simply use:

```
python -m pip install --upgrade esrpoise
```

(again replacing `python` with `python3` if necessary). All other steps (including troubleshooting, if necessary) are the same.

Installing from source

If you obtained the source code (e.g. from `git clone` or a GitHub release) and want to install from there, simply `cd` into the top-level `esrpoise` directory and run:

```
python -m pip install .
```

Add `-e` to be able to edit the code. Equivalently you can run:

```
python -m setup.py install
```

Replace `install` with `develop` to edit the code (and use `python3` if necessary).

Installing without Internet

If the computer you are using does not have an Internet connection, then you will need to:

1. Download the POISE source code from GitHub and copy it over to the target computer (`git clone https://github.com/foroozandehgroup/esrpoise`).
2. Install Python by downloading the installer from a different computer and copying it over.

3. On the target computer, install the POISE package locally by navigating to the `esrpoise` directory you copied over and doing `python -m pip install .` (note the full stop at the end).

D.3 Set up an optimisation

Basics

To set up an optimisation, you can to create a small python script which:

- loads an instance Xepr of the XeprAPI,
- calls the function `optimise()` from esrpoise.

with standard parameters

When calling `optimise()`, you should to at least pass:

- the Xepr instance,
- your parameters names, initial values, lower bounds and upper bounds as lists,
- a cost function, which can be imported from the ones present in ESR-POISE (see Cost functions),
- the maximum number of function evaluations (not technically mandatory but set to `0` by default).

Only a handful of Xepr parameters can be accessed through a simple optimisation (see Built-in parameters).

Example of standard parameter optimisation script:

```
from esrpoise import xepr_link
from esrpoise import optimise
from esrpoise.costfunctions import maxabsint_echo

# load Xepr instance
xepr = xepr_link.load_xepr()

# fine adjustment of centre field for bisnitroxide sample at X-band
xbest, fbest, message = optimise(xepr,
                                 pars=['CenterField'],
                                 init=[3450],
                                 lb=[3445],
                                 ub=[3455],
                                 tol=[0.1],
                                 cost_function=maxabsint_echo,
                                 maxfev=20)
```

Note that `xepr`, `pars`, `init`, `lb`, `ub`, and `tol` need to be input in this order, all other parameters are keywords arguments whose order does not matter.

Warning!
Make sure to chose an appropriate tolerance for your instrumentation. For example, delays and pulse duration need to be multiple of 2 ns on our instrument. We therefore must choose a tolerance which is a multiple of 2 ns when optimising those parameters.

with .def file parameters

Optimise parameters from your .def file by indicating their names. In addition to the standard parameter requirements, you should precise:

- the path of your .exp file,
- the path of your .def file.

Example (also note the use of several parameters in lists and the optimiser explicit choice):

```
# .exp and .def files location
location = '/home/xuser/xeprFiles/Data/'
exp_f = location + '2pflip.exp'
def_f = location + '2pflip.def'

# optimisation of pulse length and amplitude
xbest, fbest, message = optimise(xepr,
                                 pars=["p0", "Attenuation"],
                                 init=[8, 5],
                                 lb=[2, 0],
                                 ub=[36, 10],
                                 tol=[2, 0.5],
                                 cost_function=maxabsint_echo,
                                 exp_file=exp_f,
                                 def_file=def_f,
                                 optimiser="bobyqa",
                                 maxfev=20)
```

with user-defined parameters (advanced)

To optimise your own parameters, you should define a callback function, used to set up your parameters. The simplest is to define it in your optimisation script (after the imports and before your script code):

```
def my_callback(my_callback_pars_dict, *mycallback_args):
    """
    Parameters
    ----------
    pars_dict: dictionary
        dictionary with the name of the parameters to optimise as key and
        their value as value
    *mycallback_args
        other possible arguments for callback function
    """
    # user operations and parameters modifications
```

Indicate that your parameter is user-defined by including '`&`' at the start of its name:

```
optimise(Xepr, pars=[... , '&_', ...], ...,
               callback=my_callback, callback_args=my_callback_args)
```

You can pass arguments (as a tuple) to `callback` by using `callback_pars`.

In the following example, we modify a shape parameter (bandwidth `bw` of an HS1 pulse) with the module mrpypulse. First, we import the necessary modules and define the `callback` function:

```
import os
from esrpoise import xepr_link
from esrpoise import optimise
from esrpoise.costfunctions import maxabsint_echo
from mrpypulse import pulse


def shape_bw(callback_pars_dict, shp_nb):

    # getting  bw value from the callback parameters to be optimised
    bw = callback_pars_dict["&bw"]

    # create hyperbolic secant shape bw value
    p = pulse.Parametrized(bw=bw, tp=80e-9, Q=5, tres=0.625e-9,
                           delta_f=-65e6, AM="tanh", FM="sech")

    p.xepr_file(shp_nb)  # create shape file

    # shape path
    path = os.path.join(os.getcwd(), str(shp_nb) + '.shp')

    xepr_link.load_shp(xepr, path)  # send shape to Xepr

    return None
```

Then we can proceed with the optimisation:

```
xepr = xepr_link.load_xepr()

#  HS pulse bandwidth optimisation
xbest, fbest, message = optimise(xepr,
                                 pars=['&bw'],
                                 init=[80e6],
                                 lb=[30e6],
                                 ub=[120e6],
                                 tol=[1e6],
                                 cost_function=maxabsint_echo,
                                 maxfev=120,
                                 nfactor=5,
                                 callback=shape_bw,
                                 callback_args=(7770,))

# NB: '(7770,)' is equivalent to 'tuple([7770])'
```

with user-defined cost function (advanced)

You can define your own cost function and pass it to the function optimise. Your cost function should treat the data from one of your experiment run to return a single number which will be minimised by the optimiser.

We can for example conduct an optimisation on the spectrum with a zero-filling operation (data is here a simple time-domain FID). First, we import the necessary modules and define the cost function:

```
import numpy
from esrpoise import xepr_link
from esrpoise import optimise


def maxabsint(data):
    """
    Maximises the absolute (magnitude-mode) intensity of the spectrum.
    """
    zero_filling = 4*length(data.0.real)
    spectrum = np.fft.fft(data.0.real + 1j * data.0.imag, n=zero_filling)

    return -np.sum(np.abs(spectrum(data)))
```

Then we can proceed with the optimisation:

```
# load Xepr instance
xepr = xepr_link.load_xepr()

# fine adjustment of center field for bisnitroxide sample at X-band
xbest, fbest, message = optimise(xepr,
                                 pars=['CenterField'],
                                 init=[3450],
                                 lb=[3445],
                                 ub=[3455],
                                 tol=[0.1],
                                 cost_function=maxabsint,
                                 maxfev=20)
```

Setup Tips (advanced)

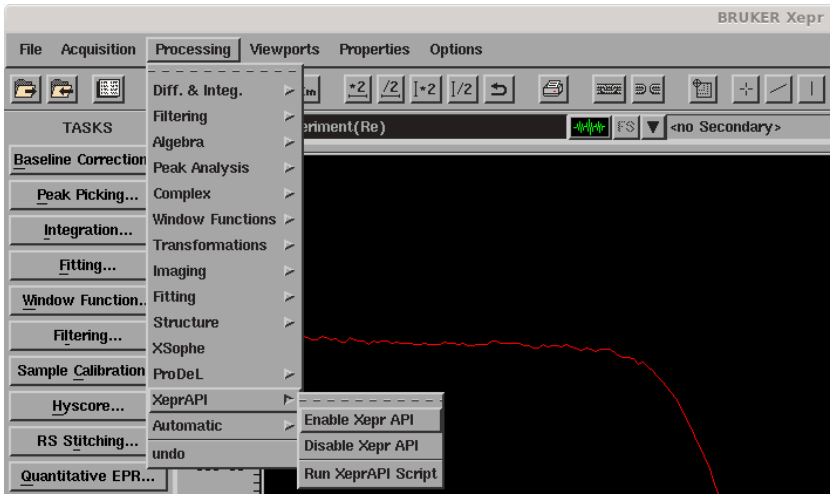
- Put several optimisations in one script.
- Automate your actions by using XeprAPI commands, for example with the functions from `xepr_link.py` and `param_set` from `main.py`
- Reuse the best parameter value(s) from the optimiser with `xbest`.
- Use `callbak` to add user-specific operation at each iteration. You do not need to indicate user-defined parameters, `callback_pars_dict` is sent back empty if no user-defined parameters are found.
- Use `acquire_esr.calls` in your callback function to access the current number of iteration(s).
- Use the parameter `nfactor` of `optimise()` to expand the distance between the first steps of the optimisers, in particular if you have a low tolerance.
- Accelerate you optimisation routine if your .shp, .def and .exp file compile fast enough with `xepr_link.COMPILATION_TIME` (see Compilation)
- When using a single script with functions, be aware of your variables scope.

D.4 Run an optimisation

Procedure

In Xepr:

- Set up your experiment as you would normally do.
- Enable XeprAPI (Processing →XeprAPI →enable XeprAPI).



- Run your experiment once by clicking on play to load it into XeprAPI (can also be done before enabling XeprAPI).

Run your optimisation script in a terminal with (replace `python` with `python3` if necessary):

```
python yourscript.py
```

At each iteration, esrpoise:

- adjusts the parameters to be optimised,
- runs the experiment,
- computes the cost function.

Once `optimise()` is done, you get a set of optimised parameters. These are set up in Xepr but your experiment is not run. You need to run it if you want to have the optimised result loaded in Xepr.

Running tips

- You can interrupt the optimisation with `ctrl+C`. It is recommend to do so while a measurement is running.

- When using .exp and .def file, save them beforehand to avoid getting a warning. Otherwise this warning pauses the optimisation and you need to manually get rid of it at each iteration.
- When running your experiment once to load it in XeprAPI, you can interrupt it by clicking on play again. This is enough to set it up, sparing the time of a full run.

D.5 Built-in parameters

Built-in parameters can have different constraints depending on your spectrometer. Values documented here are just indications. All parameters currently supported are indicated below (in addition to any variable placed in the .def file as seen in Set up an optimisation).

Bridge - Receiver Unit

- `"VideoGain"` (dB), video gain, indicative minimum tolerances: 3 dB, 6 dB
- `"Attenuation"` (dB), high power attenuation, indicative minimum tolerance: 0.01 dB
- `"SignalPhase"` (∼0.129 deg), signal phase, indicative minimum tolerance: 1
- `"TMLevel"` (%), transmitter level, 0 to 100

Bridge - MPFU control

- `"BrXPhase"`, +<x> Phase
- `"BrXAmp"`, +<x> Amplitude
- `"BrYPhase"`, +<y> Phase
- `"BrYAmp"`, +<y> Amplitude
- `"BrMinXPhase"`, -<x> Phase
- `"BrMinXAmp"`, -<x> Amplitude
- `"BrMinYPhase"`, -<y> Phase
- `"BrMinYAmp"`, -<y> Amplitude

These are rounded in Xepr to closest 0.049% (approximately, not linear).

FT EPR Parameters

- `"CenterField"`, field position (G), indicative minimum tolerance: 0.05 G

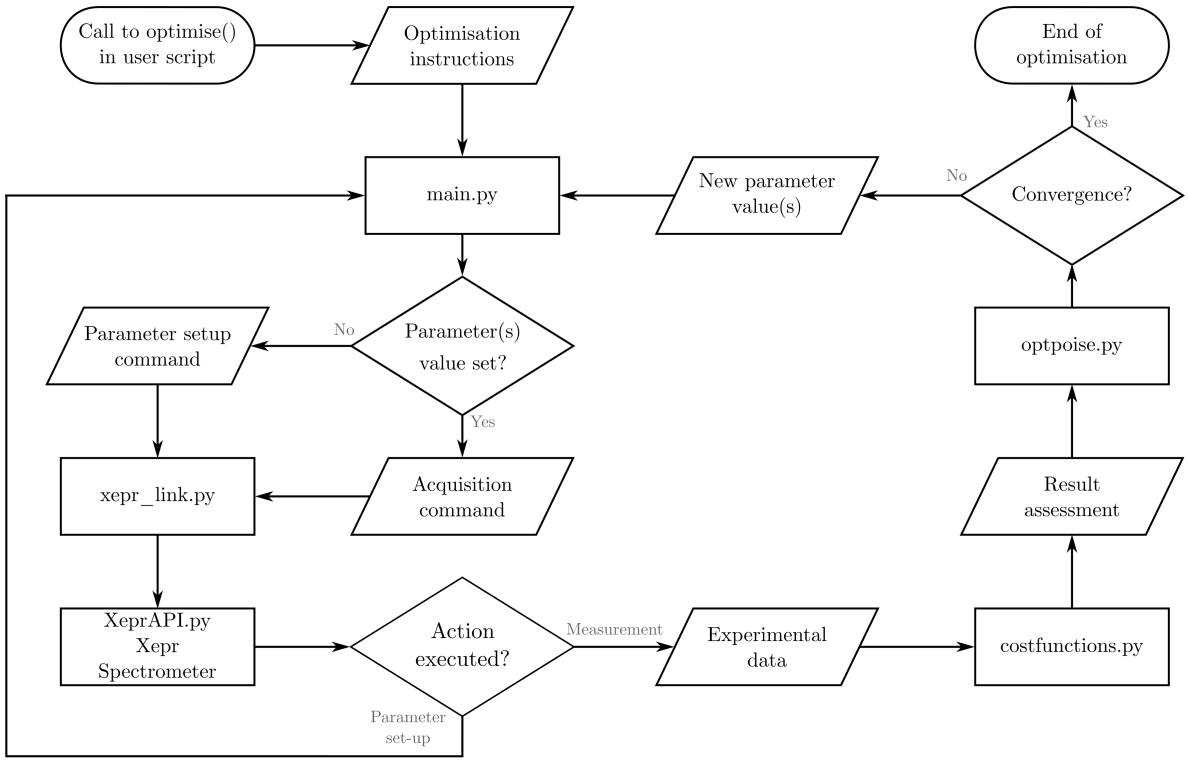
D.6 Modules

Organisation

The esrpoise code is organised into 4 modules:

- `main.py` for the optimisation to take place (set parameters, run the experiment, report results...),
- `xepr_link.py` to handle communication with Xepr,
- `costfunctions.py` which contains standard cost functions,
- `optpoise.py` which contains the necessary for the optimisers (see source code for more details).

Figure D.1: Flowchart of ESR-POISE optimisation with simplified view of the modules' actions



main.py

Contains the main code required for executing an optimisation.

SPDX-License-Identifier: GPL-3.0-or-later

esrpoise.main.**optimise**(*xepr, pars, init, lb, ub, tol, cost_function, exp_file=None, def_file=None, optimiser='bobyqa', maxfev=0, nfactor=10, callback=None, callback_args=None*)

Runs an optimisation.

Parameters:

xepr: XeprAPI.Xepr object
The instantiated Xepr object.

pars: list of str
Parameter names. Parameters starting with the character & are considered user parameters which needs to be modified with the callback function.

init: list of float
Initial value for each parameter.

lb: list of float
Lower bounds for each parameter.

ub: list of float
Upper bounds for each parameter.

tol: list of float
Optimisation tolerances for each parameter.

cost_function: function
A function which takes the data object and returns a float.

exp_file: str, default None
Experiment file (.exp) path to be used for the experiment in Xepr. Required to modify parameters in .def file.

def_file: str, default None
Definition file (.exp) path to be used for the experiment in Xepr. Required to modify parameters in .def file.

optimiser: str from {"nm", "mds", "bobyqa", "brute"}, default "nm"
Optimisation algorithm to use. The options correspond to Nelder-Mead, multidimensional search, BOBYQA, and brute-force search respectively.

maxfev: int, default 0
Maximum number of spectra to acquire during the optimisation. The default of '0' sets this to 500 times the number of parameters.

nfactor: int, default 10

Initial search region relative to tols

callback: function, default None

User defined function called when setting up parameters.

callback_args: tuple, default None

Arguments for callback function

Returns:

xbest: numpy.ndarray

Numpy array of best values found. First element corresponds to the first parameter optimised, etc.

fbest: float

Value of the cost function at x = xbest.

message: str

A message indicating why the optimisation terminated.

Notes:

Returns:

To quit the optimisation, simply type 'ctlr+C' in the terminal. It is recommended to do so during an acquisition phase of Xepr to avoid Xepr crashes.

Once the optimisation is done, the best parameters found are set up in Xepr but the experiment is not run.

esrpoise.main.**acquire_esr**(*x, cost_function, pars, lb, ub, tol, optimiser, xepr, exp_file=None, def_file=None, callback=None, callback_args=None*)

This is the function which is actually passed to the optimisation function as the "cost function", and is responsible for triggering acquisition in Xepr.

Briefly, this function does the following:

Returns np.inf immediately if the values are outside the given bounds.

Otherwise, prints the values to stdout, which triggers acquisition by the frontend.

Waits for the frontend to pass the message "done" back, indicating that the spectrum has been acquired and processed.

Calculates the cost function using the user-defined cost_function().

Performs logging throughout.

Parameters:

x: ndarray

Scaled values to be used for spectrum acquisition and cost function evaluation.

pars: list of str

Parameter names. Parameters starting with the character & are considered user parameters which needs to be modified with the callback function.

lb: list of float
Lower bounds for each parameter.
ub: list of float
Upper bounds for each parameter.
tol: list of float
Optimisation tolerances for each parameter.
optimiser: str from {"nm", "mds", "bobyqa", "brute"}, default "nm"
Optimisation algorithm to use. The options correspond to Nelder-Mead, multidimensional search, BOBYQA, and brute-force search respectively.
xepr: XeprAPI.Xepr object
The instantiated Xepr object.
cost_function: function
A function which takes the data object and returns a float.
exp_file: str, default None
Experiment file (.exp) path to be used for the experiment in Xepr. Required to modify parameters in .def file.
def_file: str, default None
Definition file (.exp) path to be used for the experiment in Xepr. Required to modify parameters in .def file.
callback: function, default None
User defined function called when setting up parameters.
callback_args: tuple, default None
Arguments for callback function

Returns:

cf_val: float
Value of the cost function.

esrpoise.main.**param_set**(*xepr, pars, val, tol, exp_file=None, def_file=None, callback=None, callback_args=None*)

Sets a variety of parameters in Xepr.

Parameters:

xepr: XeprAPI.Xepr object
The instantiated Xepr object.
pars: list of str
Parameter names. Parameters starting with the character & are considered user parameters which needs to be modified with the callback function.
val: list of floats or ndarray
values of the parameters

tol: list of float
Optimisation tolerances for each parameter.
exp_file: str, default None
Experiment file (.exp) path to be used for the experiment in Xepr. Required to modify parameters in .def file.
def_file: str, default None
Definition file (.exp) path to be used for the experiment in Xepr. Required to modify parameters in .def file.
callback: function, default None
User defined function called when setting up parameters.
callback_args: tuple, default None
Arguments for callback function

Returns:

None

esrpoise.main.**round2tol_str**(*values, tols*)

Rounds values to closest multiple of tolerance.

Parameters:

values: list or ndarray
values to round
tol: list or ndarray
values tolerances

Returns:

values_str
rounded values as a list of strings

xepr_link.py

esrpoise.xepr_link.**load_xepr**()

Initialises the Xepr module and return the Xepr object thus created.

Parameters:

None

Returns:

xepr: XeprAPI.Xepr object
The instantiated Xepr object, used for communication with the Xepr software.

esrpoise.xepr_link.**load_exp**(*xepr, exp_file*)

Loads and compiles an Xepr experiment file.

Parameters:

xepr: XeprAPI.Xepr object
The instantiated Xepr object.
exp_filestr
The Xepr experiment file (the full path with .exp extension).

Returns:
None

esrpoise.xepr_link.**load_def**(*xepr, def_file*)
Loads and compiles an Xepr definition file.

Parameters:
xepr: XeprAPI.Xepr object
The instantiated Xepr object.
def_file: str
Name of the Xepr definition file (full path with .def extension).

Returns:
None

esrpoise.xepr_link.**modif_def**(*xepr, def_file, var_name, var_value*)
Modifies definitions by modifying the .def file and reloading it.

Parameters:
xepr: XeprAPI.Xepr object
The instantiated Xepr object.
def_file: str
Name of the Xepr definition file (full path with .def extension).
var_name: list of strings
Variable names as named in the .def file.
var_value: list of strings
List of variable values to be input.

Returns:
None

esrpoise.xepr_link.**load_shp**(*xepr, shp_file*)
Loads and compiles an Xepr shape file.

Parameters:
xepr: XeprAPI.Xepr object
The instantiated Xepr object.
shp_file: str
Shape file name (full path, including .shp extension).

Returns:

None

esrpoise.xepr_link.**run2getdata_exp**(*xepr, SignalType=None, exp_name=None*)

Runs an experiment and gets the data from it.

Parameters:

xepr: XeprAPI.Xepr object
The instantiated Xepr object.

SignalType: str, by default None
To change the signal type (pick from {"TM", "Signal", "RM"})

exp_name: str, by default None
The name of the experiment to run, usually "AWGTransient" for the Signal or "AWG_1pulseSHP" for the TM.

Returns:

data: XeprAPI.Dataset
The data retrieved from Xepr. Attributes of interest are:
- data.X: the X-abscissa values of the dataset
- data.O: complex-valued numpy.ndarray of the signal
- data.O.real: real part of the signal
- data.O.imag: imaginary part of the signal

esrpoise.xepr_link.**reset_exp**(*xepr*)

Copies the current experiment and uses it to replace the current experiment.
Needed to reset the AWG after 114 sequential shape load and run.

Parameters:

xepr: XeprAPI.Xepr object
The instantiated Xepr object.

Returns:

None

costfunctions.py

Functions linked to the spectrum (frequency domain data):

esrpoise.costfunctions.**spectrum**(*data*)

Computes a spectrum from Xepr standard time domain data.

Parameters:

data: XeprAPI.Dataset
data retrieved from Xepr

Returns:

spectrum: ndarray
spectrum computed from time domain data

`esrpoise.costfunctions.`**`minabsint`**`(`*`data`*`)`
Minimises the absolute (magnitude-mode) intensity of the spectrum.

`esrpoise.costfunctions.`**`maxabsint`**`(`*`data`*`)`
Maximises the absolute (magnitude-mode) intensity of the spectrum.

`esrpoise.costfunctions.`**`minrealint`**`(`*`data`*`)`
Minimises the intensity of the real part of the spectrum. If the spectrum has negative peaks this cost function will try to maximise those.

`esrpoise.costfunctions.`**`maxrealint`**`(`*`data`*`)`
Maximises the intensity of the real part of the spectrum.

`esrpoise.costfunctions.`**`minimagint`**`(`*`data`*`)`
Minimises the intensity of the imaginary part of the spectrum. If the spectrum has negative peaks this cost function will try to maximise those.

`esrpoise.costfunctions.`**`maximagint`**`(`*`data`*`)`
Maximises the intensity of the real part of the spectrum.

`esrpoise.costfunctions.`**`zerorealint`**`(`*`data`*`)`
Tries to get the intensity of the real spectrum to be as close to zero as possible. This works by summation, so dispersion-mode peaks will not contribute to this cost function (as they add to zero).

`esrpoise.costfunctions.`**`zeroimagint`**`(`*`data`*`)`
Tries to get the intensity of the imaginary spectrum to be as close to zero as possible.

Cost functions linked to the echo (time domain signal):

`esrpoise.costfunctions.`**`minabsint_echo`**`(`*`data`*`)`
Minimises the absolute (magnitude-mode) intensity of the echo.

`esrpoise.costfunctions.`**`maxabsint_echo`**`(`*`data`*`)`
Maximises the absolute (magnitude-mode) intensity of the echo.

`esrpoise.costfunctions.`**`minrealint_echo`**`(`*`data`*`)`
Minimises the maximum intensity of the real part of the echo.

`esrpoise.costfunctions.`**`maxrealint_echo`**`(`*`data`*`)`
Maximises the maximum intensity of the real part of the echo.

`esrpoise.costfunctions.`**`minimagint_echo`**`(`*`data`*`)`
Minimises the maximum intensity of the imaginary part of the echo.

esrpoise.costfunctions.**maximagint_echo**(*data*)
Maximises the maximum intensity of the real part of the echo.

esrpoise.costfunctions.**zerorealint_echo**(*data*)
Tries to get the intensity of the real part of the echo to be as close to zero as possible.

esrpoise.costfunctions.**zeroimagint_echo**(*data*)
Tries to get the intensity of the imaginary part of the echo to be as close to zero as possible.

esrpoise.costfunctions.**maxrealint_plus_zeroimagint_echo**(*data*)
Tries to get the intensity of the imaginary part of the echo to be as close to zero as possible.

esrpoise.costfunctions.**minabsmax_echo**(*data*)
Minimises the absolute (magnitude-mode) maximum of the echo.

esrpoise.costfunctions.**maxabsmax_echo**(*data*)
Maximises the absolute (magnitude-mode) maximum of the echo.

esrpoise.costfunctions.**minrealmax_echo**(*data*)
Minimises the maximum of the real part of the echo.

esrpoise.costfunctions.**maxrealmax_echo**(*data*)
Maximises the maximum of the real part of the echo.

esrpoise.costfunctions.**minimagmax_echo**(*data*)
Minimises the maximum of the imaginary part of the echo.

esrpoise.costfunctions.**maximagmax_echo**(*data*)
Maximises the maximum of the imaginary part of the echo.

Other cost functions:

esrpoise.costfunctions.**max_n2p**(*data*)
Maximises $\eta_{2\mathrm{p}}$ parameter for DEER trace. Data should contain the 2 points of interest in position 0 and 1.

D.7 Troubleshoot

Compilation

Bugs can be created if `xepr_link` does not allow for enough time to let Xepr compile.

Increase the compilation time of the .exp, .def and .shp files (1 s by default) with the global variable `COMPILATION_TIME` from `xepr_link`:

```
xepr_link.COMPILATION_TIME = 2  # (s)

xepr = xepr_link.load_xepr()

# .exp and .def files location
location = '/home/xuser/xeprFiles/Data/'
exp_f = location + '2pflip.exp'
def_f = location + '2pflip.def'

# optimisation of pulse length and amplitude
xbest, fbest, message = optimise(xepr,
                                 pars=["p0", "Attenuation"],
                                 init=[8, 5],
                                 lb=[2, 0],
                                 ub=[36, 10],
                                 tol=[2, 0.5],
                                 cost_function=maxabsint_echo,
                                 exp_file=exp_f,
                                 def_file=def_f,
                                 optimiser="bobyqa",
                                 maxfev=20)

# run experiment with optimal parameters
xepr_link.run2getdata_exp(xepr, "Signal", exp_f)
```

If the files are compiling fast enough, decrease `COMPILATION_TIME` to accelerate the optimisation routine.

fast .def file modification

ESR-POISE does not use the function `modif_def_PlsSPELGlbTxt()` from the module `xepr_link.py` despite its ability to modify the .def file variables without referring to the .def file location.

While this function would save a couple of seconds per iteration, it can cause a freeze of the .def file modification, forcing the user to manually interrupt its script:

```
Traceback (most recent call last):
  File "crash_def.py", line 6, in <module>
    xepr_link.modif_def(xepr, ['p0'], ['8'])
  File "/home/xuser/xeprFiles/Data/esrpoise-dev/esrpoise/xepr_link.py", line
  ↪  190, in modif_def
    currentExp["ftEPR.PlsSPELSetVar"].value = cmdStr
  File "/home/xuser/.local/lib/python3.6/site-packages/XeprAPI/main.py", line
  ↪  1195, in __getitem__
    return Parameter(self, name)
  File "/home/xuser/.local/lib/python3.6/site-packages/XeprAPI/main.py", line
  ↪  1243, in __init__
    self._name = self._parent.findParam(name, findall=True)
  File "/home/xuser/.local/lib/python3.6/site-packages/XeprAPI/main.py", line
  ↪  1139, in findParam
    for par in self.getFuParList(fu):
  File "/home/xuser/.local/lib/python3.6/site-packages/XeprAPI/main.py", line
  ↪  1096, in getFuParList
    self.aqGetExpFuParList(fu, buf, 10000)
  File "<string>", line 1, in <lambda>
  File "<string>", line 1, in <lambda>
  File "/home/xuser/.local/lib/python3.6/site-packages/XeprAPI/main.py", line
  ↪  510, in _callXeprfunc
    if self._API.XeprCallFunction(funcidx) != 0:
```

This bug was observed and reproduced after a few hundred to a few thousand calls to `modif_def_PlsSPELGlbTxt()`.

Shape loading

If a bug with shape loading is encountered after a certain number of iterations (typically 114 on older versions of Xepr), it should be solved by resetting Xepr to avoid AWG overloading. Use the following lines in your callback function (requires to import `acquire_esr` from `esrpoise`):

```
if acquire_esr.calls % 114 == 0 and acquire_esr.calls != 0:
    print('reset required')
    xepr_link.reset_exp(Xepr)
```

Appendix E

Optimisation tables

This appendix presents the optimisation results from chapter 3 with the three optimiser from ESR-POISE (5 repetitions for each set of reported values). In the tables' headers, f_{best} indicates the minima of the cost function found by the optimisation, while n_{fev} indicate the total number of function evaluations conducted (i.e. acquisitions). Full grid searches are labelled as "Full grid".

E.1 Signal phase setup

Coarse setup

- One parameter: signal phase
- Experiment: Hahn-echo
- Cost function: $-\int \text{Re(echo)}$

Table E.1: Results of coarse signal phase optimisation, using a tolerance of 25 (a.u.) to implement the phase values.

Algorithm	$\boldsymbol{f}_{\textbf{best}}$	**Optimal parameter**	$\boldsymbol{n}_{\textbf{fev}}$	**Time (s)**
MDS	-1.68 ± 0.01	1843 ± 22	18 ± 1	68 ± 3
Nelder–Mead	-1.68 ± 0.01	1900 ± 47	20 ± 1	75 ± 4
BOBYQA	-1.67 ± 0.01	1866 ± 25	11 ± 1	42 ± 5

Fine adjustment

- One parameter: signal phase, starting with the optimum from the coarse phase optimisation
- Experiment: Hahn-echo (with $\tau_\pi = 2\tau_{\pi/2}$)
- Cost function: $\int \text{Im(echo)}$

Table E.2: Results of fine signal phase optimisation, using a tolerance of 5 (a.u.) to implement the phase values.

Algorithm	$f_{\mathbf{best}}$	**Optimal parameter**	$n_{\mathbf{fev}}$	**Time (s)**
MDS	3.61 ± 3.32	1893 ± 35	15 ± 1	55 ± 4
Nelder–Mead	3.55 ± 1.99	1880 ± 37	20 ± 1	76 ± 4
BOBYQA	3.76 ± 1.87	1900 ± 14	8 ± 1	31 ± 4

In this case, reducing the imaginary part to zero induces strong fluctuation in the final cost function values as the relative noise level increased strongly near the optimum.

E.2 MPFU channels phase setup

Single channel case

- One parameter: MPFU channel phase
- Experiment: Hahn-echo
- Cost function: $-\int \mathrm{Re}(\mathrm{echo})$

Table E.3: Results of single MPFU channel phase optimisation, using a tolerance of 1% to implement the phase values.

Algorithm	$f_{\mathbf{best}}$	**Optimal parameter**	$n_{\mathbf{fev}}$	**Time (s)**
MDS	-8.47 ± 0.02	54.6 ± 1.5	12	36
Nelder–Mead	-8.45 ± 0.02	55.2 ± 0.4	13 ± 1	40 ± 3
BOBYQA	-8.43 ± 0.02	55.2 ± 1.0	7	20 ± 1
Full grid	-8.49	55	100	306

Consecutive optimisations

- One parameter: MPFU channel phase
- Experiment: Hahn-echo with an additional channel implemented in the phase cycle at each optimisation
- Cost function: $-\int \mathrm{Re}(\mathrm{echo})$

Table E.4: Results of four consecutive MPFU channel phase optimisations, using a tolerance of 1% to implement the phase values. Only the f_{best} value obtained from the last optimisation is reported while n_{fev} represents the total number of function evaluations of the four consecutive optimisations. As the optimisation goal is to adjust the channel phases with respect to each other (in quadrature), the optimal parameter values found may vary and are therefore not reported here.

Algorithm	f_{best}	n_{fev}	**Time (s)**
MDS	-3.69 ± 0.01	49 ± 1	166 ± 1
Nelder–Mead	-3.70	52 ± 1	175 ± 5
BOBYQA	-3.70 ± 0.01	31 ± 1	104 ± 3
Full grid	3.67	400	1372

E.3 Magnetic field tweak

- One parameter: static magnetic field
- Experiment: Hahn-echo
- Cost function: $-\int |\text{echo}|$

Table E.5: Results of static magnetic field optimisation, using a tolerance of 0.25 G to implement the field values.

Algorithm	f_{best}	**Optimal parameter**	n_{fev}	**Time (s)**
MDS	-1.321 ± 0.002	3407.55 ± 0.29	17 ± 1	138 ± 20
Nelder–Mead	-1.321 ± 0.002	3407.40 ± 0.12	16 ± 1	141 ± 9
BOBYQA	-1.321 ± 0.002	3407.35 ± 0.12	9 ± 1	82 ± 7
Full grid	-1.314	3407.35	141	1259

In this instance, the final cost function value found with the full grid search slightly digresses from the others values found by the optimisers (which are call close to each other), likely due to instrumental drift occurring over the long experiment time.

E.4 Flip angle calibration

- Two parameters: pulse length, attenuation
- Experiment: Hahn-echo (with $\tau_\pi = 2\tau_{\pi/2}$)
- Cost function: $-\int |\text{echo}|$

Table E.6: Results of flip angle calibration optimisation, using a tolerance of 2 ns to implement the pulse length values and 1 dB to implement the attenuation.

Algorithm	$f_{\mathbf{best}}$	**Optimal parameters**	$n_{\mathbf{fev}}$	**Time (s)**
MDS	-3.14	24, 4	11	82 ± 1
Nelder–Mead	-3.16 ± 0.05	24 ± 1, 3.8 ± 0.4	16 ± 2	120 ± 20
BOBYQA	-3.80 ± 0.01	6, 2	12	90 ± 1
Full grid	-3.97	6, 1	198	1459

E.5 CHORUS amplitudes setup

- Three parameters: pulse amplitudes
- Experiment: CHORUS
- Cost function: $-\int |\text{spectrum}|$

Table E.7: Results of CHORUS amplitudes setup optimisation, using a tolerance of 1% to implement the input amplitudes. The results obtained with one run of the calibration method seen in subsection 2.3.3 are also included on the last line.

Algorithm	$f_{\mathbf{best}}$	**Optimal parameter**	$n_{\mathbf{fev}}$	**Time (s)**
MDS	-5.00	29.2 ± 0.4, 85.6 ± 0.5, 96.2 ± 0.4	42 ± 5	588 ± 68
Nelder–Mead	-5.01 ± 0.01	29.4 ± 0.5, 81.4 ± 0.5, 90.6 ± 0.8	38 ± 4	523 ± 59
BOBYQA	-4.99	29.6 ± 0.5, 87.2 ± 0.7, 99.0 ± 0.9	20 ± 1	285 ± 16
Prev. work [129]	-4.98	29, 67, 73	2560	4100

E.6 DEER pump pulse optimisation

- One parameter: HS[1] pump pulse selectivity parameter β'
- Experiment: 4-pulse DEER
- Cost function: $-\eta_{2\text{p}}$

Table E.8: Results of DEER pump pulse selectivity optimisation, using a tolerance of 1 to implement the parameter β'.

Algorithm	$f_{\mathbf{best}}$	**Optimal parameter**	$n_{\mathbf{fev}}$	**Time (s)**
MDS	-1.49 ± 0.02	5.4 ± 0.5	7	159
Nelder–Mead	-1.50 ± 0.04	5.6 ± 0.5	7	168 ± 11
BOBYQA	-1.51 ± 0.04	6.0 ± 0.6	7	150 ± 13

E.7 CHORUS hardware compensation

- Five parameters: amplitude of the excitation pulse, two complex-valued coefficients of the transfer function (two real parameters each)
- Experiment: CHORUS
- Cost function: $||\text{spectrum}^{(\text{CHORUS})} - \text{spectrum}^{(\text{field-sweep})}||_2$

Table E.9: Results of CHORUS hardware compensation optimisation, using a tolerance value of 0.1% to implement the excitation pulse amplitude and 0.05 (a.u.) to implement the transfer function coefficients. The experiment conducted at -100 MHz is reported on the table's second line.

Algorithm	$f_{\mathbf{best}}$	**Optimal parameter**	$n_{\mathbf{fev}}$	**Time (s)**
BOBYQA	1.00	38.5, -0.185, 0.410, -0.530, 0.430	113	1357
BOBYQA	1.85	35.0, 0.090, -0.875, -0.170, 0.825	125	1501

The main text measurement was done after the measurements for the appendix and the final cost function values therefore slightly differ from each other because of the noise present in the data.

Appendix F

NV spectrometer inventory

All parts selected for the NV spectrometer are listed in this appendix. Metric parts and electronics adapted to the UK were chosen where possible.

Table F.1: NV spectrometer parts list (dimensions in mm unless specified).

Set	Item designation	Qty	Supplier	Part Number (P/N)
Diamond	Diamond plate	1	Elements Six	145-500-0385
	Glass plate sample holder	1	Internal workshop	-
Laser	Verdi G2 OPSLaser-Diode System	1	Coherent	1169164
Optical table	Passive support (l=900, w=600)	1	Thorlabs	PFP6090-8
	Breadboard	1	Thorlabs	PBG52506
Lenses	Plano-convex lens (Ø25.4, f=400.0)	1	Thorlabs	LA1172-A
	Plano-convex lens (Ø25.4, f=50.0)	1	Thorlabs	LA1131-A
	Plano-convex lens (Ø25.4, f=100.0)	1	Thorlabs	LA1509-A
	Plano-convex lens (Ø25.4, f=200.0)	1	Thorlabs	LA1708-A
	Quick-release carriage set	4	Thorlabs	KB1P/M
	Plano-convex Lens (Ø12.7, f=30.0)	1	Thorlabs	LA1289-A
	Lens mount (for Ø12.7)	1	Thorlabs	LMR05/M
Mirrors	Silver mirror (Ø25)	8	Thorlabs	PF10-03-P01
	Kinematic mirror mount (for Ø25)	7	Thorlabs	KM100
Pinhole	Mounted pinhole (Ø0.2)	1	Thorlabs	P200K
	Translating lens mount	1	Thorlabs	LM1XY/M
Waveplate	Waveplate 532nm	1	Thorlabs	WPH05M-532
	Waveplate holder	1	Thorlabs	RSP1/M
Posts (for optics above)	Post (low reflectivity, l=75)	15	Thorlabs	TRA75/M
	Post holder (l=30)	15	Thorlabs	PH30/M
	Mounting base	15	Thorlabs	BA1S/M

Irises (2 for alignment)	Iris (max. aperture Ø12.0)	3	Thorlabs	IDA12/M
	Post (low reflectivity, l=40)	3	Thorlabs	TRA40/M
	Post (low reflectivity, l=50)	3	Thorlabs	TRA50/M
	Thread adapter M6 to M4	3	Thorlabs	AP6M4M
	Post holder (l=40)	3	Thorlabs	PH40/M
	Mounting base	3	Thorlabs	BA1S/M
Final beam dump	Beam block	1	Thorlabs	LB1/M
	Post (low reflectivity, l=100)	1	Thorlabs	TRA100/M
	Post holder (l=40)	1	Thorlabs	PH40/M
	Mounting base	1	Thorlabs	BA1S/M
AOM	AOM	1	IntraAction	ATM-801A2
	AOM driver	1	IntraAction	ME-802N
	Five-axis stage, (h=27.4)	1	Thorlabs	PY005/M
	Post (h=20, low reflectivity)	1	Thorlabs	TRA20/M
	Post (h=50, low reflectivity)	1	Thorlabs	TRA50/M
	Post holder (h=30)	1	Thorlabs	PH30/M
	Thread adapter M6 to M4	2	Thorlabs	AP6M4M
	Thread adapter M4 to M3	1	Thorlabs	AP4M3M
Fluoresc. measur.	Sample support	1	Internal workshop	-
	Long-pass edge filter (647 nm)	1	Laser 2000	BLP01-647R-25
	Hex. light pipe (l=75, aperture=2)	1	Edmund Optics	#63-081
	Light pipe support	1	Edmund Optics	#64-904
	APD module (Ø0.3)	1	Laser Components	A-CUBE-S3000-03
	Mini post (Ø6, l=25)	2	Thorlabs	MS1R/M
	Mini post (Ø6, l=50)	2	Thorlabs	MS2R/M
	Removable cage plate (Ø30)	1	Thorlabs	CP44F
	Threaded adapter (for Ø16)	1	Thorlabs	AD16F
	Compact five-axis stage (h=27.4)	1	Thorlabs	PY005/M
	Post (l=30, low reflectivity)	2	Thorlabs	TRA30/M
	Post holder (h=20)	1	Thorlabs	PH20/M
	Thread adapter M6 to M4	3	Thorlabs	AP6M4M
	Screw M2	4	-	-
Static magnetic field	SmCo magnets (Ø29.21, h=6.35)	2	Magnetsales	SMDC01708
	Dovetail optical rail (l=150)	1	Thorlabs	RLA150/M
	Dovetail rail carrier (l=25.4, w=25.4)	2	Thorlabs	RC1
	Compact kinematic mirror mount	2	Thorlabs	KMS/M
	Single-axis transl. stage	2	Thorlabs	MS1S/M

	Magnet arm	2	Internal workshop	-
	Rotation stage (Ø50.8)	1	Thorlabs	RP01/M
	Transl. stage	1	Thorlabs	PT1/M
	Right-angle bracket for transl. stage	1	Thorlabs	PT102/M
	XY Stage (360°)	1	Thorlabs	XYR1/M
	Mounting base (25×58×10)	4	Thorlabs	BA1S/M
	Post (low reflectivity, l=50)	2	Thorlabs	TRA50/M
	Thread adapter M6 to M4	2	Thorlabs	AP6M4M
	Screw M4	2	-	-
	Setscrew M4	2	-	-
MW delivery	Right-angle clamp for post	1	Thorlabs	RA90/M
	Post (low reflectivity, l=75)	1	Thorlabs	TRA75/M
	SMA straight solder Plug	1	Amphenol	901-9867-RFX
	Semi rigid coaxial cable	1	Micro-Coax	UT-047C-TP
	Post (low reflectivity, l=100)	1	Thorlabs	TRA100/M
	Post holder (l=40)	1	Thorlabs	PH30/M
	Mounting base	1	Thorlabs	BA1S/M
Laser safety shields	Shield/lid	17	Internal workshop	-
	Slotted pillar	13	Internal workshop	-
	Slotted pillar plug	13	Internal workshop	-
	Joiner	13	Internal workshop	-
	Top bar	17	Internal workshop	-
Laser atten.	Motorized laser attenuator	1	Eksma Optics	990-0071-532M+CP532
	Pedestal base adapter	1	Thorlabs	BE1/M
	Pillar post extension (Ø25.0, h=50)	1	Thorlabs	RS50/M
	Tapped post spacer (Ø25.0, h=10)	1	Thorlabs	RS10/M
	Tapped post spacer (Ø25.0, h=5)	1	Thorlabs	RS5/M
	Clamp fork (M6 captive screw)	1	Thorlabs	CF125C/M
	Beam block	1	Thorlabs	LB1/M
	Post (low reflectivity, l=100)	1	Thorlabs	TRA100/M
	Post holder (l=40)	1	Thorlabs	PH40/M
	Mounting base	1	Thorlabs	BA1S/M
Alignment laser	Laser diode (0.5mW, 532nm)	1	Thorlabs	CPS532-C2
	Laser diode power supply	1	Thorlabs	LDS5-EC
	Adapter	1	Thorlabs	AD11F
	Kinematic mirror mount	1	Thorlabs	KM100
	Post (low reflectivity, l=75)	2	Thorlabs	TRA75/M

	Post holder (l=30)	2	Thorlabs	PH30/M
	Mounting base	2	Thorlabs	BA1S/M
Screw kit	Setscrew and hardware kit M6	1	Thorlabs	HW-KIT3/M
Computer	Desktop	1	Dell	Optiplex 7090MT
	Monitor	1	Dell	P2319H
Pulse	Pulse blaster	1	SpinCore	SP18AP500
control	Signal generator +ext. I/Q mod.	1	SRS	SG384/3
DAQ	USB-6211 Bus-Powered M Series	1	National instruments	779676-01
	GPIB-USB-HS+ with NI-488.2	1	National instruments	783368-01
Power	MW amplifier power supply	1	RS Components	CUS-150M-28/A
supplies	AOM power supply	1	RS Components	TML 15205C
	APD power supply	1	Laser Components	A-Cube-PSU
Electronic	BNC attenuator	1	Mini-Circuits Europe	HAT-10+
compon.	Switches	4	Mini-Circuits Europe	ZASWA-2-50DRA+
	Switches	20	Mini-Circuits Europe	M3SWA-2-50DRB+
	MW amplifier	1	Mini-Circuits Europe	ZHL-16W-43-S+
Rack	Pivot foot (M12 thread)	4	RS Components	7675869
	Base plate (M12/M5 thread)	4	RS Components	7675793
	Connecting angle (for 40×40 strut)	20	RS Components	7675695
	Connecting cube (for 40×40 strut)	4	RS Components	7675711
	Aluminium strut (40×40×1000)	6	RS Components	7613319
	Aluminium strut (40×40×2000)	6	RS Components	7613313

Additional equipment (not part of the spectrometer, might be borrowed, for an operation taken care of by an external contractor or optional) includes:

- equipment for NV implementation, and diamond cutting,
- spirit level and pump to level the optical table,
- metric hexkey and spanner sets for assembly,
- epoxy glue to fix the diamond and the permanent magnets
- optic cleaning and handling equipment,
- laser power meter (e.g. FieldMaxII-TO, PM10 and OP-2 VIS from Coherent)
- voltmeter (e.g. Fluke 177),

- RF power meter (e.g. Keysight, cat. no. V 3500),
- digital oscilloscope (e.g. InfiniiVision 3000T X, 2 Channel, 1 GHz, 5 GSPS, 4 Mpts, 450 ps - 2449640),
- laser safety goggles (e.g. LaserVision F22.P1E01.1001).

Appendix G

NV spectrometer additional views

a)

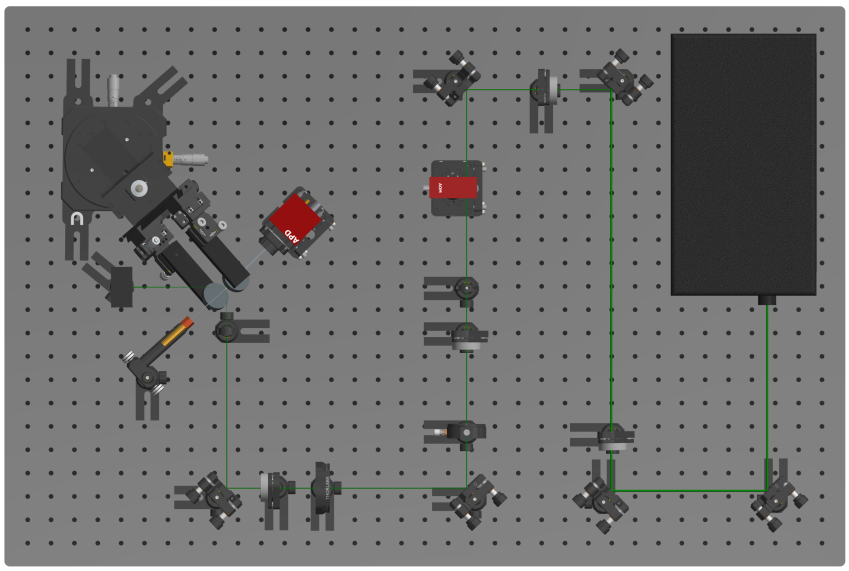


b)



Figure G.1: a) 3D CAD view of the spectrometer optic table with laser safety shields and b) current advancement of assembly at time of writing. Some individual part CAD files were obtained from Thorlabs (`https://www.thorlabs.com`, 2020 and see appendix F and for more details).

a)



b)

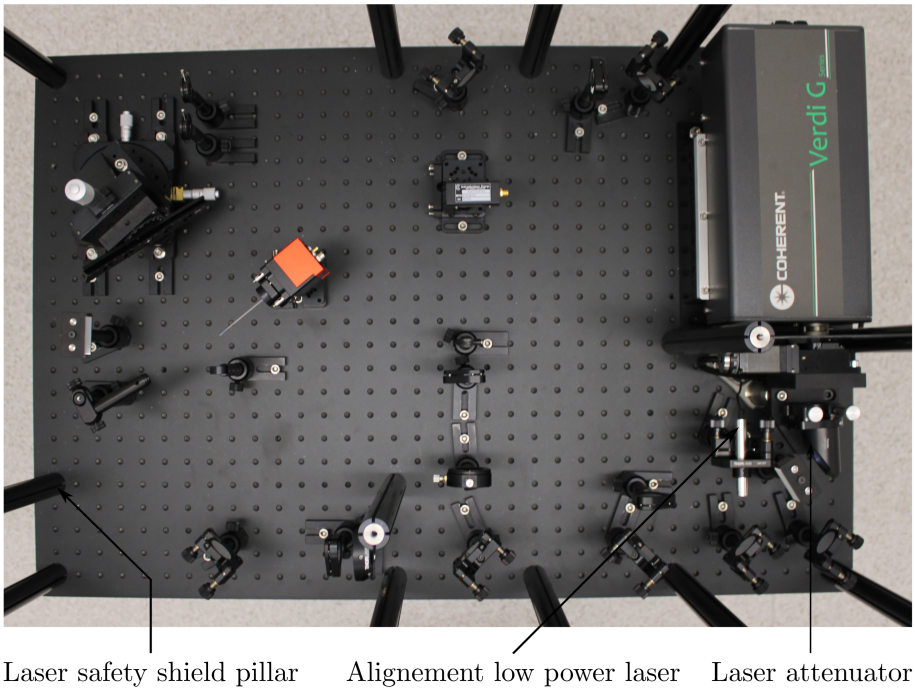


Figure G.2: a) 3D CAD top view of the spectrometer optics and b) current advancement of assembly at time of writing. Some individual part CAD files were obtained from Thorlabs (`https://www.thorlabs.com`, 2020 and see appendix F and for more details).

Bibliography

1. Blank, A., Twig, Y. & Ishay, Y. Recent trends in high spin sensitivity magnetic resonance. *J. Magn. Reson.* **280,** 20–29 (2017).
2. Ardenkjaer-Larsen, J.-H. *et al.* Facing and Overcoming Sensitivity Challenges in Biomolecular NMR Spectroscopy. *Angew. Chem. Int. Ed* **54,** 9162–9185 (2015).
3. Lee, J. H., Okuno, Y. & Cavagnero, S. Sensitivity enhancement in solution NMR: emerging ideas and new frontiers. *J. Magn. Reson.* **241,** 18–31 (2014).
4. Cavanagh, J. *Protein NMR spectroscopy : principles and practice* 2nd edition (Academic Press, 2007).
5. Keeler, J. *Understanding NMR Spectroscopy* 2nd edition (John Wiley & Sons, Somerset, 2011).
6. Levitt, M. H. *Spin dynamics: basics of nuclear magnetic resonance* 2nd edition (John Wiley & Sons, 2013).
7. Claridge, T. D. W. *High-resolution NMR techniques in organic chemistry* (Elsevier, 2016).
8. Schweiger, A. & Jeschke, G. *Principles of pulse electron paramagnetic resonance* (Oxford University Press, Oxford, 2001).
9. Brustolon, M. & Giamello, E. *Electron Paramagnetic Resonance: A Practitioner's Toolkit* (John Wiley & Sons, 2009).
10. Goldfarb, D. & Stoll, S. *EPR spectroscopy: fundamentals and methods* (John Wiley & Sons, 2018).
11. Schrödinger, E. R. J. A. Quantisierung als eigenwertproblem. *Annalen der Physik* **385,** 437–480 (1926).
12. Merzbacher, E. *Quantum Mechanics* 3rd edition (John Wiley & Sons, 1997).
13. Bureau International des Poids et des Mesures. *The International System of Units* tech. rep. (2019).
14. Hahn, E. L. Spin Echoes. *Physical Reviews* **80,** 580–594 (4 1950).
15. Bahrenberg, T., Jahn, S. M., Feintuch, A., Stoll, S. & Goldfarb, D. The decay of the refocused Hahn echo in double electron–electron resonance (DEER) experiments. *Magn. Reson.,* 161–173 (2021).

16. Viola, L. in *Quantum Error Correction* (eds Lidar, D. A. & Brun, T. A.) 105–125 (Cambridge University Press, 2013).

17. Hogben, H., Krzystyniak, M., Charnock, G., Hore, P. & Kuprov, I. Spinach – A software library for simulation of spin dynamics in large spin systems. *J. Magn. Reson.* **208,** 179–194 (2011).

18. Stoll, S. & Schweiger, A. EasySpin, a comprehensive software package for spectral simulation and analysis in EPR. *J. Magn. Reson.* **178,** 42–55 (2006).

19. Redfield, A. G. On the Theory of Relaxation Processes. *IBM Journal of Research and Development* **1,** 19–31 (1957).

20. Abragam, A. *The principles of nuclear magnetism* **32** (Oxford university press, 1961).

21. Stoll, S. in *EPR spectroscopy: fundamentals and methods* (eds Goldfarb, D. & Stoll, S.) 215–233 (John Wiley & Sons, 2018).

22. Jeschke, G., Pannier, M., Godt, A. & Spiess, H. W. Dipolar spectroscopy and spin alignment in electron paramagnetic resonance. *Chem. Phys. Lett.* **331,** 243–252 (2000).

23. Eaton, S. S. & R., E. G. in *EPR spectroscopy: fundamentals and methods* (eds Goldfarb, D. & Stoll, S.) 175–192 (John Wiley & Sons, 2018).

24. Hahn, E. L. An Accurate Nuclear Magnetic Resonance Method for Measuring Spin-Lattice Relaxation Times. *Phys. Rev.* **76,** 145–146 (1 1949).

25. Bowman, M. K. in *Electron Paramagnetic Resonance: A Practitioner's Toolkit* (eds Brustolon, M. & Giamello, E.) 159–194 (John Wiley & Sons, 2009).

26. Carr, H. Y. & Purcell, E. M. Effects of diffusion on free precession in nuclear magnetic resonance experiments. *Phys. Rev.* **94,** 630 (1954).

27. Meiboom, S. & Gill, D. Modified spin-echo method for measuring nuclear relaxation times. *Rev. Sci. Instrum.* **29,** 688–691 (1958).

28. Hürlimann, M. & Griffin, D. Spin Dynamics of Carr–Purcell–Meiboom–Gill-like Sequences in Grossly Inhomogeneous B0 and B1 Fields and Application to NMR Well Logging. *J. Magn. Reson.* **143,** 120–135 (2000).

29. Larsen, F. H., Skibsted, J., Jakobsen, H. J. & Nielsen, N. C. Solid-State QCPMG NMR of Low-γ Quadrupolar Metal Nuclei in Natural Abundance. *J. Am. Chem. Soc.* **122,** 7080–7086 (2000).

30. Palmer, A. G., Kroenke, C. D. & Loria, J. P. in *Nuclear Magnetic Resonance of Biological Macromolecules - Part B* (eds James, T. L., Dötsch, V. & Schmitz, U.) 204–238 (Academic Press, 2001).

31. Takegoshi, K., Ogura, K. & Hikichi, K. A perfect spin echo in a weakly homonuclear J-coupled two spin-12 system. *J. Magn. Reson. (1969)* **84,** 611–615 (1989).

32. Van Zijl, P. C. M., Moonen, C. T. W. & von Kienlin, M. Homonuclear J refocusing in echo spectroscopy. *J. Magn. Reson. (1969)* **89,** 28–40 (1990).

33. Aguilar, J. A., Nilsson, M., Bodenhausen, G. & Morris, G. A. Spin echo NMR spectra without J modulation. *Chem. Commun.* **48,** 811–813 (2012).

34. Torres, A. M., Zheng, G. & Price, W. S. J-compensated PGSE: an improved NMR diffusion experiment with fewer phase distortions. *Magn. Reson. Chem.* **48,** 129–133 (2010).

35. Aguilar, J. A., Adams, R. W., Nilsson, M. & Morris, G. A. Suppressing exchange effects in diffusion-ordered NMR spectroscopy. *J. Magn. Reson.* **238,** 16–19 (2014).

36. Adams, R. W., Holroyd, C. M., Aguilar, J. A., Nilsson, M. & Morris, G. A. "Perfecting" WATERGATE: clean proton NMR spectra from aqueous solution. *Chem. Commun.* **49,** 358–360 (2013).

37. Jeschke, G. in *EPR spectroscopy: fundamentals and methods* (eds Goldfarb, D. & Stoll, S.) 401–423 (John Wiley & Sons, 2018).

38. Pannier, M., Veit, S., Godt, A., Jeschke, G. & Spiess, H. W. Dead-Time Free Measurement of Dipole–Dipole Interactions between Electron Spins. *J. Magn. Reson.* **142,** 331–340 (2000).

39. Jeschke, G. *et al.* DeerAnalysis2006—a comprehensive software package for analyzing pulsed ELDOR data. *Appl. Magn. Reson.* **30,** 473–498 (2006).

40. Worswick, S. G., Spencer, J. A., Jeschke, G. & Kuprov, I. Deep neural network processing of DEER data. *Sci. Adv.* **4,** eaat5218 (2018).

41. Fábregas Ibáñez, L., Jeschke, G. & Stoll, S. DeerLab: a comprehensive software package for analyzing dipolar electron paramagnetic resonance spectroscopy data. *Magn. Reson.* **1,** 209–224 (2020).

42. Goldfarb, D. in *EPR spectroscopy: fundamentals and methods* (eds Goldfarb, D. & Stoll, S.) 359–376 (John Wiley & Sons, 2018).

43. Baum, J., Tycko, R. & Pines, A. Broadband population inversion by phase modulated pulses. *J. Chem. Phys.* **79,** 4643–4644 (1983).

44. Tycko, R. Broadband Population Inversion. *Phys. Rev. Lett.* **51,** 775–777 (1983).

45. Hioe, F. T. Solution of Bloch Equations Involving Amplitude and Frequency Modulations. *Phys. Rev. A* **30,** 2100–2103 (1984).

46. Silver, M. S., Joseph, R. I., Chen, C. N., Sank, V. J. & Hoult, D. I. Selective population inversion in NMR. *Nature* **310,** 681–683 (1984).

47. Silver, M. S., Joseph, R. I. & Hoult, D. I. Highly selective pi/2 and pi pulse generation. *J. Magn. Reson. (1969)* **59,** 347–351 (1984).

48. Silver, M. S., Joseph, R. I. & Hoult, D. I. Selective spin inversion in nuclear magnetic resonance and coherent optics through an exact solution of the Bloch-Riccati equation. *Phys. Rev. A* **31,** 2753–2755 (1985).

49. Hardy, C. J., Edelstein, W. A. & Vatis, D. Efficient Adiabatic Fast Passage for Nmr Population-Inversion in the Presence of Radiofrequency Field Inhomogeneity and Frequency Offsets. *J. Magn. Reson.* **66,** 470–482 (1986).

50. Bendall, M. R., Garwood, M., Ugurbil, K. & Pegg, D. T. Adiabatic Refocusing Pulse Which Compensates for Variable Rf Power and Off-Resonance Effects. *Magn. Reson. Med.* **4,** 493–499 (1987).

51. Uğurbil, K., Garwood, M. & Robin Bendall, M. Amplitude- and frequency-modulated pulses to achieve 90° plane rotations with inhomogeneous B1 fields. *J. Magn. Reson.* **72,** 177–185 (1987).

52. Uğurbil, K., Garwood, M. & Rath, A. R. Optimization of modulation functions to improve insensitivity of adiabatic pulses to variations in B1 magnitude. *J. Magn. Reson.* **80,** 448–469 (1988).

53. Kunz, D. Use of frequency-modulated radiofrequency pulses in MR imaging experiments. *Magn. Reson. Med.* **3,** 377–84 (1986).

54. Kunz, D. Frequency-modulated radiofrequency pulses in spin-echo and stimulated-echo experiments. *Magn. Reson. Med.* **4,** 129–136 (1987).

55. Conolly, S., Nishimura, D. & Macovski, A. A selective adiabatic spin-echo pulse. *J. Magn. Reson. (1969)* **83,** 324–334 (1989).

56. De Graaf, R. A., Luo, Y., Terpstra, M., Merkle, H. & Garwood, M. A new localization method using an adiabatic pulse, BIR-4. *J. Magn. Reson. B* **106,** 245–52 (1995).

57. Böhlen, J.-M., Rey, M. & Bodenhausen, G. Refocusing with chirped pulses for broadband excitation without phase dispersion. *J. Magn. Reson.* **84,** 191–197 (1989).

58. Fujiwara, T. & Nagayama, K. Optimized frequency/phase-modulated broadband inversion pulses. *J. Magn. Reson.* **86,** 584–592 (1990).

59. Böhlen, J.-M., Burghardt, I., Rey, M. & Bodenhausen, G. Frequency-modulated "Chirp" pulses for broadband inversion recovery in magnetic resonance. *J. Magn. Reson.* **90,** 183–191 (1990).

60. Ke, Y., Schupp, D. G. & Garwood, M. Adiabatic DANTE sequences for B1-insensitive narrowband inversion. *J. Magn. Reson.* **96,** 663–669 (1992).

61. Ermakov, V. L. & Bodenhausen, G. Broadband excitation in magnetic resonance by self-refocusing doubly frequency-modulated pulses. *Chem. Phys. Lett.* **204,** 375–380 (1993).

62. Ermakov, V. L., Böhlen, J. M. & Bodenhausen, G. Improved Schemes for Refocusing with Frequency-Modulated Chirp Pulses. *J. Magn. Reson. A* **103,** 226–229 (1993).

63. Hwang, T. L., van Zijl, P. C. & Garwood, M. Broadband adiabatic refocusing without phase distortion. *J. Magn. Reson.* **124,** 250–4 (1997).

64. Hwang, T. L., van Zijl, P. C. & Garwood, M. Fast broadband inversion by adiabatic pulses. *J. Magn. Reson.* **133,** 200–3 (1998).

65. Garwood, M. & Ke, Y. Symmetric pulses to induce arbitrary flip angles with compensation for rf inhomogeneity and resonance offsets. *J. Magn. Reson.* **94,** 511–525 (1991).

66. Kupče, Ē. & Freeman, R. Compensation for Spin-Spin Coupling Effects during Adiabatic Pulses. *J. Magn. Reson.* **127,** 36–48 (1997).

67. Freeman, R. & Kupce, E. Decoupling: theory and practice. I. Current methods and recent concepts. *NMR Biomed.* **10,** 372–80 (1997).

68. Fujiwara, T., Anai, T., Kurihara, N. & Nagayama, K. Frequency-Switched Composite Pulses for Decoupling Carbon-13 Spins over Ultrabroad Bandwidths. *J. Magn. Reson. A* **104,** 103–105 (1993).

69. Starcuk, Z., Bartusek, K. & Starcuk, Z. Heteronuclear Broadband Spin-Flip Decoupling with Adiabatic Pulses. *J. Magn. Reson. A* **107,** 24–31 (1994).

70. Fu, R. Q. & Bodenhausen, G. Ultra-broadband decoupling. *J. Magn. Reson. A* **117,** 324–325 (1995).

71. Fu, R. & Bodenhausen, G. Broadband decoupling in NMR with frequency-modulated 'chirp' pulses. *Chem. Phys. Lett.* **245,** 415–420 (1995).

72. Kupče, Ē. & Freeman, R. An adaptable NMR broadband decoupling scheme. *Chem. Phys. Lett.* **250,** 523–527 (1996).

73. Kupče, Ē. & Freeman, R. Optimized adiabatic pulses for wideband spin inversion. *J. Magn. Reson. A* **118,** 299–303 (1996).

74. Kupče, Ē., Freeman, R., Wider, G. & Wuthrich, K. Figure of merit and cycling sidebands in adiabatic decoupling. *J. Magn. Reson. A* **120,** 264–268 (1996).

75. Kupče, Ē., Freeman, R., Wider, G. & Wuthrich, K. Suppression of cycling sidebands using bi-level adiabatic decoupling. *J. Magn. Reson. A* **122,** 81–84 (1996).

76. Mulder, F. A. A., de Graaf, R. A., Kaptein, R. & Boelens, R. An Off-resonance Rotating Frame Relaxation Experiment for the Investigation of Macromolecular Dynamics Using Adiabatic Rotations. *J. Magn. Reson.* **131,** 351–357 (1998).

77. Konrat, R. & Tollinger, M. Heteronuclear relaxation in time-dependent spin systems: 15N-T1ρ dispersion during adiabatic fast passage. *Journal of Biomolecular NMR* **13,** 213–221 (1999).

78. Zweckstetter, M. & Holak, T. A. An Adiabatic Multiple Spin–Echo Pulse Sequence: Removal of Systematic Errors Due to Pulse Imperfections and Off-Resonance Effects. *J. Magn. Reson.* **133,** 134–147 (1998).

79. Titman, J. J., Davis, A. L., Laue, E. D. & Keeler, J. Selection of Coherence Transfer Pathways Using Inhomogeneous Adiabatic Pulses - Removal of Zero-Quantum Coherence. *J. Magn. Reson.* **89,** 176–183 (1990).

80. Pipe, J. G. A fast method for obtaining a "continuous" sample of the inversion-recovery curve using spatially swept adiabatic inversion. *J. Magn. Reson. (1969)* **99,** 582–589 (1992).

81. Pipe, J. G. Spatial Encoding and Reconstruction in MRI with Quadratic Phase Profiles. *Magn. Reson. Med.* **33,** 24–33 (1995).

82. Thrippleton, M. J. & Keeler, J. Elimination of Zero-Quantum Interference in Two-Dimensional NMR Spectra. *Angew. Chem. Int. Ed.* **42,** 3938–3941 (2003).

83. Mangia, S., Traaseth, N. J., Veglia, G., Garwood, M. & Michaeli, S. Probing Slow Protein Dynamics by Adiabatic $R_{1\rho}$ and $R_{2\rho}$ NMR Experiments. *J. Am. Chem. Soc.* **132,** 9979–9981 (2010).

84. Cheatham, S. Spectral simplification of proton homonuclear correlation experiments utilizing ω_1, ω_2 fluorine decoupling. *J. Fluorine Chem.* **140,** 104–106 (2012).

85. Mangia, S. *et al.* Frequency offset dependence of adiabatic rotating frame relaxation rate constants: relevance to MRS investigations of metabolite dynamics in vivo. *NMR Biomed.* **24,** 807–814 (2011).

86. Ben-Eliezer, N., Goerke, U., Ugurbil, K. & Frydman, L. Functional MRI using super-resolved spatiotemporal encoding. *Magn. Reson. Imaging* **30,** 1401–8 (2012).

87. Traaseth, N. J. *et al.* Heteronuclear Adiabatic Relaxation Dispersion (HARD) for quantitative analysis of conformational dynamics in proteins. *J. Magn. Reson.* **219,** 75–82 (2012).

88. Dumez, J. N. & Frydman, L. Multidimensional excitation pulses based on spatiotemporal encoding concepts. *J. Magn. Reson.* **226,** 22–34 (2013).

89. Dumez, J. N., Schmidt, R. & Frydman, L. Simultaneous spatial and spectral selectivity by spatiotemporal encoding. *Magn. Reson. Med.* **71,** 746–55 (2014).

90. Dumez, J.-N. Spatial encoding and spatial selection methods in high-resolution NMR spectroscopy. *Prog. Nucl. Magn. Reson. Spectrosc.* **109,** 101–134 (2018).

91. Cano, K. E., Smith, M. A. & Shaka, A. J. Adjustable, broadband, selective excitation with uniform phase. *J. Magn. Reson.* **155,** 131–9 (2002).

92. Thrippleton, M. J., Edden, R. A. E. & Keeler, J. Suppression of strong coupling artefacts in J-spectra. *J. Magn. Reson.* **174,** 97–109 (2005).

93. Ben-Eliezer, N., Irani, M. & Frydman, L. Super-resolved spatially encoded single-scan 2D MRI. *Magn. Reson. Med.* **63,** 1594–1600 (2010).

94. Power, J. E. *et al.* Increasing the quantitative bandwidth of NMR measurements. *Chem. Commun.* **52,** 2916–2919 (2016).

95. Power, J. E. *et al.* Very broadband diffusion-ordered NMR spectroscopy: (19)F DOSY. *Chem. Commun.* **52,** 6892–6894 (2016).

96. Khaneja, N. Chirp excitation. *J. Magn. Reson.* **282,** 32–36 (2017).

97. Foroozandeh, M., Nilsson, M. & Morris, G. A. Improved ultra-broadband chirp excitation. *J. Magn. Reson.* **302,** 28–33 (2019).

98. Pelupessy, P. Adiabatic Single Scan Two-Dimensional NMR Spectrocopy. *J. Am. Chem. Soc.* **125,** 12345–12350 (2003).

99. Shrot, Y., Shapira, B. & Frydman, L. Ultrafast 2D NMR spectroscopy using a continuous spatial encoding of the spin interactions. *J. Magn. Reson.* **171,** 163–170 (2004).

100. Andersen, N. S. & Kockenberger, W. A simple approach for phase-modulated single-scan 2D NMR spectroscopy. *Magn. Reson. Chem.* **43,** 795–7 (2005).

101. Lin, Y., Lupulescu, A. & Frydman, L. Multidimensional J-driven NMR correlations by single-scan offset-encoded recoupling. *J. Magn. Reson.* **265,** 33–44 (2016).

102. Tycko, R., Schneider, E. & Pines, A. Broadband population inversion in solid state NMR. *J. Chem. Phys.* **81,** 680–688 (1984).

103. Forrer, J. *et al.* Probeheads and instrumentation for pulse EPR and ENDOR spectroscopy with chirped radio frequency pulses and magnetic field steps. *Appl. Magn. Reson.* **10,** 263–279 (1996).

104. Bhattacharyya, R. & Frydman, L. Quadrupolar nuclear magnetic resonance spectroscopy in solids using frequency-swept echoing pulses. *J. Chem. Phys.* **127,** 194503 (2007).

105. O'Dell, L. A. & Schurko, R. W. QCPMG using adiabatic pulses for faster acquisition of ultra-wideline NMR spectra. *Chem. Phys. Lett.* **464,** 97–102 (2008).

106. Hung, I. & Gan, Z. On the practical aspects of recording wideline QCPMG NMR spectra. *J. Magn. Reson.* **204,** 256–65 (2010).

107. MacGregor, A. W., O'Dell, L. A. & Schurko, R. W. New methods for the acquisition of ultra-wideline solid-state NMR spectra of spin-1/2 nuclides. *J. Magn. Reson.* **208,** 103–113 (2011).

108. Harris, K. J., Lupulescu, A., Lucier, B. E., Frydman, L. & Schurko, R. W. Broadband adiabatic inversion pulses for cross polarization in wideline solid-state NMR spectroscopy. *J. Magn. Reson.* **224,** 38–47 (2012).

109. O'Dell, L. A. The WURST kind of pulses in solid-state NMR. *Solid State Nucl. Magn. Reson.* **55-56,** 28–41 (2013).

110. Altenhof, A. R., Lindquist, A. W., Foster, L. D. D., Holmes, S. T. & Schurko, R. W. On the use of frequency-swept pulses and pulses designed with optimal control theory for the acquisition of ultra-wideline NMR spectra. *J. Magn. Reson.* **309,** 106612 (2019).

111. Altenhof, A. R., Jaroszewicz, M. J., Harris, K. J. & Schurko, R. W. Broadband adiabatic inversion experiments for the measurement of longitudinal relaxation time constants. *J. Chem. Phys.* **154,** 034202 (2021).

112. Siegel, R., Nakashima, T. T. & Wasylishen, R. E. Sensitivity enhancement of MQMAS NMR spectra of spin 3/2 nuclei using hyperbolic secant pulses. *Chem. Phys. Lett.s* **403,** 353–358 (2005).

113. Wi, S. & Frydman, L. An Efficient, Robust New Scheme for Establishing Broadband Homonuclear Correlations in Biomolecular Solid State NMR. *ChemPhysChem* (2019).

114. Siegel, R., Nakashima, T. T. & Wasylishen, R. E. Sensitivity enhancement of solid-state NMR spectra of half-integer spin quadrupolar nuclei using hyperbolic secant pulses: Applications to spin-5/2 nuclei. *Chem. Phys. Lett.* **421,** 529–533 (2006).

115. Kervern, G., Pintacuda, G. & Emsley, L. Fast adiabatic pulses for solid-state NMR of paramagnetic systems. *Chem. Phys. Lett.* **435,** 157–162 (2007).

116. Siegel, R., Nakashima, T. T. & Wasylishen, R. E. Sensitivity enhancement of NMR spectra of half-integer spin quadrupolar nuclei in solids using hyperbolic secant pulses. *J. Magn. Reson.* **184,** 85–100 (2007).

117. Dey, K. K., Prasad, S., Ash, J. T., Deschamps, M. & Grandinetti, P. J. Spectral editing in solid-state MAS NMR of quadrupolar nuclei using selective satellite inversion. *J. Magn. Reson.* **185,** 326–330 (2007).

118. Hansen, M. R., Brorson, M., Bildsøe, H., Skibsted, J. & Jakobsen, H. J. Sensitivity enhancement in natural-abundance solid-state 33S MAS NMR spectroscopy employing adiabatic inversion pulses to the satellite transitions. *J. Magn. Reson.* **190,** 316–326 (2008).

119. Nakashima, T. T., Teymoori, R. & Wasylishen, R. E. Using hyperbolic secant pulses to assist characterization of chemical shift tensors for half-integer spin quadrupolar nuclei in MAS powder samples. *Magn. Reson. Chem.* **47,** 465–471 (2009).

120. Pell, A. J. *et al.* Broadband inversion for MAS NMR with single-sideband-selective adiabatic pulses. *J. Chem. Phys.* **134,** 024117 (2011).

121. Pell, A. J. & Pintacuda, G. Broadband solid-state MAS NMR of paramagnetic systems. *Prog. Nucl. Magn. Reson. Spectrosc.* **84-85,** 33–72 (2015).

122. Spindler, P. E. *et al.* Shaped optimal control pulses for increased excitation bandwidth in EPR. *J. Magn. Reson.* **218,** 49–58 (2012).

123. Spindler, P. E., Glaser, S. J., Skinner, T. E. & Prisner, T. F. Broadband inversion PELDOR spectroscopy with partially adiabatic shaped pulses. *Angew. Chem. Int. Ed. Engl.* **52,** 3425–9 (2013).

124. Doll, A., Pribitzer, S., Tschaggelar, R. & Jeschke, G. Adiabatic and fast passage ultra-wideband inversion in pulsed EPR. *J. Magn. Reson.* **230,** 27–39 (2013).

125. Kaufmann, T. *et al.* DAC-board based X-band EPR spectrometer with arbitrary waveform control. *J. Magn. Reson.* **235,** 95–108 (2013).

126. Jeschke, G., Pribitzer, S. & Doll, A. Coherence Transfer by Passage Pulses in Electron Paramagnetic Resonance Spectroscopy. *J. Phys. Chem. B* **119,** 13570–82 (2015).

127. Pribitzer, S., Doll, A. & Jeschke, G. SPIDYAN, a MATLAB library for simulating pulse EPR experiments with arbitrary waveform excitation. *J. Magn. Reson.* **263,** 45–54 (2016).

128. Doll, A. & Jeschke, G. Wideband frequency-swept excitation in pulsed EPR spectroscopy. *J. Magn. Reson.* **280,** 46–62 (2017).

129. Verstraete, J.-B., Myers, W. K. & Foroozandeh, M. Chirped ordered pulses for ultra-broadband ESR spectroscopy. *J. Chem. Phys.* **154,** 094201 (2021).

130. Spindler, P. E. *et al.* Carr–Purcell Pulsed Electron Double Resonance with Shaped Inversion Pulses. *J. Phys. Chem. Lett.* **6,** 4331–4335 (2015).

131. Doll, A. *et al.* Gd(III)-Gd(III) distance measurements with chirp pump pulses. *J. Magn. Reson.* **259,** 153–62 (2015).

132. Doll, A. *et al.* Sensitivity enhancement by population transfer in Gd(iii) spin labels. *Phys. Chem. Chem. Phys.* **17,** 7334–7344 (2015).

133. Bahrenberg, T. *et al.* Improved sensitivity for W-band Gd(III)-Gd(III) and nitroxide-nitroxide DEER measurements with shaped pulses. *J. Magn. Reson.* **283,** 1–13 (2017).

134. Bieber, A., Bücker, D. & Drescher, M. Light-induced dipolar spectroscopy - A quantitative comparison between LiDEER and LaserIMD. *J. Magn. Reson.* **296,** 29–35 (2018).

135. Breitgoff, F. D. *et al.* UWB DEER and RIDME distance measurements in Cu(II)–Cu(II) spin pairs. *J. Magn. Reson.* **308,** 106560 (2019).

136. Scherer, A., Tischlik, S., Weickert, S., Wittmann, V. & Drescher, M. Optimising broadband pulses for DEER depends on concentration and distance range of interest. *Magn. Reson.* **1,** 59–74 (2020).

137. Doll, A., Qi, M., Godt, A. & Jeschke, G. CIDME: Short distances measured with long chirp pulses. *J. Magn. Reson.* **273,** 73–82. ISSN: 1090-7807 (2016).

138. Ritsch, I., Hintz, H., Jeschke, G., Godt, A. & Yulikov, M. Improving the accuracy of Cu(ii)-nitroxide RIDME in the presence of orientation correlation in water-soluble Cu(ii)-nitroxide rulers. *Phys. Chem. Chem. Phys.* **21,** 9810–9830 (2019).

139. Schops, P., Spindler, P. E., Marko, A. & Prisner, T. F. Broadband spin echoes and broadband SIFTER in EPR. *J. Magn. Reson.* **250,** 55–62 (2015).

140. Doll, A. & Jeschke, G. EPR-correlated dipolar spectroscopy by Q-band chirp SIFTER. *Phys. Chem. Chem. Phys.* **18,** 23111–20 (2016).

141. Segawa, T. F., Doll, A., Pribitzer, S. & Jeschke, G. Copper ESEEM and HYSCORE through ultra-wideband chirp EPR spectroscopy. *J. Chem. Phys.* **143,** 044201 (2015).

142. Pribitzer, S., Segawa, T. F., Doll, A. & Jeschke, G. Transverse interference peaks in chirp FT-EPR correlated three-pulse ESEEM spectra. *J. Magn. Reson.* **272,** 37–45 (2016).

143. Doll, A. & Jeschke, G. Fourier-transform electron spin resonance with bandwidth-compensated chirp pulses. *J. Magn. Reson.* **246,** 18–26 (2014).

144. Pribitzer, S., Sajid, M., Hülsmann, M., Godt, A. & Jeschke, G. Pulsed triple electron resonance (TRIER) for dipolar correlation spectroscopy. *J. Magn. Reson.* **282,** 119–128 (2017).

145. Pribitzer, S. *et al.* Two-Dimensional Distance Correlation Maps from Pulsed Triple Electron Resonance (TRIER) on Proteins with Three Paramagnetic Centers. *Appl. Magn. Reson.* **49,** 1253–1279 (2018).

146. Wili, N. & Jeschke, G. Chirp echo Fourier transform EPR-detected NMR. *J. Magn. Reson.* **289,** 26–34 (2018).

147. Wili, N., Hintz, H., Vanas, A., Godt, A. & Jeschke, G. Distance measurement between trityl radicals by pulse dressed electron paramagnetic resonance with phase modulation. *Magn. Reson.* **1,** 75–87 (2020).

148. Casabianca, L. B., Mohr, D., Mandal, S., Song, Y. Q. & Frydman, L. Chirped CPMG for well-logging NMR applications. *J. Magn. Reson.* **242,** 197–202 (2014).

149. Casabianca, L., Sarda, Y., Bergman, E., Nevo, U. & Frydman, L. Single-Sided Stray-Field NMR Profiling Using Chirped Radiofrequency Pulses. *Appl. Magn. Reson.* **46,** 909–919 (2015).

150. Kaminker, I. & Han, S. Amplification of Dynamic Nuclear Polarization at 200 GHz by Arbitrary Pulse Shaping of the Electron Spin Saturation Profile. *J. Phys. Chem. Lett.* **9,** 3110–3115 (2018).

151. Can, T. *et al.* Frequency-Swept Integrated and Stretched Solid Effect Dynamic Nuclear Polarization. *J. Phys. Chem. Lett.* **9,** 3187–3192 (2018).

152. Scott, F. *et al.* Frequency-agile gyrotron for electron decoupling and pulsed dynamic nuclear polarization. *J. Magn. Reson.* **289,** 45–54 (2018).

153. Gao, C. *et al.* Frequency-chirped dynamic nuclear polarization with magic angle spinning using a frequency-agile gyrotron. *J. Magn. Reson.* **308** (2019).

154. Niemeyer, I. *et al.* Broadband excitation by chirped pulses: application to single electron spins in diamond. *New J. Phys.* **15,** 033027 (2013).

155. Scheuer, J. *et al.* Optically induced dynamic nuclear spin polarisation in diamond. *New J. Phys.* **18,** 013040 (2016).

156. Ajoy, A. *et al.* Enhanced dynamic nuclear polarization via swept microwave frequency combs. *Proc. Natl. Acad. Sci. U.S.A.* **115,** 10576–10581 (2018).

157. Zangara, P. *et al.* Dynamics of frequency-swept nuclear spin optical pumping in powdered diamond at low magnetic fields. *Proc. Natl. Acad. Sci. U.S.A.* **116,** 2512–2520 (2019).

158. Levitt, M. & Ernst, R. Composite pulses constructed by a recursive expansion procedure. *J. Magn. Reson. (1969)* **55,** 247–254 (1983).

159. Shaka, A. J. & Freeman, R. Composite Pulses with Dual Compensation. *J. Magn. Reson.* **55,** 487–493 (1983).

160. Levitt, M. H., Suter, D. & Ernst, R. R. Composite pulse excitation in three-level systems. *J. Chem. Phys.* **80,** 3064–3068 (1984).

161. Counsell, C., Levitt, M. & Ernst, R. Analytical theory of composite pulses. *J. Magn. Reson. (1969)* **63,** 133–141 (1985).

162. Tycko, R., Cho, H. M., Schneider, E. & Pines, A. Composite Pulses without Phase-Distortion. *J. Magn. Reson.* **61,** 90–101 (1985).

163. Levitt, M. H. Composite Pulses. *Prog. Nucl. Magn. Reson. Spectrosc.* **18,** 61–122 (1986).

164. Shaka, A. J. & Pines, A. Symmetric phase-alternating composite pulses. *J. Magn. Reson.* **71,** 495–503 (1987).

165. Skinner, T. E., Reiss, T. O., Luy, B., Khaneja, N. & Glaser, S. J. Application of optimal control theory to the design of broadband excitation pulses for high-resolution NMR. *J. Magn. Reson.* **163,** 8–15 (2003).

166. Kobzar, K., Skinner, T. E., Khaneja, N., Glaser, S. J. & Luy, B. Exploring the limits of broadband excitation and inversion pulses. *J. Magn. Reson.* **170,** 236–43 (2004).

167. Khaneja, N., Reiss, T., Kehlet, C., Schulte-Herbrüggen, T. & Glaser, S. Optimal control of coupled spin dynamics: Design of NMR pulse sequences by gradient ascent algorithms. *J. Magn. Reson.* **172,** 296–305 (2005).

168. Luy, B., Kobzar, K., Skinner, T., Khaneja, N. & Glaser, S. Construction of universal rotations from point-to-point transformations. *J. Magn. Reson.* **176,** 179–186 (2005).

169. Skinner, T. E., Reiss, T. O., Luy, B., Khaneja, N. & Glaser, S. J. Tailoring the optimal control cost function to a desired output: application to minimizing phase errors in short broadband excitation pulses. *J. Magn. Reson.* **172,** 17–23 (2005).

170. Kobzar, K., Skinner, T. E., Khaneja, N., Glaser, S. J. & Luy, B. Exploring the limits of broadband excitation and inversion: II. Rf-power optimized pulses. *J. Magn. Reson.* **194,** 58–66 (2008).

171. Kobzar, K., Ehni, S., Skinner, T., Glaser, S. & Luy, B. Exploring the limits of broadband 90° and 180° universal rotation pulses. *J. Magn. Reson.* **225,** 142–160 (2012).

172. Garwood, M., Nease, B., Ke, Y., De Graaf, R. A. & Merkle, H. Simultaneous compensation for B1 inhomogeneity and resonance offsets by a multiple-quantum NMR sequence using adiabatic pulses. *J. Magn. Reson. A* **112,** 272–274 (1995).

173. Spindler, P. E., Schops, P., Kallies, W., Glaser, S. J. & Prisner, T. F. Perspectives of shaped pulses for EPR spectroscopy. *J. Magn. Reson.* **280,** 30–45 (2017).

174. Tannus, A. & Garwood, M. Adiabatic pulses. *NMR Biomed.* **10,** 423–34 (1997).

175. Spindler, P. E., Schoeps, P., Bowen, A., Endeward, B. & Prisner, T. F. Shaped pulses in EPR. *eMagRes* **5** (2016).

176. Prisner, T. F. Shaping EPR: Phase and amplitude modulated microwave pulses. *J. Magn. Reson.* **306,** 98–101 (2019).

177. Froelich, T., Mullen, M. & Garwood, M. MRI exploiting frequency-modulated pulses and their nonlinear phase. *J. Magn. Reson.* **318,** 106779 (2020).

178. Foroozandeh, M. Spin dynamics during chirped pulses: applications to homonuclear decoupling and broadband excitation. *J. Magn. Reson.* **318,** 106768 (2020).

179. Kupče, Ē. Perspectives of adiabatic decoupling in liquids. *J. Magn. Reson.* **318,** 106799 (2020).

180. Dumez, J.-N. Frequency-swept pulses for ultrafast spatially encoded NMR. *J. Magn. Reson.* **323,** 106817 (2021).

181. Carvalho, J. P. & Pell, A. J. Frequency-swept adiabatic pulses for broadband solid-state MAS NMR. *J. Magn. Reson.* **324,** 106911 (2021).

182. Conolly, S., Glover, G., Nishimura, D. & Macovski, A. A reduced power selective adiabatic spin-echo pulse sequence. *Magn. Reson. Med.* **18,** 28–38 (1991).

183. Böhlen, J. M. & Bodenhausen, G. Experimental Aspects of Chirp NMR-Spectroscopy. *J. Magn. Reson. A* **102,** 293–301 (1993).

184. Tannüs, A. & Garwood, M. Improved performance of frequency-swept pulses using offset-independent adiabaticity. *J. Magn. Reson. A* **120,** 133–137 (1996).

185. Garwood, M. & DelaBarre, L. The return of the frequency sweep: designing adiabatic pulses for contemporary NMR. *J. Magn. Reson.* **153,** 155–77 (2001).

186. Kupče, Ē. & Freeman, R. Adiabatic Pulses for Wideband Inversion and Broadband Decoupling. *J. Magn. Reson. A* **115,** 273–276 (1995).

187. Rodrigues. Des lois géométriques qui régissent les déplacements d'un système solide dans l'espace, et de la variation des coordonnées provenant de ces déplacements considérés indépendamment des causes qui peuvent les produire. fre. *J. Math. Pures Appl.,* 380–440 (1840).

188. Verstraete, J.-B. *MRChirpLab* version 1.1. Nov. 23, 2022. `https://github.com/foroozandehgroup/MRChirpLab`.

189. Baum, J., Tycko, R. & Pines, A. Broadband and adiabatic inversion of a two-level system by phase-modulated pulses. *Phys. Rev. A* **32,** 3435–3447 (1985).

190. Kupče, Ē. & Freeman, R. Stretched adiabatic pulses for broadband spin inversion. *J. Magn. Reson. A* **117,** 246–256 (1995).

191. Landau, L. D. Zur Theorie der Energieubertragung II. *Z. Sowjetunion* **2,** 46–51 (1932).

192. Zener, C. & Fowler, R. H. Non-adiabatic crossing of energy levels. *Proc. Math. Phys. Eng. Sci.* **137,** 696–702 (1932).

193. Majorana, E. Atomi orientati in campo magnetico variabile. *Il Nuovo Cimento (1924-1942)* **9,** 43–50 (1932).

194. Stückelberg, E. Theory of inelastic collisions between atoms(Theory of inelastic collisions between atoms, using two simultaneous differential equations). *Helv. Phys. Acta,(Basel)* **5,** 369–422 (1932).

195. Meikle, H. *Modern radar systems* 2nd edition (Artech House, Boston, 2008).

196. Tsai, C. S. *Guided-wave acousto-optics: interactions, devices, and applications* (Springer Science & Business Media, 2013).

197. Siegman, A. E. *Lasers* (University Science Books, Mill Valley, Calif., 1986).

198. Bernstein, M. A., King, K. F. & Zhou, X. J. *Handbook of MRI pulse sequences* (Elsevier Academic Press, 2004).

199. Idiyatullin, D., Corum, C., Moeller, S. & Garwood, M. Gapped pulses for frequency-swept MRI. *J. Magn. Reson.* **193,** 267–273 (2008).

200. Landes, V. L. & Nayak, K. S. Simple method for RF pulse measurement using gradient reversal. *Magn. Reson. Med.* **79,** 2642–2651 (2018).

201. Skinner, T. E., Gershenzon, N. I., Nimbalkar, M. & Glaser, S. J. Optimal control design of band-selective excitation pulses that accommodate relaxation and RF inhomogeneity. *J. Magn. Reson.* **217,** 53–60 (2012).

202. Sarkar, S., Purusottam, R. N., Kumar, A. & Khaneja, N. Chirp pulse sequences for Broadband π rotation. *J. Magn. Reson.,* 107002 (2021).

203. Verstraete, J.-B. & Foroozandeh, M. Improved design of frequency-swept pulse sequences. *J. Magn. Reson.,* 107146 (2022).

204. Liu, D. C. & Nocedal, J. On the limited memory BFGS method for large scale optimization. *Math. Program.* **45,** 503–528 (1989).

205. Verstraete, J.-B. *MRChirpLab* version 1.0. Feb. 2, 2022. `https://github.com/foroozandehgroup/MRChirpLab`.

206. Sato, H. *et al.* Electron Spin Relaxation in x-Lithium Phthalocyanine. *J. Phys. Chem. B* **111,** 7972–7977 (2007).

207. Larsen, R. G. & Singel, D. J. Double electron–electron resonance spin–echo modulation: Spectroscopic measurement of electron spin pair separations in orientationally disordered solids. *J. Chem. Phys.* **98,** 5134–5146 (1993).

208. Blümler, P. *MATLAB NMR-Library*

209. Brinkmann, M., Turek, P. & André, J.-J. EPR study of the x,α and β structures of lithium phthalocyanine. *J. Mater. Chem.* **8,** 675–685 (1998).

210. Hürlimann, M. D. Carr–Purcell Sequences with Composite Pulses. *J. Magn. Reson.* **152,** 109–123 (2001).

211. Borneman, T. W., Hürlimann, M. D. & Cory, D. G. Application of optimal control to CPMG refocusing pulse design. *J. Magn. Reson.* **207,** 220–233 (2010).

212. Anand, C. K., Bain, A. D., Curtis, A. T. & Nie, Z. Designing optimal universal pulses using second-order, large-scale, non-linear optimization. *J. Magn. Reson.* **219,** 61–74 (2012).

213. Koroleva, V. D. M., Mandal, S., Song, Y.-Q. & Hürlimann, M. D. Broadband CPMG sequence with short composite refocusing pulses. *J. Magn. Reson.* **230,** 64–75 (2013).

214. Mandal, S., Koroleva, V. D. M., Borneman, T. W., Song, Y. Q. & Hürlimann, M. D. Axis-matching excitation pulses for CPMG-like sequences in inhomogeneous fields. *J. Magn. Reson.* **237,** 1–10 (2013).

215. Mandal, S., Borneman, T. W., Koroleva, V. D. M. & Hürlimann, M. D. Direct optimization of signal-to-noise ratio of CPMG-like sequences in inhomogeneous fields. *J. Magn. Reson.* **247,** 54–66 (2014).

216. Lingel, A. *et al.* Comprehensive and High-Throughput Exploration of Chemical Space Using Broadband 19F NMR-Based Screening. *Angew. Chem. Int. Ed.* **59,** 14809–14817 (2020).

217. Michaeli, S. *et al.* Exchange-influenced $T_{2\rho}$ contrast in human brain images measured with adiabatic radio frequency pulses. *Magn. Reson. Med.* **53,** 823–829. ISSN: 0740-3194 (2005).

218. Auer, R., Tollinger, M., Kuprov, I., Konrat, R. & Kloiber, K. Mathematical treatment of adiabatic fast passage pulses for the computation of nuclear spin relaxation rates in proteins with conformational exchange. *J. Biomol. NMR* **51,** 35 (2011).

219. Chao, F.-A. & Byrd, R. A. Geometric Approximation: A New Computational Approach To Characterize Protein Dynamics from NMR Adiabatic Relaxation Dispersion Experiments. *J. Am. Chem. Soc.* **138,** 7337–7345 (2016).

220. Coote, P., Bermel, W. & Arthanari, H. Optimization of phase dispersion enables broadband excitation without homonuclear coupling artifacts. *J. Magn. Reson.,* 106928 (2021).

221. Haller, J. D., Goodwin, D. L. & Luy, B. SORDOR pulses: expansion of the Böhlen-Bodenhausen scheme for low-power broadband magnetic resonance. *Magn. Reson.* **3,** 53–63 (2022).

222. Balchandani, P., Yamada, M., Pauly, J., Yang, P. & Spielman, D. Self-refocused spatial-spectral pulse for positive contrast imaging of cells labeled with SPIO nanoparticles. *Magn. Reson. Med.* **62,** 183–192 (2009).

223. Balchandani, P., Khalighi, M. M., Glover, G., Pauly, J. & Spielman, D. Self-refocused adiabatic pulse for spin echo imaging at 7 T. *Magn. Reson. Med.* **67,** 1077–1085 (2012).

224. Nyberg, N. *RBNMR* version 1.1.2.0. Feb. 1, 2022. `https://www.mathworks.com/matlabcentral/fileexchange/40332-rbnmr`.

225. Bengs, C. & Levitt, M. H. SpinDynamica: Symbolic and numerical magnetic resonance in a Mathematica environment. *Magn. Reson. Chem.* **56,** 374–414 (2018).

226. Jeschke, G. Quo vadis EPR? *J. Magn. Reson.* **306,** 36–41 (2019).

227. Dontchev, A. L. in *Lectures on Variational Analysis* (ed Dontchev, A. L.) 11–21 (Springer International Publishing, 2021).

228. Franklin, G. F., Powell, J. D. & Emami-Naeini, A. *Feedback control of dynamic systems* Eighth global (Pearson, 2020).

229. Feng, G. *et al.* Gradient-based closed-loop quantum optimal control in a solid-state two-qubit system. *Phys. Rev. A* **98,** 052341 (2018).

230. Wittler, N. *et al.* Integrated Tool Set for Control, Calibration, and Characterization of Quantum Devices Applied to Superconducting Qubits. *Phys. Rev. Applied* **15,** 034080 (3 2021).

231. Nelder, J. A. & Mead, R. A Simplex Method for Function Minimization. *Comput. J.* **7,** 308–313 (1965).

232. Powell, M. J. D. The BOBYQA algorithm for bound constrained optimization without derivatives. *University of Cambridge* **DAMTP 2009/NA06** (2009).

233. Powell, M. J. D. A View of Algorithms for Optimization without Derivatives. *University of Cambridge* **DAMTP 2007/NA03** (2007).

234. Cartis, C., Fiala, J., Marteau, B. & Roberts, L. Improving the Flexibility and Robustness of Model-based Derivative-free Optimization Solvers. *ACM Trans. Math. Softw.* **45,** Article 32 (2019).

235. Bardeen, C. J. *et al.* Feedback quantum control of molecular electronic population transfer. *Chem. Phys. Lett.* **280,** 151–158 (1997).

236. Damrauer, N. H. & Gerber, G. in *Laser Control and Manipulation of Molecules* 190–206 (American Chemical Society, 2002).

237. Weigel, A., Sebesta, A. & Kukura, P. Shaped and Feedback-Controlled Excitation of Single Molecules in the Weak-Field Limit. *J. Phys. Chem. Lett.* **6,** 4032–4037 (2015).

238. Egger, D. J. & Wilhelm, F. K. Adaptive Hybrid Optimal Quantum Control for Imprecisely Characterized Systems. *Phys. Rev. Lett.* **112,** 240503 (2014).

239. Skilton, R. A., Parrott, A. J., George, M. W., Poliakoff, M. & Bourne, R. A. Real-Time Feedback Control Using Online Attenuated Total Reflection Fourier Transform Infrared (ATR FT-IR) Spectroscopy for Continuous Flow Optimization and Process Knowledge. *Appl. Spectrosc.* **67,** 1127–1131 (2013).

240. Fitzpatrick, D. E., Battilocchio, C. & Ley, S. V. A Novel Internet-Based Reaction Monitoring, Control and Autonomous Self-Optimization Platform for Chemical Synthesis. *Org. Process Res. Dev.* **20,** 386–394 (2016).

241. Fath, V., Kockmann, N., Otto, J. & Röder, T. Self-optimising processes and real-time-optimisation of organic syntheses in a microreactor system using Nelder–Mead and design of experiments. *React. Chem. Eng.* **5,** 1281–1299 (2020).

242. Monea, C. Optimization of NQR excitation sequences using black-box techniques. *J. Magn. Reson.* **321,** 106858 (2020).

243. Yong, J. R. J. & Foroozandeh, M. On-the-Fly, Sample-Tailored Optimization of NMR Experiments. *Anal. Chem.* **93,** 10735–10739 (2021).

244. Goodwin, D. L., Myers, W. K., Timmel, C. R. & Kuprov, I. Feedback control optimisation of ESR experiments. *J. Magn. Reson.* **297,** 9–16 (2018).

245. Verstraete, J.-B., Yong, J. R. J. & Foroozandeh, M. *esrpoise* version 1.01. May 13, 2022. `https://github.com//foroozandehgroup/esrpoise`.

246. Schott, S. *XeprAPI update for Python 3* version 0.61. June 15, 2021. `https://github.com/OE-FET/XeprAPI`.

247. Dennis, J. J. E. & Torczon, V. Direct Search Methods on Parallel Machines. *SIAM J. Optim.* **1,** 448–474 (1991).

248. Verstraete, J.-B. *mrpypulse* version 1.0.0. Mar. 30, 2022. `https://github.com/foroozandehgroup/mrpypulse`.

249. Ragonneau, T. M. & Zhang, Z. *PDFO: Cross-Platform Interfaces for Powell's Derivative-Free Optimization Solvers* version 1.1. Nov. 1, 2021. `https://www.pdfo.net`.

250. Kulik, L. V., Dzuba, S. A., Grigoryev, I. A. & Tsvetkov, Y. D. Electron dipole–dipole interaction in ESEEM of nitroxide biradicals. *Chem. Phys. Lett.* **343,** 315–324 (2001).

251. Milikisyants, S., Scarpelli, F., Finiguerra, M. G., Ubbink, M. & Huber, M. A pulsed EPR method to determine distances between paramagnetic centers with strong spectral anisotropy and radicals: The dead-time free RIDME sequence. *J. Magn. Reson.* **201,** 48–56 (2009).

252. Teucher, M. & Bordignon, E. Improved signal fidelity in 4-pulse DEER with Gaussian pulses. *J. Magn. Reson.* **296,** 103–111 (2018).

253. Tait, C. E. & Stoll, S. Coherent pump pulses in Double Electron Electron Resonance spectroscopy. *Phys. Chem. Chem. Phys.* **18,** 18470–18485 (2016).

254. Fábregas Ibáñez, L. & Jeschke, G. Optimal background treatment in dipolar spectroscopy. *Physical Chemistry Chemical Physics* **22,** 1855–1868 (2020).

255. Shahriari, B., Swersky, K., Wang, Z., Adams, R. P. & de Freitas, N. Taking the Human Out of the Loop: A Review of Bayesian Optimization. *Proc. IEEE* **104,** 148–175 (2016).

256. Degen, C. L., Reinhard, F. & Cappellaro, P. Quantum sensing. *Rev. Mod. Phys.* **89,** 035002 (3 2017).

257. Jelezko, F. & Wrachtrup, J. Single defect centres in diamond: A review. *Phys. Status Solidi (a)* **203,** 3207–3225 (2006).

258. Doherty, M. W. *et al.* The nitrogen-vacancy colour centre in diamond. *Phys. Rep.* **528,** 1–45 (2013).

259. Loubser, J. H. N. & van Wyk, J. A. Electron spin resonance in the study of diamond. *Rep. Prog. Phys.* **41,** 1201–1248 (1978).

260. Jelezko, F., Gaebel, T., Popa, I., Gruber, A. & Wrachtrup, J. Observation of Coherent Oscillations in a Single Electron Spin. *Phys. Rev. Lett.* **92,** 076401 (2004).

261. Bar-Gill, N., Pham, L. M., Jarmola, A., Budker, D. & Walsworth, R. L. Solid-state electronic spin coherence time approaching one second. *Nat. Commun.* **4,** 1743 (2013).

262. Rondin, L. *et al.* Magnetometry with nitrogen-vacancy defects in diamond. *Rep. Prog. Phys.* **77,** 056503 (2014).

263. Schirhagl, R., Chang, K., Loretz, M. & Degen, C. L. Nitrogen-Vacancy Centers in Diamond: Nanoscale Sensors for Physics and Biology. *Annu. Rev. Phys. Chem.* **65,** 83–105 (2014).

264. Mamin, H. J. *et al.* Nanoscale Nuclear Magnetic Resonance with a Nitrogen-Vacancy Spin Sensor. *Science* **339,** 557 (2013).

265. Staudacher, T. *et al.* Nuclear Magnetic Resonance Spectroscopy on a (5-Nanometer)3 Sample Volume. *Science* **339,** 561 (2013).

266. Müller, C. *et al.* Nuclear magnetic resonance spectroscopy with single spin sensitivity. *Nat. Commun.* **5,** 4703 (2014).

267. Barry, J. F. *et al.* Optical magnetic detection of single-neuron action potentials using quantum defects in diamond. *Proc. Natl. Acad. Sci. U.S.A.* **113,** 14133 (2016).

268. Van der Est, A. in *EPR spectroscopy: fundamentals and methods* (eds Goldfarb, D. & Stoll, S.) 3–16 (John Wiley & Sons, 2016).

269. Gruber, A. *et al.* Scanning Confocal Optical Microscopy and Magnetic Resonance on Single Defect Centers. *Science* **276,** 2012–2014 (1997).

270. G., D. & F., H. M. Optical studies of the 1.945 eV vibronic band in diamond. *Proc. R. Soc. Lond. A.* **348,** 285–298 (1976).

271. Rogers, L. J. *et al.* Singlet levels of the NV-centre in diamond. *New J. Phys.* **17,** 013048 (2015).

272. Bucher, D. B. Principles of Nano- and Microscale NMR-Spectroscopy with NV-Diamond Sensors. *eMagRes,* 363–370 (2019).

273. Bucher, D. B. *et al.* Quantum diamond spectrometer for nanoscale NMR and ESR spectroscopy. *Nat. Protoc.* **14,** 2707–2747 (2019).

274. Tetienne, J.-P. *et al.* Spin properties of dense near-surface ensembles of nitrogen-vacancy centers in diamond. *Phys. Rev. B* **97,** 085402 (8 2018).

275. Smith, J. M., Meynell, S. A., Jayich, A. C. B. & Meijer, J. Colour centre generation in diamond for quantum technologies. *Nanophotonics* **8,** 1889–1906 (2019).

276. Ohno, K. *et al.* Engineering shallow spins in diamond with nitrogen delta-doping. *Appl. Phys. Lett.* **101,** 082413 (2012).

277. Wyk, J. A. v., Reynhardt, E. C., High, G. L. & Kiflawi, I. The dependences of ESR line widths and spin - spin relaxation times of single nitrogen defects on the concentration of nitrogen defects in diamond. *J. Phys. D: Appl. Phys.* **30,** 1790–1793 (1997).

278. Xu, L. *et al.* High-efficiency fluorescence collection for NV- center ensembles in diamond. *Opt. Express* **27,** 10787–10797 (2019).

279. Duan, D. *et al.* Efficient nitrogen-vacancy centers' fluorescence excitation and collection from micrometer-sized diamond by a tapered optical fiber in endoscope-type configuration. *Opt. Express* **27,** 6734–6745 (2019).

280. Glenn, D. R. *et al.* High-resolution magnetic resonance spectroscopy using a solid-state spin sensor. *Nature* **555,** 351–354 (2018).

281. Allert, R. D., Briegel, K. D. & Bucher, D. B. Advances in nano- and microscale NMR spectroscopy using diamond quantum sensors. *Chem. Commun.* **58,** 8165–8181 (2022).

282. Blümich, B. Low-field and benchtop NMR. *J. Magn. Reson.* **306,** 27–35 (2019).

283. Demas, V. & Prado, P. J. Compact magnets for magnetic resonance. *Concepts Magn. Reson. A* **34A,** 48–59 (2009).

284. Guina, M., Rantamäki, A. & Härkönen, A. Optically pumped VECSELs: review of technology and progress. *J. Phys. D: Appl. Phys.* **50,** 383001 (2017).

285. Heintzmann, R. in *Fluorescence Microscopy* 393–401 (John Wiley & Sons, 2013). ISBN: 9783527671595.

286. Craik, D. P. L. *qdSpectro* version 1.0.1. July 15, 2022. `https://doi.org/10.5281/zenodo.3378208`.

287. Zienkiewicz, O. C., Taylor, R. L. & Zhu, J. Z. *The finite element method: its basis and fundamentals* (Elsevier, 2005).

288. Bi, Z. *Finite Element Analysis Applications: A Systematic and Practical Approach* (Academic Press, 2017).

289. Reddy, J. N. *Introduction to the Finite Element Method* 4th edition (McGraw-Hill Education, New York, 2019).

290. Bjørk, R., Smith, A. & Bahl, C. R. H. Analysis of the magnetic field, force, and torque for two-dimensional Halbach cylinders. *J. Magn. Magn. Mater.* **322,** 133–141 (2010).

291. Blümler, P. Proposal for a permanent magnet system with a constant gradient mechanically adjustable in direction and strength. *Concepts Magn. Reson. B: Magn. Reson. Eng.* **46,** 41–48 (2016).

292. Rooney, W. *MRI: From Picture to Proton* (Cambridge University Press, 2003).

293. Reijerse, E. & Savitsky, A. in *eMagRes* 187–206 (John Wiley & Sons, 2017).

294. Pyrhonen, J., Jokinen, T. & Hrabovcova, V. *Design of rotating electrical machines* (John Wiley & Sons, 2013).

295. Lovchinsky, I. *et al.* Nuclear magnetic resonance detection and spectroscopy of single proteins using quantum logic. *Science* **351,** 836–841 (2016).

296. Le Sage, D. *et al.* Optical magnetic imaging of living cells. *Nature* **496,** 486–489 (2013).

297. Boretti, A., Rosa, L., Blackledge, J. & Castelletto, S. Nitrogen-vacancy centers in diamond for nanoscale magnetic resonance imaging applications. *Beilstein J. Nanotechnol.* **10,** 2128–2151 (2019).

298. Dirk-Jan, K. *FMINLBFGS: Fast Limited Memory Optimizer* version 1.8.0.0. Nov. 15, 2021. `https://www.mathworks.com/matlabcentral/fileexchange/23245-fminlbfgs-fast-limited-memory-optimizer`.

299. Foroozandeh, M. & Singh, P. Optimal control of spins by Analytical Lie Algebraic Derivatives. *Automatica* **129,** 109611 (2021).

300. Gershenzon, N. I. *et al.* Linear phase slope in pulse design: Application to coherence transfer. *J. Magn. Reson.* **192,** 235–243 (2008).

301. Asami, S. *et al.* Ultrashort Broadband Cooperative Pulses for Multidimensional Biomolecular NMR Experiments. *Angew Chem. Int. Ed.* **57,** 14498–14502 (2018).

302. Rosenfeld, D. & Zur, Y. Design of adiabatic selective pulses using optimal control theory. *Magn. Reson. Med.* **36,** 401–409 (1996).

303. Ehni, S. *et al.* Concurrent J-evolving refocusing pulses. *J. Magn. Reson.* **336,** 107152 (2022).

304. Tošner, Z., Brandl, M. J., Blahut, J., Glaser, S. J. & Reif, B. Maximizing efficiency of dipolar recoupling in solid-state NMR using optimal control sequences. *Sci. Adv.* **7,** eabj5913 (2021).

305. Nguyen, T. T. & Glaser, S. J. An optimal control approach to design entire relaxation dispersion experiments. *J. Magn. Reson.* **282,** 142–153 (2017).